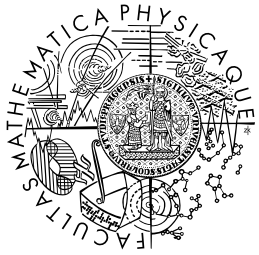

FACULTY
OF MATHEMATICS
AND PHYSICS
Charles University

DOCTORAL THESIS

Emil Varga

Experimental and numerical investigation of quantum turbulence in He II.

Department of Low Temperature Physics

Supervisor of the doctoral thesis:	prof. RNDr. Ladislav Skrbek, DrSc.
Study programme:	Physics
Study branch:	Physics of Condensed Matter and Materials Research

Prague 2018

I declare that I carried out this doctoral thesis independently, and only with the cited sources, literature and other professional sources.

I understand that my work relates to the rights and obligations under the Act No. 121/2000 Sb., the Copyright Act, as amended, in particular the fact that the Charles University has the right to conclude a license agreement on the use of this work as a school work pursuant to Section 60 subsection 1 of the Copyright Act.

In Prague date 15.7.2018 signature of the author

Title: Experimental and numerical investigation of quantum turbulence in He II.

Author: Emil Varga

Department: Department of Low Temperature Physics

Supervisor: prof. RNDr. Ladislav Skrbek, DrSc., Department of Low Temperature Physics

Abstract: Superfluid ^{4}He (He II) is a quantum liquid whose flow is strongly affected by quantum mechanical effects. This thesis presents experimental and numerical studies of turbulent flows in He II – *quantum turbulence*. Experimentally, quantum turbulence is investigated in thermal counterflow, pure superflow and coflow using second sound attenuation, precision local thermometry and by visualisation of helium excimer molecules. The steady state and decay of the vortex line density in pure superflow and counterflow is studied and the universal quasi classical decay is characterised by measurements of the effective kinematic viscosity. General dynamical behaviour is studied in detail in unsteady thermal counterflow, with various theoretical models tested. A new model where the mean tangle curvature is dependent on the vortex line density is proposed. Temperature dependence and enhancement of intermittency in quasi-classical flow in the wake of a moving grid is found using visualisation. Numerically, the interaction of the tangle of quantized vortices with solid tracers is investigated, where a back reaction of the seeding particles on the tangle is identified and its relevance to visualisation experiments is discussed. Additionally, an interesting and as-yet overlooked spherical counterflow is studied, where a possible critical temperature for the creation of turbulence was found. The findings are explained in terms of a transparent physical model.

Keywords: superfluidity turbulence helium

First and foremost I would like to thank my supervisor Ladik Skrbek for help and guidance throughout the duration of the doctoral programme. The experiments performed in Prague would not have been possible without him and the tremendous help of friends and colleagues S. Babuin, M. J. Jackson, D. Schmoranzer, P. Švančara and all other colleagues, students and friends in the laboratory of superfluidity.

The presented work was graciously supported by the Czech Science Foundation and the Granting Agency of the Charles University, which allowed for construction and upgrade of experimental setups and also two visits with the group of C. F. Barenghi and Y. A. Sergeev at the Newcastle University studying numerical simulations based on the vortex filament model to whom I would also like to extend my thanks.

The experimental work on visualisation using helium excimer molecules was only possible thanks to the hospitality of W. Guo and the National High Magnetic Field Laboratory in Tallahassee, Florida, and generous financial support of Karel Urbánek fund of the Charles University. The work I performed at the NHMFL would not have been possible without the help and support of J. Gao and B. Mastracci.

Last but not least I am grateful to my family for supporting me throughout my studies.

Contents

Introduction

Flows of fluids at sufficiently high velocities exhibit chaotic properties. This phenomenon is called turbulence. Turbulent behaviour of fluids underpins much of our every day experiences, ranging from the drag experienced by a moving vehicle to a certain degree of unpredictability of tomorrows' weather. Flows of fluids, in particular turbulent ones, have been the subject of scientific inquiry for well over a century and turbulence is sometimes regarded as the last unsolved problem of classical physics. The presented thesis aims to explore this classical problem of turbulence in a quantum liquid, specifically the superfluid ^{4}He. Such phenomenon is called quantum turbulence [1].

While turbulence is chaotic and unpredictable, it is not random [2]. The turbulent velocity field is not a featureless, continuous analogue of white noise. An important characteristic of turbulent flows is the presence of dynamics occurring at many scales simultaneously. Eddies and vortices with a range of sizes and strengths are embedded in the turbulent flow. The scenario of the behaviour of this multitude of scales (for three-dimensional turbulence) can be described in terms of the Richardson cascade, illustrated in Fig. 1. The size of the largest eddies is given by the scale of the energy injection. These large eddies break up, due to the non-linear effects of the governing Navier-Stokes equations, into smaller eddies with negligible loss of energy. This process repeats itself recursively until the small scale of turbulence is reached – the Kolmogorov length scale – where the viscous dissipation dominates over the non-linear effects. At this scale, the small eddies are dissipated into heat via friction.

Sandwiched between the large (energy injection) and small (dissipation) scales is the *inertial range of scales*, where energy is conserved as it flows from the larger to the smaller scales. On the assumption of homogeneity, isotropy and self-similarity of the turbulent flow within the inertial range, Kolmogorov [3] and Obukhov [4] derived a statistical theory (so-called K41) of turbulence, successfully predicting, among other things, the distribution of the turbulent kinetic energy across scales. While the homogeneity and isotropy of turbulence can be well approximated by a suitable choice of the experimental conditions, self-similarity of turbulence across scales was found to be broken [5], a phenomenon referred to as the turbulence intermittency.

In the presented thesis, turbulence was studied in the superfluid ^{4}He, typically called He II. He II belongs to a wider class of quantum fluids, of which other notable examples are the several superfluid phases of ^{3}He or the Bose-Einstein condensates of cold atomic gasses. Turbulence in He II has two primary features [6] that distinguish it from the classical version: (i) the two-fluid nature – He II behaves as if consisting of two interpenetrating fluid components – the normal and the superfluid, and (ii) the presence of a complex tangle of thin topological defects – quantized vortices – in the superfluid component.

Many aspects of classical turbulence have their quantum turbulence counterparts. Energy is distributed across scales and (for three-dimensional turbulence) cascades (typically) towards the small scales [7]. Decay of quantum turbulence is observed in many cases to proceed in a patently classical fashion. He II, when stirred classically, behaves approximately as a single-component classical fluid

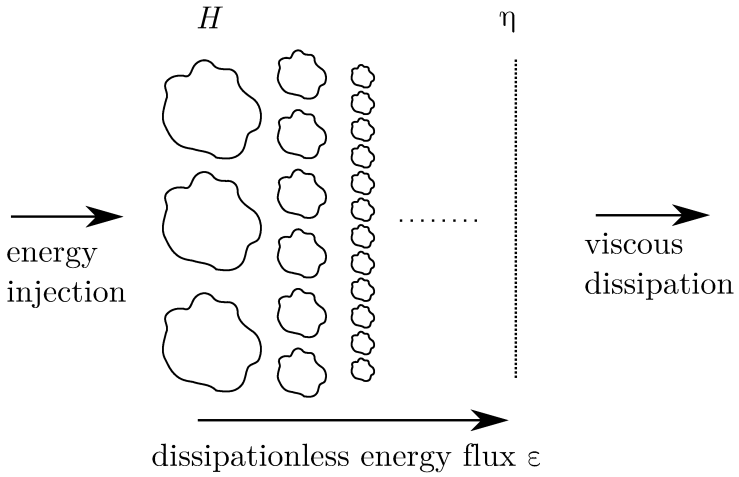

Figure 1: The Richardson cascade. Large eddies are split up to smaller and smaller eddies recursively with no loss of energy, thus transferring the energy from the large scales to the small at rate $\epsilon = -\mathrm{d}\,E/\mathrm{d}\,t$. The process continues until the dissipation scale η is reached, where the eddies are dissipated into heat via the viscosity.

with an effective viscosity [8, 9]. However, even from the very first pioneering experiments of Hall and Vinen [10, 11] and Vinen [12, 13, 14, 15], important differences were apparent. The two-fluid nature of He II allows for flows with no classical analogues, such as the thermal counterflow, where the two fluids flow in anti-parallel directions with zero net mass transport. The mutual friction between the two components can cause dissipation on all scales [16, 17], not just the smallest. The small scale of quantum turbulence is not marked by the simple dominance of viscous effects, but also by the importance of discrete nature of individual quantized vortices on scales comparable with their separation [18]. Unique types of turbulence exist at very low temperatures either in He II, where viscous dissipation of the normal component is absent or in ^{3}He-B, where the normal component is clamped by the system walls due to the high viscosity [19, 20].

Presented in the thesis is the experimentally investigated behaviour of quantum turbulence in the steady-state counterflow (Sec. 3.2) where the temperature gradient is measured directly inside the flow even very close to the heat source; decays (Sec. 3.3), which are found to be strongly affected by the motion of the normal component relative to the walls of the system; and more general non-steady counterflow (Sec. 3.4), where the general dynamical behaviour of the vortex tangle is studied and an estimation of the mean tangle curvature is proposed. Additionally, decaying coflow turbulence is studied (Sec. 3.5) using the He_2^* visualisation experimental technique [21, 22] where non-classical, temperature-dependent behaviour of turbulence intermittency is found.

Two problems are studied numerically. First, the interaction of solid particles with the vortex tangle (Sec. 4.2), an important problem relevant to the interpretation of visualisation studies. Second, a spherically symmetric thermal counterflow (Sec. 4.3), which exhibits an interesting property of possible existence of a critical temperature above which the turbulence does not develop.

The thesis is structured as follows. Chapter 1 provides a brief overview of the superfluidity in ^{4}He and the relevant literature. The methods of investigation, both experimental and numerical, are described in detail in Chapter 2. The results of the thesis are separated into two Chapters, the experimental results are shown in Chapter 3 and the numerical results in Chapter 4. The main analysis and discussion is presented alongside the data in Chapters 3 and 4. The obtained results are followed by a brief overall discussion and the conclusions.

The research presented in this thesis was published in several articles listed in the Attachments. Reprints of a selection of articles most relevant to the thesis are provided as attachments, including preprints of two submitted articles where the peer review has not yet concluded at the time of submission of the thesis.

1. Superfluidity and quantum turbulence

This chapter briefly summarises the basic facts on the superfluidity in ^{4}He in Sec. 1.1 and provides an overview of the turbulence in this quantum fluid in Sec. 1.2.

1.1 Superfluid helium-4

Helium-4 boils at atmospheric pressure at approximately 4.2 K. As can be seen in the phase diagram in Fig. 1.1, ^{4}He possesses no triple point and remains liquid down to the absolute zero at ambient pressures. Upon cooling, however, ^{4}He does undergo a second-order phase transition into a superfluid phase denoted as He II (the phase above the transition being known as He I). The superfluid transition, often called the λ transition, occurs at a weakly pressure dependent temperature T_λ with $T_\lambda \approx 2.17$ K at saturated vapour pressure.

He II exhibits several non-classical features [6]. Following the two-fluid model of Landau and Tisza, He II can be described as consisting of two interpenetrating and semi-independent fluid components: the superfluid and the normal component. Each component supports its own velocity field – $\mathbf{v}_\mathrm{s}$ and $\mathbf{v}_\mathrm{n}$, respectively – and has a temperature dependent density, shown in Fig. 1.2 – ρ_s, ρ_n – with the sum of the densities equal to the total density of He II, ρ. The mass flux is then given by

$$\mathbf{j} = \rho_s \mathbf{v}_\mathrm{s} + \rho_n \mathbf{v}_\mathrm{n}. \tag{1.1}$$

The normal fluid behaves approximately classically – possessing non-vanishing viscosity and entropy. The superfluid component, on the other hand, has zero viscosity and entropy (the entire entropy content of He II being carried by the normal fluid). Furthermore, the superfluid velocity is given by the gradient of the macroscopically coherent phase,

$$\mathbf{v}_\mathrm{s} = \frac{\hbar}{m_4} \nabla S, \tag{1.2}$$

where m_4 is the mass of the ^{4}He atom and $\hbar = h/2\pi$ stands for the reduced Planck constant. This immediately leads to the quantisation of circulation Γ around a closed loop $\mathcal{C}$,

$$\Gamma = \oint_\mathcal{C} \mathbf{v}_\mathrm{s} \,\mathrm{d}\mathbf{l} = \frac{\hbar}{m_4} \oint_\mathcal{C} \nabla S \,\mathrm{d}\mathbf{l} = \frac{\hbar}{m_4} 2\pi n = n\kappa, \tag{1.3}$$

where the second-to-last expression follows due to the requirement that the macroscopic wave function must be single-valued and

$$\kappa = \frac{h}{m_4} \approx 9.997 \times 10^{-4} \text{ cm}^2/\text{s} \tag{1.4}$$

is the quantum of circulation. In a simply connected region (i.e., closed loops can be arbitrarily continuously deformed) the circulation around any closed loop is

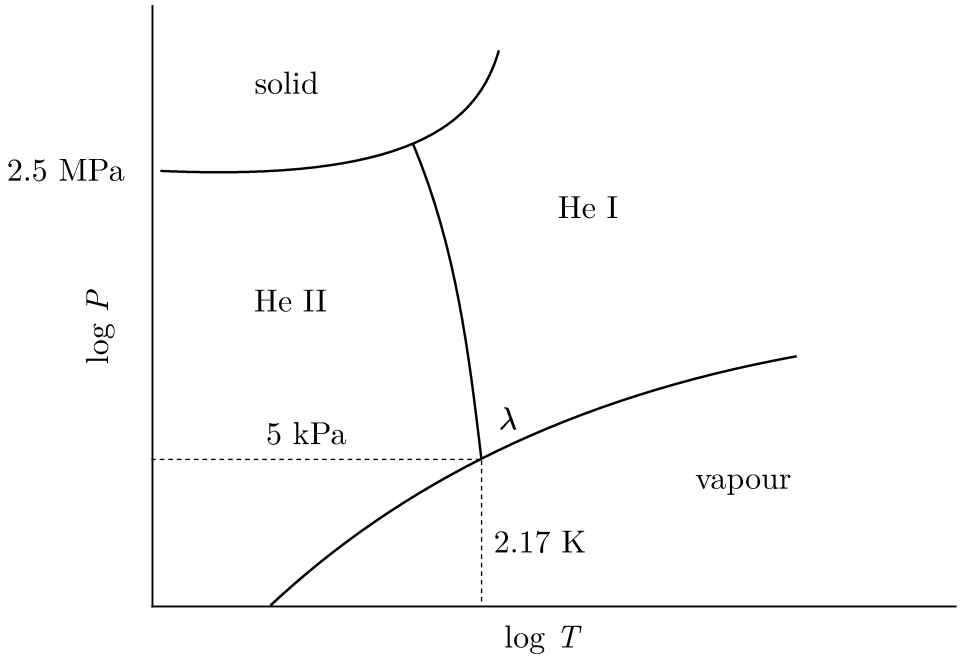

Figure 1.1: Sketch of the phase diagram of ^{4}He .

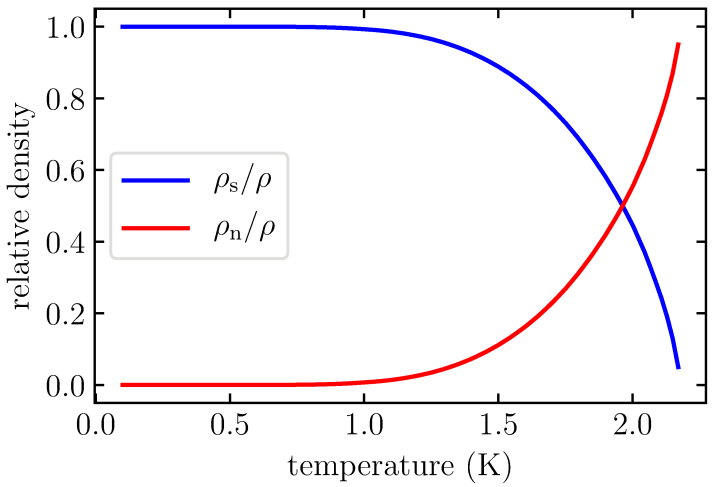

Figure 1.2: Temperature dependence of the normal and superfluid densities.

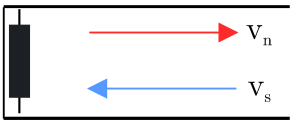

Figure 1.3: Experimental arrangement of thermal counterflow. A resistive heat source is placed at the closed end of a flow channel with the opposite end open to the helium bath.

identically zero, $n \equiv 0$. Vortices in the superfluid component of He II – *quantized vortices* – take the form of thin topological defects (i.e., the vortices cannot terminate within the fluid) each of which carry a single quantum of circulation and on whose cores the superfluidity is suppressed. The quasi-particle thermal excitations composing the normal fluid scatter off the cores of quantized vortices [23] and thus couple the two components together, a process known as *mutual friction* (see Sec. 2.2.1 for the discussion of the effect the mutual friction has on the motion of the vortices).

The two-fluid behaviour allows for considerably more freedom in the types of motions (notable non-classical example being the thermal counterflow discussed in the next section) that can exist in He II. An important wave process unique to He II is the second sound, where the normal and superfluid components of He II oscillate in anti-phase with total density approximately constant, thus creating a wave of temperature or entropy (ordinary sound, the wave of pressure or density, is referred to as the first sound). The mutual friction attenuates second sound, which can be exploited for measurement of vortex line density [24] – the total length of quantized vortices per unit volume, as discussed in more detail in Sec. 2.1.3.

1.2 Quantum turbulence in He II

Quantum turbulence in He II takes the form of a complex tangle of quantized vortices which interacts with (possibly turbulent) normal fluid through the mutual friction [1]. Quantum turbulence can be generated in a wide variety of experimental setups, ranging from quasi classical stirring and pipe flows (see Sec. 1.2.1), vibrating forks [25, 26, 27] and wires [28] to flows generated by a heat flux (see below) or through injection and dragging of ions [29].

Historically, starting from the pioneering experiments of Hall and Vinen [10, 11], the most studied form of quantum turbulence in He II is that occurring in the thermal counterflow. A heat source is placed at the closed end of the flow channel and its other end is left open to the helium bath, as shown in Fig. 1.3. The heater, dissipating power $\dot{Q}$, deposits entropy $\dot{Q}/T$ in the system at temperature T, which is carried away by the normal fluid into the bath. To balance the outflow of the normal component, the superfluid flows toward the heater, where it is converted to the normal fluid. The resulting counterflow velocity is given by

$$v_{\mathrm{ns}} = v_{\mathrm{n}} - v_{\mathrm{s}} = \frac{\dot{Q}}{\rho S T A}, \tag{1.5}$$

where A is the cross section area of the channel and S is the entropy density of He II.

Early experiments of Gorter and Mellink [30] revealed that the heat conductivity of He II above a certain critical heat flux is strongly non-linear, with the temperature gradient along the counterflow channel depending on the supplied heat flux as

$$\nabla T \propto \dot{Q}^m, \tag{1.6}$$

where m varies between approximately 3 and 3.5, depending on the temperature [31]. As a side note, classical turbulence, specifically the thermal convection, can also be activated via heat flux. The mechanism, however, is not the advection of the produced entropy as in counterflow but rather buoyancy caused by the thermal expansion which also necessitates presence of an additional volumetric force such as the gravity.

The temperature distribution is also very different in counterflow and convection. Whereas in thermal convection the temperature is approximately constant in the turbulent bulk between the hot and cold ends with the temperature gradient concentrated to the vicinity of the end plates, the temperature gradient in thermal counterflow is spatially constant, temperature having a linear profile along the entire turbulent channel. Interestingly, recent visualisation experiments of Hrubcová *et al.* [32] demonstrated a boundary region near the heat source in thermal counterflow, although, this has not yet been observed with thermometry (see Sec. 3.2).

A common and easily experimentally accessible characteristic of quantum turbulence is the vortex line density L – the total length of the quantized vortex lines per unit volume. In a steady-state thermal counterflow, the vortex line density (VLD) was found to scale with the counterflow velocity v_{ns} as

$$L = \gamma^2 (v_{\mathrm{ns}} - v_{\mathrm{c}})^2, \tag{1.7}$$

where v_{c} is the critical velocity typically of the order of 1 mm/s and γ is a temperature dependent parameter. The temperature gradient in thermal counterflow stems from the balance between the friction that the vortices exert on the normal fluid (and vice versa) through the effect of mutual friction and the mechanocaloric force [33][1] linear in ∇T. In light of this, the Gorter Mellink expression can be rewritten as $\nabla T \propto L v_{\mathrm{ns}}$ for a steady state homogeneous counterflow.

For a general time evolution of vortex line density, Vinen [14] derived, using primarily dimensional arguments, the dynamical equation for vortex line density which reads

$$\frac{\mathrm{d}\,L}{\mathrm{d}\,t} = \left(\frac{\mathrm{d}\,L}{\mathrm{d}\,t}\right)_{\mathrm{gen.}} + \left(\frac{\mathrm{d}\,L}{\mathrm{d}\,t}\right)_{\mathrm{decay}} = \frac{1}{2}\chi_1 B \frac{\rho_n}{\rho} v_{\mathrm{ns}} L^{3/2} - \frac{\chi_2}{2\pi}\kappa L^2, \tag{1.8}$$

where B is a temperature-dependent mutual friction coefficient [34] and χ_1, χ_2 are temperature-dependent free parameters. This equation correctly describes the steady state (i.e, $\dot{L} = 0$) scaling of vortex line density $L \propto v_{\mathrm{ns}}^2$, although it does not account for the finite critical velocity, as the $L = 0$ fixed point of Eq. (1.8) is always unstable for a non-zero v_{ns}. This issue is sometimes rectified by the addition of an unspecified, geometry-dependent term $g(L, v_{\mathrm{ns}})$ which absorbs the phenomena relating to critical velocities.

[1] Which is responsible for the fountain effect.

The dynamical equation (1.8) was put on more solid footing by Schwarz [35] who derived it on the basis of vortex filament model (Sec. 2.2.1) in the local induction approximation, and for tangles of relatively low density and small deviations from the steady state. In this version the equation reads

$$\frac{\partial L}{\partial t} = \alpha I_l v_{\mathrm{ns}} L^{3/2} - \beta \alpha c_2^2 L^2, \tag{1.9}$$

where

$$\beta = \frac{\kappa}{4\pi} \log\left(\frac{1}{c_1 L^{1/2} \xi}\right), \tag{1.10}$$

with ξ denoting the vortex core parameter, I_l one of the anisotropy parameters introduced by Schwarz [35] and c_1 and c_2 are defined through $\bar{S} = c_1 L^{1/2}$, $\tilde{S} = c_2 L^{1/2}$ where $\bar{S}$ and $\tilde{S}$ are mean and RMS, respectively, curvatures of the vortex lines in the turbulent tangle. Recently, this form of the dynamical equation (as well as its mere existence [36]) was challenged on theoretical and numerical grounds [37, 38] with several new proposals. Restricting the attention to cases of homogeneous turbulence (i.e., no vortex flux term) and without new and as-yet experimentally inaccessible terms, the proposals (apart from abandoning the concept altogether) can be summarised in the form

$$\frac{\partial L}{\partial t} = \mathcal{A}_n v_{\mathrm{ns}}^n L^{2-n/2} - \mathcal{B}_n L^2, \tag{1.11}$$

where $\mathcal{A}_n$, $\mathcal{B}_n$ are adjustable parameters and n is 1, 2, or 3. It is found in Sec. 3.4 that the region of validity of Eq. (1.9) is greater than perhaps expected, especially if one is less concerned with the decay. Moreover, the agreement with experiments, including early decay, can be significantly improved if the geometrical factor c_2, connecting RMS tangle curvature and inter-vortex distance, is allowed to vary.

The Vinen-like equations (1.11) predict the free decay ($v_{\mathrm{ns}} = 0$) of vortex line density as $L \propto t^{-1}$. This was indeed observed for counterflow of small intensity [39, 13] or in the very early stages of more intense counterflow and pure superflow [40, 41] (see Sec. 3.3). Even though the Vinen equation was developed to describe counterflow experiments, the t^{-1} decay was observed also in the zero-temperature limit [29]. The decay term in the Vinen equation arises from a picture of random collisions and annihilations of the vortices, that is, the so-called "ultra quantum" decay t^{-1} is observed for tangles with no structure on scales larger than the inter-vortex distance (the so-called quantum length scale).

The VLD dynamical equations outlined above are applicable to the thermal counterflow and pure superflow, i.e., flows with forced difference between the normal and superfluid mean velocities. Coflow (flow with no forced difference between the mean normal and superfluid velocities) was found to scale [9] as $L \propto v^{3/2}$, with v denoting the mean flow velocity in the pipe. Vinen-like equations also do not correctly describe the free decay of vortex line density, regardless of the flow type (Sec. 3.3). Experimentally, the late stage decay typically displays quasi-classical $t^{-3/2}$ scaling (for all types of flow; discussed in more detail in the next section). For the early decay of thermal counterflow, a non-monotonous time dependence of vortex line density is typically observed (see Fig. 3.9). Non monotonous behaviour cannot, in principle, be described by a first-order autonomous system $\partial L/\partial t = F(L)$ (such as Eq. (1.11) for $v_{\mathrm{ns}} = 0$).

Clearly, the behaviour of counterflow, especially its free decay, is too complex to allow satisfactory description in terms of the VLD dynamics alone. Using novel visualisation method of laser-induced fluorescence of the He_2^* molecules, several non-classical features of thermal counterflow previously unaccounted for were observed. The turbulent fluctuations in the thermal counterflow can be significantly higher than in classical turbulence [42, 43], with turbulence intensity (ratio of the velocity fluctuations to the mean flow velocity) ranging from about 10% at low temperatures to nearly 100% at high temperatures (compared to a typical value of about 5%–10% in classical pipe flow turbulence [44]).

Furthermore, and more importantly, the structure functions of the normal fluid velocity field, and by extension the scaling of the turbulent energy spectrum, can be studied [21]. It was found that in the steady state thermal counterflow, the energy spectrum roll-off exponent changes with temperature and heat flux [42] but is always higher than the 5/3 of the Kolmogorov K41 theory. During the decay, the energy spectrum was found to evolve in time from a non-classical to a classical one with this transition roughly coinciding with transition to the quasi-classical $t^{-3/2}$ decay of vortex line density. Note that a roll-off exponent higher than 5/3 signifies energy dissipation at all scales, contrary to the dissipation-free inertial range of classical turbulence. It is believed that this dissipation is caused by mutual friction attenuating eddies in the two components which are torn apart by the mean counterflow [16, 17].

The re-distribution of the energy across scales manifested by the change in roll off exponent of the energy spectrum causes influx of energy from the large to the small scales, which is believed to be the mechanism behind the appearance of the non-monotonic decay [41, 17] (see Sec. 3.3 for detailed discussion).

1.2.1 Quasi-classical quantum turbulence

In certain cases quantum turbulence displays a quasi-classical character, behaving as a single-component liquid characterised by an effective viscosity. For He II in the two fluid regime, the single-fluid behaviour stems from locking of the flows of the two fluids by the mutual friction [45]. Examples include flow stirred by counter-rotating discs [46], pressure-driven flows past a grid [47, 9], decaying turbulence in the wake of a moving grid [8, 48] (see also Sec. 3.5) or polarised tangles in the zero temperature limit [29].

An important idea in the quasi-classical treatment of quantum turbulence is the identification of dissipation $\epsilon \equiv -\,\mathrm{d}\,E/\,\mathrm{d}\,t$ of the turbulent kinetic energy E with the vortex line density L through an effective viscosity ν_{eff},

$$\epsilon = \nu_{\mathrm{eff}} \left(\kappa L\right)^2 , \tag{1.12}$$

in analogy with the classical expression $\epsilon = \nu \left\langle \omega^2 \right\rangle$, where $\left\langle \omega^2 \right\rangle$ is the mean square vorticity.

Indeed, defining Reynolds number in analogy with classical relationships as

$$\mathrm{Re}_\kappa \equiv \frac{\epsilon^{1/3} H^{4/3}}{\kappa} \equiv \frac{v H}{\kappa}, \tag{1.13}$$

where v is the root mean square of velocity fluctuations and $H \equiv v^3/\epsilon$ is the

characteristic length scale of the flow, and substituting back to (1.12) leads to

$$\frac{\ell}{H} = \left(\frac{\nu_{\mathrm{eff}}}{\kappa}\right)^2 \mathrm{Re}_\kappa^{-3/4}. \tag{1.14}$$

Relationship (1.14) is indeed observed experimentally in a steady state coflow (pressure-driven simultaneous flow of both components) [9], with the effective viscosity ν_{eff} approximately independent of the temperature above roughly 1 K, although the data suffer from large experimental scatter. For low temperatures below roughly 0.8 K the observed effective viscosity is flow-dependent, with a general trend to decrease with decreasing temperature [49, 50]. The effective viscosity of He II, unlike viscosity in classical fluids, is *not* a material parameter of He II. Dissipation of turbulence in He II is necessarily an interplay of normal fluid viscosity, dynamics of individual vortices and (above 1 K) the mutual friction, thus it should not be expected a priori that a single parameter will be able to describe the multitude of possible flows.

In terms of the VLD and the mean flow velocity V, Eq. (1.14) reads $L \propto V^{3/2}$. Coflow turbulence in a channel was found [24] to be inhomogeneous (transversally to the flow direction), meaning that the vortex line density must be understood as a spatial average over the channel cross section.

Historically, the common method to measure the effective viscosity is through a quasi-classical decay of quantum turbulence characterised by $L \propto t^{-3/2}$ late-decay scaling. This decay regime is commonly present not only in the coflow [47, 8] but also in thermal counterflow and pure superflow [40, 51] (also Fig. 3.7) and in the zero-temperature limit [29, 49]. Skrbek *et al.* [48] and Stalp *et al.* [8] developed a theory of a *classical* decay based on the assumption of the presence of the Kolmogorov energy spectrum $E = C\epsilon^{2/3}k^{-5/3}$, where $C \approx 1.5$ is the Kolmogorov constant. Assuming further that the large scale of turbulence is saturated by the size of the system and using the dissipation relationship Eq. (1.12) one can obtain [48]

$$L(t) = \frac{H\,(3C)^{3/2}}{2\pi\kappa\nu_{\mathrm{eff}}^{1/2}} t^{-3/2}, \tag{1.15}$$

which allows determination of the effective viscosity from the scaling prefactor of a quasi-classical decay. It should be noted that to simply arrive at the correct scaling $L \propto t^{-3/2}$ the assumption of the Kolmogorov spectrum can be relaxed [52, 53]. Assuming that the large eddies, of velocity scale U and spatial scale H, decay roughly within their turnover time H/U one gets for the energy dissipation $-\mathrm{d}\,E/\mathrm{d}\,t = \epsilon = U^3/H = E^{3/2}/H$ with $E \approx U^2$. Solving for E, $E \propto t^{-2}$, thus $\epsilon \propto t^{-3}$ and substituting back to Eq. (1.12) one immediately gets $L \propto t^{-3/2}$, although the prefactors in this approach are less controlled.

With the advent of the visualisation based on the laser-induced fluorescence of the He_2^* molecules it became possible to measure the turbulent kinetic energy of the normal fluid (as mean square velocity fluctuations). Assuming the normal and superfluid velocity fields are fully coupled, one can compare the decay of vortex line density with the decay of kinetic energy and use Eq. (1.12) directly to obtain the effective viscosity. The results obtained for thermal counterflow [51] are in agreement with previous experiments, strengthening the validity of Eq. (1.12).

To a lesser degree, studies of quasi-classical quantum turbulence progressed beyond vortex line density scaling and effective viscosity. Numerical approaches based on a continuous model of quantum turbulence [54, 55] studied the scaling of longitudinal velocity structure functions of higher order. The longitudinal velocity structure function of order n is defined as

$$S_n^{\parallel}(R) = \langle [\delta \mathbf{u}(\mathbf{r}, \mathbf{R}) \cdot \mathbf{R}/R]^n \rangle \,, \tag{1.16}$$

where $\delta \mathbf{u}(\mathbf{r}, \mathbf{R}) \equiv \mathbf{u}(\mathbf{r} + \mathbf{R}) - \mathbf{u}(\mathbf{r})$ is a velocity difference with separation $\mathbf{R}$ and $\mathbf{u}$ is the turbulent velocity field which is assumed to be homogeneous and isotropic. The Kolmogorov theory predicts scaling of the structure functions as $S_n^{\parallel}(R) \propto R^{\zeta_n}$ with $\zeta_n^{\mathrm{K41}} = n/3$. Real turbulent flows deviate from this exact scaling, a phenomenon called intermittency. The numerical studies of Boué *et al.* [54] and Biferale *et al.* [55] found intermittency in coflowing He II to be temperature-dependent with maximum deviation from the classical scaling near 1.85 K. This finding was challenged by the experiment of Rusaouen *et al.* [56], based on the measurements of pressure fluctuations, who observed *no* temperature dependence of intermittency in a wide range of temperatures.

Transverse structure functions $S_n^{\perp}$ pertaining to the normal fluid velocity alone are experimentally accessible through the helium excimer molecules visualisation [22, 21]. Transverse structure functions, defined similarly to (1.16) with the projection transverse to the separation vector $\mathbf{R}$ (see Eq. 3.15), ought to scale equivalently to the longitudinal ones for homogeneous and isotropic turbulence [2]. The scaling of these structure functions (see Sec. 3.5) was indeed found to follow the prediction of numerical studies of Boué *et al.* [54] and Biferale *et al.* [55], in apparent contradiction with the results of Rusaouen *et al.* [56]. A possible scenario explaining this discrepancy will be discussed in Sec. 3.5, however, intermittency of He II coflow must still be regarded as an open question.

2. Methods of investigation

This chapter describes the methods of investigation of the quantum turbulence in He II. Experimental methods, primarily the second sound attenuation [24], and the arrangement of the experiments are described in Sec. 2.1. The complementary numerical work based on the vortex filament model [57] is discussed, including the description of the implementation used, in Sec. 2.2.

2.1 Experimental methods and set-ups

The experimental part of the thesis is concerned with various types of flows of He II in channels of square cross section. The produced turbulence was probed in three ways: the vortex line density was measured by the second sound attenuation [24, 58]; the temperature profile of the flow was probed by miniature local thermometers inside the channel; and the flow of the normal fluid component was visualised using laser-induced fluorescence of metastable helium excimer molecules [22].

The channels used for the experiments and the basic experimental arrangement is described in Sec 2.1.1. Local thermometry in the thermal counterflow is discussed in Sec. 2.1.2. The main method, vortex line density measurements using second sound attenuation, is the topic of Sec. 2.1.3 and the experimental section concludes with the helium excimer visualisation method described in Sec. 2.1.4.

2.1.1 Experimental setup

The flows investigated can be grouped into three classes (see Fig. 2.1): *thermal counterflow*, opposing flows of the normal and superfluid component with zero mass flow [15]; *pure superflow*, net flow of the superfluid component only [59]; and *coflow*, simultaneous flow of both components with no forcing difference [9]. Thermal counterflow is constructed by placing a heat source at the closed end of the flow channel open to helium bath on the opposite end. The supplied heat $\dot{Q}$ leads to the creation of the normal component and its outflow from the channel with velocity v_n, which is compensated by the inflow of the superfluid component with velocity v_s to maintain the overall density of helium. The resulting relative velocity is

$$v_\mathrm{ns} = v_\mathrm{n} - v_\mathrm{s} = \frac{\dot{Q}}{\rho S T A}, \tag{2.1}$$

where T is the temperature, A the channel cross section, S the entropy density and ρ the total density of liquid helium. Pure superflow is constructed using the so-called superleaks, porous filters made of sintered silver powder, which allow through-flow of the inviscid superfluid component but not the viscous normal fluid component [60, 59, 40]. The flow itself is activated by squeezing a calibrated bellows attached to the channel through such a superleak [59, 40] or by a fountain pump [61, 60] (although accurate determination of the superfluid velocity in the fountain pump can be error-prone [62]). The coflow is achieved in two different ways, either by simply removing the superleaks from the ends of the channel [9, 47] (possibly replacing them with flow conditioner or grids transparent to

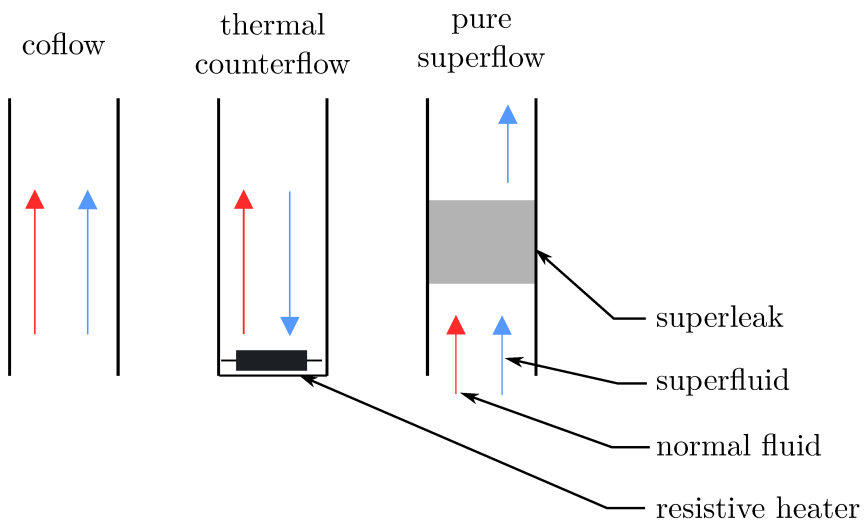

Figure 2.1: The three types of flows investigated. Coflow can be either a pressure-driven flow (e.g., forced by a compressible bellows [47, 9]) or flow resulting from mechanical stirring (e.g., a grid towed through stationary helium). Pure superflow is also a pressure-driven flow forced by a bellows (not shown), with the flow "filtered" using a superleak [59, 40] – a porous plug with sub-μm channels made by sintering silver powder to about 50% of bulk silver density that allows through-flow of superfluid component only.

both components) or by towing a grid through stationary helium [8, 48]. The channels used for the experiments are sketched in figures 2.2 – channels S7 (7×7 mm) and S10 (10×10 mm) and 2.3 – channel L7 ("long" 7×7 mm, approximately double the length of S7). Additional channel, belonging to the visualisation setup of the group in Tallahassee [22, 21] was used for the towed grid experiments and is described in Ref. [22] and briefly in Sec. 3.5.

The flow channels were fully immersed in He II in a simple bath cryostat where helium vapours could be pumped by a rotary vane pump in series with a roots blower, with the lowest practical temperature of the bath approximately 1.2 K. Temperature stabilisation was implemented using a bath heater controlled by a PID loop. The stabilised bath temperature was measured using either a carbon or Ge-on-GaAs film resistance thermometer (see also Sec. 2.1.2). The readout electronics used were the Lake Shore 336 and Lake Shore 332 temperature controllers[1]. The stability of the bath temperature in a steady state was about 0.1 mK. The maximum departure from the set point after large changes in supplied heat flux was about 1 mK, lasting typically for several seconds.

[1]The temperature control provided by these instruments was found to be unsuitable and were therefore used only for readout. The actual temperature control was implemented via home-made LabVIEW routines.

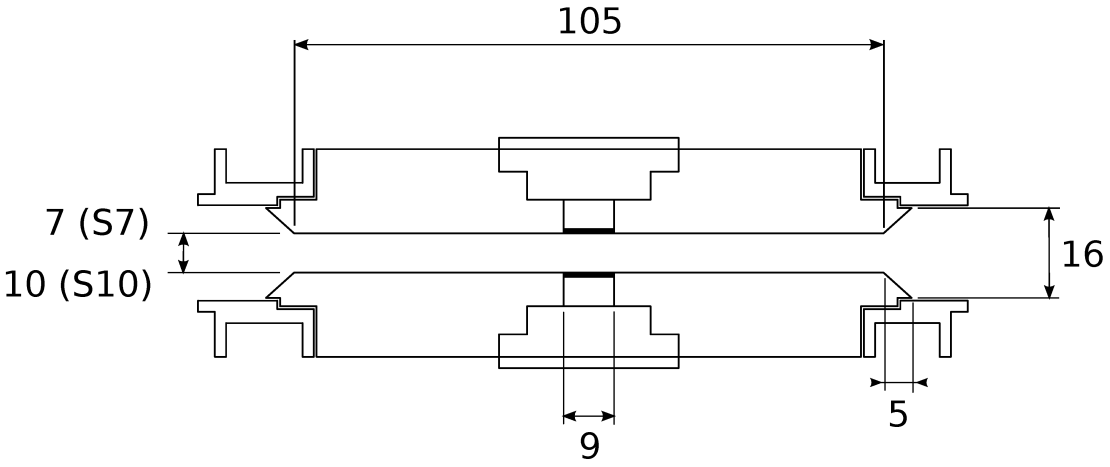

Figure 2.2: Sketch of the channel S7 (short, 7 mm inner side). The flow section of the channel is 105 mm long with the second sound sensors placed in the centre. Additional channel, referred to as S10, was also used which differed from S7 only in the inner channel size which was 10 mm instead of 7 mm. In the cryostat, the channels were positioned vertically for bellows-activated flows (coflow, pure superflow) and horizontally for thermal counterflow.

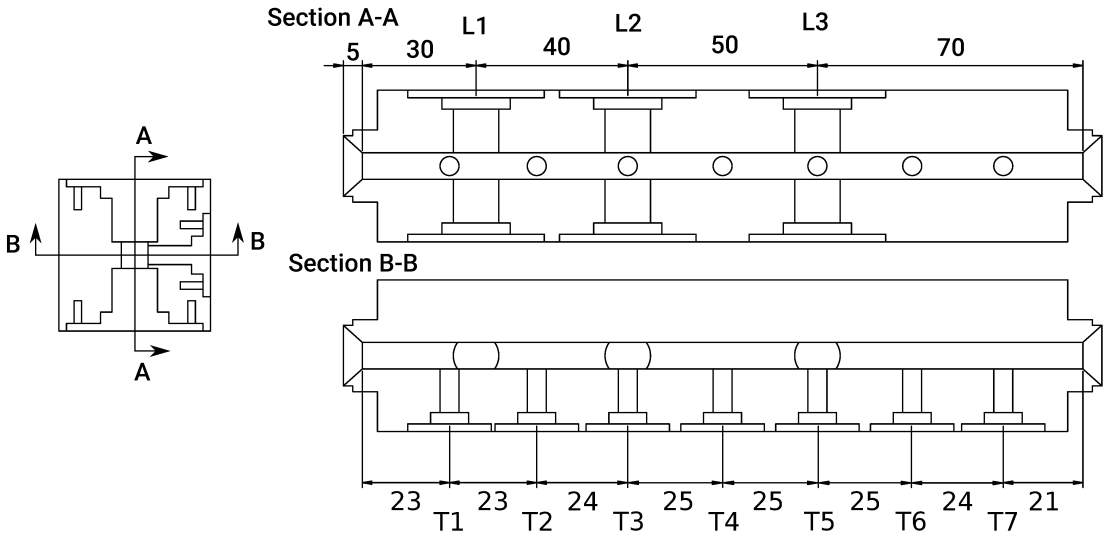

Figure 2.3: Sketch of the channel L7 (long, 7 mm inner side). Compared to the the channels S7 and S10 from Fig. 2.2, this channel features three sets of the second sound sensors L1 – L3 and also allows measurement of the local temperature using the seven thermometers T1 – T7 mounted on the inner wall of the channel. In one set of thermal counterflow measurements an additional thermometer (not shown) was placed on a thin capillary on the axis of the channel whose position could be adjusted *in-situ* by a linear motor (see Sec. 3.2). In the cryostat, the channel was positioned vertically.

2.1.2 Thermometry

In the thermal counterflow set up in channel L7 (Fig. 2.3) temperature was monitored inside the channel by up-to 7 miniature Ge-on-GaAs film resistance thermometers from the Microsensor company[2] (type TTR-G in the micropackage version). Additional thermometer of the same type was placed in the bath as a reference and as an input for the temperature control. The resistances of the thermometers were read using a commercial Lake Shore 336 and 332 temperature controllers which read the thermometers with input power less than 10^{-8} W in order to limit sensor self-heating.

Calibration was performed in-situ below 4.2 K against the temperature of the helium bath determined from the saturated vapour pressure. Specifically, the temperature T as a function of the resistance R was fit using

$$\log T = C_8(\log R), \tag{2.2}$$

where C_8 is 8th order Chebyshev polynomial. The calibration curves for the thermometers are shown in Fig. 2.4 for temperatures below T_λ. The absolute error of the calibration is estimated as the standard deviation of the fit residuals and is about 1 mK throughout the range. The thermometers are mostly used to measure relative changes in time, i.e. $\Delta T(t) = T(t) - T(t = 0)$ (see Sec. 3.2.1) with $t = 0$ some chosen reference point in time. The error of $\Delta T(t)$ is given by the error of the slope of $T(R)$. The typical slope (depending on the temperature and the used thermometer) $T'(R) \approx 20 \pm 2 \times 10^{-3}$ mK/kΩ (with the error determined by bootstrap) in the range 1.4 – 2.17 K. The error on ΔT (measured ΔT being typically of the order of 10 mK) resulting from calibration is thus typically negligible compared to the instrumentation noise, which is of the order of 100 μK (see Fig. 3.3).

2.1.3 Second sound attenuation

Second sound, the wave of temperature or entropy accompanied by the relative motion of the two components of He II, is damped by the presence of quantized vortices [10, 24]. The damping coefficient (the complex part of a wave vector of a plane wave) is [59]

$$\tilde{\alpha} = \frac{B\kappa L}{4c_2} \sin^2 \vartheta, \tag{2.3}$$

where B is the mutual friction constant, L is the vortex line density (total length of quantized vortices per unit volume), c_2 is the velocity of second sound and ϑ is the angle between orientation of vortex lines and direction of propagation of the second sound. For an isotropic tangle (that is, all angles θ are equally likely) the last term is replaced by $\langle \cos^2 \theta \rangle = 2/3$.

Typically one does not measure the damping of a propagating plane wave directly but rather the damping constant of a resonator where second sound standing wave is created, with the flow channel acting as the resonator. In the resonator, a second sound transducer and a receiver (of identical construction) are placed. The second sound transducer/receiver consists of a gold-plated porous

[2] microsensor.com.ua

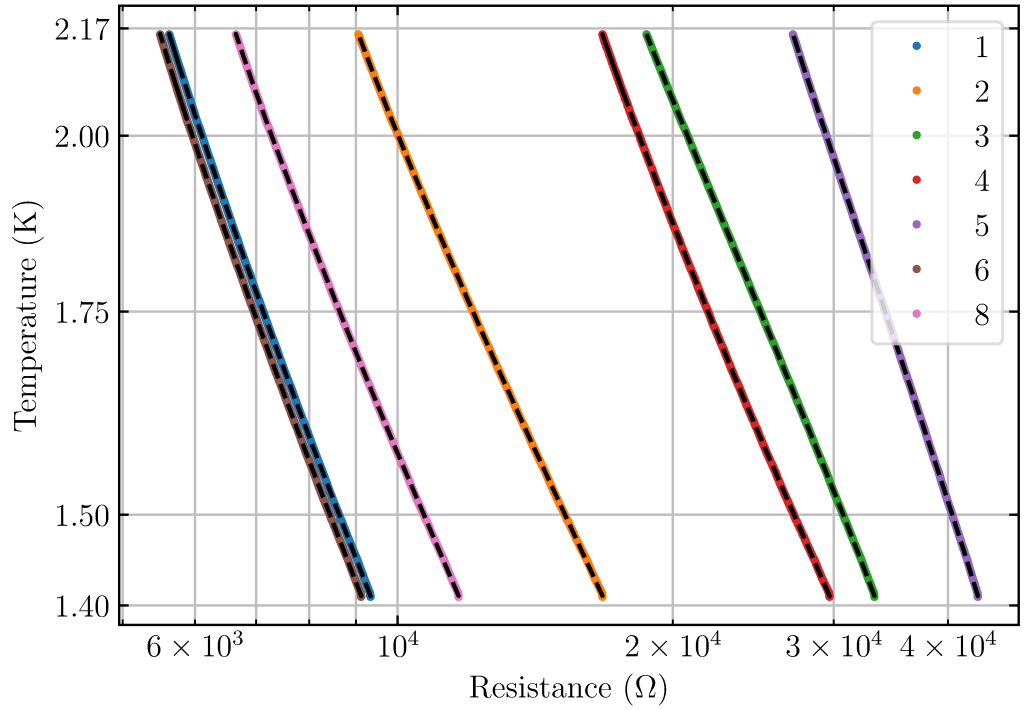

Figure 2.4: Typical calibration curves of the thermometers used in the L7 channel, in logarithmic axes. The black dashed lines show the fit to Eq. (2.2).

membrane (with pores of roughly 100 nm) capacitively coupled to a brass electrode. The membrane is held at a bias voltage $V_{\text{bias}} \approx 100$ V and the backing electrode is held near ground. To create a second sound wave, the membrane is actuated by sine-wave voltage, created by a function generator, connected to the backing brass electrode. The second sound is detected as oscillating current, measured using a lock-in amplifier, between the backing electrode and ground, induced by the oscillating biased membrane.

A typical resonance for several different flow velocities (vortex line densities) is shown in Fig. 2.5.

It can be shown [59] that the vortex line density inside the resonator is given by

$$L = \frac{6\pi\Delta f}{B\kappa}\left(\frac{a_0}{a} - 1\right), \tag{2.4}$$

where a and a_0 are the in-phase amplitudes (real parts of the phasor) of the second sound resonance with and without the presence of turbulence and Δf is the quiescent resonance width. This method of obtaining vortex line density is necessarily relative, as it compares two levels of attenuation. That is, the calculated value L is relative to the remnant vorticity present in the quiescent state, which is not directly accessible with second sound attenuation. Inferences about the remnant vortex line density L_R can be made by comparing the attenuation before turbulence is created and after it decays [40] with typical values being $L_R \lesssim 10^3$ cm^{-2}.

For inhomogeneous tangles, the vortex line density inferred through the Eq. (2.4) depends on the resonance mode used, due to different spatial locations of

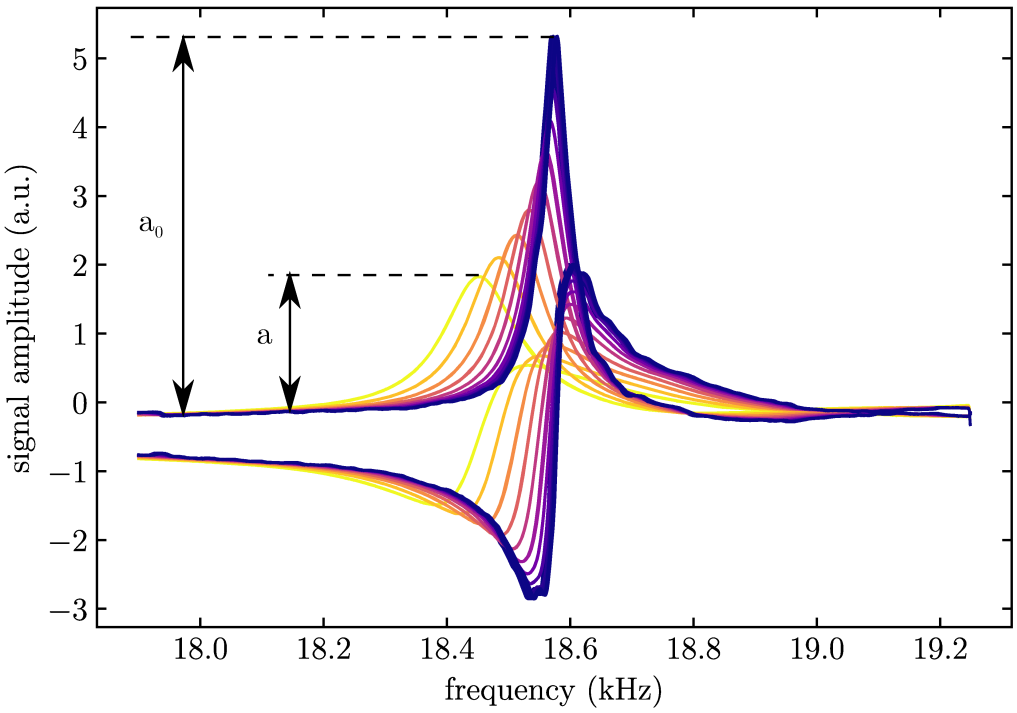

Figure 2.5: Increased attenuation of a second sound resonance with increasing flow velocity (and thus increasing vortex line density). The shift in the central frequency is caused by the temperature increase. The shown data were measured in the channel L7 with the sensors L1 at the temperature 1.95 K in thermal counterflow with the heater power spanning approximately 0 – 250 mW.

the nodes of the standing second soud wave within the resonator [24]. The value L_n measured by the n-th mode is given by (for a one-dimensional resonator and assuming symmetry around the centre of the resonator)

$$L_n = \langle L(x) \rangle_x - \frac{1}{D} \int_0^D L(x) \cos(2\pi n x) \, \mathrm{d}\, x, \tag{2.5}$$

where $L(x)$ is the "true" distribution and integration is over the entire one-dimensional resonator of length D. The mode-dependence of L_n is given by the appropriate Fourier component of $L(x)$. For sufficiently high n, the Fourier component can be neglected (due to convergence of the Fourier series) and L_n is simply the mean vortex line density in the resonator. Note that knowing L_n, the inverse problem can be solved and the variation of $L(x)$ could be, in principle, probed by measuring L_n for different n. This, however, requires high quality of multiple low-lying modes of the second sound resonator which are often disrupted.[3] The experiments in this thesis used $n \geq 10$, unless specified otherwise, and the measured vortex line density is taken as the spatial average of the tangle.

To measure the vortex line density using Eq. (2.4), one requires only the resonance amplitude a and not the entire resonance peak. Measurements of L well resolved in time can thus be obtained, if one can measure the amplitude a in time reliably. Typically, the amplitude is measured by tuning the resonator to its resonance frequency and measuring the resulting response with a lock-in amplifier. A significant flaw of this approach, however, is that because of the temperature dependence of the second sound velocity, the resonance might shift due to temperature change during an experiment (problem especially with heat flux-activated counterflow) which results in spurious change in a if measured at fixed frequency. A method of compensating this shift will be explained below.

The time resolution of the vortex line density measurement is limited primarily by two factors: the width of the second sound resonance and the time constant of the lock-in amplifier. The time constant of the lock-in amplifier was set to 10 ms for all time-resolved measurements and to 100 ms for measurements of the second sound spectra. The width of the resonance peak depends on the level of attenuation and on the particular experimental conditions. The typical values for the non-attenuated peaks are in the range of 30 – 100 Hz and 100 – 300 Hz for vortex line densities of about 10^5 cm^{-2}. The data acquisition of the presented experiments was either hardware-timed at 100 points per second and sampled from analog outputs of a Stanford Research SR830 lock-in amplifier using a National Instruments PCIe-6361 DAC card or by direct communication through a GPIB bus at roughly 50-60 points per second (with sampling not uniform in time).

Compensation for temperature shift of the resonator[4]

The creation and the decay of turbulence can cause sufficiently large and abrupt changes in the temperature that can easily overwhelm the PID control, which might take tens of seconds to stabilise. Moreover, in a long channel the thermal

[3] The reason for this is, unfortunately, not satisfactorily understood.

[4] The presented compensation method was published in Ref. [63], reproduced in Attachment 1.

gradient naturally associated with the thermal counterflow can produce significant shift (several mK) in temperature near the heat source relative to the bath temperature which cannot be removed even with perfect temperature control in the bath. These temperature changes shift the second sound resonance, as shown in Fig. 2.5 for the case of thermal counterflow, and invalidate the time-resolved measurement of the second sound amplitude at fixed frequency.

This difficulty can be overcome by considering the shape of the resonance peak in the plane of the complex amplitude $\tilde{a}$. Plotting the amplitude of second sound signal in the complex plane in the vicinity of the resonance for different attenuation levels, see Fig. 2.6, one obtains a set of (distorted) circles. These curves do not depend on the slight temperature shift (for a fixed attenuation). For a second sound signal at fixed attenuation level (i.e., constant vortex line density) subject to changes in temperature (sufficiently small not to affect mutual friction parameters significantly) or frequency, the complex amplitude will move only along the "circle" corresponding to the particular level of attenuation. By measuring the resonances beforehand, one can calibrate, by suitable interpolation, a relevant part of the plane of the complex amplitude to obtain the correct *real* amplitude a from the off-resonant complex amplitude $\tilde{a}$.

It is clear though that departing too far from the central frequency decreases the resolution. Another difficulty arises when the resonance peaks are disturbed (e.g., by neighbouring spurious resonances) – the circles of the complex amplitude can cross and thus it is not possible to uniquely assign real resonant amplitude to the complex amplitude. These difficulties limit the applicability of the compensation method only to a certain neighbourhood of the central frequency of the resonance (typically about the width of the resonance) that depends on the particular shape of the resonance peak.

The two-dimensional calibration was implemented using radial basis functions (RBF) interpolation (using an open-source implementation [64]) with linear basis functions, i.e.,

$$a(\tilde{a}) = \sum_n A_n \varphi(\tilde{a} - \tilde{a}_n), \tag{2.6}$$

with $\varphi(x) = |x|$, the sum running through the points on the calibration resonance curves and A_n determined by fitting.

The RBF method was chosen due to its ability to withstand small extrapolation, which can occur for very low attenuation which is strongly affected by the uncontrolled remnant vortex line density. The linear basis functions were chosen primarily for reasons of simplicity (especially the absence of free parameters). Choice of different basis functions (e.g., the so-called multiquadric $\phi(r) = \sqrt{(r/\varepsilon)^2 + 1}$ with ε a free parameter) was found to have negligible effect on the interpolated results, except for the small extrapolation parts where the more complicated functions can produce undesired oscillations.

2.1.4 Helium excimer molecular tagging velocimetry

Molecular tagging velocimetry (MTV) is a flow visualisation method developed for the study of classical turbulence with high spatial resolution which is applicable in hostile environments [65, 66]. In general, the method involves "tagging" of suitable molecules in a predefined region of the flow and subsequently following

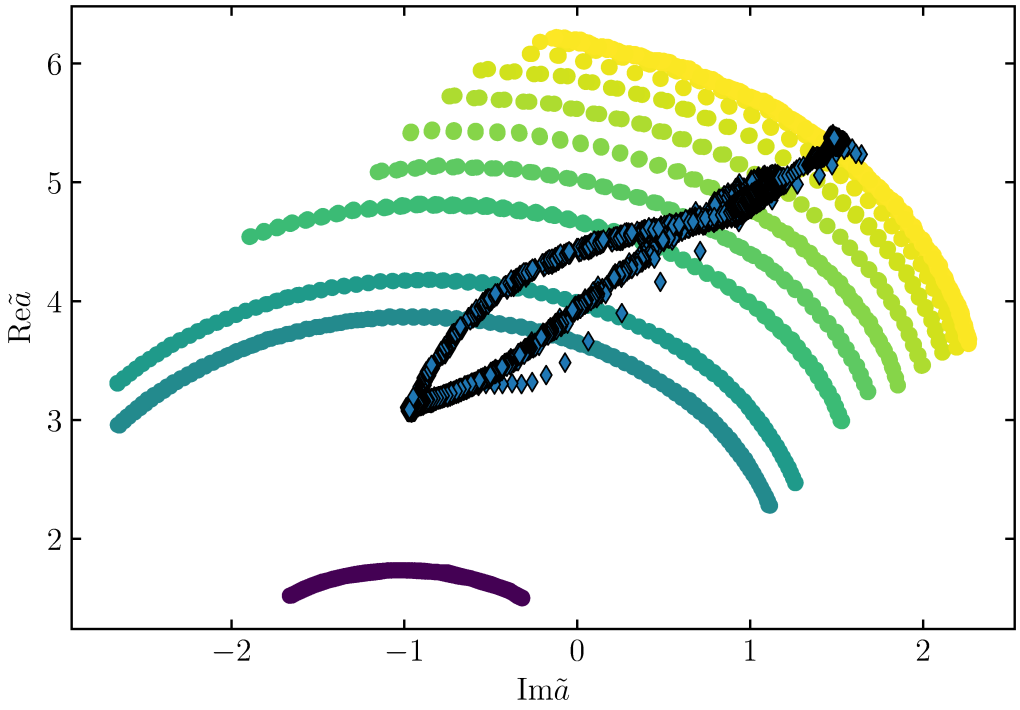

Figure 2.6: The complex amplitude of the second sound signal (points on the arcs, the colour indicates the amplitude of the resonance) for frequencies near resonance in a complex plane (i.e., the X (real) and Y (imaginary) output of the lock-in). The superimposed path shows a trajectory of the complex amplitude for a typical measurement. One can ascribe an amplitude, or directly the vortex line density, to the individual circles. This allows determination of the real part of the *resonant* amplitude a from slightly *off-resonant* complex amplitude without changing the excitation frequency. Note that due to fairly large computational demand of the RBF interpolation, not the entire resonance curve is used to calculate the amplitude along the path. The figure shows only the points that were used for the interpolation.

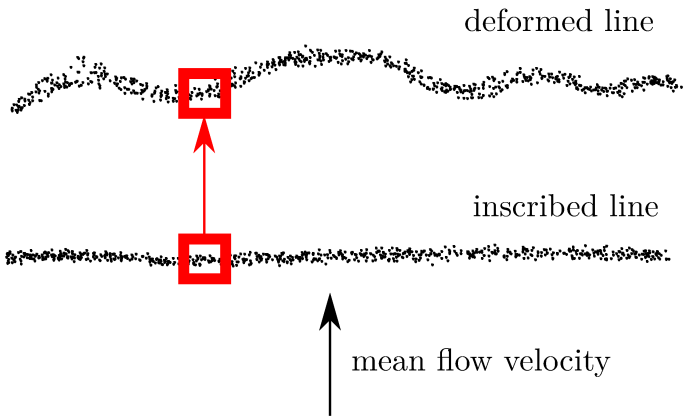

Figure 2.7: A sketch of the molecular tagging velocimetry in a straight line geometry. The molecular tracers are tagged along the straight line which is defromed by the flow. The local velocity is estimated as the displacement in the transversal direction divided by the drift time that is allowed to pass after inscription of the line. Note that only one component of velocity is accessible.

their motion, observing the advection and deformation of the tagged cloud of molecules. This technique has been successfully applied, e.g., to the study of turbulent jets [67] where it allowed measurements of high-order structure functions and intermittency corrections.

The tagging of the molecules typically involves exciting a molecule to a higher electronic state using laser light [67], or in the case of He II also radiation [68] or ions created by sharp tungsten tips at high voltage [69, 70]; conversely, the observation of the molecules is typically accomplished by laser-induced fluorescence.

The most straightforward arrangement consists of tagging molecules along a straight line. The tagged molecules (tracers) are advected by the flow and the tracer line deforms (see Fig. 2.7). Assuming that the drift time between inscription and visualisation of the line is sufficiently short, the displacement of the deformed line from the inscribed one in the transversal direction divided by the drift time is used to estimate the local velocity. Only one component of the velocity is thus accessible, but with fairly large spatial resolution, limited only by the width of the tracer line which is determined by excitation method and its focusing.

An MTV-like technique was recently developed by the Tallahassee group [21, 22] which allows for selective visualisation of the motion of the normal fluid component only [70, 71]. The method is based on laser-induced fluorescence of helium excimer molecules. Helium excimer molecules (a bound state of two helium atoms with one atom in an excited state) have nm sizes and, above roughly 1 K, are fully entrained by the normal fluid [71]. In the experiment, the molecules are *created* by intense femtosecond pulses [72] and are visualised using 905 nm infrared laser [22]. The method was successfully applied in the past to the study of thermal counterflow [21, 43, 41]. In Sec. 3.5 this method is used to study normal fluid flow in the quasi-classical grid-generated turbulence, with an emphasis on

the higher-order structure functions.

2.2 Numerical simulations

Numerical simulations of quantum turbulence can be grouped into three main categories according to the scales they resolve: (i) microscopic models based on the non-linear Schrodinger equation [73], (ii) the mesoscopic vortex filament model [57], and (iii) macroscopic models that ignore the discrete nature of the quantized vortices [7]. The microscopic non-linear Schrodinger equation excels at the approximation of the dynamics of a weakly interacting Bose-Einstein condensate at zero temperature. Its main advantage is the ability to self-consistently describe the dynamics of the system at the level of individual quantized vortices, including their intrinsic nucleation [74] and reconnections [75]. The disadvantages include difficulties with incorporating finite-temperature effects (i.e., the two-fluid behaviour) and the fact that He II is not a weakly interacting gas, but rather a strongly interacting liquid.

On the opposite end of the spectrum of scales lie the macroscopic models predominantly based on the Hall-Vinen-Bekarevich-Khalatnikov (HVBK) model[5]. The basic formulation of the HVBK model [77] consists of two Navier-Stokes equations for the normal and superfluid component, with the dynamic viscosity of He-II used for the normal component and an effective viscosity ν_{eff} for the superfluid component, supplemented by equations for normal and superfluid pressures. The main advantage of this approach lies in the ease of modelling of full two-way coupling between normal and superfluid component. Since the superfluid vorticity is assumed to be continuous and non-quantized, this model clearly cannot describe any process occurring near or below the scales of vortex-vortex separation.

The numerical work presented in this thesis is concerned solely with the mesoscopic vortex filament model, which retains the discreteness of quantized vortices but no longer resolves their internal structure, described in detail in the following subsection. This model has the ability to resolve the dynamics of a vortex tangle with the resolution of individual vortices and its interaction with the normal fluid. However, it should be noted that that full two-way coupling between normal and superfluid component remains a challenge with this model and so far has been used only with relatively small resolution [78].

2.2.1 The vortex filament model

The vortex filament model pioneered by K. W. Schwarz [79, 35] uses the quantized vortices as the basic building blocks of the dynamics of quantum turbulence. The quantized vortices, or vortex lines, within the vortex filament model (VFM) are modelled as one-dimensional space curves without internal structure, as sketched in Fig. 2.8. The vortex line is parameterized by its arc length ξ with the positions on the line denoted by $\mathbf{s}(\xi)$. Differentiation of the vortex position $\mathbf{s}(\xi)$ with respect

[5] Other, less popular, approach is the so-called "one fluid model" [76], where He II is modelled as a single-component liquid with heat, or sometimes vortex line density, taken as another independently flowing quantity.

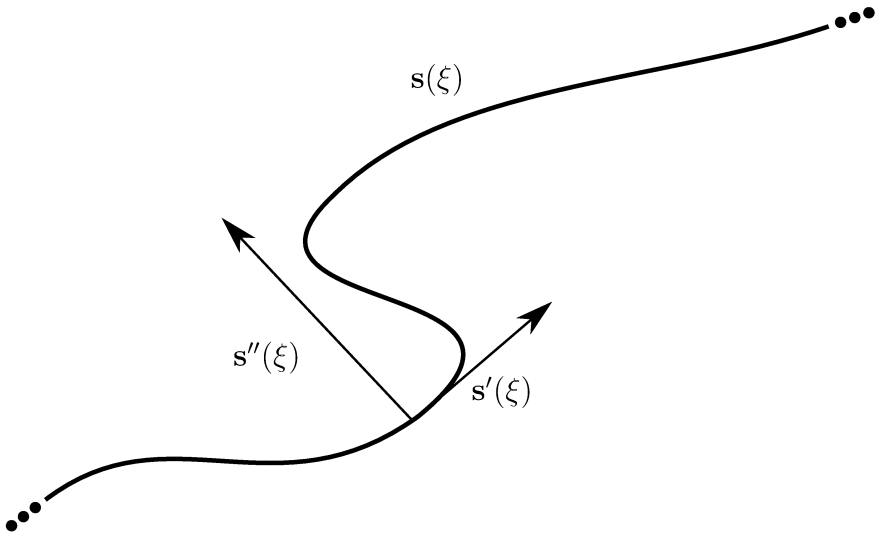

Figure 2.8: Sketch of a vortex filament. The vortex is parametrized with its arc-length ξ. Differentiation of the vortex position $\mathbf{s}(\xi)$ with respect to the arc length yields the local tangent of unit length $\mathbf{s}'$. The magnitude of the second derivative $\mathbf{s}''$ the local curvature.

to the arc length yields the unit tangent $\mathbf{s}'(\xi)$ and the normal $\mathbf{s}''(\xi)$ which has the magnitude of local curvature (i.e., inverse of local radius of curvature).

The superfluid velocity induced by the vortex lines at point $\mathbf{r}$, not lying on a vortex, is given by the Biot-Savart integral

$$\mathbf{v}_s(\mathbf{r}) = \frac{\kappa}{4\pi} \int_{\mathcal{L}} \frac{\mathrm{d}\,\mathbf{s} \times (\mathbf{r} - \mathbf{s})}{|\mathbf{s} - \mathbf{r}|^3}, \tag{2.7}$$

where the integration runs through the entire vortex tangle. For points on the line, that is $\mathbf{r} = \mathbf{s}(\eta)$ for some η, the integral (2.7) logarithmically diverges. The reason for this divergence is the fact that the vortex was assumed to be infinitely thin. Real vortices have cores of finite size where Eq. (2.7) is no longer applicable. The typical way to remove this singularity [23] is to integrate the first three terms of the Taylor expansion of the integrand in the close vicinity (typically the discretisation length of the simulation) of $\mathbf{s}(\eta)$ excluding a yet smaller range comparable to the width of the vortex core (of the order of 1 Å). The resulting self-induced superfluid velocity on the vortex is

$$\mathbf{v}_s^{\mathrm{SI}}(\eta) = \beta \mathbf{s}' \times \mathbf{s}'' + \frac{\kappa}{4\pi} \int_{\mathcal{L}'} \frac{\mathrm{d}\,\mathbf{s} \times (\mathbf{s}(\eta) - \mathbf{s})}{|\mathbf{s} - \mathbf{s}(\eta)|^3}, \tag{2.8}$$

where the first term originates from the local integration in the neighbourhood of $\mathbf{s}(\eta)$ with [79]

$$\beta = \frac{\kappa}{4\pi} \log\left(\frac{R}{a}\right), \tag{2.9}$$

where a is the vortex core parameter and R some suitably chosen length. The integral in the second term on the right in Eq. (2.8) runs through the remainder of the tangle. Neglecting the non-local velocity and retaining only the first term results in the so-called Local Induction Approximation (LIA). Although less precise

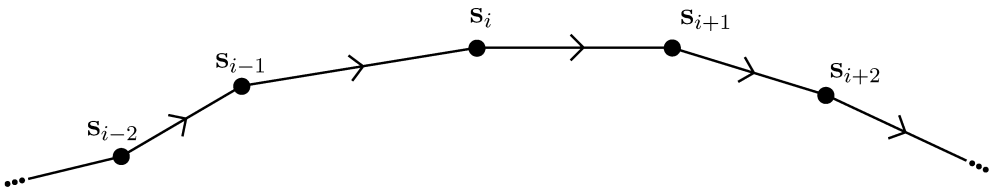

Figure 2.9: Discretisation of the vortex filament. Discretisation of a vortex is dynamic – the connectivity of the individual discretisation points (referred to as *nodes*) can change due to reconnections or to maintain resolution when points are added or removed. The arrow indicates the direction of circulation.

and prone to non-physical behaviour [80], LIA reduces the algorithmic complexity of the simulation,[6] which is the reason why it was historically the focus of pioneering numerical studies in the field [35].

Since the vortices are assumed to be massless, the vortex line velocity $\mathbf{v}_L$ will adjust itself to nullify the force acting on the vortex. In the absence of mutual friction (i.e., in the limit of zero temperature), the vortices would be subject only to the Magnus force, resulting from the superflow encircling them, and would thus be completely advected by the superfluid velocity $\mathbf{v}_L = \mathbf{v}_s = \mathbf{v}_s^{\mathrm{SI}} + \mathbf{v}_s^{\mathrm{ext}}$, where $\mathbf{v}_s^{\mathrm{ext}}$ is any externally imposed superflow. At finite temperature, mutual friction couples [10, 11] the vortex velocity to the normal fluid velocity $\mathbf{v}_n$ via the mutual friction parameters α and α' [23]

$$\mathbf{v}_L = \mathbf{v}_s + \alpha \mathbf{s}' \times (\mathbf{v}_n - \mathbf{v}_s) - \alpha' \mathbf{s}' \times [\mathbf{s}' \times (\mathbf{v}_n - \mathbf{v}_s)]. \tag{2.10}$$

An important part of the dynamics of quantized vortices, and of quantum turbulence, are the vortex reconnections, which occur when two vortices collide and change their topology. As the VFM does not resolve internal structure of the vortices, reconnections cannot be handled implicitly by the discretised equations of motion but must be programmed in explicitly. This can be accomplished in several ways, however, the exact algorithm used has little effect on the results of the simulations [81, 82]. The exact algorithm used in this work will be described below after the necessary implementation details.

Implementation

The vortex filaments are discretised into a piece-wise linear space curves as sketched in Fig. 2.9. The simulation evolves in time the individual discretisation points, which will be referred to as *nodes*, $\mathbf{s}_i$. The indices of the nodes in this subsection must be understood in terms of local ordering along the vortex (i.e., $\mathbf{s}_{i+1}$ is a forward neighbour along the vortex of $\mathbf{s}_i$) and not as, e.g., in an array in computer memory which imposes no ordering and nodes with neighbouring indices can belong to different vortices altogether.

The derivatives of the line necessary for the calculation of the locally induced velocity (Eq. (2.8)) are calculated using a 4-th order finite difference scheme on an uneven mesh. As an approximation for the arc length between two points, the

[6] The non-local Biot-Savart integral in Eq. (2.8), when discretised (see below), yields expressions similar to N-body simulations with pair interactions. The algorithmic complexity of LIA simulation is $O(n)$ whereas that of the full Biot-Savart simulation is $O(n^2)$.

cumulative length of the line segments is used, for example the distance along the line between points $\mathbf{s}_i$ and $\mathbf{s}_{i+2}$ is $\xi_2 = |\mathbf{s}_{i+1} - \mathbf{s}_i| + |\mathbf{s}_{i+2} - \mathbf{s}_{i+1}|$. In general, the distance ξ_k between the points $\mathbf{s}_i$ and $\mathbf{s}_{i+k}$, with $\mathbf{s}_i$ some specified reference point, is (for $k \neq 0$)

$$\xi_k = \sum_{j=0}^{|k|-1} |\mathbf{s}_{i+(j+1)\,\mathrm{sgn}\,k} - \mathbf{s}_{i+j\,\mathrm{sgn}\,k}|. \tag{2.11}$$

The derivatives at a node $\mathbf{s}_i$ are calculated using (with $\mathbf{s}_i$ the reference for all ξ_k)

$$\mathbf{s}_i' = -\frac{\xi_1\xi_{-1}\xi_{-2}}{d_2}\bar{\mathbf{s}}_2 + \frac{\xi_2\xi_{-1}\xi_{-2}}{d_1}\bar{\mathbf{s}}_1 - \frac{\xi_1\xi_2\xi_{-2}}{d_{-1}}\bar{\mathbf{s}}_{-1} + \frac{\xi_1\xi_2\xi_{-1}}{d_{-2}}\bar{\mathbf{s}}_{-2}, \tag{2.12a}$$

$$\mathbf{s}_i'' = 2\left(\frac{a_2}{d_2}\bar{\mathbf{s}}_2 - \frac{a_1}{d_1}\bar{\mathbf{s}}_1 + \frac{a_{-1}}{d_{-1}}\bar{\mathbf{s}}_{-1} - \frac{a_{-2}}{d_{-2}}\bar{\mathbf{s}}_{-2}\right), \tag{2.12b}$$

where $\bar{\mathbf{s}}_k = \mathbf{s}_{i+k} - \mathbf{s}_i$ and

$$a_2 = -\xi_1\xi_{-1} - \xi_1\xi_{-2} + \xi_{-1}\xi_{-2}, \tag{2.13a}$$

$$a_1 = -\xi_2\xi_{-1} - \xi_2\xi_{-2} + \xi_{-1}\xi_{-2}, \tag{2.13b}$$

$$a_{-1} = -\xi_1\xi_2 + \xi_1\xi_{-2} + \xi_2\xi_{-2}, \tag{2.13c}$$

$$a_{-2} = -\xi_1\xi_2 + \xi_1\xi_{-1} + \xi_2\xi_{-1}, \tag{2.13d}$$

with the denominators given by

$$d_2 = \xi_2(\xi_2 - \xi_1)(\xi_{-1} + \xi_2)(\xi_{-2} + \xi_2), \tag{2.14a}$$

$$d_1 = \xi_1(\xi_2 - \xi_1)(\xi_{-1} + \xi_1)(\xi_{-2} + \xi_1) \tag{2.14b}$$

$$d_{-1} = \xi_{-1}(\xi_{-1} + \xi_1)(\xi_{-1} + \xi_2)(\xi_{-2} - \xi_{-1}) \tag{2.14c}$$

$$d_{-2} = \xi_{-2}(\xi_{-2} + \xi_1)(\xi_{-2} + \xi_2)(\xi_{-2} - \xi_{-1}). \tag{2.14d}$$

Given a known tangent $\mathbf{s}_i'$ and normal $\mathbf{s}_i''$ the locally-induced superfluid velocity in Eq. (2.8) can be calculated, with β typically taken [79] as

$$\beta = \frac{\kappa}{4\pi}\log\left(\frac{2\sqrt{\xi_+\xi_-}}{\sqrt{e}a}\right), \tag{2.15}$$

with $\xi_\pm$ being the distances to the nearest nodes. From known superfluid velocity at the node $\mathbf{s}_i$, its velocity is easily calculated from Eq. (2.10).

Marching in time is implemented using the 4th order Runge-Kutta scheme. In order to maintain spatial resolution, the discretisation of the vortices dynamically changes (nodes are added or removed) so as to keep the inter-node distances $|\mathbf{s}_{i+1} - \mathbf{s}_i|$ within a specified range $(\xi_{\min}, \xi_{\max})$, typically of the order 10^{-4} – 10^{-3} cm. Very short vortices (less than 5 nodes) are removed from the simulation.

The final component of the dynamics of the vortices not captured by the equations above are the reconnections. When two vortices collide, they reconnect and thus change the topology of the tangle. The importance of the reconnections lies in the fact that they create sharp cusps on the vortices (as sketched in Fig. 2.10) which move with large velocity due to the second derivative in the locally induced velocity and thus tend to be the regions of strong dissipation due

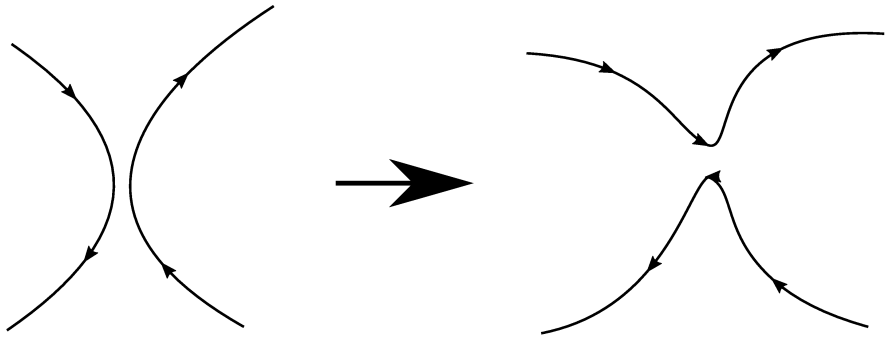

Figure 2.10: Creation of sharp cusps during reconnections. The region near the cusp will have large locally-induced velocity due to the second derivative in Eq. (2.8). These regions tend to experience strong dissipation due to mutual friction.

to mutual friction [45] (arising from the dissipative term proportional to α in Eq. (2.10)).

In the implementation the reconnection occurs provided that certain reconnection criteria are met. These criteria are:

1. two nodes $\mathbf{s}_i$, $\mathbf{s}_j$ approach closer than some reconnection distance l_r, typically $l_r \approx \xi_{\max}$,
2. nodes $\mathbf{s}_i$ and $\mathbf{s}_j$ are not immediate neighbours,
3. the instantaneous relative velocity of the nodes is such that their distance would decrease
4. the angle between $\mathbf{s}'_i$ and $\mathbf{s}'_j$ is larger than 5 deg (parallel vortices do not reconnect),
5. the total length of the line decreases after the reconnection (reconnection is dissipative).

When these criteria are met, the topology of the vortices changes from $(\mathbf{s}_{i-1} \to \mathbf{s}_i \to \mathbf{s}_{i+1})$ and $(\mathbf{s}_{j-1} \to \mathbf{s}_j \to \mathbf{s}_{j+1})$ to $(\mathbf{s}_{i-1} \to \mathbf{s}_{j+1})$ and $(\mathbf{s}_{j-1} \to \mathbf{s}_j \to \mathbf{s}_i \to \mathbf{s}_{i+1})$ or $(\mathbf{s}_{j-1} \to \mathbf{s}_{i+1})$ and $(\mathbf{s}_{i-1} \to \mathbf{s}_i \to \mathbf{s}_j \to \mathbf{s}_{j+1})$ (see Fig. 2.11), depending on which configuration minimises the line length.

The simulation software created as part of this thesis, and written fully by the author of the thesis, is released as Free Software under the GNU General Public License and can be obtained from a public Git repository[7] or from the disc attached to the thesis.

[7] https://bitbucket.org/emil_varga/openvort/

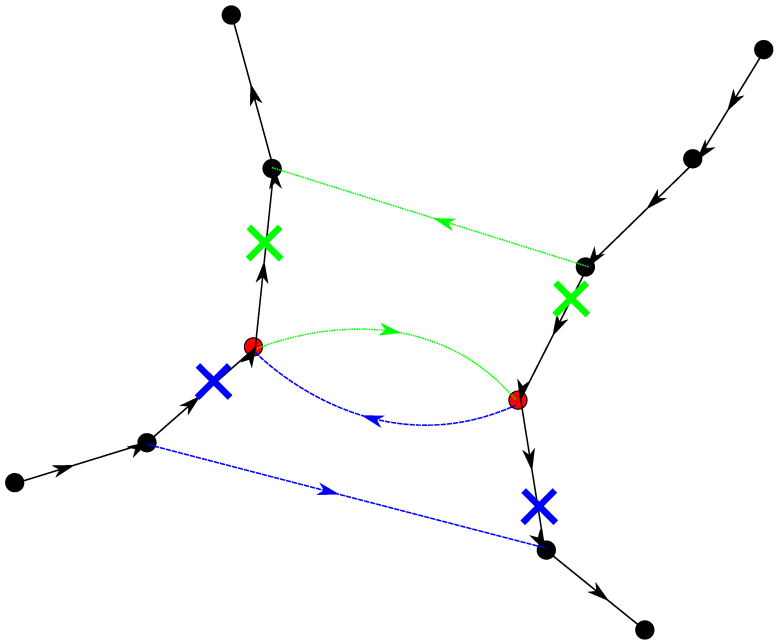

Figure 2.11: Reconnection of the discrete nodes along the vortices. The reconnection is triggered by the proximity of the two red points. The segments crossed out by a "X" would be deleted and the segments indicated by the coloured dashed lines would be added. Note that two different post-reconnection topologies of the lines are possible, indicated by the two colours. The topology that minimises the length is realised in the simulation.

3. Experimental results

3.1 Introduction

This chapter summarises the obtained experimental data on the investigated types of quantum turbulence in superfluid ^{4}He. All flows reported below fall within a broad range of channel flow experiments, where the turbulence is established in a bounded channel of a square cross-section. Analogous experiments with classical working medium such as water or air are relatively commonplace [44]. The properties of turbulence are often studied with respect to changes in Reynolds number (or similar dimensionless variable) by varying the flow speed, typical dimension (e.g., the width of a wind tunnel) or the kinematic viscosity (e.g., by changing the working medium or changing the temperature for certain media). Superfluid helium, thanks to its two-fluid nature, allows also to tune the relative velocity between the two fluids. This relative, or *counterflow*, velocity turns out to have significant impact on the observed flow properties.

The primary experimental characterisation of turbulence in this work is via the vortex line density, the total length of the quantized vortices per unit volume, measured through second sound attenuation as described in Sec. 2.1.3. Additional major method used is the visualisation of the normal fluid flow using laser-induced fluorescence of helium excimer molecules discussed in Sec. 3.5.

This Chapter is structured as follows. Section 3.2 is concerned with the vortex line density and temperature distribution in the steady state of quantum turbulence and its dependence on flow parameters (temperature and velocity). Data concerning decaying turbulence is presented in Sec. 3.3, focusing on the decay of thermal counterflow and pure superflow. Sec. 3.4 describes the measurements of the dynamics of vortex line density in an unsteady counterflow. Lastly, Sec. 3.5 is dedicated to visualisation study of intermittency in decaying coflow turbulence in the wake of a towed grid.

3.2 Steady state turbulence

The steady state vortex line density as a function of mean flow velocity is shown in Fig. 3.1 for all three classes of the investigated flow [59, 9, 24]. One can immediately observe the strong influence of the *presence* of non-vanishing mean counterflow velocity on the properties of turbulence. Most notably the observed scaling is different: $L \propto V^{3/2}$ for the coflow and $L \propto V^2$ for counterflow and superflow. Note the similarity between thermal counterflow and pure superflow – not only the scaling is identical [59], but the absolute values of the vortex line density are similar as well. This is hardly a surprise if one considers that for an unbounded system these two flows are simply Galilean transform of each other. However, real systems are not unbounded and the turbulence generated by the two flows can decay quite differently [40], as will be shown in Sec. 3.3.

Apart from the vortex line density, an important property of a steady state flow is the temperature distribution along the channel. Thermal counterflow results in approximately constant temperature gradient (linear temperature profile) along the streamwise direction of the channel [31, 63] (although very near the heat

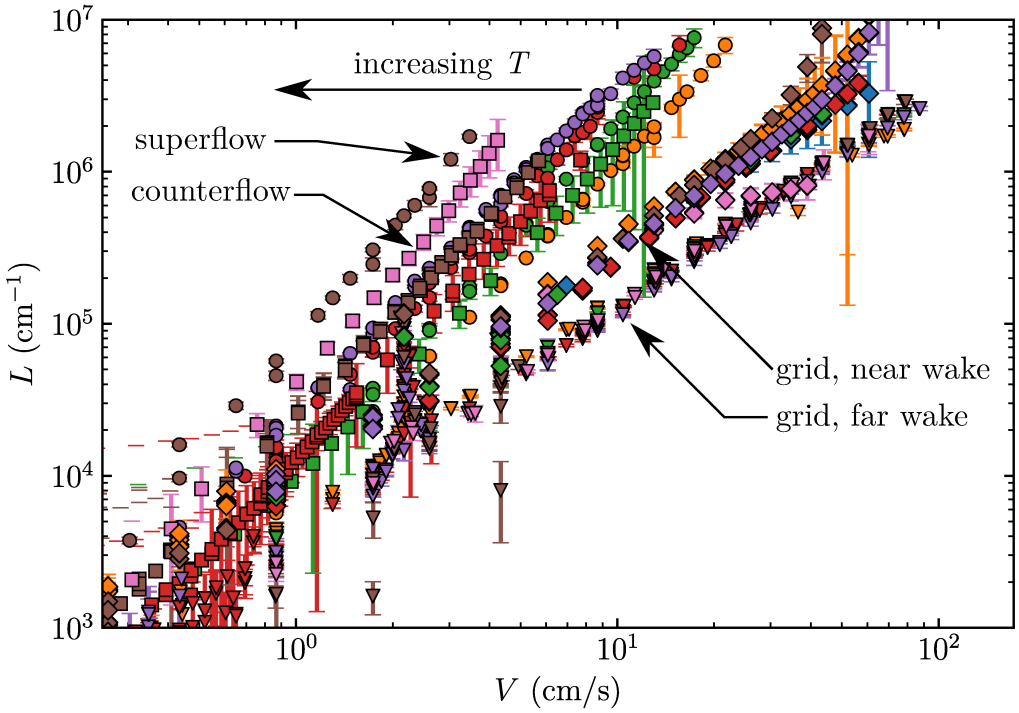

Figure 3.1: Steady state vortex line density for the three investigated types of quantum turbulence. Superflow (measured in channel S7, [59]) – ●; thermal counterflow (measured in S10, [40]) – ■; coflow (measured in S10, [9], wake behind a grid – ▼; far wake behind a flow conditioner – ◆. Different colours denote different temperatures. The temperature-independent grid flows span roughly 1.2 K – 2.16 K. For counterflow and superflow, the temperature dependence of the slopes is shown in Fig. 3.2. Note the strong effect of the relative velocity on the amount of vortex lines present in the turbulence. The flow velocity V stands for the mean counterflow, superfluid or overall velocity for the thermal counterflow, superflow or coflow, respectively.

source a possible boundary layer has been reported [32]). Pure superflow is expected to behave in a similar fashion while coflow is expected to be approximately isothermal. Although temperature profile data for pure superflow and coflow are not available, measurements of the local temperature in thermal counterflow are shown below in Sec. 3.2.1.

3.2.1 Steady state counterflow

The steady state behaviour of vortex line density in counterflow follows from the steady state solution of Eq. (1.8) (i.e., $\dot{L} = 0$)

$$L = \gamma^2 (v_{\mathrm{ns}} - v_{\mathrm{c}})^2, \tag{3.1}$$

where $v_{\mathrm{ns}} - v_{\mathrm{c}}$ is typically used instead of just the counterflow velocity to account for the existence of non-zero critical velocity [14, 15], under which one observes no measurable vortex line density. The critical v_{c} is typically of the order of 1 mm/s and depends on the channel width for pure superflow [59] and, in the case of thermal counterflow, also on the temperature [83].

The steady state solution of Eq. (1.8) suggests that γ depends only on temperature and not on v_{ns}. For sufficiently large channels (of near-unity aspect ratio) and sufficiently high velocity, this does appear to be the case, see Fig. 3.2. In narrow channels two states of turbulence have been observed [84, 85] with γ switching from a low value (TI state) to a higher value (TII state) as the counterflow velocity is increased. A possible TI/TII transition was also observed in a wide channel [21], although the significant experimental scatter makes a decisive conclusion difficult.

Even though thermal counterflow and pure superflow would be a simple Galilean transforms of each other in an unbounded system, Fig. 3.2 reveals that γ of pure superflow is systematically higher than for thermal counterflow. This can only be explained by the different relative motion of the normal fluid with respect to the walls of the channel in the two flows and thus its possibly different turbulent state. The difference between pure superflow and thermal counterflow is even more pronounced during the decay (see Sec. 3.3).

Forced relative motion of the normal and superfluid component activated using a heat flux (i.e., the thermal counterflow) is an arrangement somewhat reminiscent of Rayleigh-Bénard convection (RBC) in classical fluids [86]. An important difference between the two flows, however, lies in the distribution of the thermal gradient along the flow. In the classical turbulent convection the temperature gradient is restricted to the boundary layers in the vicinity of the heating and cooling plate with the central region having mostly constant temperature. In thermal counterflow, on the other hand, the temperature gradient is constant (in other words, the temperature distribution is linear) in the bulk of the flow [31, 63], as shown in Fig. 3.4 (measured in a slowly ramping heat flux, as illustrated in Fig. 3.3).

Recent visualisation experiments [32], however, revealed an enhancement of vortex line density in close vicinity of the heat source in thermal counterflow at low heat inputs suggesting an existence of a boundary layer akin to the case in RBC. Similarly, enhancement of vortex line density has been observed near solid boundaries both experimentally [87] and numerically [88, 89]. Moreover, there

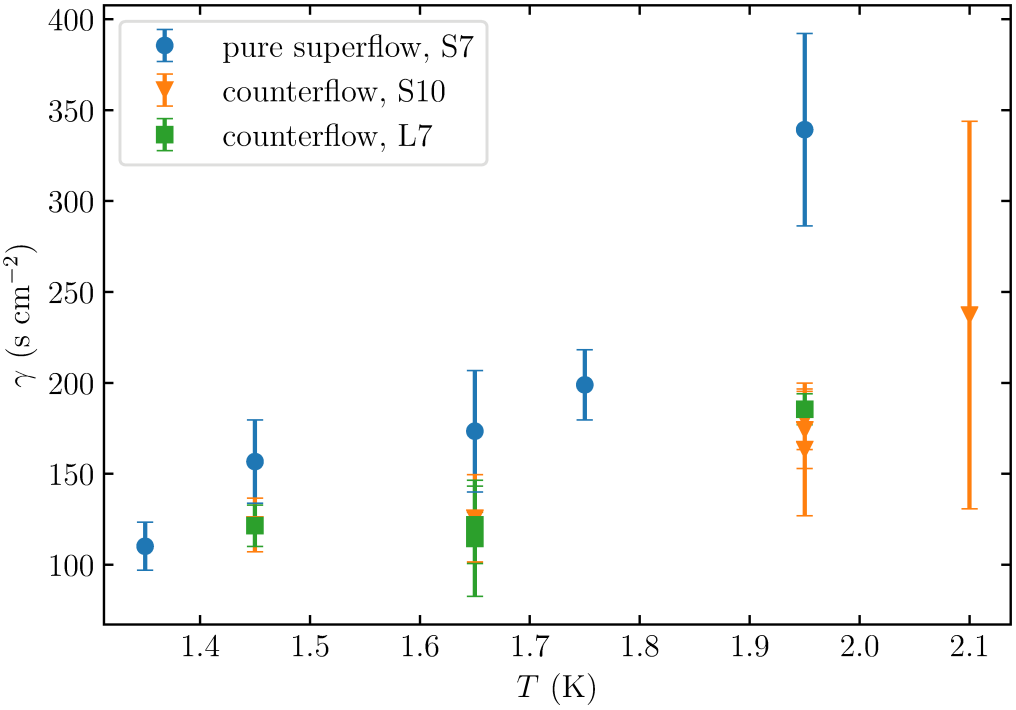

Figure 3.2: The steady state counterflow vortex line density scaling prefactor γ for the thermal counterflow and pure superflow measured in all three channels (see Fig. 2.2 and Fig. 2.3). The values are consistent with the values reported in the literature in the TII state of turbulence in wide channels [85].

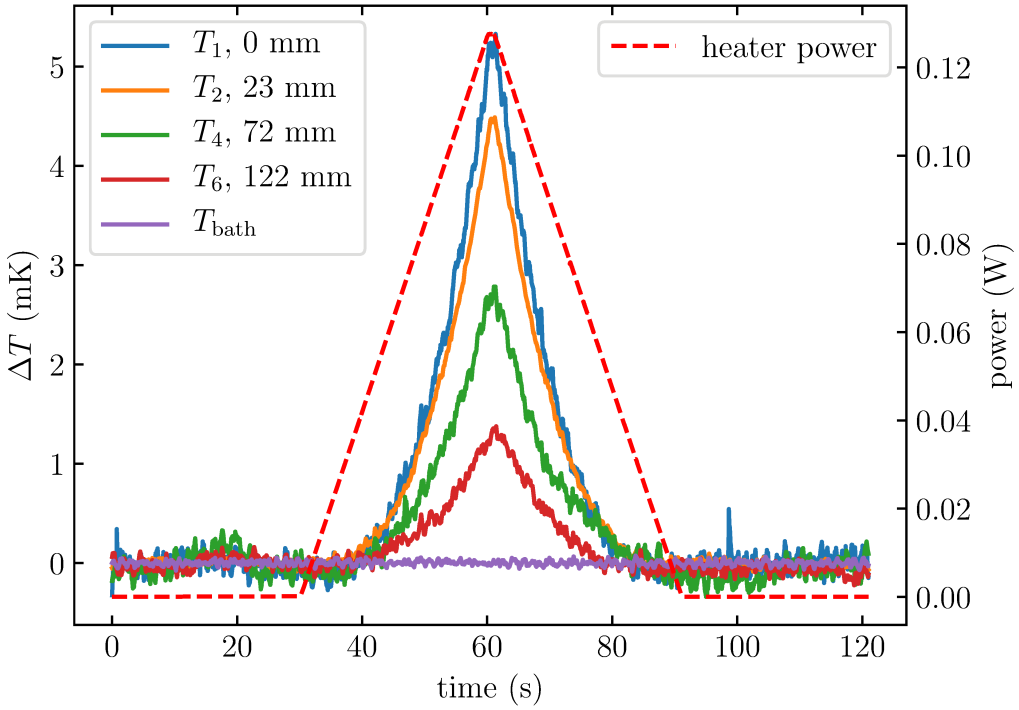

Figure 3.3: Distribution of the temperature along a channel in slowly ramping thermal counterflow. Shown is the temperature change from the initial state as the heat flux is slowly increased. The legend shows distance of the thermometers from a reference position of T_1 (see Fig. 2.3). The bath thermometer shows the temperature stability of the helium bath. Measured in the channel L7 at 1.45 K.

exists numerical evidence of significant entrance length effects [90]. Thermal conductivity of He-II depends on the vortex line density, therefore increased vortex line density in thermal counterflow ought to translate into higher temperature gradient. These developments led to the measurement of temperature distribution in the vicinity of a flat heater using a miniature (1 mm) thermometer mounted on a movable shaft coupled to a precision linear motor. The results are shown in Fig. 3.6. Immediately one can observe no significant increase in the temperature gradient close to the heater. This might appear to be a contradiction with the experiments of Hrubcová *et al.* [32], who observed roughly an order-of-magnitude increase in L near the heater compared to the bulk, what would correspond to $1-2$ orders of magnitude increase in temperature gradient. However, the heat flux accessible for direct thermometry in the present measurement was significantly higher than in Ref. [32] [1] which might translate to a significantly narrower boundary layer not resolvable by the used thermometer.

[1] The limiting factor for the low heat flux is the instrumentation noise and the temperature stability of the He II bath, whose fluctuations might overshadow the change due to counterflow heat flux.

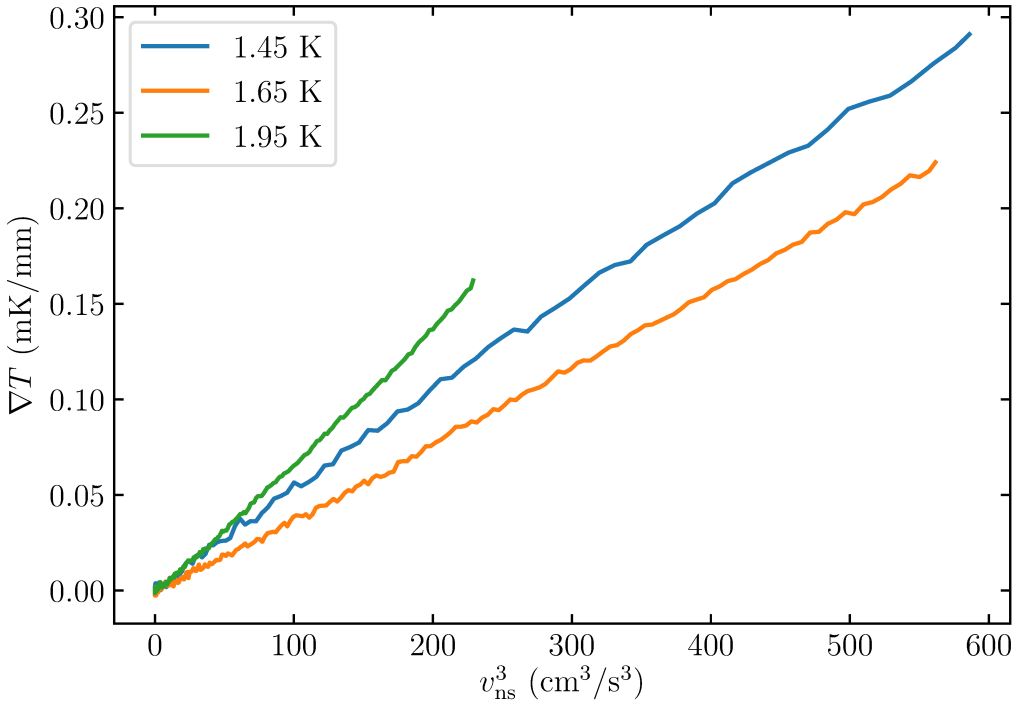

Figure 3.4: The linear temperature gradient measured in the channel L7 as a function of the counterflow velocity for temperature 1.45 K, 1.65 K and 1.95 K. The scaling of the x-axis v_{ns}^3 yields straight lines for power laws $\nabla T \propto v_{ns}^3$.

3.3 Decaying turbulence[2]

When energy input to the flow is stopped, the turbulence starts to decay. Monitoring the changes in the second sound resonance amplitude allows for time-resolved measurement of the vortex line density as outlined in Sec. 2.1.3. Time resolved second sound attenuation measurements, especially at low vortex line densities, often suffer from significant noise. In order to improve the signal/noise ratio, all transients shown in this section have been measured typically 100 times and averaged point-wise.

Regardless of the type of the steady-state flow, provided that the quantum length scale is much smaller than the system size, sufficiently late in the decay the mutual friction between the normal and the superfluid component is expected to couple the motion of the two fluids together [8, 48, 45]. Because of this coupling, it is not surprising that the late-time decay is universal across all investigated flows, and has the quasi-classical form (see Sec. 1.2.1) $L \propto t^{-3/2}$, as shown in Fig. 3.7 for a direct comparison between thermal counterflow and pure superflow. A more complete picture of the available counterflow and superflow decay data is presented in Figs. 3.10, 3.11 and 3.12.

This quasi-classical decay can be used to measure the effective kinematic viscosity ν_{eff}, which must be understood as a characteristic of the energy dissipation process rather than a material constant akin to the ordinary viscosity. The temperature-dependence of ν_{eff} obtained via the Eq. (1.15), and its comparison

[2]Results of this section were published in Ref. [40], reproduced as Attachment 2.

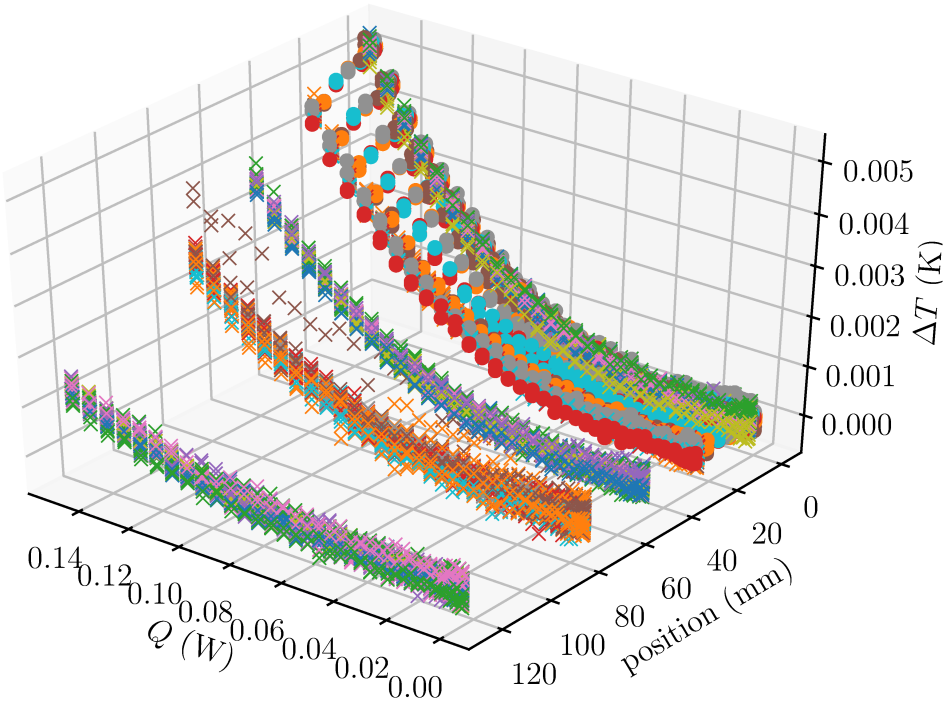

Figure 3.5: Temperature change in thermal counterflow as a function of heat flux and distance from the heater, measured in channel L7 at approximately 1.45 K. The crosses indicate data obtained with stationary wall-mounter thermometers, the circles correspond to the positionable motor-mounter thermometer. Data from several runs is overlaid to indicate repeatability.

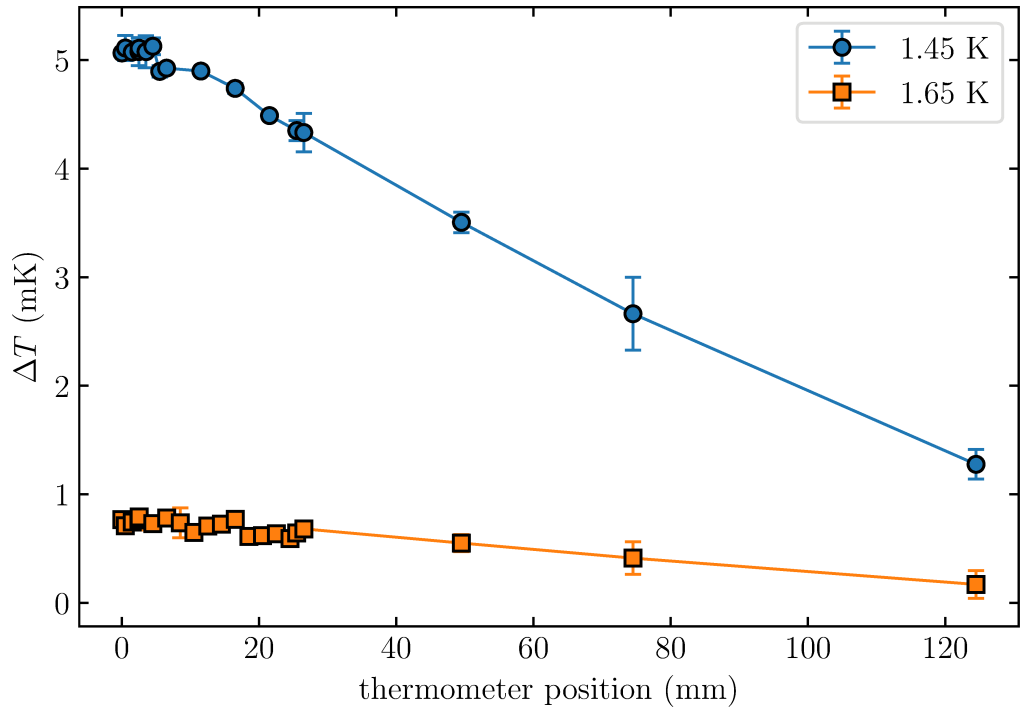

Figure 3.6: Distribution of the temperature in thermal counterflow for a constant heat flux at 1.45 and 1.65 K. The flat heater is located at position 0. The measurement was performed with a thermometer in roughly spherical enclosure of approximately 1 mm diameter mounted on a shaft of the same diameter (the channel cross-section being 7 mm square). The thermometer was attached to a shaft of a linear motor mounted on the outside of the cryostat flange. The closest position to the heater was approximately 0.25 mm. Heat flux for both temperatures was approximately 300 mW/cm^2.

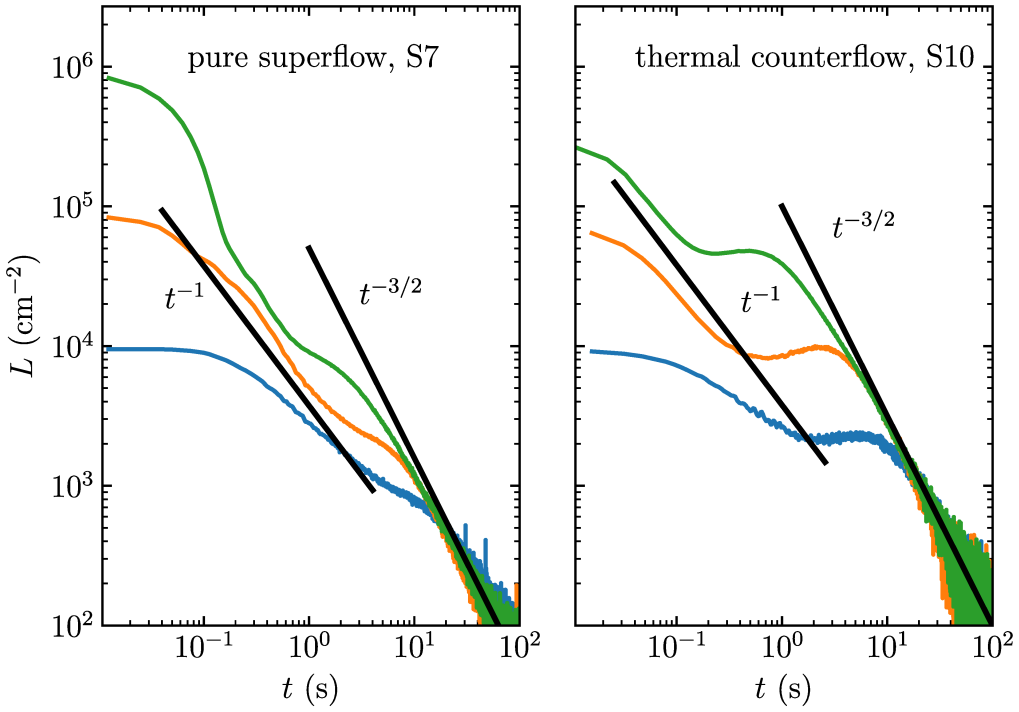

Figure 3.7: The time dependence of vortex line density in decaying pure superflow (left, channel S7) and thermal counterflow (right, channel S10), both at 1.65 K. The origin of time is set to the instant when the forcing was switched off. All flows display universal late-time quasi-classical scaling $L \propto t^{-3/2}$.

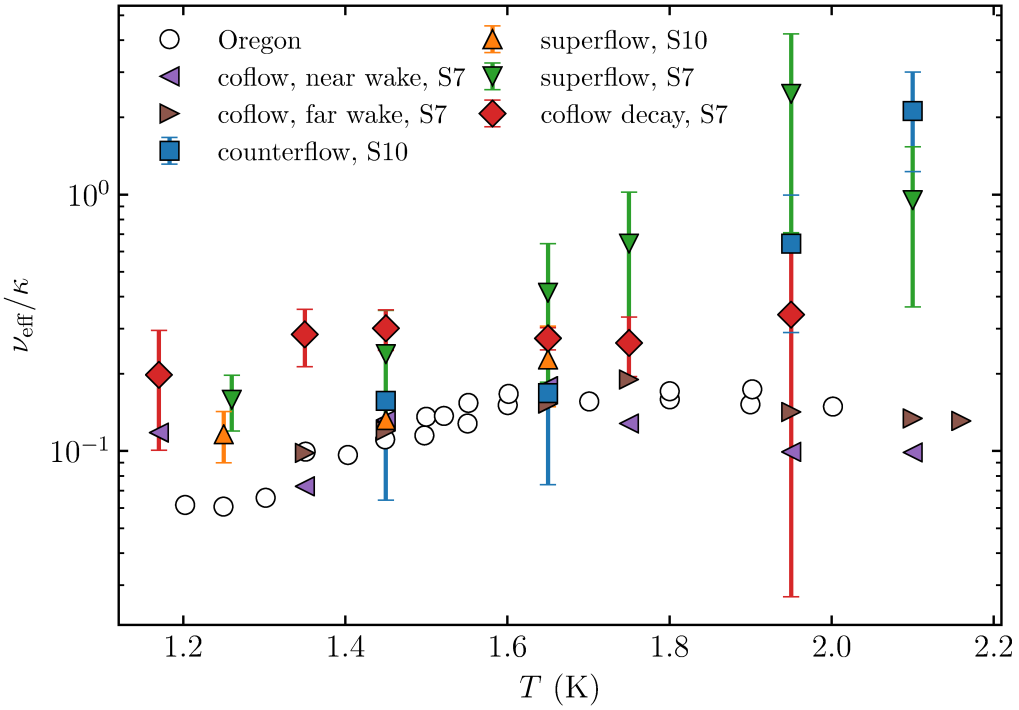

Figure 3.8: The effective viscosity of He II as a function of temperature in the two-fluid regime. Counterflow and superflow data are obtained as fits of Eq. (1.15) to late-time decays shown in Figs. 3.10,3.11 and 3.12. Coflow decay data is obtained in a similar fashion and was reported in Ref. [47]. The steady state coflow viscosities are obtained through Eq. (1.14) and were reported in Ref. [9]. The decay viscosities are averages of decays starting from different steady state vortex line densities, the associated standard deviation is taken as the error. The steady state coflow viscosities suffer from large experimental uncertainty (factor of 10), the associated error bars are not shown to avoid obscuring the figure. The Oregon data are after Ref. [8].

with coflow experiments [47, 9, 8], is shown in Fig. 3.8.

While the late decay is mostly independent of the type of the steady state flow, the early decay, shown in Fig. 3.9 and Figs. 3.10, 3.11 and 3.12 is strongly affected by the particular configuration of the normal and superfluid flows. In the simplest case of coflow [47], where the two components are coupled even in the steady state, the decay of vortex line density displays quasi-classical behaviour that persists throughout the entire decay process, and connects smoothly to the initial steady state. Contrary to that, superflow and counterflow have forced relative movement of the components and the decay first transitions through an intermediate behaviour characterised by fast early decay followed by a possibly non-monotonous transition to the quasi-classical late regime, see Fig. 3.9. The origin of the early fast part lies in the elimination of randomly oriented unstructured part of the tangle and follows the prediction of the Vinen equation (1.8) $L \propto t^{-1}$. The non-monotonous behaviour, often called simply the "bump" is connected with re-distribution of energy across the scales [41].

Following Gao *et al.*, the appearance of the bump can be understood as follows

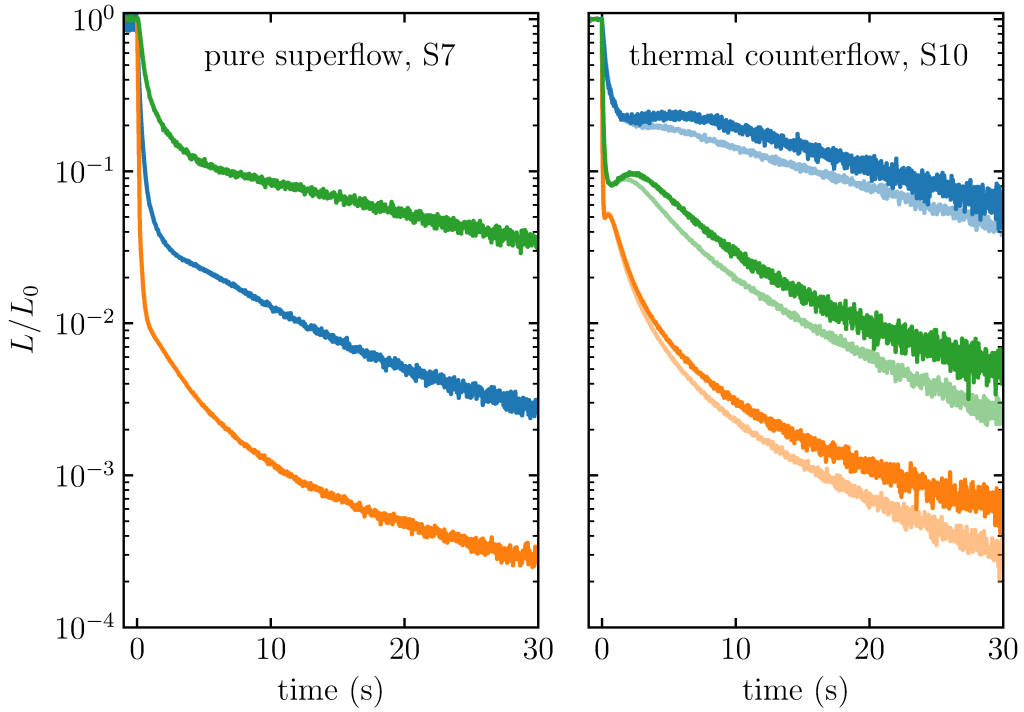

Figure 3.9: Early decay for thermal counterflow and pure superflow in log-linear scale. While the coflow displays [47] a smooth transition from steady state to quasi-classical behaviour, the counterflow and superflow transitions to the late-time quasi-classical behaviour through intermediate, and possibly non-monotonic regimes. The lighter, lower curves in the counterflow panel demonstrate the flushing effect of a small residual counterflow. At $t = 0$, the heat flux was not switched to zero but to a small sub-critical value (10 mW for the cases shown). The resulting flow appears to carry vortices away from the channel.

[41]. In thermal counterflow, there are two length scales at which the energy is injected. First, at small scales, the energy is taken from the mean flow by ballooning of favourably oriented vortex loops and Kelvin waves via the action of mutual friction [79]. This mechanism is expected to act primarily near the scale of intervortex separation $\ell = 1/\sqrt{L}$. Second, at large scales, by analogues of classical flow instabilities. The large scale mechanism ought to act on the scale of the size of the system, i.e., the channel width D.

The small scale energy injection is conjectured [16, 17] to induce a "quantum peak" in the turbulent energy spectrum located at the intervortex distance ℓ. In the absence of imposed counterflow, the two fluid components should be coupled at scales exceeding ℓ by mutual friction, causing He II to behave quasi-classically, as outlined above. The energy injected at large scales would be distributed along a classical Richardson cascade following a classical K41 $k^{-5/3}$ spectrum. This will not be the case with imposed difference between the normal and superfluid mean velocities, which will pull similarly sized eddies in the two components apart, causing additional dissipation across all scales [16].

It was found [21, 42] that the energy spectrum in steady state thermal counterflow (for scales larger than the intervortex distance ℓ) is steeper than the K41 spectrum[3]. The exact roll-off exponent of the normal fluid energy spectrum depends on the temperature and heat flux [42], but is always larger in magnitude than the classical 5/3.

A useful way to interpret this non-classical spectrum $E(k)$ is through k-dependent energy flux $\epsilon(k)$, i.e.,

$$E(k) = C[\epsilon(k)]^{2/3}k^{-5/3}. \tag{3.2}$$

For the special case [21] of $E(k) \propto k^{-2}$, $\epsilon(k) \propto k^{-1/2}$. Generally, steeper spectrum signifies diminishing flux ϵ with increasing k. In particular, in steady state thermal counterflow, the flux of energy originating at large scales to the quantum peak at small scales is negligible. When the counterflow is switched off and the decay starts, the quasi-classical spectrum establishes (thus ϵ ceases to be k-dependent) and energy flow to inter-vortex scale resumes. The quasi-classical spectrum is established only in finite time (roughly the turnover of the large eddies), during which the quantum peak in the energy spectrum decays to be subsequently partially replenished by the restored energy flux, thus resulting in temporary increase in vortex line density (seen experimentally as the "bump" in temporal decay of VLD).

Note that in the pure superflow, the normal fluid is not directly forced and can be entrained freely by the superflow at large scales (apart from inducing mean flow, which is blocked by the superleaks). It is thus a reasonable assumption that the pure superflow energy spectrum is closer to a quasi-classical one and the energy flux to small scales is suppressed to a lesser degree, which would in turn translate to a less pronounced bump. This is indeed observed as can be seen in Figs. 3.11 and 3.12. Note an interesting geometrical effect, that actual reversal in $L(t)$ appears for superflow only in the 10 mm S10 channel and is never present

[3]Note that a similarly steeper-than-classical spectrum was also observed in coflow in the decaying turbulent wake behind a towed grid, see Sec. 3.5. This situation is, however, complicated by the fact that the turbulence in this case never reaches the steady state.

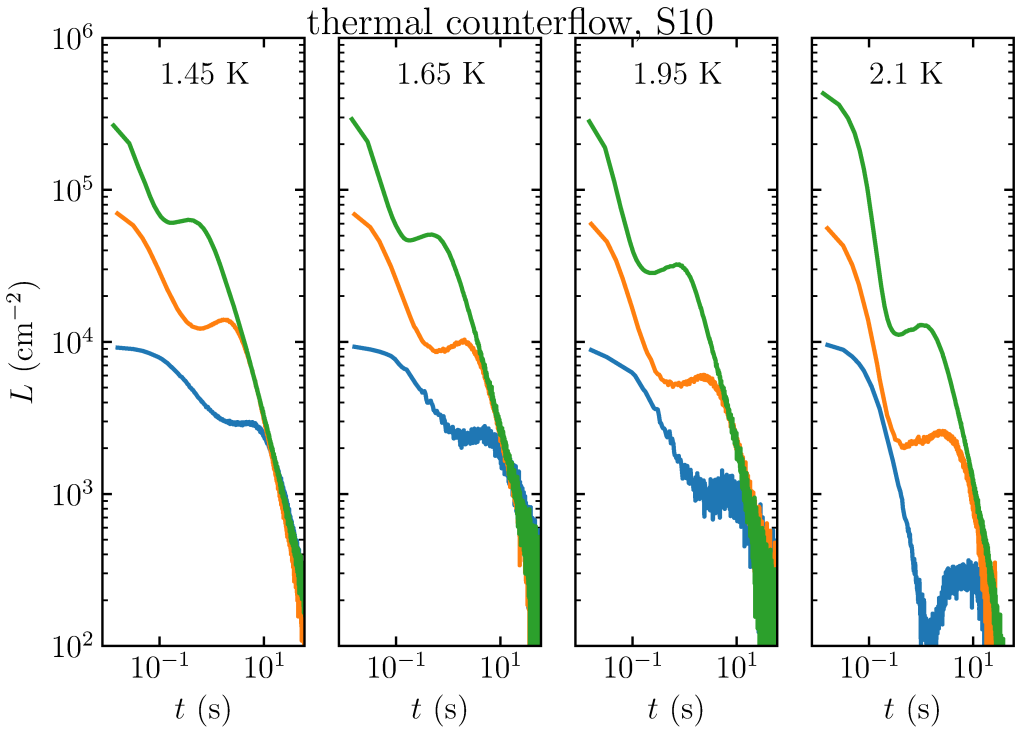

Figure 3.10: Decaying counterflow turbulence from three different initial vortex line densities, measured in S10 channel at the indicated temperatures. Note the universal presence of the "bump" and near-perfect overlap of the quasi-classical decay regimes for large times. The large non-monotonicity on the curve for $L_0 = 10^4$ at 2.1 K is likely caused by temperature instability. This case was not used for calculation of the effective viscosity shown in Fig. 3.8.

in the 7 mm S7 channel, even when the decays start from the same initial vortex line density.

3.4 Dynamics of vortex line density in unsteady thermal counterflow[4]

Previous sections were concerned with either the statistically steady or decaying-in-time vortex line density. However, for thermal counterflow, the Vinen equation (1.8) of the dynamics of the vortex line density is formally valid for general quasi-stationary time evolution, which has been more concretely substantiated by the derivation of Schwarz [35] based on the local induction approximation (see Sec. 2.2.1) of dynamics of the quantized vortex lines.

It is well known that the Vinen equation fails to capture experimental observations in late and intermediate decay of counterflow (Sec. 3.3) (with possible exception of very low heat fluxes [41]). Several theoretical attempts have been made to generalise the Vinen (or Schwarz) equation by, for example, taking account of possible flux of the vortex lines due to spatial variation of their density

[4]The results presented in this section were published in Ref. [58], reproduced as Attachment 3.

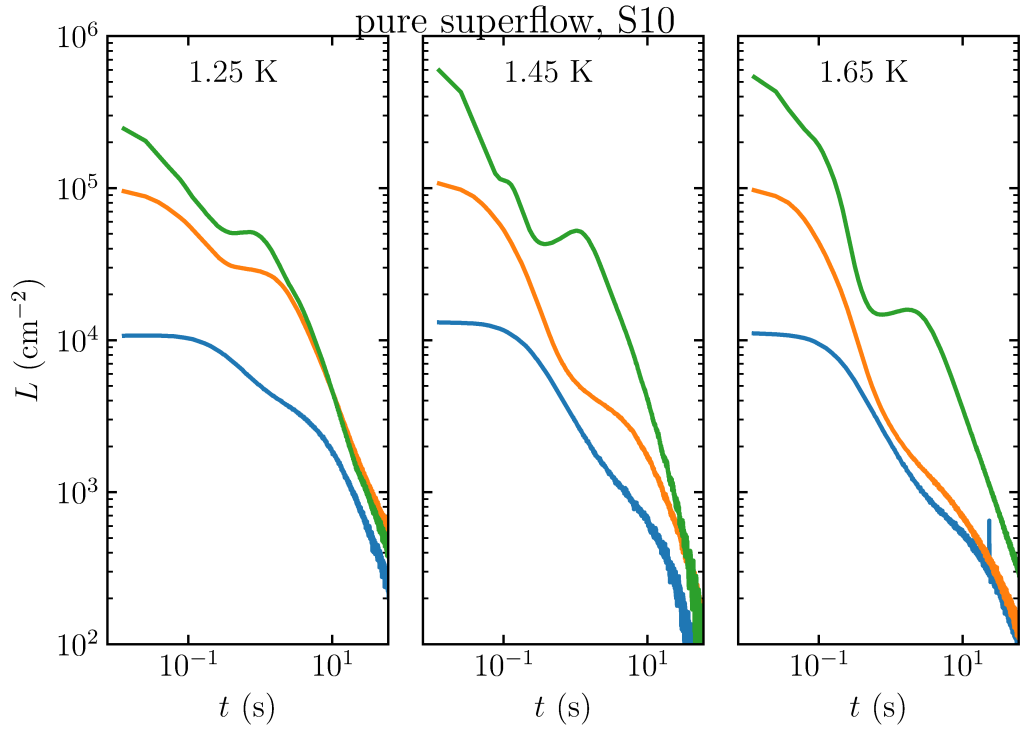

Figure 3.11: Decaying pure superflow turbulence from three different initial vortex line densities, measured in S10 channel at the indicated temperatures.

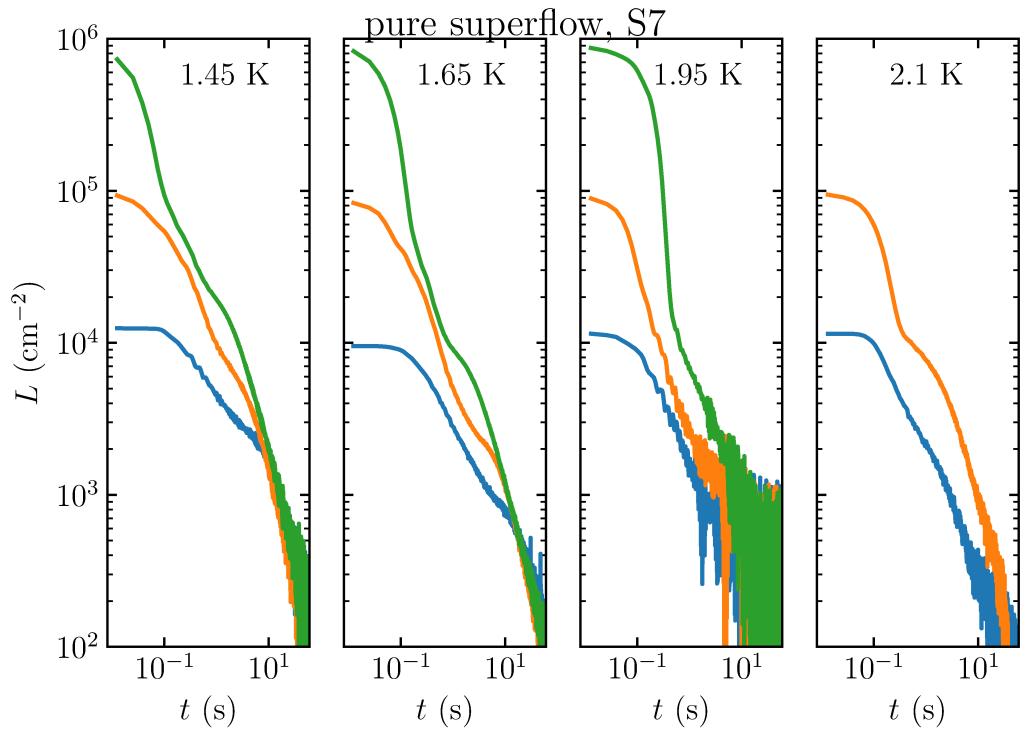

Figure 3.12: Decaying pure superflow turbulence from three different initial vortex line densities, measured in S7 channel at the indicated temperatures.

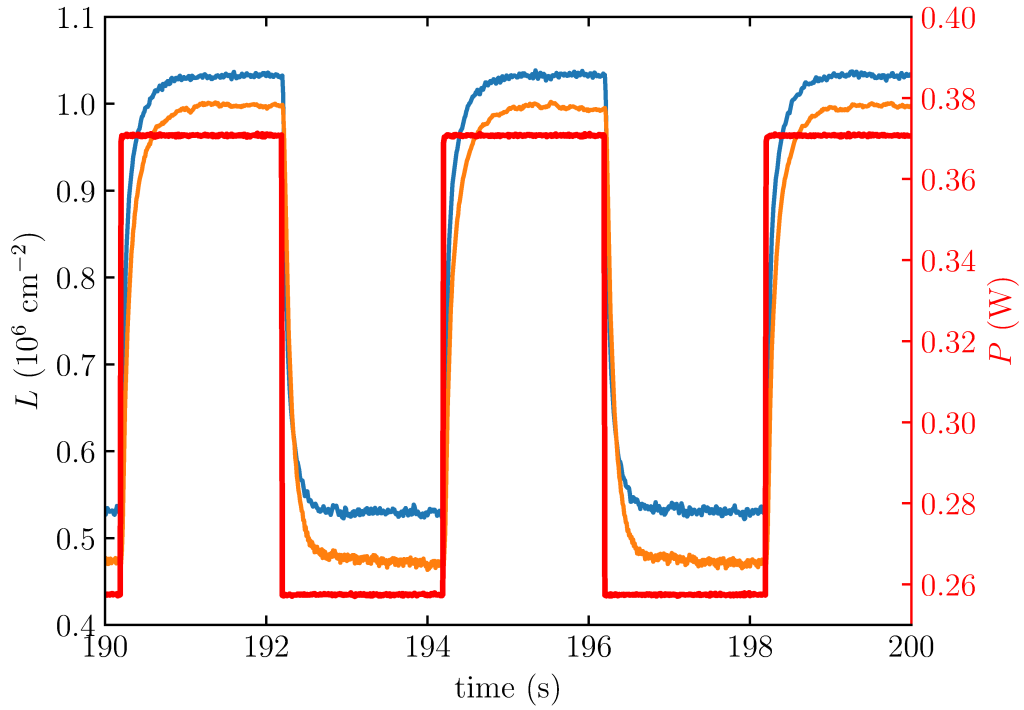

Figure 3.13: Vortex line density response to the square wave-modulated heat flux. The VLD from sensors L1 and L2 (see Fig. 2.3) is shown by the blue and orange curves (left y-axis). The heat flux is shown by the red curve with sharp steps (right y-axis). The shown case was measured at 1.95 K with modulation corresponding to steady state vortex line densities 5×10^5 and 10^6 cm^{-2}.

or allowing for existence of independent dynamics of, for example, the anisotropy parameters of the vortex tangle [91, 37, 92].

To test the boundaries of the validity of the Vinen equation and to ascertain the validity of the attempts to generalise it, dynamics of the vortex line density in thermal counterflow with well defined and non-trivial time dependence was studied. The counterflow velocity was modulated by a square wave (Fig. 3.13) which resulted in time-dependent vortex line density $L(t)$ exhibiting periodic switching in vortex line density between two steady-state values (for sufficiently long periods). The experiments were carried out in the channel L7 (Fig. 2.3) using sensors L1 and L2. No significant difference was observed between turbulence properties at different sensor locations, apart from slight, but systematic, variation in the steady state VLD which is probably affected by sensor quality or local machining imperfections [63]. Notably, no indication of propagating vortex front when flow is first switched on was observed [63], contrary to studies in narrow [93, 94, 95] or non-uniform [96] channels, but rather the tangle appears to grow uniformly along the channel – e.g., growing from seed loops pinned to the walls. For validation of the system, the steady state measurement of vortex line density was carried out, shown in Fig. 3.14. The resulting coefficients γ, shown in Fig. 3.2, are consistent with values reported in the literature and counterflow measurements in the channel S10 (Fig. 2.2).

In order to be able to study the response of vortex line density to the non-

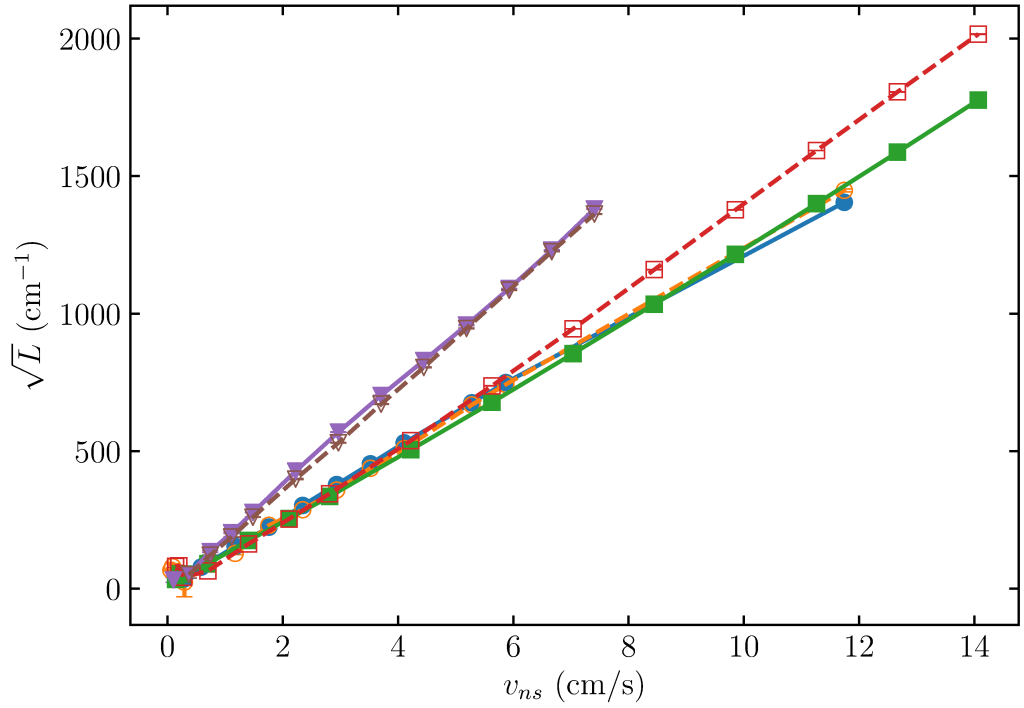

Figure 3.14: The steady state vortex line density in thermal counterflow in the channel L7. Filled symbols are measured using second sound sensor L1, empty using sensor L2, see Fig. 2.3. ●, ○ – 1.45 K, ■, □ – 1.65 K, ▼, ▽ – 1.95 K.

stationary heat flux, parasitic effects occurring upon the switching of the heat flux that might affect the flow must be characterised. Two such processes were identified which can be described through their characteristic times – *kinetic* and *thermal*. In order for the measurements to be meaningful, the modulation pulse width and the observed properties of the VLD dynamics ought to occur on time scales large compared to these characteristic times.

(1) Kinetic characteristic time. Assuming that the fluid inside the channel is initially at rest, the energy necessary to set the fluid into motion – that is, the kinetic energy of the flow – has to be supplied. The kinetic energy of the counterflow per unit volume is

$$E_{\mathrm{kin}} = \frac{1}{2}\rho_s v_{\mathrm{s}}^2 + \frac{1}{2}\rho_n v_{\mathrm{n}}^2 = \frac{1}{2}\frac{\rho_n \rho_s}{\rho} v_{\mathrm{ns}}^2. \tag{3.3}$$

The only source of energy in the channel is the counterflow heater which supplies a constant heat flux $\dot{q} = \dot{Q}/A$ where $\dot{Q}$ is the dissipated power and A the cross-section area of the channel. This heater will supply the kinetic energy (3.3) in time $t_{\mathrm{char}}^{\mathrm{kin}}$, i.e.

$$t_{\mathrm{char}}^{\mathrm{kin}} = \frac{E_{\mathrm{kin}} V}{\dot{Q}} = \frac{1}{2}\frac{\rho_n}{\rho_s \rho S^2 T^2} L_{\mathrm{ch}} \dot{q}, \tag{3.4}$$

where V is the volume of the channel and L_{ch} is its length. The characteristic times for experimental temperatures and heat fluxes are shown in Fig. 3.15. Note that some modulations used in the experiment do not turn the heater off

completely during the course of one period. For these transitions, the heater has to supply only the difference in energy between the higher and the lower state. Thus for these cases the characteristic time would be somewhat reduced. Note also that the kinetic energy of the flow outside the channel is neglected, therefore Eq. 3.4 should be understood as an order-of-magnitude estimate.

(2) Thermal characteristic time. As has been shown in Sec. 3.2.1, a temperature gradient is always present in thermal counterflow. To establish the temperature gradient, heat must be supplied to warm up the helium appropriately. This time is estimated in a similar fashion to Ref. [97]. Assuming linear temperature profile of constant gradient ∇T, the excess heat necessary is

$$\Delta Q = \rho A c \int_0^{L_{\mathrm{ch}}} \mathrm{d}\, x x |\nabla T| = \frac{1}{2} \rho A c L_{\mathrm{ch}} \Delta T \tag{3.5}$$

where ΔT is the temperature difference between the two ends of the channel and c is the heat capacity of He II. For sufficiently high vortex line densities $\dot{q} = \zeta(T) \nabla T^{1/3}$ where $\zeta(T)$ is a temperature-dependent parameter (see Fig. 3.4). Differentiating Eq. (3.5) with respect to time yields

$$\dot{q} = \frac{1}{2} \rho A c L_{\mathrm{ch}} \dot{\Delta T} = \zeta(T) \left[\frac{\Delta(t)}{L_{\mathrm{ch}}} \right]^{1/3} . \tag{3.6}$$

Solving Eq. (3.6) for ΔT, and assuming that $\Delta T(t = 0) = 0$, the temperature gradient ΔT_f corresponding to a given heat flux $\dot{q}$ is reached in a time

$$t_{\mathrm{char}}^{\mathrm{th}} = \frac{3 c \rho |\Delta T_f^{2/3}|}{4 \zeta} L_{\mathrm{ch}}^{4/3} . \tag{3.7}$$

The temperature distribution, and thus ΔT_f and $\zeta(T)$, are measured inside the channel L7 by the wall-mounted thermometers. The resulting thermal characteristic times in the experiments are shown in Fig. 3.15, and can be bounded from above for all experimental cases by roughly 60 ms. It was only possible to read out the thermometer resistances with an approximately 100 ms time constant in order to suppress noise sufficiently, therefore it was not possible to observe this temperature buildup directly.

Additional limitation comes from the time resolution of the second sound measurement (see Sec. 2.1.3), namely the width of the second sound peak (typically larger than 50 Hz) and the lock-in time constant (10 ms). Since all parasitic processes ought to take place in parallel, we can take overall *parasitic characteristic time* approximately 60 ms as the worst-case scenario. The vortex line density is sampled at a fixed rate of 100 points per second, meaning that the first six points after each individual transition in the pulse train are possibly affected by parasitic effects unrelated to the intrinsic dynamics of vortex line density. The pulse widths used were 200, 500, 1000 and 2000 ms. The parasitic characteristic time might pose a problem for the fastest pulses, however, the bulk of the study was focused on the 2000 ms and 1000 ms cases.

The transients resulting from the periodic switching of the heat flux are well reproducible and averaging can be used to significantly reduce the experimental noise on $L(t)$ to the point where numerical differentiation is possible, as can be seen in Fig. 3.16. Access to the time derivative of the vortex line density allows

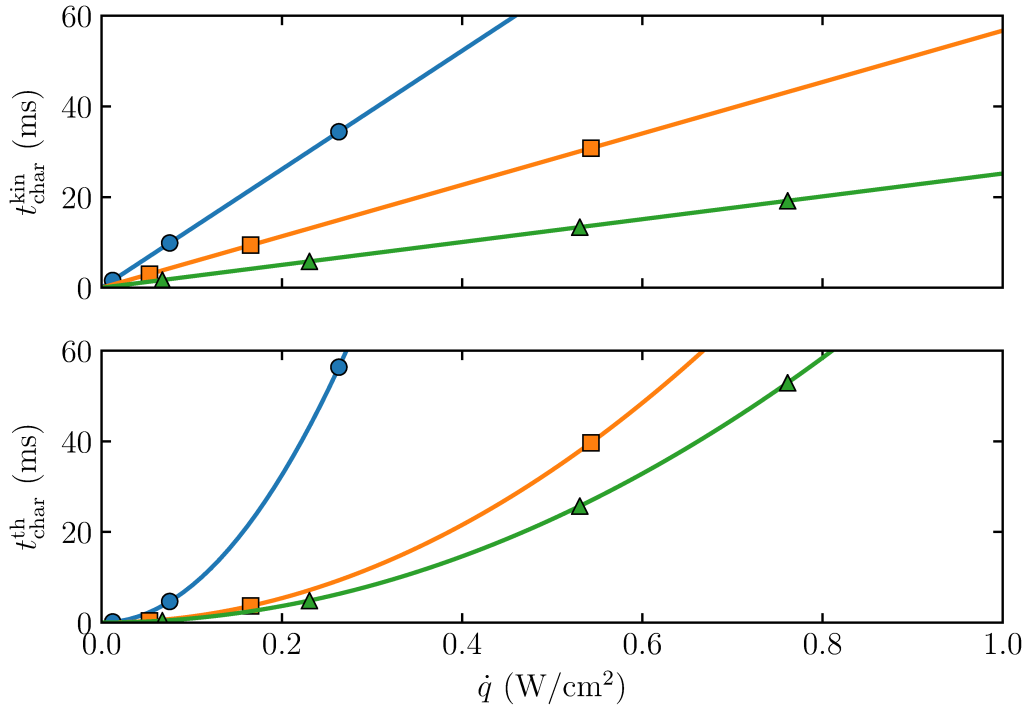

Figure 3.15: Characteristic times of the parasitic effects. Top panel: kinetic characteristic time $t^{\mathrm{kin}}_{\mathrm{char}}$ necessary to accelerate the fluid inside the channel to the velocity corresponding to the heat flux through Eq. (2.1). Bottom panel: thermal characteristic time required to supply the heat necessary to establish the counterflow temperature gradient. The points indicate the experimental configuration at which measurements took place for temperatures ● – 1.45 K, ■ – 1.65 K, ▲ – 1.95 K. The characteristic times are calculated for modulations alternating between zero and the indicated heat flux. Modulations that do not go to zero have shorter characteristic times. The lines show the functional dependencies (3.4) and (3.7) for 1.45 K, 1.65 K and 1.95 K (top to bottom).

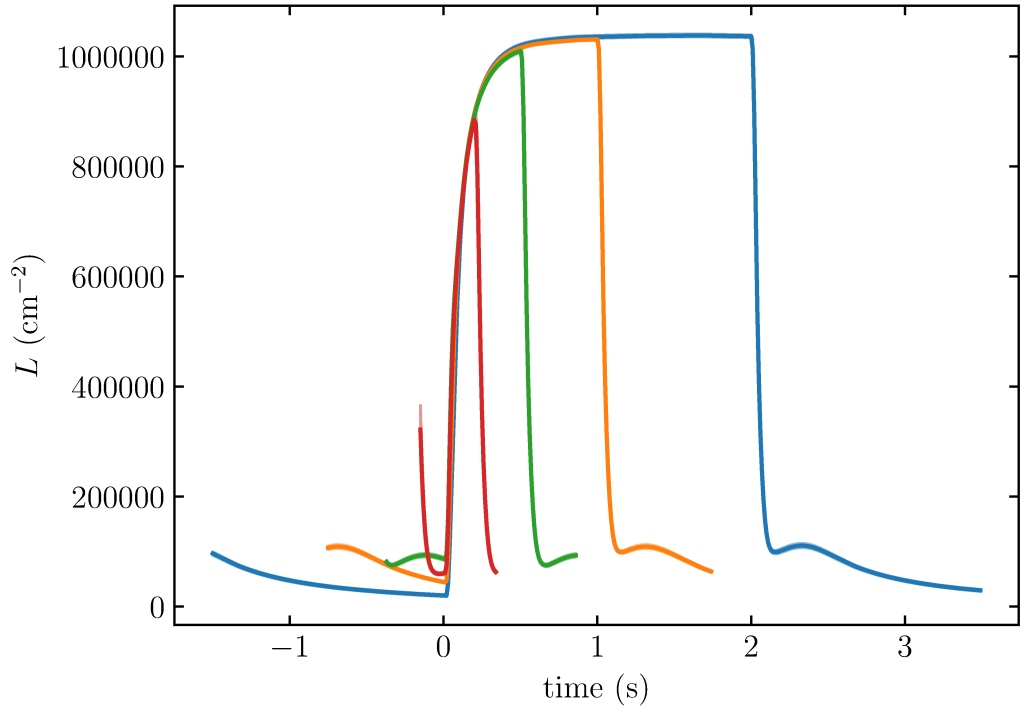

Figure 3.16: Averaged pulses for different modulation pulse widths. The shown pulse widths are 0.2, 0.5, 1 and 2 s. The heat flux was pulsed between 0 and 266 mW (corresponding to steady state VLD of about 10^6 cm^{-2}) at 1.45 K. Each curve is an average of several thousand transients. The standard deviation is not visible on the scale of the figure. The rising edge of the heat flux is used as the time origin. The width of the rising edge is roughly 300 μs and VLD is measured every 10 ms.

for studying the dynamics more directly. In particular, assuming that the the dynamics of the vortex line density (averaged across the size of the system) is governed by a first-order ordinary differential equation of the from $\dot{L} = f(L; v_{\mathrm{ns}})$, knowing $\dot{L}$ one can obtain a direct picture of the dynamical equation in the phase space, assuming such equation exists.

The particular phase space can be chosen essentially at will. A natural choice would be, for example, $(L,\ \dot{L})$. For the particular cases of Vinen-like equation with varying exponents of v_{ns} (see Eq. (1.11)) a more suitable choice is

$$\left(\frac{1}{\sqrt{\ell}}, -\frac{\mathrm{d}}{\mathrm{d}\,t}\frac{1}{\ell}\right), \tag{3.8}$$

where $\ell(t) = L(t)/L_0$ and L_0 is the vortex line density corresponding to the steady-state that would be produced by the instantaneous counterflow velocity. In these variables the general type of the Vinen-like equation (1.11) reads

$$-\frac{\mathrm{d}}{\mathrm{d}\,t}\left(\frac{1}{\ell}\right) = L_0 D_n \left[\left(\frac{1}{\sqrt{\ell}}\right)^n - 1\right], \tag{3.9}$$

where the cases of $n = 1, 2, 3$ attracted attention in the literature [14, 37, 38, 92, 36]. An idealised sketch of the phase trajectory of VLD in modulated counterflow

is shown in Fig. 3.17. The particular case of the Schwarz equation reads

$$-\frac{\mathrm{d}}{\mathrm{d}\,t}\left(\frac{1}{\ell}\right) = \alpha\beta c_2^2\left(\frac{1}{\sqrt{\ell}} - 1\right), \tag{3.10}$$

where α is the mutual friction parameter and

$$\beta = \frac{\kappa}{4\pi}\ln\left(\frac{1}{c_1 L^{1/2}\xi}\right), \tag{3.11}$$

with $\xi \approx 1$Å. The c_1 and c_2 coefficient are defined through $\langle|\mathbf{s}''|\rangle = c_1 L^{1/2}$ and $\sqrt{\langle|\mathbf{s}''|^2\rangle} = c_2 L^{1/2}$ with $\mathbf{s}''$ the local curvature vector of a vortex (i.e., the second derivative of the vortex line with respect to the arc length along the vortex, see Sec. 2.2.1).

The above definition of the dimensionless vortex line density ℓ is not suitable for free decay, where $L_0 = 0$. Therefore for decays (for consistency all decays, not just the free decay) the dimensionless vortex line density is defined as $\tilde{\ell}(t) = L(t)/L_\mathrm{i}$, where L_i is the initial vortex line density from which the decay originates. With these variables equations (3.9) and (3.10) read

$$-\frac{\mathrm{d}}{\mathrm{d}\,t}\left(\frac{1}{\tilde{\ell}}\right) = L_\mathrm{i} D_n\left[\left(\frac{v_\mathrm{ns}}{v_\mathrm{ns}^\mathrm{i}}\right)^n\left(\frac{1}{\sqrt{\tilde{\ell}}}\right)^n - 1\right] \tag{3.12}$$

and

$$-\frac{\mathrm{d}}{\mathrm{d}\,t}\left(\frac{1}{\tilde{\ell}}\right) = \alpha\beta c_2^2 L_\mathrm{i}\left(\frac{v_\mathrm{ns}}{v_\mathrm{ns}^\mathrm{i}}\frac{1}{\sqrt{\tilde{\ell}}} - 1\right), \tag{3.13}$$

respectively, where v_ns^i is the initial counterflow velocity associated with the L_i. In the following, the growth and decay phase trajectories in the dimensionless coordinates are never shown together and the $\tilde{\ell}$ notation is dropped.

Plotting the experimentally obtained dynamics of the vortex line density in the phase space given by (3.8) one obtains a phase trajectory as in Fig. 3.18 for $T = 1.45$ K, heat flux switching between 0 and 266 mW (corresponding to $v_\mathrm{ns} \approx 1$ m/s and $L_0 = 10^6$ cm^{-2}) and for several different pulse widths of the square wave modulation. The trajectories in Fig. 3.18 showcase several important features: the non-monotonicity of the decay appears as the loop in the decay part of the curve (and as such cannot be described by a functional relationship of the form $\dot{L} = f(L)$); the approach to the steady state from the growth side is monotonous; the growth does not depend on the pulse width, while the decay is clearly dependent on the history. For these reasons, the vortex line density growth appears to be a more suitable transient process for studying the intrinsic dynamics of the vortex tangle[5]. Additionally, theories of VLD dynamics ought to be valid for both growth and decay transients, but the growth received scant experimental attention to date, with few notable exceptions [98].

Focusing thus on the growth of VLD and its approach to the steady state, an example shown in Fig. 3.19, one immediately sees that assessing the relative suitability of the three proposed forms of the Vinen equation – Eq. (3.9) with $n = 1, 2, 3$ – is an ill-posed problem. For sparse tangles, all functional forms yield adequate fit whereas for higher densities none of the models provides a satisfactory description.

[5] Assuming, of course, that VLD-centric description of quantum turbulence is not an over-simplification so severe as to render development of a meaningful theory impossible.

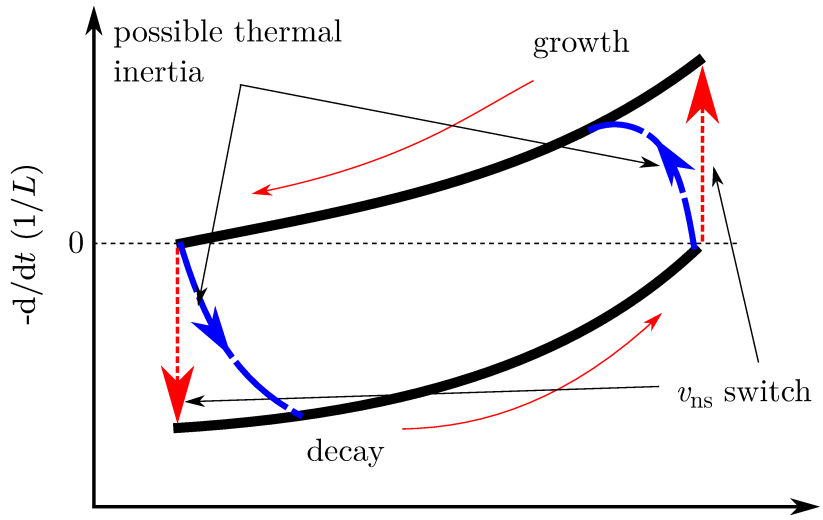

Figure 3.17: An idealised sketch of a phase trajectory of vortex line density according to Eq. (3.9) (in phase space given by (3.8)) for square wave-modulated counterflow.

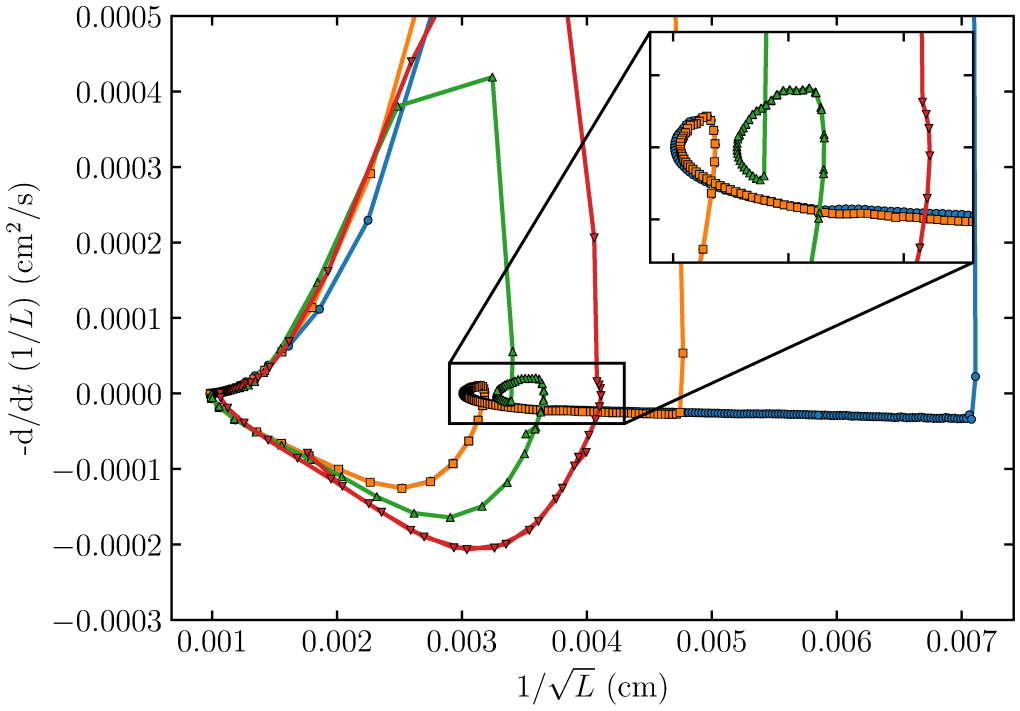

Figure 3.18: Phase trajectories of the vortex line density at 1.45 K and heat flux switching between 0 and 266 mW ($L_0 \approx 10^6 \mathrm{cm}^{-2}$, see also Tab. 3.1 for details). Different curves correspond to different pulse widths of the square wave modulation, shown are 0.2, 0.5, 1 and 2 s.

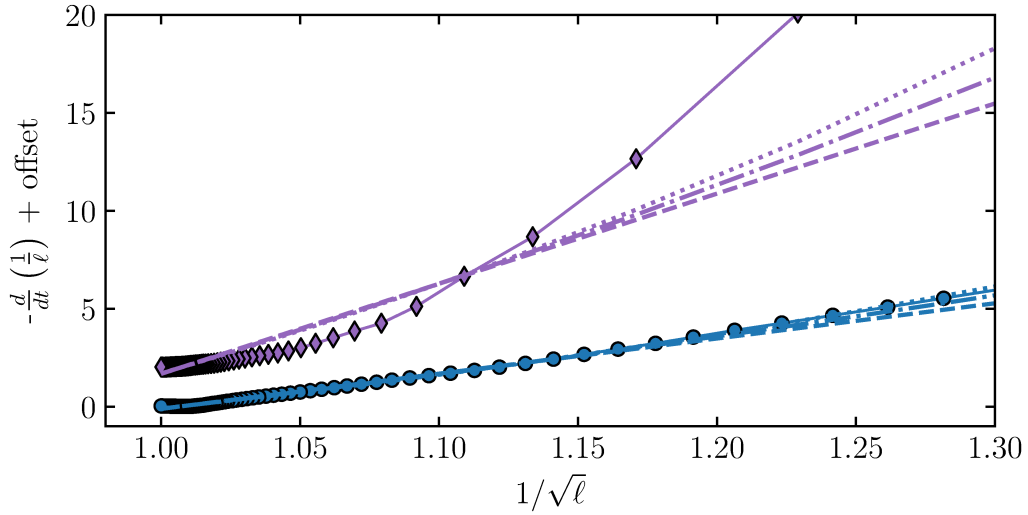

Figure 3.19: Growth part of the vortex line density phase trajectory at 1.45 K for sparse (●, VLD modulation between 0 and 10^5 cm^{-2}) and dense (◆, VLD modulation between 10^5 and 10^6 cm^{-2}) tangles, see Tab. 3.1. The dashed, dash-dotted and dotted lines are fits to Eq. (3.9), with $n = 1, 2$ and 3, respectively. The fit was performed in the range $\ell \in [1, 1.2]$. For the sparse case, all models provide an adequate description; for the dense case all models provide a poor fit.

Further analysis is based on the Schwarz equation (3.10) (i.e., $n = 1$) due to the fact that it is currently the simplest available theory of the macroscopic VLD dynamics based on the microscopic motion of the vortices [35].

Growth part of the phase trajectory together with a plot of Eq. (3.10) using numerical prediction of c_2 from Ref. [35] is shown in Fig. 3.20. For sparse tangles, the agreement between experiment and numerical prediction is remarkable, especially given the fact that during the decay from even these relatively low densities the "bump" is clearly visible. Denser tangles, however, appear to approach the steady state more slowly than expected. This could, of course, have several reasons – for example, siphoning of energy into creation of normal fluid turbulence. For the present purpose, the use of the dynamical equation (3.10) is retained with a postulate that c_2 ought to be L-dependent (and neglecting, for this rather qualitative analysis, the possible L-dependence of c_1 which appears only in the logarithmic term β).

Extracting the effective curvature parameter c_2 from the growth curves of Fig. 3.20 yields results shown in Fig. 3.21. A marked decrease in c_2 is observed as the intervortex separation decreases. If one were to maintain the original interpretation of c_2, this result suggests that the vortices exhibit fewer kinks than would be expected from a homogeneous isotropic tangle. This would be consistent with the idea of vortex bundles or regions of mostly straight and parallel vortices coupled (through the mutual friction) to the normal fluid eddies. Indeed, numerical simulations of Sherwin-Robson *et al.* [82] suggest that the curvature of the tangle decreases when normal fluid turbulence is introduced. In addition, simulations of Kondaurova *et al.* [81] observed increase in c_2 during free decay, i.e., as the vortex line density decreases. However, no decrease of c_2 with increasing

Temperature	1.45 K	1.65 K	1.95 K
symbol	●	●	
v_{ns} (cm/s)	2.4/0.0	2.5/0.0	
L_1, L_2	$7.9 \pm 0.3/1.9 \pm 0.3$	$7.4 \pm 0.4/0.8 \pm 0.3$	
(10^4 cm^{-2})	$6.4 \pm 0.7/1.3 \pm 0.7$	$8.2 \pm 0.1/1.6 \pm 0.2$	
symbol	■	■	●
v_{ns} (cm/s)	2.4/0.4	2.5/0.8	1.8/0.5
L_1, L_2	$7.9 \pm 0.2/1.9 \pm 0.3$	$7.5 \pm 0.3/1.3 \pm 0.3$	$9.7 \pm 0.2/0.8 \pm 0.3$
(10^4 cm^{-2})	$6.5 \pm 0.7/1.6 \pm 0.7$	$8.3 \pm 0.3/1.5 \pm 0.3$	$8.5 \pm 0.2/0.5 \pm 0.3$
symbol			■
v_{ns} (cm/s)			4.3/1.8
L_1, L_2			$54 \pm 0.4/10 \pm 0.7$
(10^4 cm^{-2})			$48 \pm 0.4/8.5 \pm 0.5$
symbol	▲**	▲	▲
v_{ns} (cm/s)	8.4/0.0	8.3/0.0	6.1/0.0
L_1, L_2	$97 \pm 0.5/11 \pm 0.3$	$83 \pm 0.3/1.3 \pm 0.2$	$100 \pm 0.5/1.8 \pm 0.5$
(10^4 cm^{-2})	$96 \pm 2.4/13 \pm 0.7$	$100 \pm 0.3/2.0 \pm 0.2$	$99 \pm 0.5/1.7 \pm 0.5$
symbol	▼*	▼	▼
v_{ns} (cm/s)	8.4/0.4	8.3/0.8	6.1/0.5
L_1, L_2	$99 \pm 0.8/5.7 \pm 0.3$	$83 \pm 0.3/1.5 \pm 0.3$	$100 \pm 0.4/0.6 \pm 0.5$
(10^4 cm^{-2})	$98 \pm 2.3/6.3 \pm 0.7$	$100 \pm 0.6/0.91 \pm 0.3$	$98 \pm 0.6/1.0 \pm 0.6$
symbol	◆*	◆	
v_{ns} (cm/s)	8.4/2.4	8.3/2.5	
L_1, L_2	$99 \pm 0.5/9.2 \pm 0.2$	$83 \pm 0.2/7.6 \pm 0.1$	
(10^4 cm^{-2})	$98 \pm 2.4/8.7 \pm 0.6$	$100 \pm 0.4/7.3 \pm 0.2$	
symbol			◆
v_{ns} (cm/s)			6.1/4.3
L_1, L_2			$100 \pm 0.4/53 \pm 0.4$
(10^4 cm^{-2})			$100 \pm 0.7/48 \pm 0.6$

Table 3.1: Experimental datasets of Figs. 3.19, 3.20 and 3.22. The pulse width for the displayed cases was 2 s except for 1.45 K where it was 1 s (marked * near the symbol) or 0.5 s (marked **). The values shown are in the format X_{high}/X_{low}, the "high" and "low" subscripts correspond to the square-wave modulated heat flux being in the higher or lower state. For counterflow velocity v_{ns}, average across the entire duration of the pulse is shown. For L, L_{high} is the VLD 10 ms before the heat pulse is switched to the lower state and L_{low} corresponds to the overall minimum. Ensemble averaging is used to calculate the L_{high} and L_{low} and the standard deviation of this average is shown as the error. The two lines of VLD correspond to second sound sensors L1 and L2 (see Fig. 2.3).

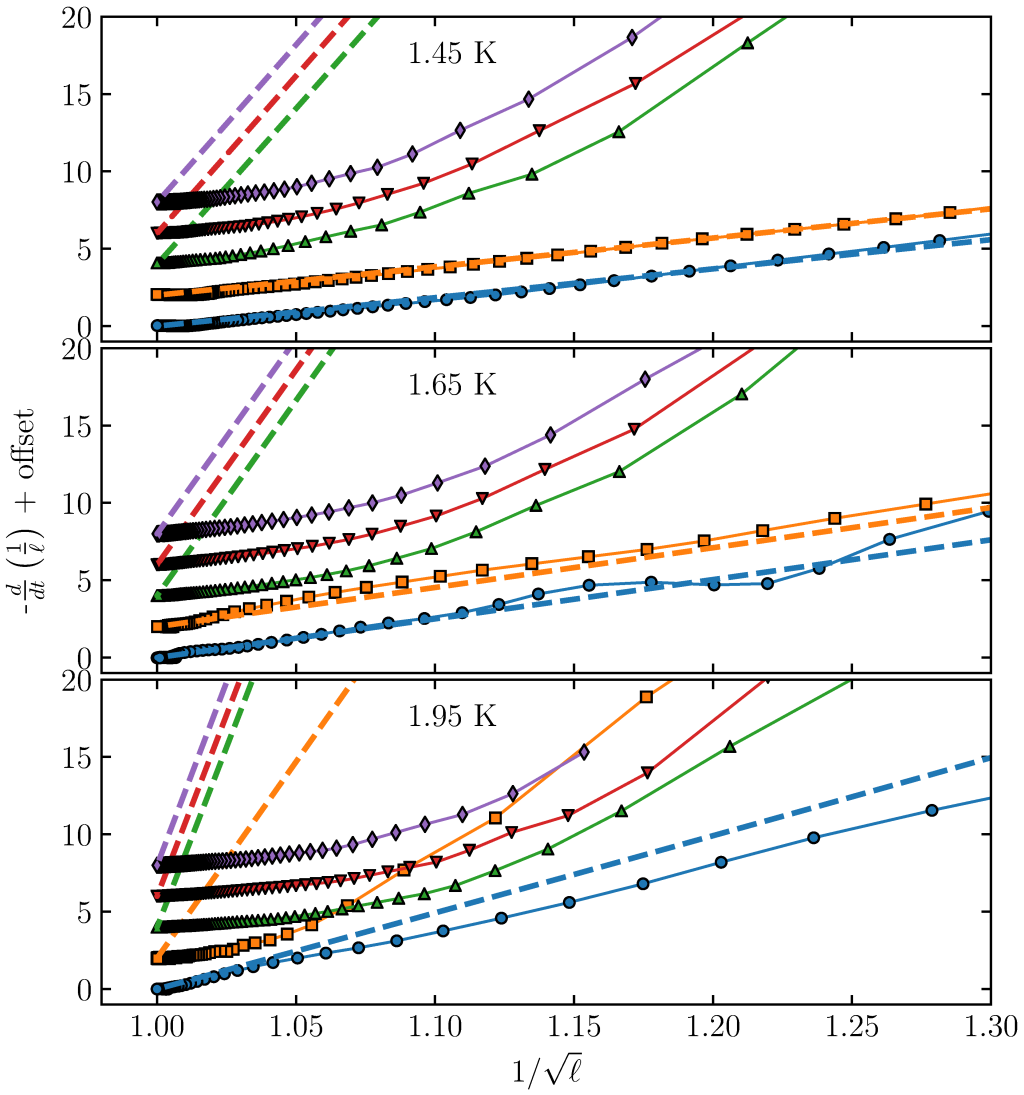

Figure 3.20: Growth part of the phase portrait for different temperatures and counterflow modulations. See also Tab. 3.1 for the details on the data sets.The dashed lines are given by Eq. (3.10) with numerically obtained c_2 in Ref. [35]. It should be emphasised that no fitting was used in this comparison. The low-density curves show almost perfect agreement with numerical simulation even for the cases where one observes a prominent non-monotonicity in the decay.

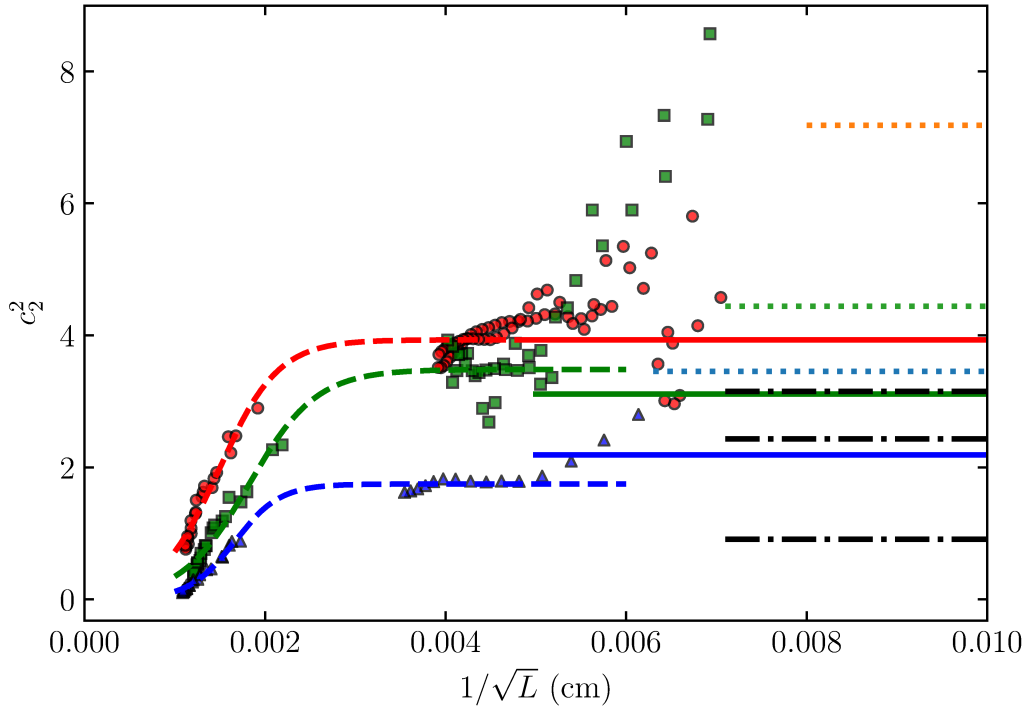

Figure 3.21: The curvature parameter c_2 as a function of (dimensional) inter-vortex distance for three different temperatures: 1.45 K (●), 1.65 K (■), and 1.95 K (▲). The experimental values are compared with several numerical studies: The horizontal full lines show c_2 interpolated for experimental temperatures from values calculated by Schwarz [35] corresponding to 1.45, 1.65 and 1.95 K (top to bottom). The dashed lines are least squares fits to Eq. (3.14). Black dash-dotted lines on the right: numerical simulations of a vortex tangle with uniform normal fluid, synthetic turbulence and frozen Navier-Stokes turbulence in normal fluid, respectively from top to bottom, from Ref. [82]. See text for estimation of c_2 from average curvature. Dotted lines on the right: c_2 from Ref. [81] for 1.3 K, 1.6 K and 1.9 K (top to bottom). Lines from Ref. [82] and Ref. [81] terminate at the minimum inter-vortex distance these simulations achieved (except for the top dashed 1.3 K case, where the inter-vortex spacing was 125 μm).

steady state vortex line density has been observed in the simulations. The data in Ref. [82] are reported in terms of the mean curvature $\bar{S}$, whereas the RMS curvature $\tilde{S}$ is necessary for the estimation of c_2. The RMS curvature is obtained using the estimation of Kondaurova *et al.* [81] $\tilde{S} = \bar{S}\sqrt{3/2}$ which is then used to calculate c_2 from the reported $\bar{S}$ and steady state vortex line density in Ref. [82].

For the ease of handling, the experimental values of the effective c_2 are fit to a simple formula

$$c_2^2(\delta) = C\left[1 + \tanh\left(\frac{\delta - \phi}{\vartheta}\right)\right], \tag{3.14}$$

where C, ϕ and ϑ are adjustable parameters and δ is the inter-vortex spacing. The obtained values for different temperatures are listed in Tab. 3.2.

Even though it is a priori clear that the time dependence of $L(t)$ during the

Temperature	ϕ (cm)	ϑ (cm)	C
1.45 K	1.49 10^{-3}	6.54 10^{-4}	1.85
1.65 K	1.82 10^{-3}	7.46 10^{-4}	1.83
1.95 K	1.66 10^{-3}	5.03 10^{-4}	0.95

Table 3.2: Fit parameters of the c_2 function (3.14) for the three experimental temperatures.

decay cannot be fully accounted for by the dynamical equation of the type (3.10), the use of the effective c_2 from Fig. 3.21 for the decay improves the agreement between the observed experimental behaviour and Eq. (3.10). The experimental decay phase trajectories and the corresponding theoretical curves are shown in Fig. 3.22. For sparse tangles, or for the cases with shallow modulation, the use of L-dependent effective c_2 effects little change, as is to be expected since the growth is also well described by a constant c_2. On the other hand, for dense tangles and large transients, the agreement in the initial decay rate is greatly improved by the use of effective the c_2.

It is tempting to postulate that the effective L-dependent c_2 is the real measure of the RMS curvature of the tangle. However, two difficulties must be noted. First, the derivation of Eq. (1.9) is strictly valid only near the equilibrium [35]. It is questionable whether the transients reported here can be regarded as such.

Second, if one accepts the possibility of a variable c_2, an issue arises connected to the steady state vortex line density. The coefficient γ of Eq. (3.1) determining the steady state L_0 depends on c_2, yet no change in γ is observed with increasing v_{ns} (or L_0) – that is, no obvious deviation from $L \propto v_{\mathrm{ns}}^2$ in Fig. 3.14. However, considering the Schwarz equation (1.9) for L, the steady state VLD scaling coefficient is $\gamma = \bar{I}_l/c_2^2$, where I_l is [35], roughly speaking, the average (over the tangle) value of the binormal $\mathbf{s}' \times \mathbf{s}''$ projected along the counterflow direction , i.e., γ depends also on the distribution of the binormal $\mathbf{s}' \times \mathbf{s}''$. It is clearly a speculation to claim that I_l depends on vortex line density in a similar fashion to c_2 so that γ remains constant, but it is not surprising that I_l ought to be L-dependent if c_2 is.

These two difficulties remain an open question. Regardless, the agreement with numerical simulations suggests that even for fairly dense tangles (i.e., $L_0 = 10^5$ cm^2 – cases where non-monotonicity of the decay is clearly present) the effective c_2 is indeed a measure of RMS tangle curvature and thus the effective c_2 for higher densities ought to be at least related to it. The physical relevancy of the effective c_2 is also strengthened by the significant improvement of the prediction of the initial decay rate for very dense tangles.

3.5 Intermittency enhancement in decaying coflow turbulence[6]

The Kolmogorov theory of homogeneous and isotropic turbulence (K41) assumes that the turbulence is self-similar within the inertial range. Real turbulent flows

[6]The results of this section were submitted to *Physical Review Fluids*, reproduced as Attachment 4 .

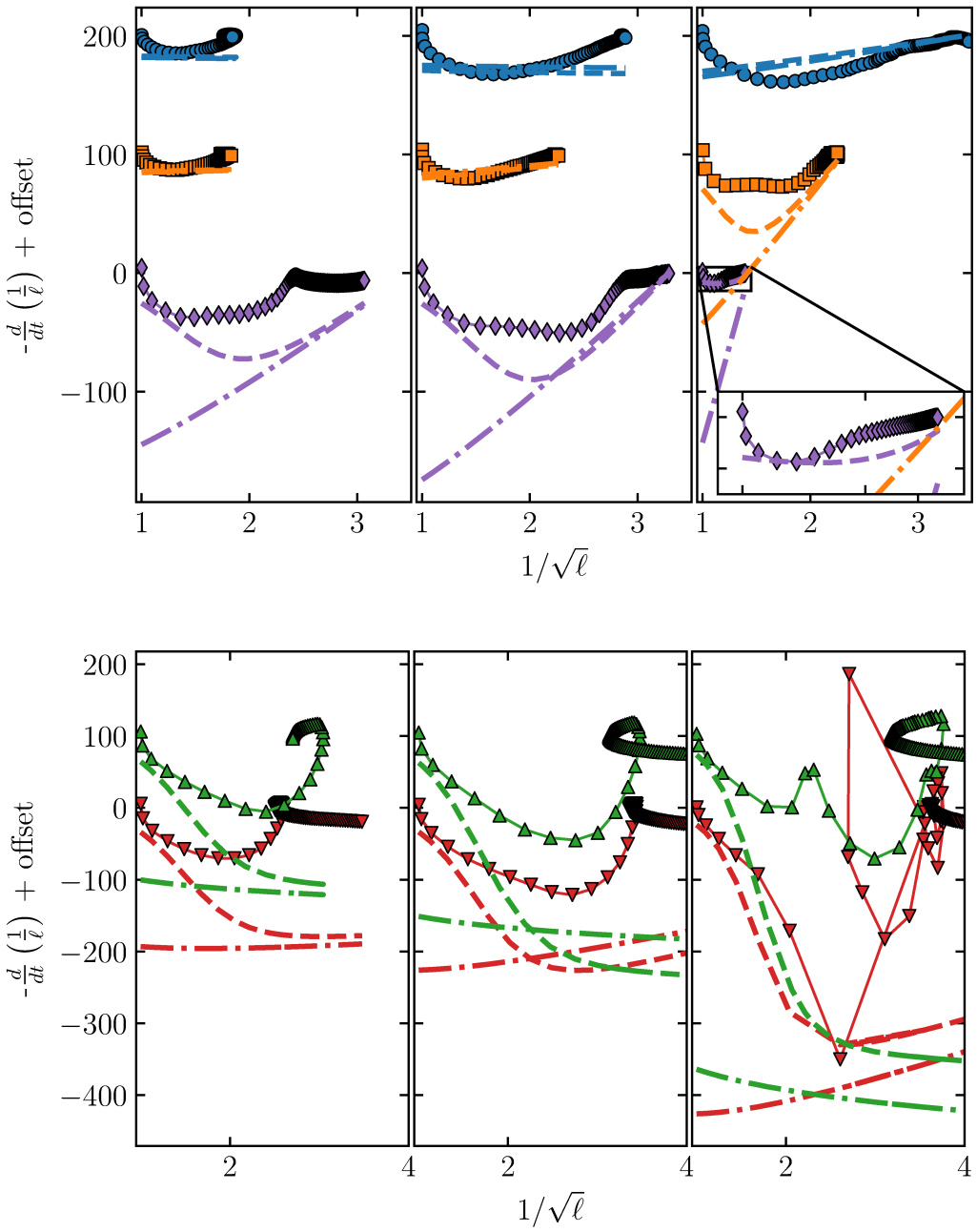

Figure 3.22: Phase portrait of the decaying turbulence. The lines show theoretical predictions using c_2 coefficients either obtained by Schwarz [35] (dash-dotted lines) or obtained from the fit (3.14) of the experimental data (dashed lines). Temperatures are (left to right) 1.45 K, 1.65 K and 1.95 K. The y-axis offset increment is 100 in the units of the axis. List of shown data sets is in Tab. 3.1. (top) Smaller transients for which nominal $L_{\mathrm{high}}/L_{\mathrm{low}} \leq 100$ or $L_{\mathrm{high}} = 10^5$ cm^{-2}. (bottom) Larger transients for which nominal $L_{\mathrm{high}}/L_{\mathrm{low}} \geq 100$ and $L_{\mathrm{high}} = 10^6$ cm^{-2}. For 1.95 K, very early after switching the heat flux, it is very challenging to compensate for the resulting shifts in the second sound resonance, hence the disruptions in the decay curves.

do not fulfil this assumption exactly, a phenomenon termed turbulent intermittency [2]. Physical manifestation of intermittency is typically observed as sudden high-intensity bursts of velocity that occur more commonly than one would expect for self-similar turbulence.

All classical turbulent flows display similar intermittent behaviour [99], thus a natural question arises whether this universality can be extended to the quasi-classical flows of He II. The quasi-classical behaviour of He II (above 1 K) is typically thought to arise from the coupling of the velocity fields through the mutual friction [45]. This coupling, however, cannot be complete and must necessarily break down near the inter-vortex distance ℓ_Q (sometimes called the *quantum length scale* of the flow) due to the quantisation of circulation in the superfluid component [45, 37, 17]. Indeed, it has been observed that even quasi-classical flows of He II display non-classical statistics when probed as sufficiently small lengths scales [18, 100]. Decoupling at larger scales would necessarily lead to additional dissipation by the mutual friction which would break the scale-invariance of the inertial range and thus lead to intermittency.

As the mutual friction is temperature dependent, it is reasonable to expect temperature dependence also in the turbulent statistics. Recent numerical studies [54, 55] suggested that intermittency in coflowing He II is in fact temperature dependent and, additionally, enhanced for certain temperatures. However, experimental studies of intermittency by measurements of pressure fluctuations for a wide range of temperatures [56] found no temperature dependence and intermittency corrections similar to those in classical turbulence.

Reliable determination of intermittency in He II requires generation of homogeneous turbulence and measurement techniques with spatial resolution comparable to ℓ_Q. In the present work, quasi-classical quantum turbulence in the wake of a moving grid was studied using helium excimer tracer line tagging velocimetry technique [21, 22] (see Sec. 2.1.4) and simultaneously with vortex line density measurements using the second sound attenuation.

The experiment was performed with the Tallahassee He_2^* visualisation setup, sketched in Fig. 3.23 and described in detail in Ref. [22]. In the experiment, He_2^* molecules are created along a straight line, initially 100 μm thick and spanning the width of the channel, and then allowed to be advected by the turbulent flow for a brief drift time t_{drift} (typically 10 – 30 ms). From the displacement of the initial to the deformed line, Fig. 3.24, one can calculate the local velocity in the streamwise direction y as a function of the transverse direction x, i.e., $v_y(x)$. The molecules are created by a series of high-intensity femtosecond laser pulses [72] and are visualised using the laser-induced fluorescence using a separate laser sheet at 905 nm wavelength [68].

The photographs of the deformed tracer lines in the wake of the moving grid are obtained as follows (see Fig. 3.25). The grid starts moving at some time $t < 0$ from a position roughly 50 mm below the visualisation region (the end position being about 10 cm above the visualisation region). The origin of time is set to the instant when the grid crosses the position where the tracer line will be inscribed. The inscription of the line is delayed by the decay time t_d of interest. Finally, after a brief drift time t_{drift} a photograph of the deformed line is taken using the laser induced fluorescence. For all experimental configurations (temperature and grid velocity) and decay times, the measurement is repeated multiple times (order

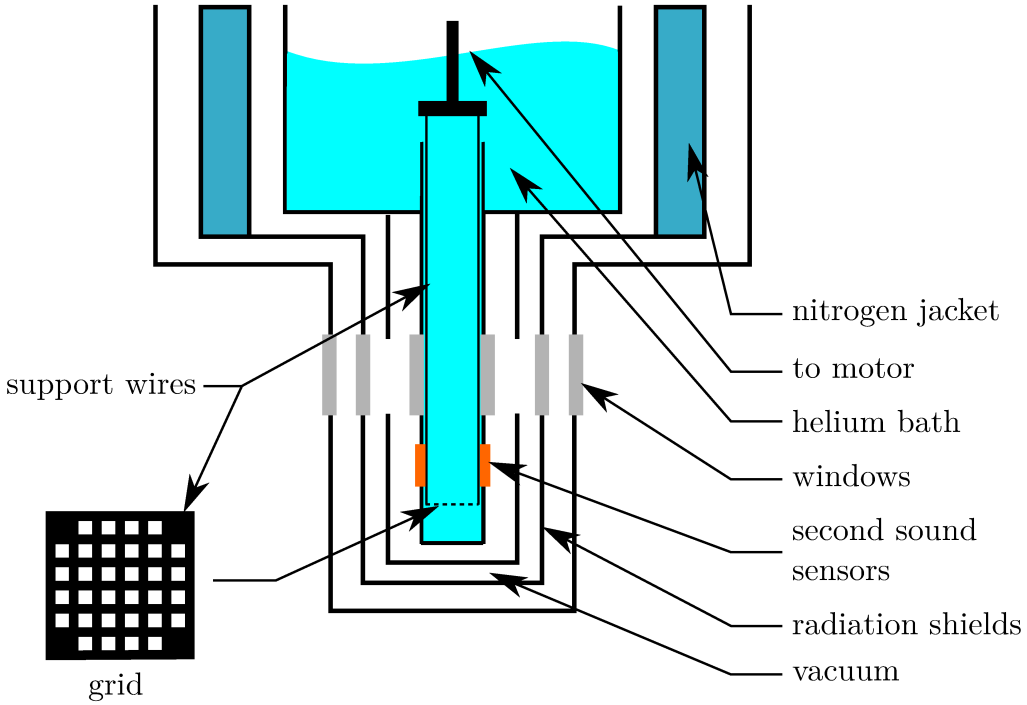

Figure 3.23: A sketch of the experimental apparatus and the towed grid. The grid moves in a roughly 10×10 mm square channel of about 30 cm length and is supported at the four corners where straight rods are soldered. The turbulence was created by pulling the grid through stationary helium in the channel. The grid is constructed from a woven wire of 0.41 mm width and openings of 0.86 mm. The transparency of the grid is 56%.

of 100). For each tracer line photograph the grid is towed anew, with about 30 s wait time between pulls of the grid.

The repeated measurements of the velocity field are used to measure mean velocity profile $\langle v_y(x)\rangle$ and the profile of velocity fluctuations $\sqrt{\langle v_y(x)^2\rangle}$, the results are shown in Fig. 3.26. Note that the profile of the fluctuations shows the standard deviation of the ensemble average, rather than fluctuations in time. For very short decay times the velocity profile is strongly inhomogeneous and consistent with a large eddy spanning the entire width of the channel. This is probably due to the imperfect nature of the used grid (particularly the closed edges) and its support system. However, this large-scale inhomogeneity decays relatively quickly, within about 4 s for the 300 mm/s grid velocity. Note also that the profile of the velocity fluctuations is approximately homogeneous throughout the decay and generally does not display any large-scale structure commensurate with the presumable large vortex.

For better characterisation of the decaying turbulence, vortex line density was measured concurrently using second sound attenuation and compared with the decay of the turbulent kinetic energy, as shown in Fig. 3.27. The turbulent kinetic energy K is estimated as the mean-square of the velocity fluctuations profile shown in Fig. 3.26, with the average taken over the transverse spatial extent of the line. The decay of the 300 mm/s case shows only the late-time

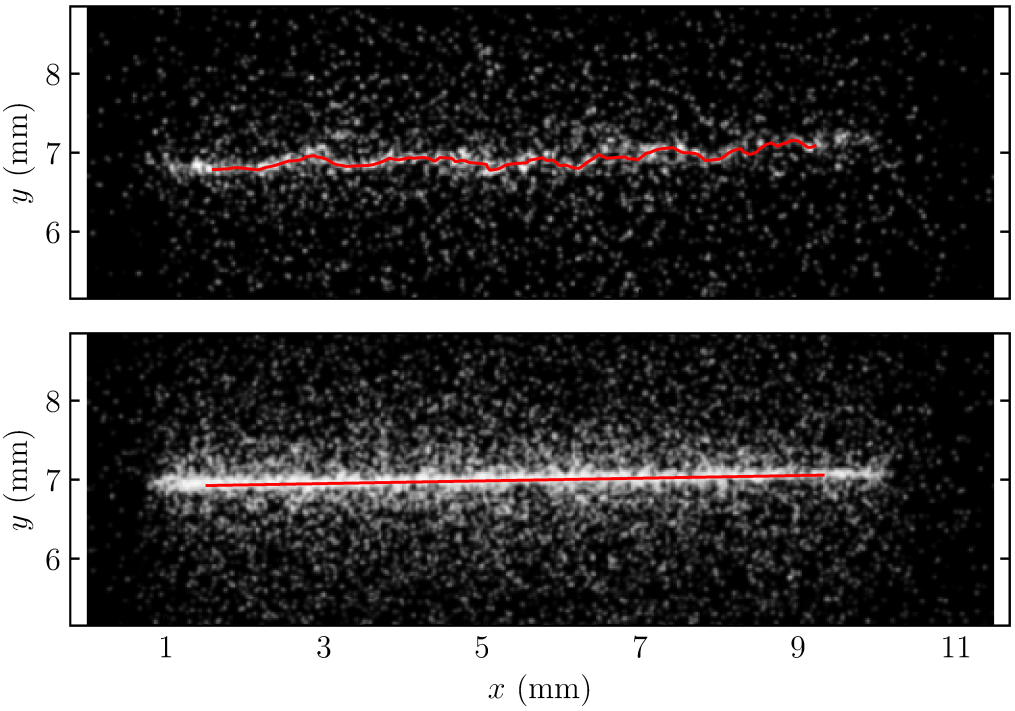

Figure 3.24: Comparison of a reference (bottom) and deformed (top) tracer lines. The relative displacement and the known drift time is used to estimate the local velocity.

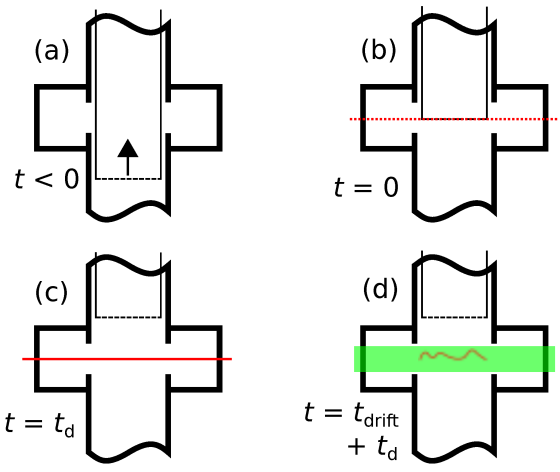

Figure 3.25: The sequence leading to a single photograph of the deformed tracer line: (a) the grid starts moving at some time $t < 0$ from a position below the visualisation region; (b) as the origin of time $t = 0$ the instant when the grid crosses the visualisation region is taken; (c) the tracer line is created with femtosecond pulses after a specified decay time t_d; (d) after a short drift time t_{drift} the position of the line is read using fluorescence induced by a laser sheet.

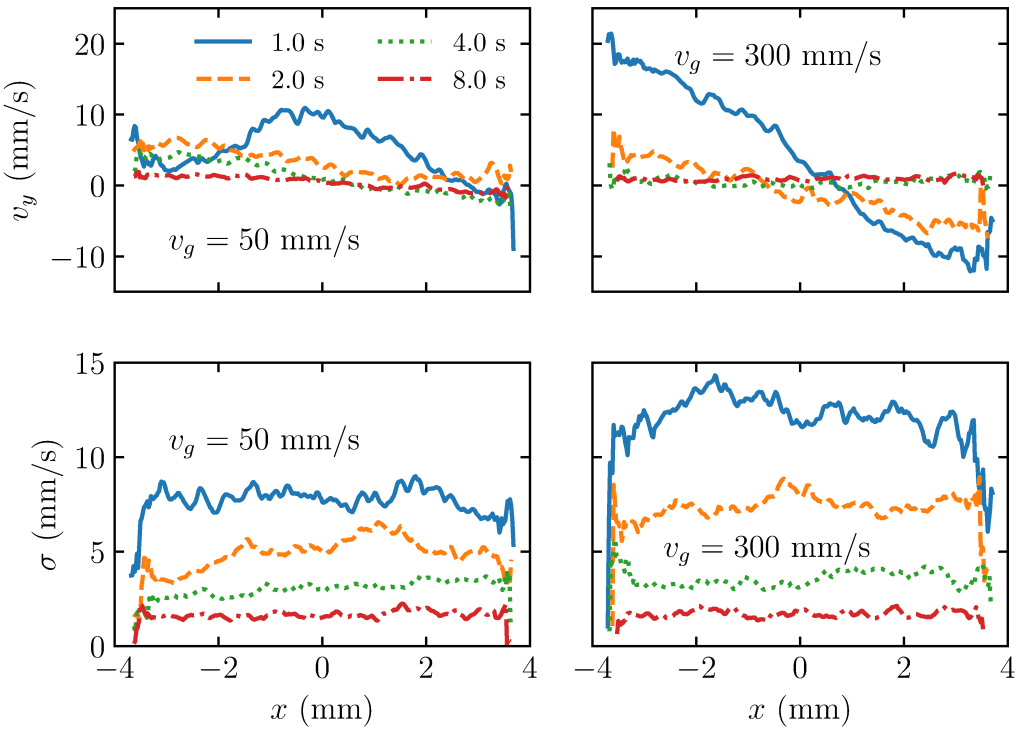

Figure 3.26: The profiles of the normal fluid velocity (top) and turbulent fluctuations (bottom) across the channel for two grid velocities – 50 mm/s (left) and 300 mm/s (right) and several decay times shown in the legend. All data shown were measured at 1.85 K. The strongly inhomogeneous velocity field observed for the very early decays is consistent with a vortex spanning the width of the channel. Note that despite the possible presence of the large vortex, the fluctuations appear homogeneous.

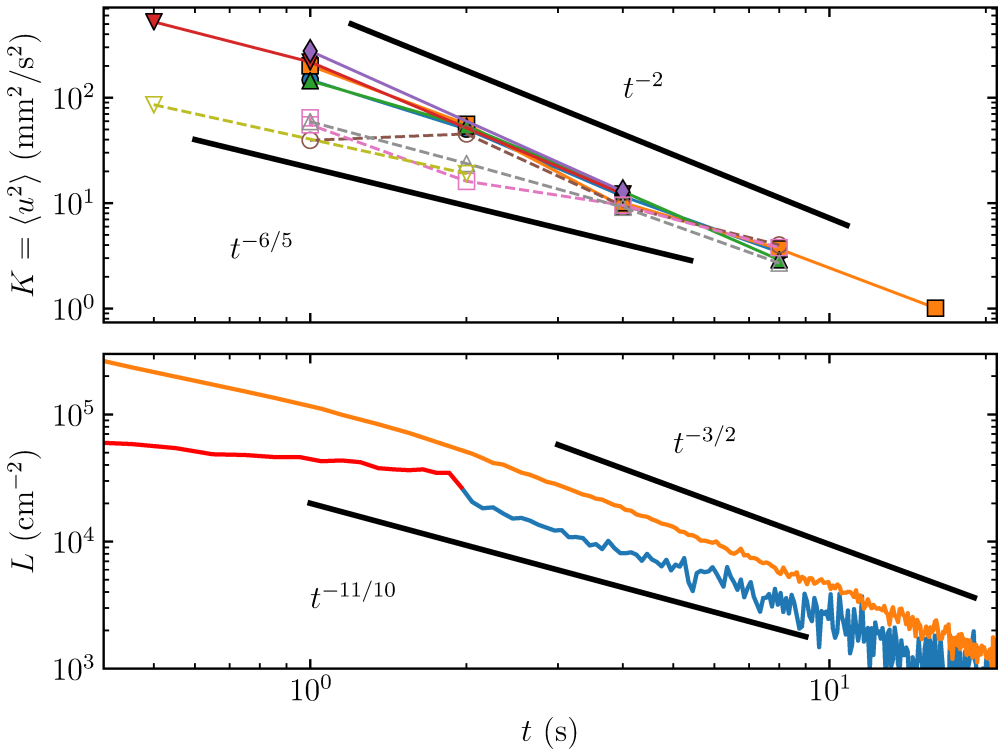

Figure 3.27: Top: Decay of turbulent kinetic energy (mean-square velocity fluctuations). The filled symbols relate to the faster, 300 mm/s, grid velocity and the empty to 50 mm/s. Bottom: Decay of vortex line density measured by second sound attenuation. The higher, orange, line corresponds to 300 mm/s and the lower to 50 mm/s grid velocity. For the slower grid velocity, the time for the grid to come to rest was longer and overlapped with the displayed data. This is indicated by the red part of the curve. Two regimes of decay are clearly seen. For the 300 mm/s case, the decay is in the late state, when the outer scale of turbulence is saturated by the size of the system. For 50 mm/s, the saturation does not occur until approximately 8 s. The indicated power laws are based on a theoretical calculation of Refs. [8, 48].

regime $K \propto t^{-2}$ and $L \propto t^{-3/2}$ where the outer scale of turbulence is saturated by the system size [8, 48]. On the other hand, the slower 50 mm/s case also features the regime when the large scale is apparently still growing [8]. Note that despite the large scale inhomogeneity in the wake of the grid in the initial stages of the decay, both the decay of the turbulent energy and vortex line density exhibit characteristics of quasi-classical homogeneous isotropic turbulence.

The intermittent behaviour of turbulence is studied, in a fashion similar to Ref. [67], using the transverse velocity structure functions $S_n^\perp(r)$ defined for the particular case at hand as

$$S_n^\perp(r) \equiv \langle |\delta_r v_y(x)|^n \rangle \equiv \langle |v_y(x) - v_y(x+r)|^n \rangle_x \tag{3.15}$$

where $\delta_r v_y(x)$ is the transverse velocity increment, $v_y(x)$ is the y-component of the velocity field measured along the tracer line (spanning direction x), r is the separation distance and the average is taken over all admissible positions on the line and the entire ensemble. The Kolmogorov-Obhukov theory of classical turbulence

(K41) predicts that for (non-intermittent) homogeneous isotropic turbulence [2]

$$S_n^{\perp}(r) \propto r^{\zeta_n^{\perp}}, \text{where } \zeta_n^{\perp} = n/3. \tag{3.16}$$

Given that the theory of quasi-classical decay of Ref. [8, 48] assumed classical scaling of turbulent energy spectra one would expect classical K41-like scaling of normal fluid (transverse) velocity structure functions for the entire duration of the decay, in particular [2] $S_2^{\perp} \propto r^{2/3}$. This is, however, not the case as seen in Fig. 3.28. Initially, the scaling is compatible with, if somewhat higher than, the K41 scaling, however, beyond approximately the 4 s mark the scaling exponents become notably smaller than 2/3. The increased exponents in the initial stage are likely due to strong inhomogeneity in the wake closely behind the grid (i.e., the flow through individual grid openings [44, 101]). In the late decay, the turbulence is likely no longer fully developed and might be affected by the counterflow caused by a weak radiative heating through the optical windows.

Often quoted as the only exact result in the study of turbulence is the Kolmogov 4/5 law which states that in homogeneous isotropic turbulence the *longitudinal* third order velocity structure function is given by

$$S_3^{\parallel}(r) = -\frac{4}{5}\varepsilon r, \tag{3.17}$$

where ε is the energy dissipation rate [2]. Longitudinal structure functions are not accessible in the present experiment, however, for homogeneous and isotropic turbulence the scaling ought to be identical for both the longitudinal and the transverse cases [67]. The third order structure function at 4 s decay time for 300 mm/s grid velocity case and various temperatures is shown in Fig. 3.29. Especially for the high temperatures the linear scaling is apparent.

The classical scaling in the full range of the decay can be recovered using the so-called extended self-similarity hypothesis (ESS) [102]. The scaling of the structure functions is not determined directly from their dependence on the separation distance r but rather by plotting structure functions of different orders against each other. The third order structure function S_3 is used as the reference. Plots of S_2 vs. S_3 and the corresponding scaling exponents are shown in Fig. 3.30. Both the 50 mm/s and 300 mm/s cases maintain classical scaling $\zeta_2 = 2/3$. See also Fig. 3.31 for the ESS plot of higher-order structure functions.

Note that around the 4 s decay time the large inhomogeneity decays (Fig. 3.26) and the scaling of $S_2^{\perp}(r)$ exhibits classical scaling even without the use of extended self-similarity hypothesis. For these reasons the 4 s decay time is studied more closely in the rest of the section.

The deviation of scaling exponents $\zeta_n^{\perp}$, obtained from ESS plots as in Fig. 3.31, from their classical values $n/3$ is shown in Fig. 3.32 for the case of 4 s decay time and 300 mm/s grid velocity. The temperature dependence is evident. Additionally, the strongest deviation is observed in the vicinity of 1.85 K, in agreement with numerical predictions of Biferale *et al.* [55]. It should be noted that while the result is robust for $t_d = 4$ s, the situation is less clear for the short decay times and the slower grid velocity (see Sec. 3.5.1 for a discussion of uncertainties).

This result may appear contradictory to recent experiments of Rusaouen *et al.* [56], who observed no appreciable temperature dependence of intermittency corrections. There, the authors calculated the structure functions of the velocity

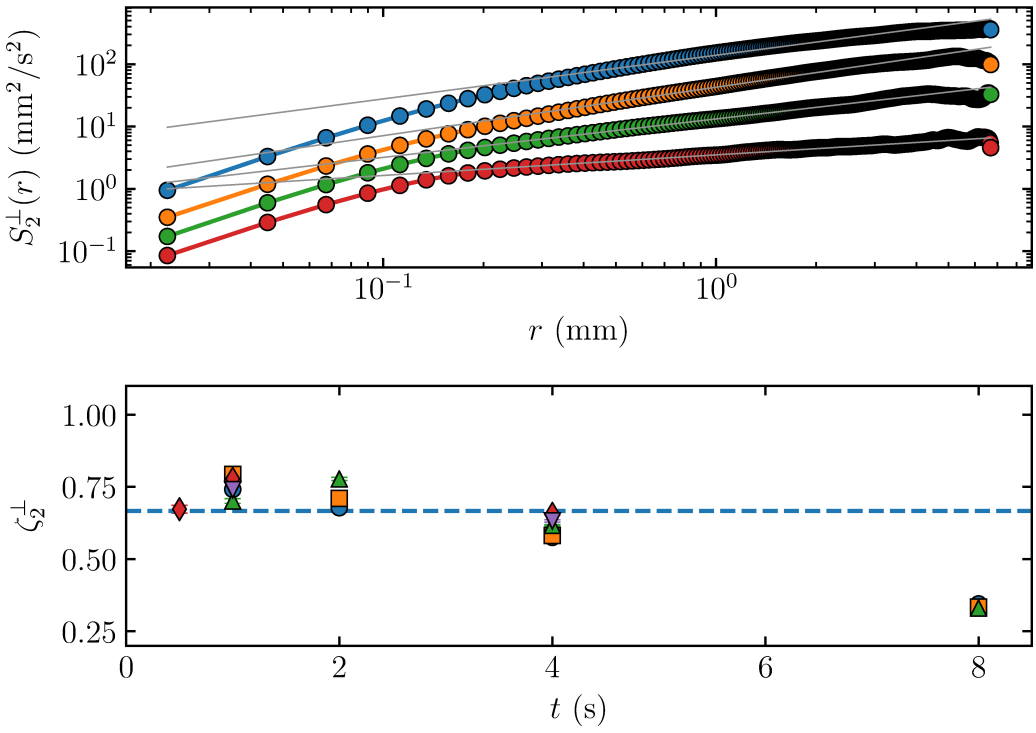

Figure 3.28: Second-order transverse velocity structure functions $S_2^\perp(r)$ (top) and the time evolution of their scaling exponents $\zeta_2^\perp$ (bottom) determined through a direct fit to $S_2^\perp(r)$. The structure functions shown were measured at 1.85 K, 300 mm/s grid towing velocity and decay times of 1, 2, 4 and 8 s (curves top to bottom). The scaling exponents are shown for the available temperatures: 1.45 K (●), 1.65 K (■), 1.85 K (▲), 2.0 K (◆), 2.15 K (▼). The dashed horizontal line shows the K41 scaling $\zeta_2^\perp = 2/3$.

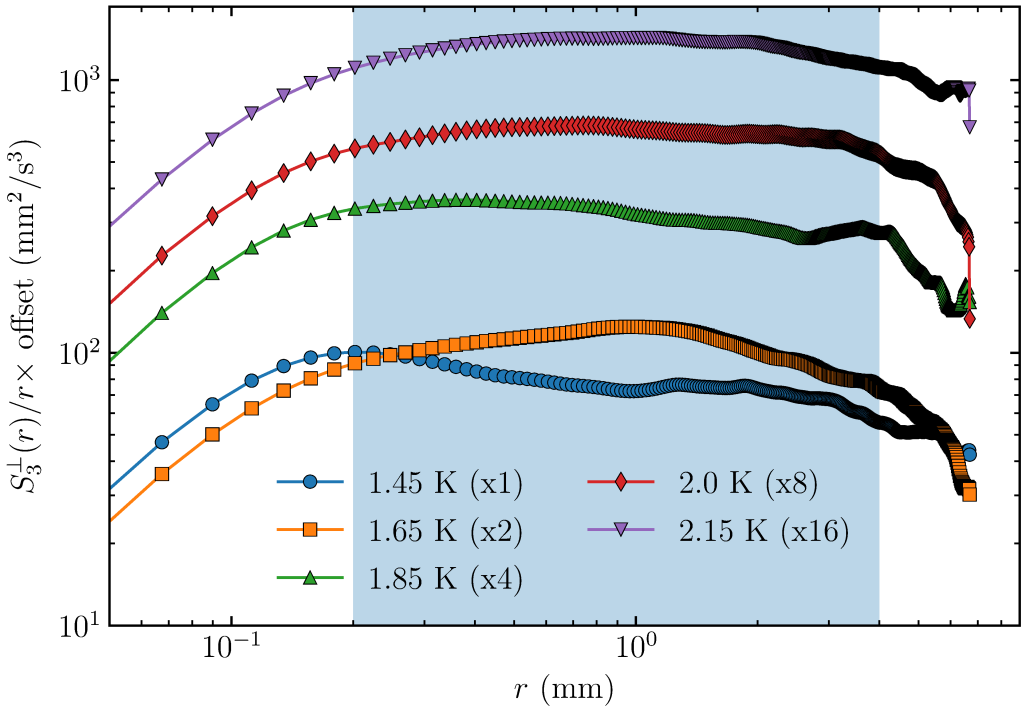

Figure 3.29: The third order transverse structure function $S_3^{\perp}(r)$ compensated by the expected linear scaling. The curves corresponding to different temperatures are offset for clarity (see the figure legend). The linear scaling is clearly evident, especially for the higher temperatures, in agreement with the Kolmogorov 4/5 law. The extent of the linear scaling, as highlighted, is taken as the approximate extent of the inertial range.

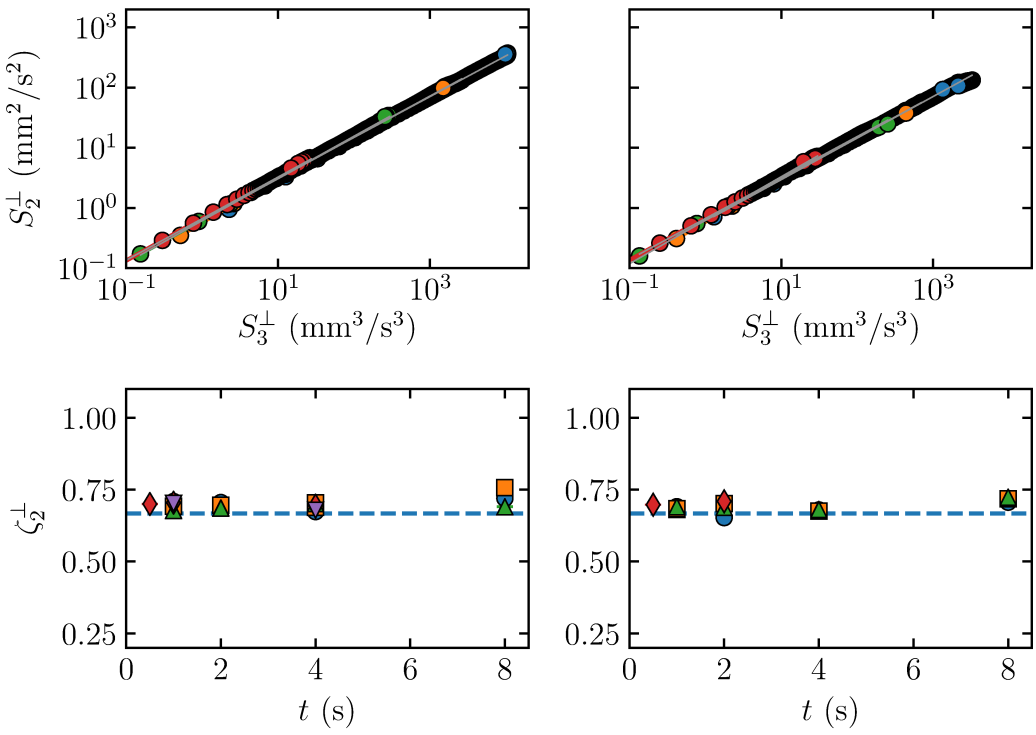

Figure 3.30: The extended self similarity plots of the second order structure function – $S_2^\perp(S_3^\perp)$ (top) and the corresponding scaling exponents (bottom). The grid velocities are either 300 mm/s (left) or 50 mm/s (right). The structure functions are shown for the temperature 1.85 K and decay times 1, 2, 4 and 8 s. The scaling exponents are shown for the available temperatures: 1.45 K (●), 1.65 K (■), 1.85 K (▲), 2.0 K (◆), 2.15 K (▼). The dashed horizontal lines show the K41 scaling $\zeta_2^\perp = 2/3$.

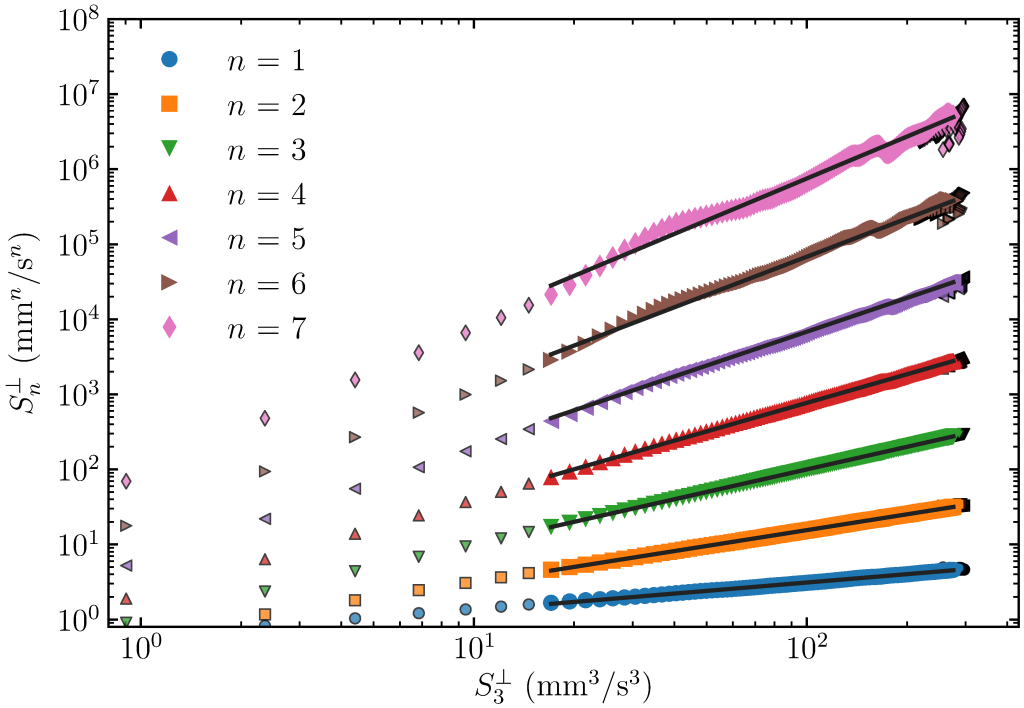

Figure 3.31: The extended self similarity plots of $S_n^\perp$ for $n = 1 - 7$. The highlighted data points fall within the region highlighted in Fig. 3.29, i.e., the presumed inertial range. The black lines represent fits to the expected power law scaling. The particular cases shown are for 1.85 K, 300 mm/s grid velocity and 4 s decay time.

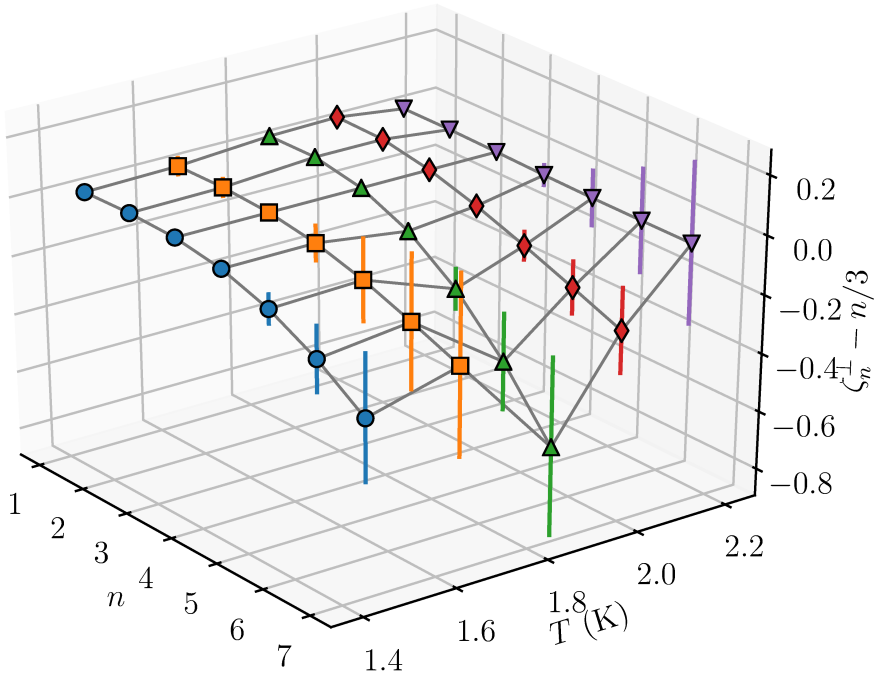

Figure 3.32: Deviation of the scaling exponents from the K41 theory $\zeta_n = n/3$ for several experimental temperatures. The strongest deviation clearly occurrs in the vicinity of 1.85 K, in accordance to the numerical expectations [54, 55]. The data shown is for 300 mm/s grid velocity and 4 s decay time. The corresponding temperatures of the datasets are ● – 1.45 K, ■ – 1.65 K, ▲ – 1.85 K, ◆ – 2.00 K, ▼ – 2.15 K

fluctuations from measurements of fluctuating pressure in the wake of a flat disc. There are at least two possible reasons for this difference. First, Biferale *et al.* [55] identify a "flip-flop" scenario – a random two-way energy transfer between the two fluid components mediated by the mutual friction – as the mechanism responsible for the temperature dependence and enhancement of intermittency in quantum turbulence. It is not clear how pressure fluctuations, which are related to both fluid components, respond to this inter-component energy transfer.

Second, the size of the cantilever used to probe the pressure in the Grenoble experiment [56] is typically larger than the inter-vortex distance. The smallest accessible length scale in the present experiment is limited by the width of the tracer line – roughly 100 μm, which is comparable to the quantum length scale $\ell_Q \simeq L^{-1/2}$ at 4 s during the decay and increases further as the decay progresses (Fig. 3.27), thus the tracer line tracking is sensitive at the inter-vortex scales.

The inter-vortex distance in the experiments of Rusaouen *et al.* [56] can be estimated following Babuin *et al.* [9]. Taking the outer scale of turbulence in the Grenoble experiment to be the channel size $\simeq 5$ cm, effective kinematic viscosity $\nu_{\text{eff}} \simeq 0.1\kappa$, the κ-based large scale Reynolds number at 1.85 K is roughly 6×10^4. This corresponds to $\ell_{\text{Q}} \approx 7\mu$m. The sensing area of the cantilever probe is 32×375 μm, which translates to more than 100 vortex lines, even if the likely increase of L in the vicinity of any obstacles [87, 32] is neglected. Thus it is to be expected that the experiment of Rusaouen *et al.* [56] measures the same intermittency corrections as in classical turbulence.

3.5.1 Estimation of the errors

In order to determine the robustness of the obtained intermittency corrections the uncertainties of the structure functions and the scaling exponents must be estimated. Transverse velocity structure functions $S_n^\perp$ are defined through the probability density functions (PDF) of the transverse velocity increments

$$S_n^\perp(r) = \langle|\delta v(r)|^n\rangle \tag{3.18}$$
$$= \int_{-\infty}^{\infty} \mathrm{d}\,x|x|^n\,\mathrm{PDF}_r(x), \tag{3.19}$$

where PDF_r is the probability distribution function of the transverse velocity increment $\delta v(r) = v_y(x+r) - v_y(x)$ for a given separation r. Structure functions of relatively high order n are required to estimate the intermittent properties of turbulence. High order structure functions are sensitive to rare events – events of low probability which would contribute to the "tails" of the statistical distribution. In samples of limited size, these tails could be under-resolved, what could lead to an erroneous estimation of the structure functions. A simple strategy to estimate the errors due to lack of statistics is adopted: an estimate of the PDF is calculated from the measured data, which is then extended beyond the range of experimental data using a fit to a particular choice of a heavy-tailed statistical distribution. The difference between the value obtained through Eq. (3.19) using either a non-extrapolated or extrapolated PDF is then used as the estimate of the error caused by under-resolved tails of the statistical distribution.

The estimate of the PDF is calculated from the measured velocity increments

using kernel density estimation (KDE) as

$$\mathrm{PDF}_r^{\mathrm{KDE}}(x) = \frac{1}{N}\sum_{i=1}^{N}\frac{1}{\sqrt{2\pi b}}e^{-(x-\delta v(r)_i)^2/2b^2}, \tag{3.20}$$

where the sum runs through all N measured samples of $\delta v(r)_i$ at a given separation r. The result, for a particular case, is shown in Fig. 3.33. The number of samples for the 4 s decay data sets is shown in Fig. 3.34.

To estimate the error in calculating a given moment, the PDF estimate is extrapolated either by natural extension of the KDE (3.20) outside the range of the data set or by using fits to either the normal (Gaussian) distribution,

$$\mathrm{PDF}_r^{\mathrm{N}}(v) = \frac{1}{\sqrt{2\pi s^2}}\exp\left(-\frac{v^2}{2s^2}\right), \tag{3.21}$$

or a particular case of heavy-tailed distribution

$$\mathrm{PDF}_r^{\mathrm{HT}}(v) = \frac{\exp(s^2/2)}{4m}\left[1-\mathrm{ERF}\left(\frac{\log\left(\frac{|v|}{m}\right)+s^2}{\sqrt{2}s}\right)\right], \tag{3.22}$$

where s and m are adjustable parameters. This form of the PDF was found to describe Lagrangian accelerations [103] but in this case it is used simply for reasons of convenience (Eulerian transverse velocity increments are measured), as it allows for smooth varying of the weight of the tails. Note that using a distribution with power-law tails would be inconsistent as such distribution would render moment of sufficiently high order infinite. Using the two fits and the KDE a new PDF is constructed with the shape of an envelope (point-wise maximum) of the three estimates. Point-wise maximum breaks the normalisation of the probability density function which needs to be re-normalised to integral of unity. This effectively decreases the probability in the central peak and moves it towards the tails. An illustration of this procedure is in Fig. 3.35 for calculating the 6th order moment of a distribution.

The error of the moment is estimated as the absolute value of the difference between the moment calculated using natural extension of the KDE (3.20) and the re-normalised PDF. Graphically, this is given approximately by the area under the tails of the re-normalised PDF outside the range of the data set, shown by the shaded area in Fig. 3.35. For calculation of the value of the structure function $\mathrm{PDF}^{\mathrm{KDE}}$ is used. This estimate has a very sharp cutoff (faster than the fit of the normal distribution) outside the range of the experimental data set (essentially equivalent to extending a histogram with zeros) so that the value is not affected by a particular choice of the extrapolation. The result is shown in Fig. 3.36. The errors of the structure functions render flatness (ratio $S_4^\perp/(S_2^\perp)^2$) unusable for quantitative analysis of intermittency. The structure functions are also calculated directly from the ensemble average (3.18). The intermittency corrections resulting from both procedures are shown in Fig. 3.37, where they are compared with the classical theory of intermittency of She and Leveque [99], which shows that the intermittency in quantum turbulence is indeed enhanced at 1.85 K.

Due to a degree of arbitrariness in the choice of the heavy-tailed distribution, the definition of the renormalized PDF and the definition of the error itself, the

errors are also calculated using a bootstrapping scheme [104]. The set of all N measured samples entering the calculation of $S_n^\perp$ in Eq. (3.18) is sampled at random (with possible repetitions and omissions) to form $B = 5000$ new synthetic sets of length N. The standard deviation of the moment (3.18) for these new B data sets is used as the error. The resulting error bars were significantly smaller than those calculated using the renormalized PDF and the results were consistent with the straightforward calculation by directly averaging the sample and are thus not shown here.

Additionally, a similar bootstrapping scheme was also used to estimate the error of the scaling exponent itself. Using structure functions calculated via the direct ensemble averaging (3.18), the power law fit was performed only in a randomly chosen sub-interval of the range indicated in Figs. 3.29 and 3.31. Repeating this fit for $B = 5000$ randomly chosen intervals yields a distribution of the scaling exponents, the mean and standard deviation of which are taken as the estimate of the scaling exponent and its error. The results are shown in the inset of Fig. 3.37.

One might justifiably become alarmed by the correlation between the number of samples in Fig. 3.34 and the deviation from K41 scaling in Fig. 3.37. This, however, appears to be a coincidence. The correlation is not present for other data sets and artificially restricting the data sets at 4 s to random choice (with replacement) of 10000, 5000 or 2000 samples does not have a strong effect on the observed scaling exponents (although the quality of the structure functions does decrease, as is to be expected). In particular, the minimum near 1.85 K persists unaffected.

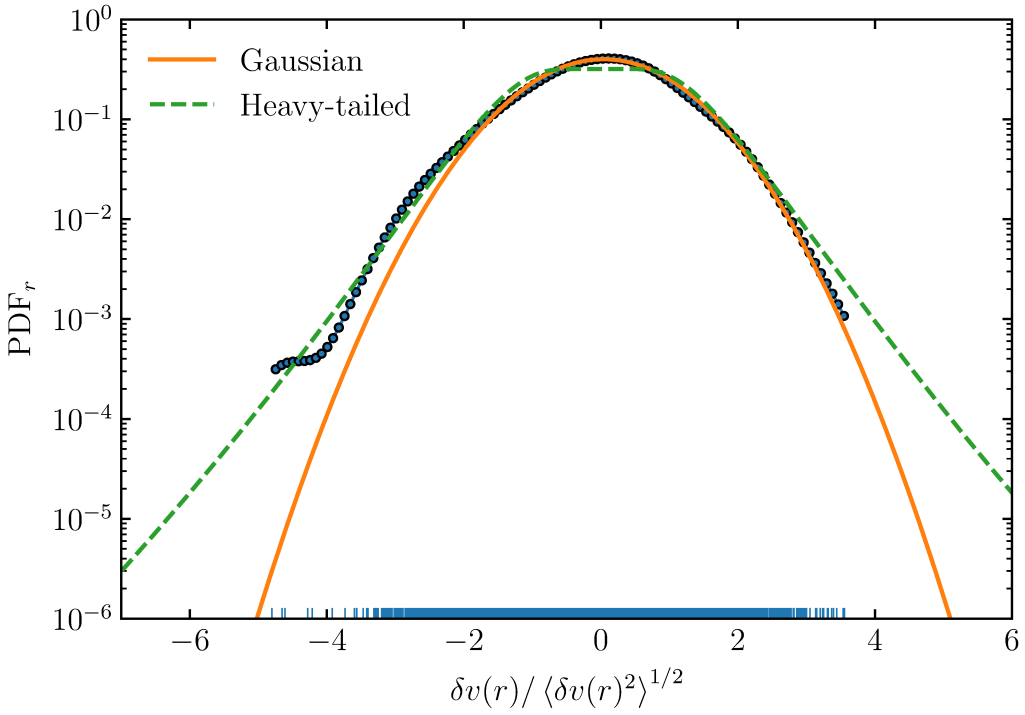

Figure 3.33: Probability density function of the transverse velocity increments at 1.45 K, 300 mm/s grid velocity and separation $r = 2$ mm. The lines are fits to a Gaussian distribution (3.21) and a particular choice of a heavy-tailed distribution (3.22). The rug plot shows the actual data set.

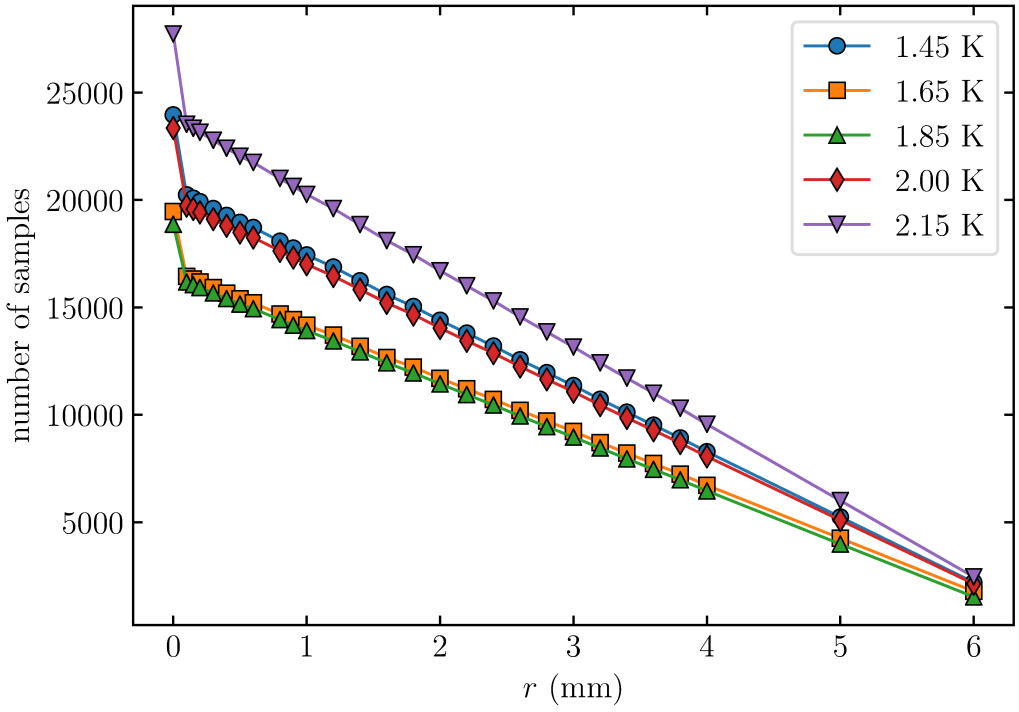

Figure 3.34: The number of samples of the transverse velocity increment for 4 s decay time and 300 mm/s grid velocity data sets at different temperatures and separations. The $r = 0$ points correspond to the number of velocity samples.

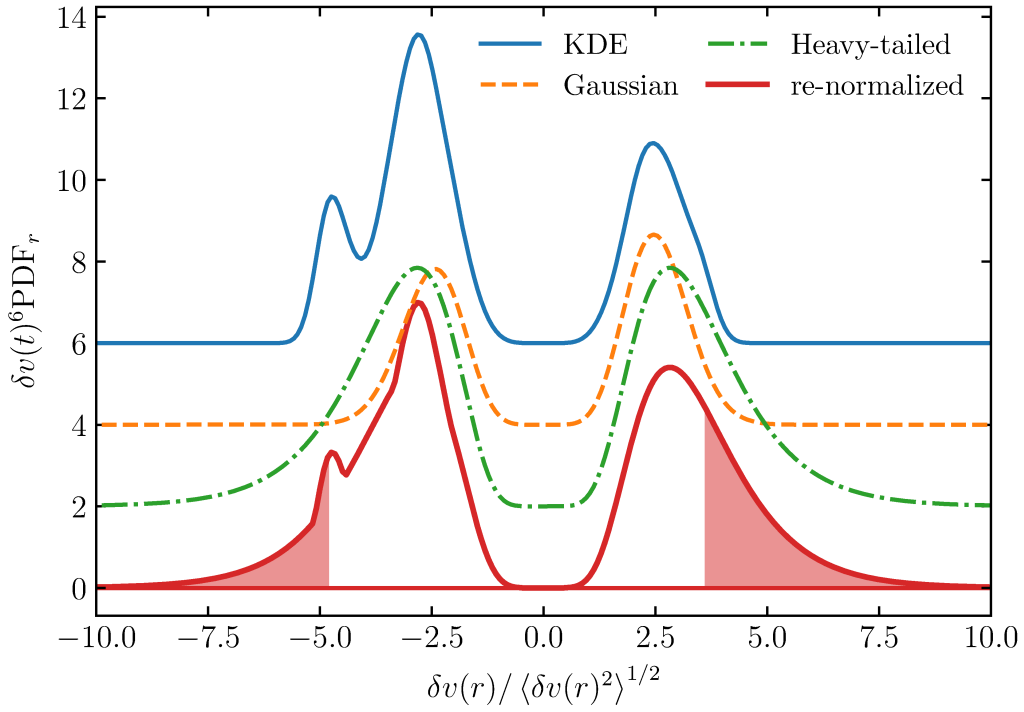

Figure 3.35: Calculation of the sixth moment of the velocity increment distribution. The curves are offset along the y-axis for clarity with an increment of 2 in the units of the axis. The data set is the same as in Fig. 3.33.

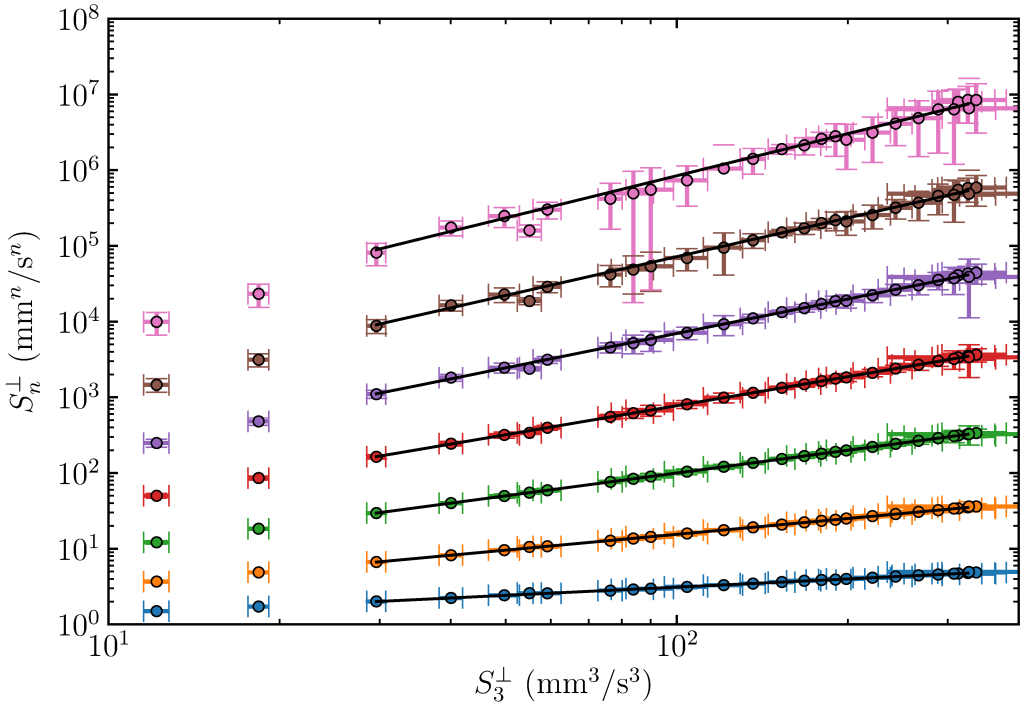

Figure 3.36: Structure functions $S_n^\perp$ for $n = 1$– 7 (bottom to top) and their estimated errors due to insufficient statistics. The curves are equivalent (same data set) to Fig. 3.31.

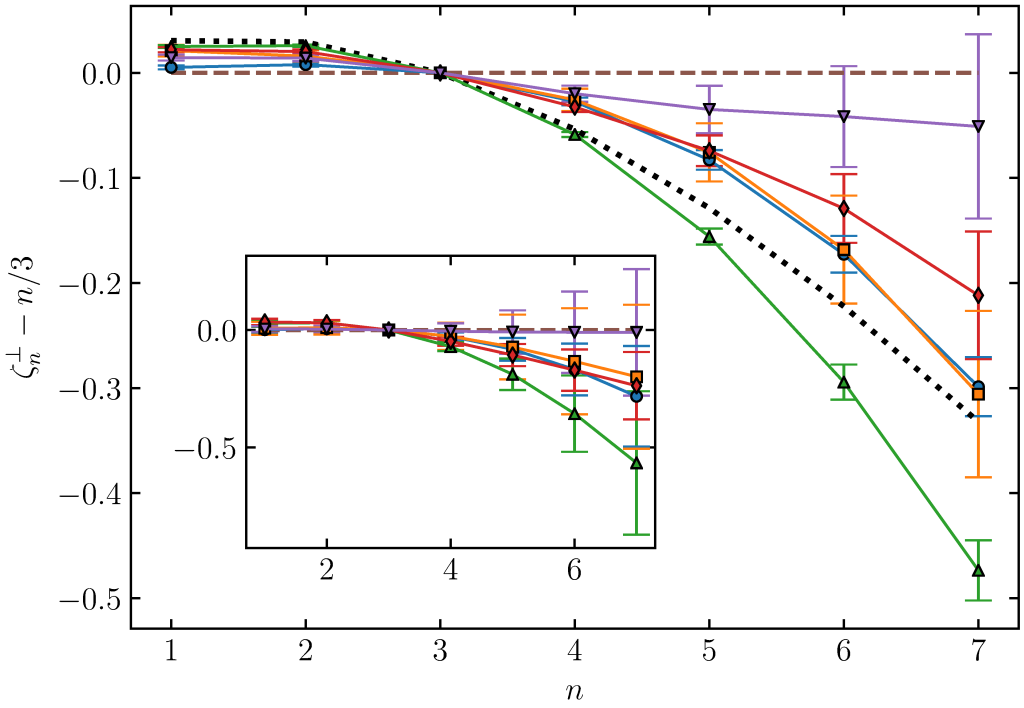

Figure 3.37: Structure function scaling exponents calculated from PDF-derived structure functions. The error bars are the standard errors of a total least squares linear regression (also known as orthogonal distance regression). The inset shows scaling exponents of structure functions calculated using Eq.3.18, the error bars in the inset were calculated using a bootstrapping scheme (see text). All data are for 4 s decay time and 300 mm/s grid velocity. The temperatures are ● – 1.45 K, ■ – 1.65 K, ▲ – 1.85 K, ◆ – 2.00 K, ▼ – 2.15 K. The black dotted line shows the theoretical prediction of She and Leveque for classical intermittency [99].

4. Numerical simulations

4.1 Introduction

This chapter presents the results obtained with the numerical simulations. Two main topics are explored. First, the behaviour of inertial particles in thermal counterflow, primarily their interaction with the vortex tangle, is presented in Sec. 4.2. This study was motivated primarily by the advent of visualisation experiments using frozen hydrogen or deuterium particles [105]. Second, in Sec. 4.3, a counterflow resulting from a point heat source is studied. This very simple geometry, while lacking motivation in currently available experimental data, features an interesting property in that it lacks a preferred direction which, in standard channel-bounded counterflow, causes slight anisotropy of the tangle.

The numerical software used for the work presented in this chapter was based on the *qvort* code of A. Baggaley and others [106] for the results in Sec. 4.2 or written completely by the author of the thesis for the results in Sec. 4.3.

4.2 Interaction of the solid particles and the vortex tangle in thermal counterflow[1]

The most widespread method of visualising the flow of He II is by the use of small solid particles of frozen gas, typically hydrogen or deuterium [105]. The particles are illuminated, usually by a thin sheet of laser light, and their motion is captured by a camera. An important subclass of visualisation studies is formed by the particle tracking velocimetry (PTV), where the paths of individual particles are followed in a Lagrangian sense [18].

When a particle is inserted into He II it is subject to forces due to both normal and superfluid components. Both components exert inertial forces (i.e., pressure) and, in addition, the particle also experiences viscous drag due to the normal component. A simplified equation of motion for a free spherical particle moving in He II is [108]

$$\frac{\mathrm{d}\,\mathbf{v}_p}{\mathrm{d}\,t} = \frac{\rho_s}{\rho}\frac{\mathrm{D}\,\mathbf{v}_s}{\mathrm{D}\,t} + \frac{\rho_s}{\rho}\frac{\mathrm{D}\,\mathbf{v}_n}{\mathrm{D}\,t} - \frac{\mathbf{v}_p - \mathbf{v}_n}{\tau}, \tag{4.1}$$

where τ is the viscous relaxation time due to the Stokes drag, $\tau = 2a^2\rho/9\mu_n$ with a being the particle radius, μ_n standing for the dynamic viscosity of the normal component and the particles are assumed to be neutrally buoyant, i.e., their density is the same as the total density of He II, ρ. The material derivative is defined as

$$\frac{\mathrm{D}\,\mathbf{v}}{\mathrm{D}\,t} = \frac{\partial \mathbf{v}}{\partial t} + (\mathbf{v}\cdot\nabla)\,\mathbf{v}. \tag{4.2}$$

The normal fluid flow is assumed to be steady and uniform in the present simulation, therefore $\mathrm{D}\,\mathbf{v}_n/\,\mathrm{D}\,t = 0$. The time and space derivatives of the superfluid velocity field are calculated using exact expressions obtained by differentiating Eq. (2.7).

[1] The results of this section were published in Ref. [107], reproduced as Attachment 5.

The equation of motion (4.1) is, of course, simplified. A particle is assumed to be infinitesimally small and spherical, thus neglecting any modification of the flow fields in its vicinity, including its wake. For the interaction with quantized vortices this becomes an issue only very close to the vortex. For a real solid particle the quantized vortex would bend toward the particle [109], an effect which is neglected in the present approximation.

The velocity field around a quantized vortex induces a pressure field which pushes solid particles toward the core of the vortex. When a particle approaches the vortex sufficiently closely (within some *trapping distance*), it may become trapped. A trapped particle experiences additional forces due to the presence of the vortex: (i) tension of the vortex (i.e., the energy of a vortex per unit length) since the vortex is no longer required to be smooth at the point of trapping; (ii) Magnus force due to circulation around the particle; (iii) mutual friction. Including these three additional forces to the equation of motion of the particle one obtains

$$\begin{aligned}\frac{\mathrm{d}\,\mathbf{v}_p}{\mathrm{d}\,t} = \frac{\mathbf{v}_n - \mathbf{v}_p}{\tau} + \frac{\rho_s}{\rho}\frac{\mathrm{D}\,\mathbf{v}_s'}{\mathrm{D}\,t} + \Big\{ T_0(\mathbf{s}_+' - \mathbf{s}_-') + \rho_s\kappa\mathbf{s}' \times (\mathbf{v}_p - \mathbf{v}_s) \\ + \Big(\gamma_0\mathbf{s}' \times [\mathbf{s}' \times (\mathbf{v}_p - \mathbf{v}_n)] + \gamma_0'\mathbf{s}' \times (\mathbf{v}_p - \mathbf{v}_n)\Big)\Delta\xi \Big\}\frac{1}{M_{\mathrm{eff}}},\end{aligned} \tag{4.3}$$

where $M_{\mathrm{eff}} = 3/2\rho V_p$ is the effective mass of the particle (V_p being its volume), T_0 is the vortex tension – the energy of vortex per unit length, $s_\pm'$ are left and right tangents of the vortex line (which is allowed to be non-smooth) and γ_0, γ_0' are the mutual friction coefficients. The vortex tension is defined as

$$T_0 = \frac{\rho_s\kappa^2}{4\pi}\log\left(\frac{2\sqrt{\ell_+\ell_-}}{\sqrt{e}\xi_0}\right), \tag{4.4}$$

with l_+, l_- the distances to neighbouring discretisation points and $\xi_0 \approx 1$ Å the vortex core parameter. The mutual friction constants γ and γ_0 are related to the more commonly used α and α' through [23]

$$\gamma_0 = \frac{\rho_s\kappa\alpha}{z^2 + \alpha^2}, \tag{4.5}$$

$$\gamma_0' = \rho_s\kappa\frac{\alpha^2 - \alpha' z}{z^2 + \alpha^2}, \tag{4.6}$$

with $z = 1 - \alpha'$.

From the point of view of the implementation, when a particle approaches a vortex discretisation point sufficiently closely, the particle becomes labelled as trapped and is placed on the vortex discretisation point. If the particle is assumed to be inertial, Eq. (4.3) is used for the motion of the particular discretisation node instead of Eq. (2.10) (i.e., the vortex is locally deformed due to the presence of the particle). If the particle is assumed to be an ideal tracer, trapped particle follows the motion of the trapping vortex without disturbing it in any way.

A trapped particle can become free through processes sketched in Fig. 4.1. Both processes involve a self-reconnection of the vortex with the trapped particle. Either a small loop is emitted which is annihilated on the particle or the reconnection happens on a sharp cusp near the particle[2].

[2]Even though these two processes are qualitatively somewhat different, they are both handled by the same reconnection and small-loop-annihilation algorithm.

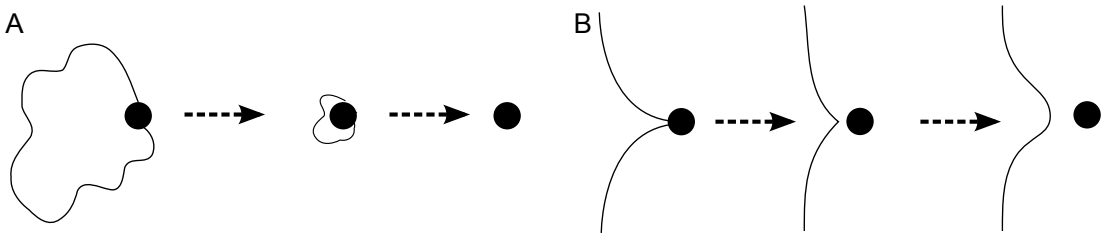

Figure 4.1: A sketch of two mechanisms of a trapped particle de-trapping from a vortex.

A series of simulations was ran for material parameters corresponding to 1.9 K (taken from Ref. [34]) and particle size 5 μm (equal to the trapping distance). This corresponds to the viscous relaxation time $\tau = 0.6$ ms. A statistically converged counterflow tangle is used as the initial condition. Into this tangle a number of initially stationary particles is inserted at $t = 0$ with random positions and their motion is evolved in time using Eqs. (4.1) and (4.3). As the particles move, they interact with and are trapped onto the quantized vortices with the trapping rate (relative number of trapped particles) shown in Fig. 4.2. Both ideal tracers and inertial interacting particles, for several different particle counts are shown. It is obvious that accounting for the dynamics of the trapped particles and their backreaction on the vortex greatly increases the de-trapping rate. The trapping rate also weakly depends on the particle count, which is most likely due to effect on vortex line density (see Fig. 4.3 and the text below).

A trapped particle experiences Stokes drag due to the flow of the normal fluid component. This drag indirectly acts on a quantized vortex, deforming it in the direction of the normal fluid flow. This additional channel of energy transfer between the large scale normal fluid flow and the tangle of quantized vortices causes an increase of the vortex line density, as one can see in Fig. 4.3, left. As the Stokes drag acts primarily in the mean flow direction of the normal fluid, the tangle ought to stretch globally in this direction, which is indeed the case as can be seen in Fig. 4.3, right. The polarisation here is defined as

$$p = \frac{2L_x}{L_y + L_z}, \tag{4.7}$$

where $L_{\hat{k}}$ is the vortex line density projected along the direction $\hat{k}$ (with the counterflow velocity being oriented along x-direction).

Detailed understanding of the motion of particles in turbulent flow is important for interpretation of the visualisation experiments developed for He II in recent years. The results presented here clearly show that inertial particles do not behave as passive tracers of the flow and in large numbers can affect the global tangle characteristics significantly, as can be seen from the increase of the vortex line density and tangle polarisation in Fig. 4.3. Experiments using a relatively small number of particles such as the particle tracking velocimetry [18, 110] (order of 1 particle/mm^3) are less likely to suffer from these effects, however, visualisation experiments relying on large particle density such as PIV [111] ought to be analysed with care.

Furthermore, even for low particle number densities, when the tangle is affected only weakly, the statistics of motion of the particles are significantly dif-

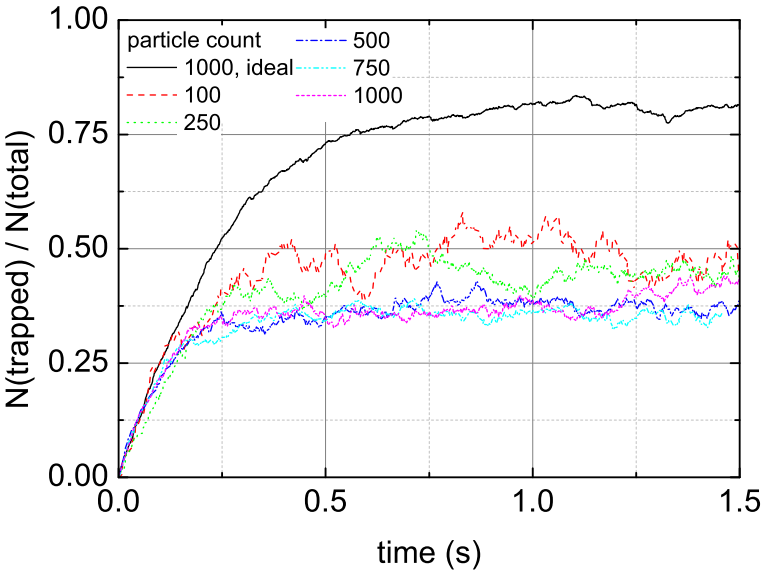

Figure 4.2: Trapping rate for idealised tracer and inertial particles. Inertia of particles clearly increases the chance of liberating the particle from a vortex due to increased local curvature.

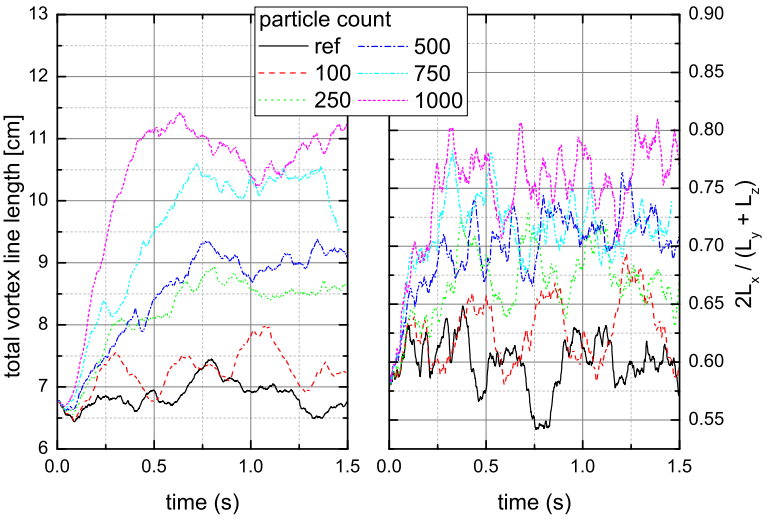

Figure 4.3: Total vortex line density (left) and tangle polarisation (right) for fixed counterflow velocity and different particle counts. Trapped particles provide additional mode of energy transfer from the large-scale counterflow to the vortex tangle through the Stokes drag, hence the increase in total vortex line density with increasing number of particles. Correspondingly, the tangle becomes more stretched in the direction of the normal fluid flow, i.e., the direction of the Stokes drag. The reference black curves correspond to a run with the particles calculated as passive tracers.

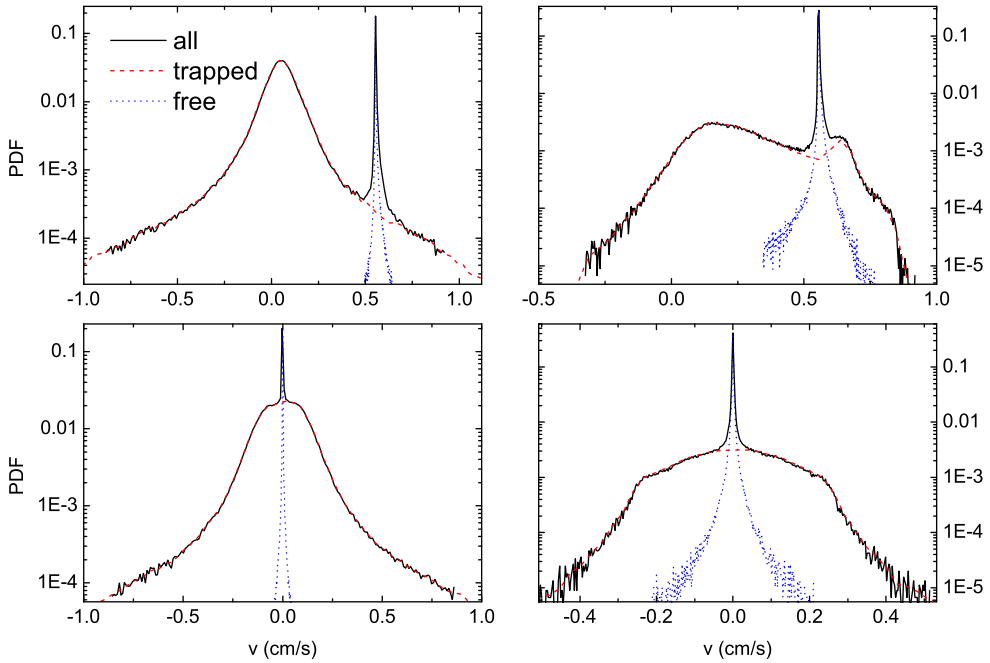

Figure 4.4: The probability density functions of the particle velocity component – streamwise (top row) and transverse (bottom row) to the counterflow direction (the velocity of the normal fluid is positive). Data for ideal tracers (left) and intertial particles (right) are shown. The inertial particles' PDFs are based on the run with 1000 particles.

ferent from ideal tracers, as seen in Fig. 4.4. Trapped particles deform the vortex locally and cause it to move with slightly artificial velocity, i.e., the particles do not act as passive probes of intrinsic tangle dynamics, even in small concentrations. Lastly, it should be noted that the sharp peaks corresponding to free particles in Fig. 4.4 are generally not observed in experiments [112], although particle trajectories that could be consistent with the numerical PDFs have been observed for small velocities [113]. A likely cause for this discrepancy, apart from a wide distribution of particle sizes and shapes in experiments, is absence of normal fluid turbulence in the simulations, which is likely to be present in the experiment.

4.3 Spherically symmetric counterflow[3]

An idealised point heat source in unbounded helium results in spherically symmetric counterflow. As in ordinary channel-bound rectilinear counterflow, the heater generates entropy at rate $\dot{Q}/T$ which is carried away by the normal fluid component. This outflux is balanced by the influx of the superfluid component.

Assuming spherical symmetry of the flow fields and the heater placed at the origin, the radial velocity of the normal fluid component v_{n} through a shell of radius r is

$$v_{\mathrm{n}} 4\pi r^2 \rho S = \frac{\dot{Q}}{T}, \tag{4.8}$$

[3]The results of this section were submitted to *Journal of Low Temperature Physics*, reproduced as Attachment 6.

where S is the entropy per unit mass. The superfluid velocity is given by the standard counterflow condition $\rho_s v_\mathrm{s} = \rho_n v_\mathrm{n}$. In the following, the velocity will be identified by the radial counterflow velocity on the 5 mm shell denoted by $v_\mathrm{ns}^\mathrm{5mm}$.

The velocity field given by (4.8) has a singularity at the origin. This singularity is removed in the simulation in a two-fold way. The prescribed counterflow velocity field used has a radial profile of the form

$$v_\mathrm{ns}(r) = \frac{v_0}{4\pi r^2} e^{-(r_\mathrm{cutoff}/r)^2} \tag{4.9}$$

where v_0 is a prescribed strength and r_cutoff is set to be 150 μm. Second, an additional cutoff r_O is introduced. If a vortex loop is *fully* contained within a sphere of radius r_O it is removed from the simulation. This is to prevent a pile-up of nearly-parallel loops near the origin. In a hypothetical experiment, these would collide with the walls of the heater and thus would be destroyed. In the simulation, they are mostly inactive in outer turbulence but cause large increase in the number of necessary vortex nodes thus slowing down the calculation considerably. In all runs the r_O was set to 200 μm. The simulation was implemented as described in detail in Sec. 2.2. The discretisation length was maintained between 1 and 2 $\times 10^{-3}$ cm (a subset of the result was checked also for discretisation between 2 and 4 $\times 10^{-3}$ cm). The time step used was 6.4$\times$ 10^{-4}, 10^{-5} or 10^{-6} s for $v_\mathrm{ns}^\mathrm{5mm}$ = 0.1, 1 or 10 mm/s, respectively.

As the initial condition, a few (less than 10) random vortex loops are placed in the vicinity of the origin, see Fig. 4.5. The centre of the loops is placed randomly, with uniform distribution, in a cube of 1 mm length centered on the origin. The radius of loops is chosen with uniform distribution between 50 μm and 1 mm. The direction of the loops (i.e., the direction from which the winding of the loop is positive) is chosen randomly with isotropic distribution.

The converging flow of the superfluid component causes the vortices to bend toward the origin. This creates sections of the vortex oriented nearly radially and thus parallel with prescribed counterflow velocity. Straight vortex lines in parallel counterflow are unstable [23] and small perturbations quickly expand to large-amplitude Kelvin waves, as illustrated in Fig. 4.6. Note that the wavelength of the initial perturbation is likely influenced by the spatial discretisation of the vortices (between 10 and 20 μm).

The Kelvin waves converging on the origin from random directions cause frequent reconnections and creation of a tangle in the neighbourhood of the origin, as seen in Fig. 4.7 for a simulation corresponding to 1.3 K. The development of a localised tangle is, however, strongly dependent on the temperature. As can be seen from the plots in Fig. 4.8 of total vortex line length as a function of time, for sufficiently low temperatures a dense tangle is created from the initial seed loops while for high temperatures the vortices are quickly annihilated at the origin. The time in Fig. 4.8 is normalised by the "fall time" t_fall, a time it would take a superfluid Lagrangian particle to fall to the origin from a given distance r. The Lagrangian particle would move toward the origin with velocity given by the local superfluid velocity, i.e.

$$\frac{\mathrm{d}\, r}{\mathrm{d}\, t} = -v_\mathrm{ns}(r)\frac{\rho_n}{\rho}, \tag{4.10}$$

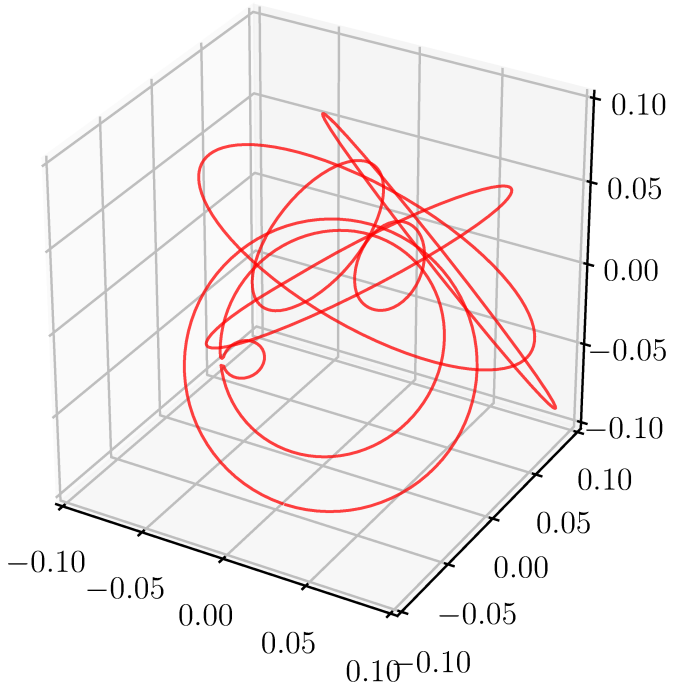

Figure 4.5: An example of the random initial condition used for the simulation of spherically symmetric counterflow. The axes labels are in cm. Loops of random orientation and size (uniformly distributed radii between 50μm and 1 mm) are placed in a cube of 1 mm side length centered on origin.

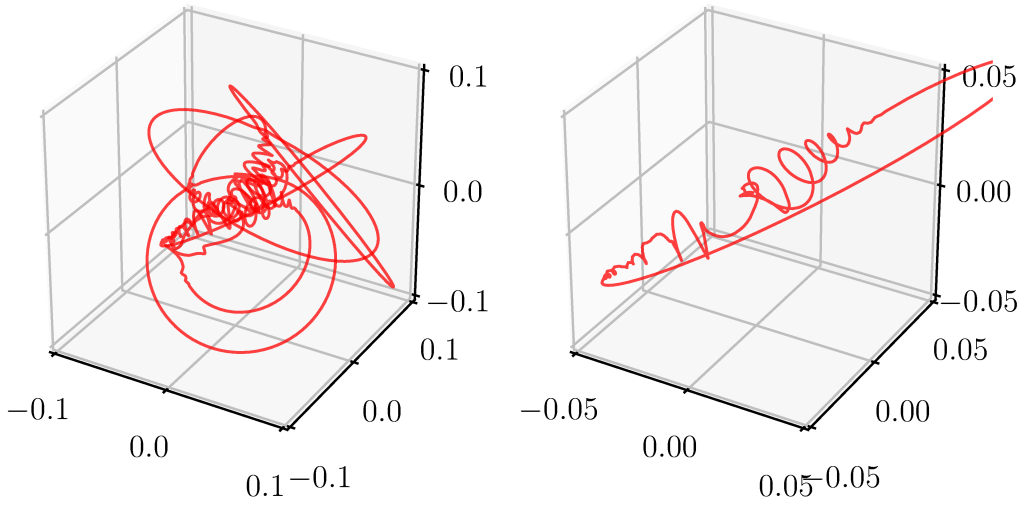

Figure 4.6: Kelvin waves excited on the radially oriented vortices. The figure on the left shows the state of the tangle after 16 ms of evolution from the initial condition shown in Fig.4.5. The specific conditions were $T = 1.3$ K and $v_{\rm ns}^{\rm 5mm} = 1$ mm/s. Helical Kelvin waves of large amplitude are clearly visible on sections of the vortex oriented in radial direction. The right panel shows a single enlarged vortex from the tangle on the left.

where $v_{\rm ns}(r)$ is given by Eq. (4.9) (neglecting the exponential cutoff). Integrating the differential equation from a given initial position r to $r = 0$ yields

$$t_{\rm fall}(r, T) = \frac{4\pi r^3}{3v_0}\frac{\rho}{\rho_n}. \tag{4.11}$$

For the normalisation fall time in Fig. 4.8, $r_0 = 1$ mm is chosen, as this distance is comparable to the initial distance of the vortices from the origin.

As can be seen in a "phase diagram" in Fig. 4.9, the minimum temperature for the existence of a stable tangle is in the vicinity of 1.45 K and appears to decrease with increasing velocity, a behaviour contrasting with rectilinear thermal counterflow or superflow [83, 59], where a stable tangle is possible at all temperatures and the critical velocity typically decreases with increasing temperature for thermal counterflow or is mostly temperature independent for pure superflow. An obvious generalisation of this result is that turbulence cannot be generated in spherically symmetric thermal counterflow for temperatures higher than some critical temperature T_c.

Both these observations can be elucidated by a simple physical model. In order for a stable tangle to develop, a sustainable mechanism (one that does not depend on the existence of the large seed vortices) of increase of vortex length must exist. One such mechanism might be the escape of vortex loops from the tangle, which

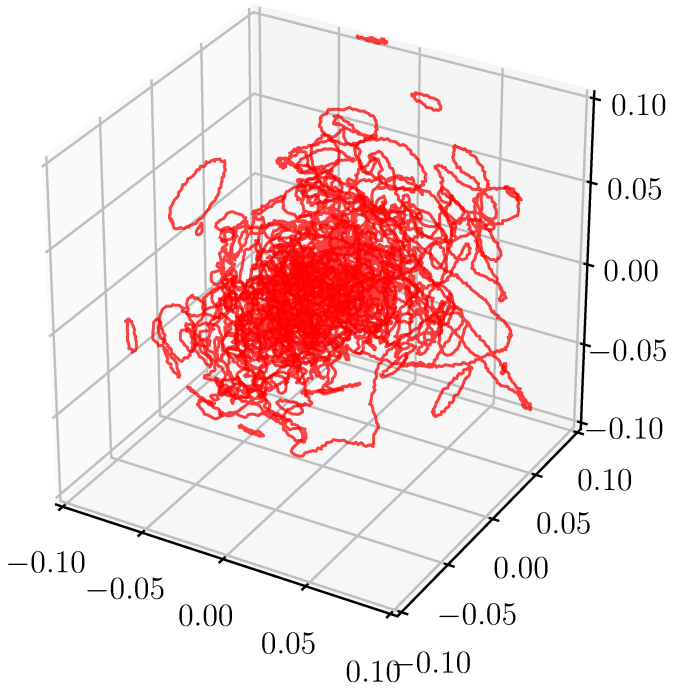

Figure 4.7: Tangle of quantized vortices in the neigbourhood of the origin. The simulation parameters correspond to $T = 1.3$ K and $v_{\rm ns}^{\rm 5mm} = 0.1$ mm/s.

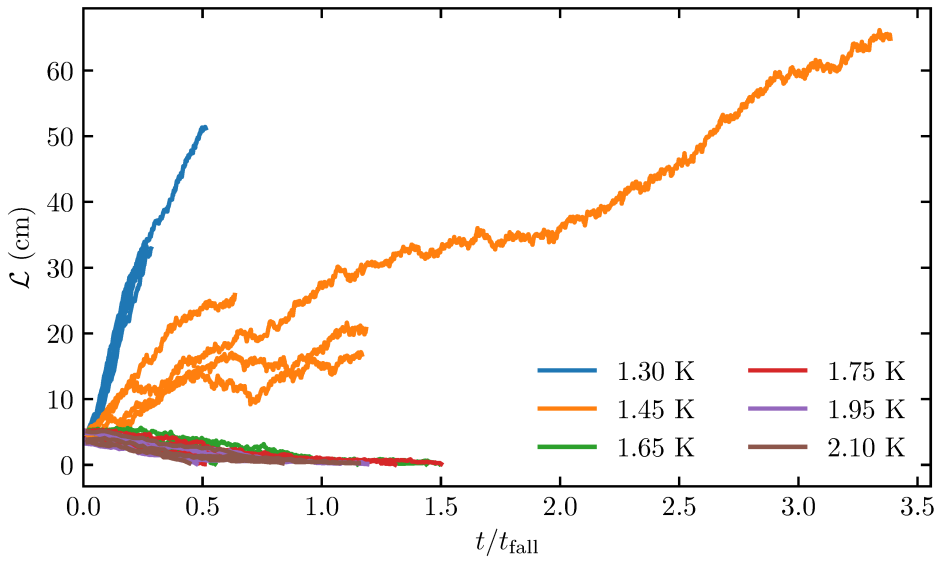

Figure 4.8: Time evolution of the total vortex line length at several different temperatures for the case of $v_{\rm ns}^{\rm 5mm} = 0.1$ mm/s. Results obtained from 4 different (random) initial conditions are shown for every temperature. The time is compensated by the "fall time" from r =1 mm given by Eq. (4.11).

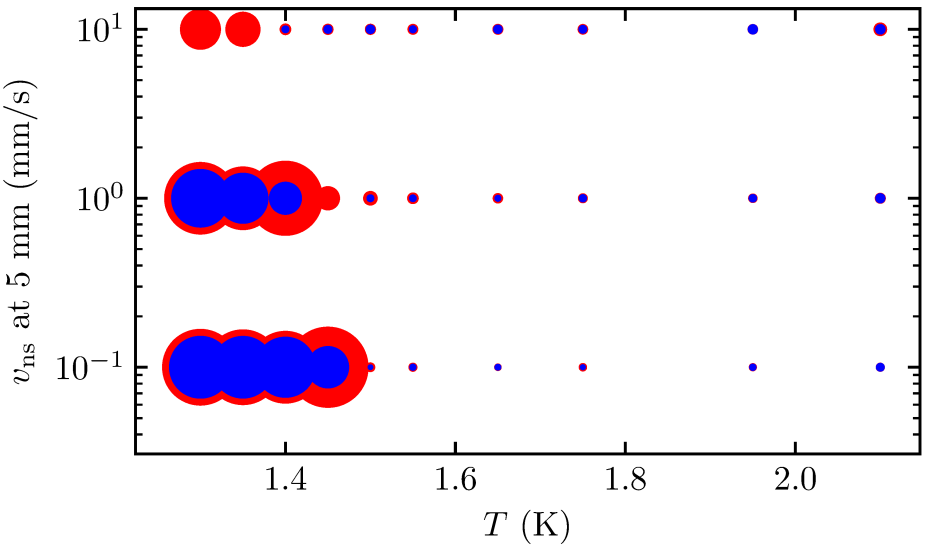

Figure 4.9: Phase diagram of the development of sustained turbulence. The velocity on the y-axis shows $v_{\mathrm{ns}}^{5\mathrm{mm}}$ – the counterflow velocity on the 5 mm shell around origin. The size of the points is proportional to the total length of the vortices; the outer radius (red) is proportional to $\bar{\mathcal{L}}_f + \sigma_{\mathcal{L}}$ and the inner (blue) to $\bar{\mathcal{L}}_f - \sigma_{\mathcal{L}}$ where $\mathcal{L}_f$ is the total vortex length at the end of simulation run, $\bar{\mathcal{L}}_f$ is the average of $\mathcal{L}_f$ for different runs and $\sigma_{\mathcal{L}}$ is the associated standard deviation. The existence of sustained turbulence appears to be bounded by both velocity and temperature. For the 10 mm/s case at 1.3 K and 1.35 K, one simulation run in the ensemble experienced a (presumably) transient tangle of very high density which essentially halted the calculation.

subsequently expand and slow down. The vortex loop expands until it is so slow that it is pulled back towards the tangle. Obviously, outward-propagating and expanding loops are crucial for this mechanism to work, therefore the sizes and positions of such vortex rings in the field of the spherical counterflow are now determined.

Assuming the ring and flow source geometry as in Fig. 4.10, the motion of the vortex ring is determined by

$$\dot{\mathbf{s}} = \mathbf{v}_s^R + \mathbf{v}_s^O + \alpha \mathbf{s}' \times (\mathbf{v}_n - \mathbf{v}_s), \tag{4.12}$$

where $\mathbf{v}_s^R$ is the self induced velocity of the ring oriented along the x direction, with the magnitude given by [23]

$$v_s^R = \frac{\kappa}{4\pi R}\left[\log\left(\frac{8R}{a}\right) - \frac{1}{2}\right], \tag{4.13}$$

with $a \approx 10^{-10}$ m denoting the vortex core parameter. The second term is the inward-facing spherical superflow of magnitude $v_s^O = v_{\mathrm{ns}}\rho_n/\rho_s$. The last term is the mutual friction, with $\mathbf{v}_n$ and $\mathbf{v}_s$ standing for the total normal and superfluid velocities. The resulting configurations of d and R where the ring is outward-propagating ($\dot{s}_x > 0$) and expanding ($\dot{s}_y > 0$ for the special point in Fig. 4.10) are shown in Fig. 4.11. The number of possible configurations clearly decreases as the temperature increases. For increasing velocities, the effect is related to the system size. The favourable ring geometries shift to grater distances d which fit the initial condition more poorly. The rings that are too large or too close to the origin are being pulled toward the origin and/or are shrinking. Rings that are too small, on the other hand, have large enough self-induced velocity to escape the flow completely.

The numerically predicted temperature-dependent behaviour of spherically symmetric counterflow ought to be relatively simple to test experimentally, for example using a setup as proposed, simplified, in Fig. 4.12. The initial seed loops would be provided by rectilinear thermal counterflow constructed around a miniature heater. The development of turbulence would be monitored by standard second sound attenuation technique, which could even hypothetically allow for spatial mapping of the tangle [24], if one develops.

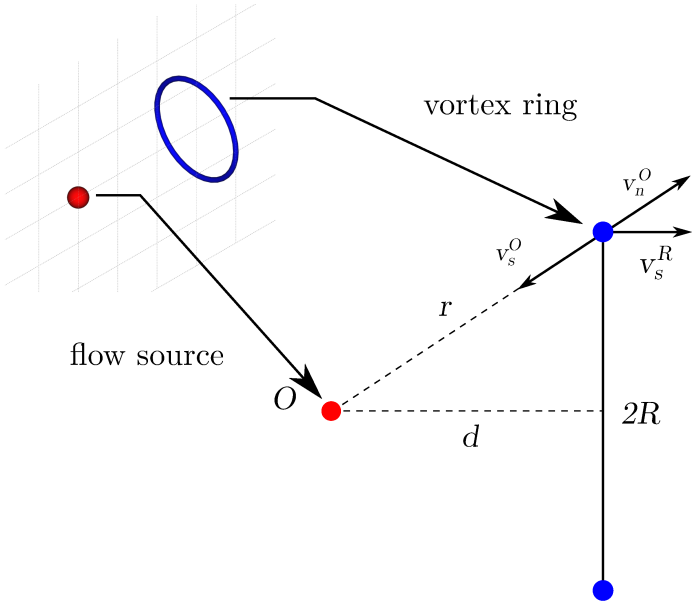

Figure 4.10: Geometry of the ring placed in the field of spherical counterflow. The velocity $\mathbf{v}_\mathrm{s}^R$ is the self-induced velocity of the ring and $\mathbf{v}_\mathrm{n,s}^O$ is the spherical flow due to the heat source at the origin.

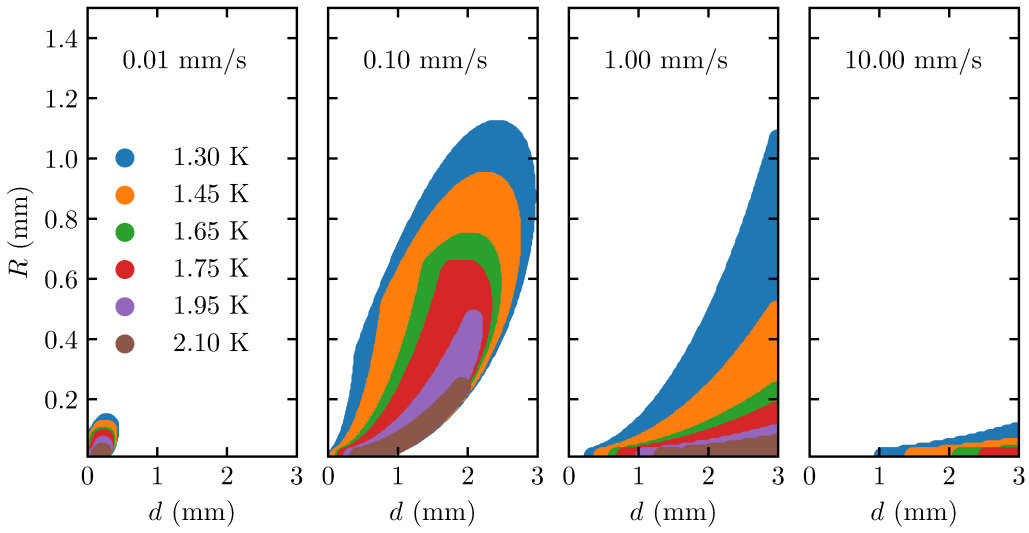

Figure 4.11: Parameters allowing growth and spreading of vortex rings placed in a field of spherical counterflow, for different temperatures (see legend) and different v_ns on the 5 mm shell (see the labels in the panels). The shaded regions indicate positions and sizes of rings which grow and move away from the singularity. The geometry of the ring is assumed to be as in Fig. 4.10.

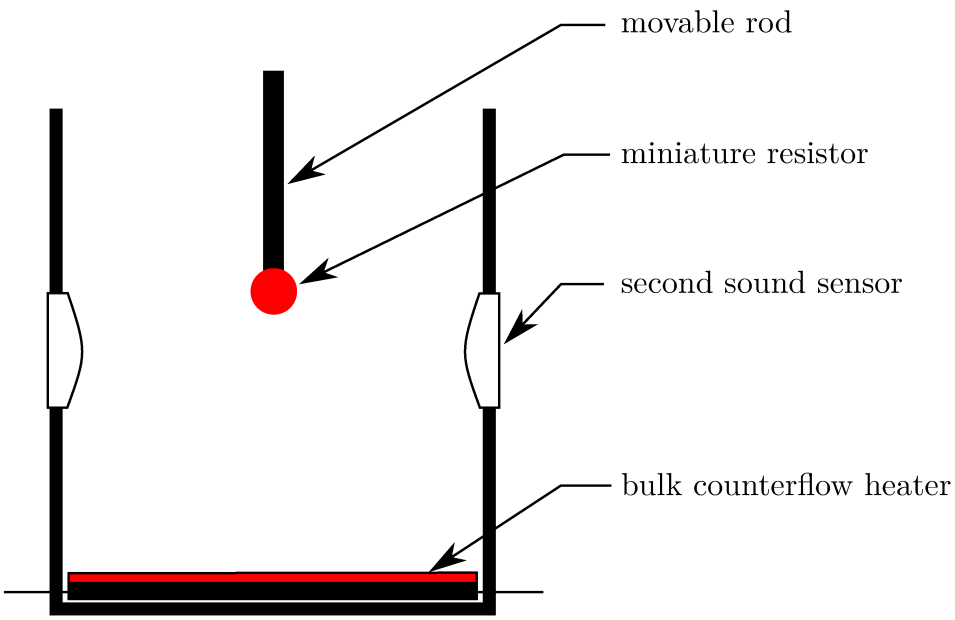

Figure 4.12: A proposed experimental test of the spherically symmetric counterflow.

Discussion and conclusions

Historically, the most thoroughly studied form of quantum turbulence, thermal counterflow, still poses significant challenges to its complete understanding. Geometrical effects in counterflow appear to play a significant role which has been scarcely explored so far. The work presented in this thesis approached this complicated problem experimentally, by comparing thermal counterflow and pure superflow in the steady state (Sec. 3.2) and decay (Sec. 3.3). In pure superflow, the mean velocity of the normal fluid component is zero with respect to the walls of the channel, contrary to thermal counterflow. In an infinite, unbounded system, thermal counterflow and pure superflow are clearly just Galilean transformations of the same flow, however, the presence of the walls influences both the absolute value of the steady state vortex line density (Fig. 3.2) and important details of the decay. Specifically, the non-monotonous "bump" in the early stages of the decay (Fig. 3.9) is weakened or absent completely. In light of the theories of the bump [51, 17], this signifies a non-trivial alteration of the energy spectrum of the flow simply due to the introduction of walls to the system. The decreased intensity of the bump hints at a shallower spectrum, closer to the classical K41 $E \propto k^{-5/3}$ case. A tentative reason for this may lie in the fact that the normal fluid is not forced by the heat flux and can conform to the flow of the superfluid on a wider range of scales, i.e., coupled eddies that form in the intermediate range of scales are not torn apart by the mean counterflow.

Another geometric effect that is gaining attention concerns boundary layers [88, 89, 87] and entrance length effects [90] and, in particular, a possible boundary layer in the vicinity of the heat source in counterflow turbulence [32]. The possible boundary layer in the vicinity of the heater is of particular interest due to its similarity to the boundary layer in classical thermal convection. Attempts at detecting this boundary layer were made with a movable miniature temperature sensor in close proximity to the heater (Fig. 3.6). However, this revealed no significant deviation from the constant temperature gradient in the bulk. It should be noted that the boundary layer here may have been significantly narrower than in the experiments of Hrubcová *et al.* [32], and may actually be smaller than the spatial resolution of the movable thermometer.

Due to the revived theoretical debate [37, 38, 36] concerning the dynamical behaviour of the vortex line density in thermal counterflow, the general dynamics of $L(t)$ in non-stationary counterflow was studied experimentally (Sec. 3.4). Low-noise measurements of vortex line density allowed for the phase trajectories of $L(t)$ to be inferred directly, without restricting the study to a mere comparison of the solutions of the proposed differential equations. It was found that the theory of Schwarz [35], the simplest currently available theory derived on the basis of mesoscopic dynamics of individual vortex lines, has a surprisingly wide range of applicability, showing a near perfect match between experimentally and numerically determined tangle parameters. Furthermore, even outside this range of applicability, a fair agreement between theory and experiment can be restored if one allows a geometrical coefficient connecting the mean tangle curvature and vortex line density to vary, which is in line with numerical simulations that attempted to capture the effects of normal fluid turbulence.

In a somewhat separate development from the studies of counterflow, decay in the wake of a moving grid was studied by laser-induced fluorescence of He_2^* molecules created by field ionisation using high-intensity femtosecond laser pulses, a visualisation method developed by the group in Tallahassee [21]. The decay of vortex line density in this system (Fig. 3.27) is the archetypical quasi-classical decay [8, 48], however, non-classical scaling in the energy spectrum was found both in the very early and very late decay (Fig. 3.28). Additionally, in the time frame when the turbulence displayed classical characteristics, higher-order statistics revealed temperature-dependent intermittency(Fig. 3.32) with a maximum deviation from K41 scaling in the vicinity of 1.85 K, in agreement with pre-existing numerical predictions [54, 55]. This suggests that coflow of He II is significantly more complex than the framework of full coupling of the two components and the effective viscosity (Eq. (1.12)) can account for.

The second part of this thesis considered numerical simulations based on the vortex filament model, which were used to study two particular problems pertaining to thermal counterflow. First, the modification of the vortex tangle by seeding the flow with solid particles, a situation that models the visualisation technique [105] based on the observation of frozen particles of gas (typically hydrogen, deuterium [18] or air [114]). It was found that the particles trapped on the vortices can act as an additional channel of energy transfer from the mean normal fluid flow to the vortex tangle, which only usually proceeds through expansion of vortex rings by mutual friction. Particles also behave significantly differently from idealised tracers when trapped, modifying the local geometry of the vortex and resulting in statistical properties of their motion significantly different than those of the vortices or the velocity field themselves, a fact which could have implications for experimental studies focusing on the statistical properties of the motion of the particles such as particle tracking velocimetry (PTV).

Second, thermal counterflow in a spherical geometry was studied, which can be easily realised using a miniature heater, but to the author's knowledge was not yet studied experimentally. Rectilinear thermal counterflow (i.e., a flow in a channel) is naturally slightly polarised due to the expansion of favourably oriented vortex loops lying in the plane perpendicular to the direction of the mean counterflow velocity. This preferential direction is absent in this spherical case. It was found that turbulence in this geometry can develop from initial seed loops only at sufficiently low temperatures, whereas at high temperatures the vortices are quickly compressed toward the origin and annihilated. Note that in rectilinear counterflow, critical counterflow velocity was found to *decrease* [84, 83] with increasing temperature and vortex line density generally grows with temperature for fixed counterflow velocity.

In view of the considerable variety of the studied flows, certain questions remain unresolved: Is there a region of increased temperature gradient in the vicinity of the heat source in thermal counterflow akin to Rayleigh-Bénard Convection in classical liquids? Is the effective c_2 deduced in Sec. 3.4 an actual measure of the curvature of the tangle or is the quasi-stationary theory of the vortex line density dynamics of Schwarz and Vinen simply not applicable to large transients? Can the apparent critical temperature emerging in the numerical simulation of spherical counterflow be reproduced experimentally? It is the hope of the author that these outstanding questions will help motivate further study

of this beautiful and interesting physical system.

Bibliography

[1] Barenghi, C. F., Skrbek, L., and Sreenivasan, K. R. Introduction to quantum turbulence. *Proc. Natl. Acad. Sci.*, **111**(Supplement 1), 4647–4652 (2014).

[2] Frisch, U. *Turbulence: The legacy of A. N. Kolmogorov*. Cambridge university press (1995).

[3] Kolmogorov, A. N. The local structure of turbulence in incompressible viscous fluid for very large reynolds numbers. In *Dokl. Akad. Nauk SSSR*, volume 30, 299–303 (1941).

[4] Obukhov, A. Energy distribution in the spectrum of a turbulent flow. *AN URSS*, **4**, 453–466 (1941).

[5] Kolmogorov, A. N. A refinement of previous hypotheses concerning the local structure of turbulence in a viscous incompressible fluid at high Reynolds number. *J. Fluid Mech.*, **13**, 82 (1962).

[6] Tilley, D. R. and Tilley, J. *Superfluidity and Superconductivity*. Institute of Physics Publishing, Bristol and Philadelphia, third edition (1990).

[7] Barenghi, C. F., L'vov, V. S., and Roche, P.-E. Experimental, numerical, and analytical velocity spectra in turbulent quantum fluid. *Proc. Natl. Acad. Sci.*, **111**(Supplement 1), 4683–4690 (2014).

[8] Stalp, S. R., Skrbek, L., and Donnelly, R. J. Decay of grid turbulence in a finite channel. *Phys. Rev. Lett.*, **82**(24), 4831 (1999).

[9] Babuin, S., Varga, E., Skrbek, L., Lévêque, E., and Roche, P.-E. Effective viscosity in quantum turbulence: A steady-state approach. *Europhys. Lett.*, **106**(2), 24006 (2014).

[10] Hall, H. E. and Vinen, W. The rotation of liquid helium II I. Experiments on the propagation of second sound in uniformly rotating helium II. *Proc. R. Soc. A*, **238**(1213), 204–214 (1956).

[11] Hall, H. E. and Vinen, W. F. The rotation of liquid helium II II. The theory of mutual friction in uniformly rotating helium II. *Proc. R. Soc. A*, **238**(1213), 215–234 (1956).

[12] Vinen, W. F. Mutual friction in a heat current in liquid helium II. I. Experiments on steady heat currents. *Proc. R. Soc. A*, **240**(1220), 114–127 (1957).

[13] Vinen, W. Mutual friction in a heat current in liquid helium II. II. Experiments on transient effects. *Proc. R. Soc. A*, **240**(1220), 128–143 (1957).

[14] Vinen, W. F. Mutual Friction in a Heat Current in Liquid Helium II. III. Theory of the Mutual Friction. *Proc. R. Soc. A*, **242**(1231), 493–515 (1957).

[15] Vinen, W. F. Mutual friction in a heat current in liquid helium II. IV. Critical heat currents in wide channels. *Proc. R. Soc. A*, **243**(1234), 400–413 (1958).

[16] Khomenko, D., L'vov, V. S., Pomyalov, A., and Procaccia, I. Counterflow-induced decoupling in superfluid turbulence. *Phys. Rev. B*, **93**(1), 014516 (2016).

[17] Babuin, S., L'vov, V. S., Pomyalov, A., Skrbek, L., and Varga, E. Coexistence and interplay of quantum and classical turbulence in superfluid ^{4}He: Decay, velocity decoupling, and counterflow energy spectra. *Phys. Rev. B*, **94**(17), 174504 (2016).

[18] La Mantia, M., Švančara, P., Duda, D., and Skrbek, L. Small-scale universality of particle dynamics in quantum turbulence. *Phys. Rev. B*, **94**(18), 184512 (2016).

[19] Eltsov, V., Hänninen, R., and Krusius, M. Quantum turbulence in superfluids with wall-clamped normal component. *Proc. Natl. Acad. Sci.*, **111**(Supplement 1), 4711–4718 (2014).

[20] Fisher, S. N., Jackson, M. J., Sergeev, Y. A., and Tsepelin, V. Andreev reflection, a tool to investigate vortex dynamics and quantum turbulence in ^{3}He-B. *Proc. Natl. Acad. Sci.*, **111**(Supplement 1), 4659–4666 (2014).

[21] Marakov, A., Gao, J., Guo, W., Van Sciver, S. W., Ihas, G. G., McKinsey, D. N., and Vinen, W. F. Visualization of the normal-fluid turbulence in counterflowing superfluid ^{4}He. *Phys. Rev. B*, **91**(9), 094503 (2015).

[22] Gao, J., Marakov, A., Guo, W., Pawlowski, B. T., Van Sciver, S. W., Ihas, G. G., McKinsey, D. N., and Vinen, W. F. Producing and imaging a thin line of He_2^* molecular tracers in helium-4. *Rev. Sci. Instrum.*, **86**(9), 093904 (2015).

[23] Donnelly, R. J. *Quantized Vortices in Helium II*. Cambridge University Press, Cambridge (1991).

[24] Varga, E., Babuin, S., and Skrbek, L. Second-sound studies of coflow and counterflow of superfluid ^{4}He in channels. *Phys. Fluids*, **27**(6), 065101 (2015).

[25] Blažková, M., Človečko, M., Gažo, E., Skrbek, L., and Skyba, P. Quantum Turbulence Generated and Detected by a Vibrating Quartz Fork. *J. Low Temp. Phys.*, **148**(3), 305–310 (2007).

[26] Blaauwgeers, R., Blazkova, M., Človečko, M., Eltsov, V. B., de Graaf, R., Hosio, J., Krusius, M., Schmoranzer, D., Schoepe, W., Skrbek, L., Skyba, P., Solntsev, R. E., and Zmeev, D. E. Quartz Tuning Fork: Thermometer, Pressure- and Viscometer for Helium Liquids. *J. Low Temp. Phys.*, **146**(5), 537–562 (2007).

[27] Schmoranzer, D., Jackson, M., Tsepelin, V., Poole, M., Woods, A., Človečko, M., and Skrbek, L. Multiple critical velocities in oscillatory flow of superfluid ^{4}He due to quartz tuning forks. *Phys. Rev. B*, **94**(21), 214503 (2016).

[28] Jackson, M., Bradley, D. I., Guénault, A. M., Haley, R. P., Pickett, G. R., and Tsepelin, V. Observation of quantum turbulence in superfluid ^{3}He-B using reflection and transmission of ballistic thermal excitations. *Phys. Rev. B*, **95**(9), 094518 (2017).

[29] Walmsley, P. and Golov, A. Coexistence of quantum and classical flows in quantum turbulence in the T=0 limit. *Phys. Rev. Lett.*, **118**(13), 134501 (2017).

[30] Gorter, C. J. and Mellink, J. H. On the irreversible processes in liquid helium II. *Physica*, **15**(3-4), 285–304 (1949).

[31] Van Sciver, S. W. *Helium cryogenics*. Springer Science & Business Media (2012).

[32] Hrubcová, P., Švančara, P., and La Mantia, M. Vorticity enhancement in thermal counterflow of superfluid helium. *Phys. Rev. B*, **97**, 064512 (2018).

[33] Landau, L. and Lifshitz, E. *Fluid Mechanics*. Pergamon Press (1987).

[34] Donnelly, R. J. and Barenghi, C. F. The Observed Properties of Liquid Helium at the Saturated Vapor Pressure. *J. Phys. Chem. Ref. Data*, **27**(6), 1217–1274 (1998).

[35] Schwarz, K. W. Three-dimensional vortex dynamics in superfluid ^{4}He: Homogeneous superfluid turbulence. *Phys. Rev. B*, **38**(4), 2398–2417 (1988).

[36] Nemirovskii, S. K. Comment on "Dynamics of the density of quantized vortex lines in superfluid turbulence". *Phys. Rev. B*, **94**(14), 146501 (2016).

[37] Khomenko, D., Kondaurova, L., L'vov, V. S., Mishra, P., Pomyalov, A., and Procaccia, I. Dynamics of the density of quantized vortex lines in superfluid turbulence. *Phys. Rev. B*, **91**(18), 180504 (2015).

[38] Khomenko, D., L'vov, V. S., Pomyalov, A., and Procaccia, I. Reply to "Comment on 'Dynamics of the density of quantized vortex lines in superfluid turbulence' ". *Phys. Rev. B*, **94**(14), 146502 (2016).

[39] Gao, J., Guo, W., Vinen, W. F., Yui, S., and Tsubota, M. Dissipation in quantum turbulence in superfluid ^{4}He. *Phys. Rev. B*, **97**, 184518 (2018).

[40] Babuin, S., Varga, E., Vinen, W. F., and Skrbek, L. Quantum turbulence of bellows-driven ^{4}He superflow: Decay. *Phys. Rev. B*, **92**(18), 184503 (2015).

[41] Gao, J., Guo, W., L'vov, V. S., Pomyalov, A., Skrbek, L., Varga, E., and Vinen, W. F. Decay of counterflow turbulence in superfluid ^{4}He. *JETP Lett.*, **103**(10), 648–652 (2016).

[42] Gao, J., Varga, E., Guo, W., and Vinen, W. F. Energy spectrum of thermal counterflow turbulence in superfluid helium-4. *Phys. Rev. B*, **96**(9), 094511 (2017).

[43] Gao, J., Varga, E., Guo, W., and Vinen, W. Statistical Measurement of Counterflow Turbulence in Superfluid Helium-4 Using He_2^* Tracer-Line Tracking Technique. *J. Low Temp. Phys.*, **187**(5-6), 490–496 (2017).

[44] Comte-Bellot, G. and Corrsin, S. The use of a contraction to improve the isotropy of grid-generated turbulence. *J. Fluid Mech.*, **25**(4), 657–682 (1966).

[45] Vinen, W. F. and Niemela, J. J. Quantum turbulence. *J. Low Temp. Phys.*, **128**(5), 167–231 (2002).

[46] Maurer, J. and Tabeling, P. Local investigation of superfluid turbulence. *Europhys. Lett.*, **43**, 29 (1998).

[47] Babuin, S., Varga, E., and Skrbek, L. The Decay of Forced Turbulent Coflow of He II Past a Grid. *J. Low Temp. Phys.*, **175**(1-2), 324–330 (2014).

[48] Skrbek, L. and Stalp, S. R. On the decay of homogeneous isotropic turbulence. *Phys. Fluids*, **12**(8), 1997 (2000).

[49] Zmeev, D. E., Walmsley, P., Golov, A., McClintock, P. V., Fisher, S. N., and Vinen, W. Dissipation of quasiclassical turbulence in superfluid he 4. *Phys. Rev. Lett.*, **115**(15), 155303 (2015).

[50] Walmsley, P. and Golov, A. Quantum and quasiclassical types of superfluid turbulence. *Phys. Rev. Lett.*, **100**(24), 245301 (2008).

[51] Gao, J., Guo, W., and Vinen, W. F. Determination of the effective kinematic viscosity for the decay of quasiclassical turbulence in superfluid ^{4}He. *Phys. Rev. B*, **94**, 094502 (2016).

[52] Vinen, W. Quantum turbulence: Achievements and challenges. *J. Low Temp. Phys.*, **161**(5-6), 419–444 (2010).

[53] Walmsley, P., Golov, A., Hall, H., Levchenko, A., and Vinen, W. Dissipation of quantum turbulence in the zero temperature limit. *Phys. Rev. Lett.*, **99**(26), 265302 (2007).

[54] Boué, L., L'vov, V., Pomyalov, A., and Procaccia, I. Enhancement of Intermittency in Superfluid Turbulence. *Phys. Rev. Lett.*, **110**(1), 014502 (2013).

[55] Biferale, L., Khomenko, D., L'vov, V., Pomyalov, A., Procaccia, I., and Sahoo, G. Turbulent statistics and intermittency enhancement in coflowing superfluid ^{4}He. *Phys. Rev. Fluids*, **3**, 024605 (2018).

[56] Rusaouen, E., Chabaud, B., Salort, J., and Roche, P.-E. Intermittency of quantum turbulence with superfluid fractions from 0% to 96%. *Phys. Fluids*, **29**(10), 105108 (2017).

[57] Hanninen, R. and Baggaley, A. Vortex filament method as a tool for computational visualization of quantum turbulence. *Proc. Natl. Acad. Sci.*, **111**(Supplement 1), 4667–4674 (2014).

[58] Varga, E. and Skrbek, L. Dynamics of the density of quantized vortex lines in counterflow turbulence: Experimental investigation. *Phys. Rev. B*, **97**(6), 064507 (2018).

[59] Babuin, S., Stammeier, M., Varga, E., Rotter, M., and Skrbek, L. Quantum turbulence of bellows-driven ^{4}He superflow: Steady state. *Phys. Rev. B*, **86**(13), 134515 (2012).

[60] Chagovets, T. and Skrbek, L. Steady and decaying flow of He II in a channel with ends blocked by superleaks. *Phys. Rev. Lett.*, **100**(21), 215302 (2008).

[61] Baehr, M. L., Opatowsky, L., and Tough, J. Transition from dissipationless superflow to homogeneous superfluid turbulence. *Phys. Rev. Lett.*, **51**(25), 2295 (1983).

[62] Babuin, S., Varga, E., Stammeier, M., and Skrbek, L. Mechanically Versus Thermally Generated Quantum Turbulence of ^{4}He Superflow. *J. Low Temp. Phys.*, **171**(5-6), 551–562 (2013).

[63] Varga, E., Babuin, S., L'vov, V. S., Pomyalov, A., and Skrbek, L. Transition to Quantum Turbulence and Streamwise Inhomogeneity of Vortex Tangle in Thermal Counterflow. *J. Low Temp. Phys.*, **187**(5-6), 531–537 (2017).

[64] Jones, E., Oliphant, T., Peterson, P., *et al.* SciPy: Open source scientific tools for Python (2001–). [Online; accessed 27.6.2018].

[65] Miles and, R. B. and Lempert, W. R. Quantitative flow visualization in unseeded flows. *Ann. Rev. Fluid Mech.*, **29**(1), 285–326 (1997).

[66] Miles, R. B., Grinstead, J., Kohl, R. H., and Diskin, G. The relief flow tagging technique and its application in engine testing facilities and for helium-air mixing studies. *Meas. Sci. Technol.*, **11**(9), 1272 (2000).

[67] Noullez, A., Wallace, G., Lempert, W., Miles, R. B., and Frisch, U. Transverse velocity increments in turbulent flow using the RELIEF technique. *J. Fluid Mech.*, **339**, 287–307 (1997).

[68] Rellergert, W. G., Cahn, S. B., Garvan, A., Hanson, J. C., Lippincott, W. H., Nikkel, J. A., and McKinsey, D. N. Detection and imaging of He_2^* molecules in superfluid helium. *Phys. Rev. Lett.*, **100**(2), 025301 (2008).

[69] Guo, W., Wright, J. D., Cahn, S. B., Nikkel, J. A., and McKinsey, D. N. Metastable Helium Molecules as Tracers in Superfluid ^{4}He. *Phys. Rev. Lett.*, **102**, 235301 (2009).

[70] Guo, W., Cahn, S. B., Nikkel, J. A., Vinen, W. F., and McKinsey, D. N. Visualization Study of Counterflow in Superfluid ^{4}He using Metastable Helium Molecules. *Phys. Rev. Lett.*, **105**, 045301 (2010).

[71] Zmeev, D. E., Pakpour, F., Walmsley, P. M., Golov, A. I., Guo, W., McKinsey, D. N., Ihas, G. G., McClintock, P. V. E., Fisher, S. N., and Vinen, W. F. Excimers He_2^* as tracers of quantum turbulence in He4 in the T=0 Limit. *Phys. Rev. Lett.*, **110**(17), 175303 (2013).

[72] Benderskii, A. V., Zadoyan, R., Schwentner, N., and Apkarian, V. A. Photodynamics in superfluid helium: Femtosecond laser-induced ionization, charge recombination, and preparation of molecular Rydberg states. *J. Chem. Phys.*, **110**(3), 1542 (1999).

[73] Berloff, N. G., Brachet, M., and Proukakis, N. P. Modeling quantum fluid dynamics at nonzero temperatures. *Proc. Natl. Acad. Sci.*, **111**(Supplement 1), 4675–4682 (2014).

[74] Stagg, G. W., Parker, N. G., and Barenghi, C. F. Superfluid boundary layer. *Phys. Rev. Lett.*, **118**(13), 135301 (2017).

[75] Koplik, J. and Levine, H. Vortex reconnection in superfluid helium. *Phys. Rev. Lett.*, **71**(9), 1375 (1993).

[76] Mongiovi, M. S., Jou, D., and Sciacca, M. Non-equilibrium thermodynamics, heat transport and thermal waves in laminar and turbulent superfluid helium. *Phys. Rep.* (2017).

[77] Holm, D. D. Introduction to hvbk dynamics. In *Quantized vortex dynamics and superfluid turbulence*, 114–130. Springer (2001).

[78] Yui, S., Tsubota, M., and Kobayashi, H. Three-Dimensional Coupled Dynamics of The Two-Fluid Model in Superfluid ^{4}He: Deformed Velocity Profile of Normal Fluid in Thermal Counterflow. *Phys. Rev. Lett.*, **120**(15), 155301 (2018).

[79] Schwarz, K. W. Three-dimensional vortex dynamics in sperfluid ^{4}He. Line-line and line-boundary interactions. *Phys. Rev. B*, **31**(9), 5782–5804 (1985).

[80] Adachi, H., Fujiyama, S., and Tsubota, M. Steady-state counterflow quantum turbulence: Simulation of vortex filaments using the full Biot-Savart law. *Phys. Rev. B*, **81**(10), 104511 (2010).

[81] Kondaurova, L., L'vov, V. S., Pomyalov, A., and Procaccia, I. Structure of a quantum vortex tangle in ^{4}HeHe counterflow turbulence. *Phys. Rev. B*, **89**, 014502 (2014).

[82] Sherwin-Robson, L. K., Barenghi, C. F., and Baggaley, A. W. Local and nonlocal dynamics in superfluid turbulence. *Phys. Rev. B*, **91**(10), 104517 (2015).

[83] Schwarz, K. Critical velocity for a self-sustaining vortex tangle in superfluid helium. *Phys. Rev. Lett.*, **50**(5), 364 (1983).

[84] Childers, R. K. and Tough, J. Helium II thermal counterflow: Temperature-and pressure-difference data and analysis in terms of the Vinen theory. *Phys. Rev. B*, **13**(3), 1040 (1976).

[85] Martin, K. and Tough, J. Evolution of superfluid turbulence in thermal counterflow. *Phys. Rev. B*, **27**(5), 2788 (1983).

[86] Musilová, V., Králík, T., La Mantia, M., Macek, M., Urban, P., and Skrbek, L. Reynolds number scaling in cryogenic turbulent Rayleigh–Bénard convection in a cylindrical aspect ratio one cell. *J. Fluid Mech.*, **832**, 721–744 (2017).

[87] La Mantia, M. Particle dynamics in wall-bounded thermal counterflow of superfluid helium. *Phys. Fluids*, **29**(6), 065102 (2017).

[88] Baggaley, A. W. and Laizet, S. Vortex line density in counterflowing He II with laminar and turbulent normal fluid velocity profiles. *Phys. Fluids*, **25**(11), 115101 (2013).

[89] Baggaley, A. W. and Laurie, J. Thermal counterflow in a periodic channel with solid boundaries. *J. Low Temp. Phys.*, **178**(1-2), 35–52 (2015).

[90] Bertolaccini, J., Lévêque, E., and Roche, P.-E. Disproportionate entrance length in superfluid flows and the puzzle of counterflow instabilities. *Phys. Rev. Fluids*, **2**(12), 123902 (2017).

[91] Lipniacki, T. Evolution of the line-length density and anisotropy of quantum tangle in ^{4}he. *Phys. Rev. B*, **64**(21), 214516 (2001).

[92] Khomenko, D., L'vov, V., Pomyalov, A., and Procaccia, I. Dynamics of the vortex line density in superfluid counterflow turbulence. *Phys. Rev. B*, **97**(1), 014508 (2018).

[93] Mendelssohn, K. and Steele, W. Quantized growth of turbulence in he ii. *Proc. R. Soc. A*, **73**(1), 144 (1959).

[94] Peshkov, V. and Tkachenko, V. Kinetics of the destruction of superf luidity in helium. *JETP Lett.*, **14**(5) (1962).

[95] Castiglione, J., Murphy, P., Tough, J., Hayot, F., and Pomeau, Y. Propagating and stationary superfluid turbulent fronts. *J. Low Temp. Phys.*, **100**(5-6), 575–595 (1995).

[96] Kafkalidis, J., Klinich III, G., and Tough, J. Superfluid turbulence in a nonuniform rectangular channel. *Phys. Rev. B*, **50**(21), 15909 (1994).

[97] Gordeev, A., Chagovets, T., Soukup, F., and Skrbek, L. Decaying Counterflow Turbulence in He II. *J. Low Temp. Phys.*, **138**(3-4), 549–554 (2005).

[98] Schwarz, K. W. and Rozen, J. R. Transient behavior of superfluid turbulence in a large channel. *Phys. Rev. B*, **44**(14), 7563–7577 (1991).

[99] She, Z.-S. and Leveque, E. Universal Scaling Laws in Fully Developed Turbulence. *Phys. Rev. Lett.*, **72**, 336 (1994).

[100] Švančara, P. and La Mantia, M. Flows of liquid ^{4}He due to oscillating grids. *J. Fluid Mech.*, **832**, 578 (2017).

[101] Sreenivasan, K. R. and Antonia, R. A. The phenomenology of small-scale turbulence. *Ann. Rev. Fluid Mech.*, **29**(1), 435–472 (1997).

[102] Benzi, R., Ciliberto, S., Baudet, C., Ruiz Chavarria, G., and Tripiccion, R. Extended Self-similarity in the Dissipation Range of Fully Developed Turbulence. *Europhys. Lett.*, **24**, 275 (1993).

[103] Mordant, N., Crawford, A. M., and Bodenschatz, E. Three-Dimensional Structure of the Lagrangian Acceleration in Turbulent Flows. *Phys. Rev. Lett.*, **93**(21), 214501 (2004).

[104] Efron, B. Nonparametric estimates of standard error: The jackknife, the bootstrap and other methods. *Biometrika*, **68**(3), 589–599 (1981).

[105] Guo, W., La Mantia, M., Lathrop, D. P., and Van Sciver, S. W. Visualization of two-fluid flows of superfluid helium-4. *Proc. Natl. Acad. Sci.*, **111**(Supplement 1), 4653–4658 (2014).

[106] Baggaley, A. W. and Barenghi, C. F. Tree method for quantum vortex dynamics. *J. Low Temp. Phys.*, **166**(1-2), 3–20 (2012).

[107] Varga, E., Barenghi, C., Sergeev, Y., and Skrbek, L. Backreaction of tracer particles on vortex tangle in helium II counterflow. *J. Low Temp. Phys.*, **183**(3-4), 215–221 (2016).

[108] Poole, D., Barenghi, C., Sergeev, Y., and Vinen, W. Motion of tracer particles in he ii. *Phys. Rev. B*, **71**(6), 064514 (2005).

[109] Kivotides, D., Barenghi, C. F., and Sergeev, Y. A. Interactions between particles and quantized vortices in superfluid helium. *Phys. Rev. B*, **77**(1), 014527 (2008).

[110] Mastracci, B. and Guo, W. Exploration of thermal counterflow in He II using particle tracking velocimetry. *Phys. Rev. Fluids*, **3**, 063304 (2018).

[111] Zhang, T. and Van Sciver, S. W. Large-scale turbulent flow around a cylinder in counterflow superfluid ^{4}he (he (ii)). *Nature Physics*, **1**(1), 36 (2005).

[112] La Mantia, M. and Skrbek, L. Quantum, or classical turbulence? *Europhys. Lett.*, **105**(4), 46002 (2014).

[113] La Mantia, M. Particle trajectories in thermal counterflow of superfluid helium in a wide channel of square cross section. *Phys. Fluids*, **28**(2), 024102 (2016).

[114] Fonda, E., Meichle, D. P., Ouellette, N. T., Hormoz, S., and Lathrop, D. P. Direct observation of kelvin waves excited by quantized vortex reconnection. *Proc. Natl. Acad. Sci.*, **111**(Supplement 1), 4707–4710 (2014).

List of Abbreviations

QT ..... Quantum Turbulence
VLD ..... Vortex Line Density
RMS ..... Root-Mean-Square
VFM ..... Vortex Filament Model
BEC ..... Bose-Einstein Condensate
RBC ..... Rayleigh-Bénard Convection
HVBK .... Hall-Vinen-Bekarevich-Khalatnikov, a continuous model of two-fluid hydrodynamics
PTV ..... Particle Tracing Velocimetry

Attachments

Complete list of publications by the author

S. Babuin, M. Stammeier, E. Varga, M. Rotter, and L. Skrbek. Quantum turbulence of bellows-driven ^{4}He superflow: Steady state, *Phys. Rev. B* 86, 134515 (2012)

S. Babuin, E. Varga, M. Stammeier, and L. Skrbek. Mechanically Versus Thermally Generated Quantum Turbulence of ^{4}He Superflow, *J. Low Temp. Phys* 171, 551–562 (2013)

E. Varga, C. F. Barenghi, Y. A. Sergeev, and L. Skrbek, Two-dimensional simulation of vortex points and tracer particles in counterflowing He-II. EPJ Web of Conferences 67, 02124 (2014)

S. Babuin, E. Varga, and L. Skrbek. The Decay of Forced Turbulent Coflow of He II Past a Grid, *J. Low Temp. Phys.* 175, 324–330 (2014)

S. Babuin, E. Varga, L. Skrbek, E. Lévêque, and P.-E. Roche, Effective viscosity in quantum turbulence: a steady-state approach. EPL 106 24006 (2014)

E. Varga, S. Babuin, and L. Skrbek , Second-sound studies of coflow and counterflow of superfluid ^{4}He in channels, *Phys. Fluids* 27, 065101 (2015)

S. Babuin, E. Varga, W. F. Vinen, L. Skrbek, Quantum Turbulence of Bellows-Driven ^{4}He Superflow: Decay, *Phys. Rev. B* 92 (18), 184503 (2015)

E. Varga, C. F. Barenghi, Y. A. Sergeev, and L. Skrbek, Backreaction of tracer particles on vortex tangle in helium II counterflow, *J. Low Temp. Phys.* 183, 215-221 (2016)

J. Gao, W. Guo, V.S. L'Vov, A. Pomyalov, L. Skrbek, E. Varga, W. F. Vinen, The decay of counterflow turbulence in superfluid 4He, *JETP Lett.* 103 (10), 732-736 (2016)

J. Gao, E. Varga, W. Guo, W. F. Vinen, Statistical Measurement of Counterflow Turbulence in Superfluid Helium-4 Using He*2 Tracer-Line Tracking Technique, *J. Low Temp. Phys.* 187 (5–6), 490–496, (2017)

E. Varga, S. Babuin, V. S. L'vov, A. Pomyalov, L. Skrbek, Transition to Quantum Turbulence and Streamwise Inhomogeneity of Vortex Tangle in Thermal Counterflow, *J. Low Temp. Phys.* 187 (5–6), 531 – 537 (2017)

S. Babuin, V.S. L'vov, A. Pomyalov, L. Skrbek, E. Varga, Coexistence and interplay of quantum and classical turbulence in superfluid 4He: Decay, velocity decoupling, and counterflow energy spectra, *Phys. Rev. B* 94(17) 174504 (2016)

J. Gao, E. Varga, W. Guo, and W. F. Vinen, Energy spectrum of thermal counterflow turbulence in superfluid helium-4, *Phys. Rev. B* 96 94511 (2017)

E. Varga, L. Skrbek, Dynamics of the density of quantized vortex lines in counterflow turbulence: Experimental investigation, *Phys. Rev. B* 97(6) 64507 (2018)

E. Varga, J. Gao, W. Guo, and L. Skrbek, Intermittency enhancement in quantum turbulence, submitted to *Phys. Rev. Fluids*, arXiv preprint arXiv:1806.11353

E. Varga, Peculiarities of spherically symmetric counterflow, submitted to *J. Low Temp. Phys.*

Selected publications of the author

1. Transition to Quantum Turbulence and Streamwise Inhomogeneity of Vortex Tangle in Thermal Counterflow
2. Quantum Turbulence of Bellows-Driven ^{4}He Superflow: Decay
3. Dynamics of the density of quantized vortex lines in counterflow turbulence: Experimental investigation
4. Intermittency enhancement in quantum turbulence
5. Backreaction of tracer particles on vortex tangle in helium II counterflow
6. Peculiarities of spherically symmetric counterflow

J Low Temp Phys
DOI 10.1007/s10909-016-1683-9

Transition to Quantum Turbulence and Streamwise Inhomogeneity of Vortex Tangle in Thermal Counterflow

E. Varga[1] · **S. Babuin**[2] · **V. S. L'vov**[3] · **A. Pomyalov**[3] · **L. Skrbek**[1]

Received: 7 July 2016 / Accepted: 19 October 2016

Abstract We report preliminary results of the complementary experimental and numerical studies on spatiotemporal tangle development and streamwise vortex line density (VLD) distribution in counterflowing ^{4}He. The experiment is set up in a long square channel with VLD and local temperature measured in three streamwise locations. In the steady state, we observe nearly streamwise-homogeneous VLD. Experimental second-sound data as well as numerical data (vortex filament method in a long planar channel starting with seeding vortices localized in multiple locations) show that the initial build-up pattern of VLD displays complex features depending on the position in the channel, but some tangle properties appear uniform along its length.

Keywords Superfluid ^{4}He · Quantum turbulence · Thermal counterflow

1 Introduction

Various aspects of quantum turbulence (QT) generated in thermal counterflow of superfluid ^{4}He has been the subject of numerous studies since the pioneering experiments and their phenomenological description of Vinen [1–4]. Along with his studies of steady-state counterflow, he was also interested in transient effects such as temporal development of temperature difference ΔT and vortex line density (VLD), based on experiments performed with two relatively large channels ($\simeq$0.5 cm) of

✉ E. Varga
varga.emil@gmail.com

1 Faculty of Mathematics and Physics, Charles University, 121 16 Prague, Czech Republic

2 Institute of Physics ASCR, Na Slovance 2, 180 00 Prague, Czech Republic

3 Department of Chemical Physics, Weizmann Institute of Science, 76100 Rehovot, Israel

Published online: 26 October 2016

constant rectangular cross section. Vinen's interesting observations, however, cannot give direct spatial information on generation of VLD, as his second-sound system detected the whole volume of the channel simultaneously. Later, depending on experimental conditions such as the applied heat load, geometry of the channel, wall material and/or roughness, a number of various scenarios of vortex tangle development were observed or theoretically predicted, from stationary turbulent plugs to propagating fronts [5–14]. Observation of turbulent fronts filling a long thin circular thermal counterflow pipe, propagating into it from both the cold and hot ends, was first claimed by Mendelssohn and Steele [5]. Many investigations followed; let us mention here detailed investigations of propagating and stationary turbulent fronts in rather narrow uniform as well as nonuniform counterflow channels performed by Tough's group (see [6] and references therein). These studies in narrow channels were based primarily on measurements of the temperature difference ΔT (and in some cases the chemical potential difference $\Delta\mu$ [7]) over the counterflow channel and therefore cannot provide direct information about the spatiotemporal development of VLD in the channel.

In order to study, the development and streamwise structure of the vortex tangle in counterflow QT, several localized probes are required. Such a setup is very difficult to realize experimentally in narrow channels of characteristic cross section below $\approx$1 mm^2, where two turbulent states, referred to as T1 and T2 have been observed—see, e. g., [7]. On the other hand, multiple turbulent states are generally not observed in channels of large cross section of order $\approx$1 cm^2. According to current understanding, the existence of multiple turbulent states is a consequence of the two fluid behavior of superfluid ^{4}He at temperatures above about 1 K, as either of its two components (or both of them, coupled with the mutual friction force) might become turbulent; the outer scale of QT, i.e., the channel dimensions, ought to play a significant role. This paper report our first results of our planned complementary experimental, theoretical and numerical studies of counterflow QT, namely on the spatiotemporal development of VLD and its streamwise distribution in counterflowing ^{4}He.

2 Experimental Setup

We have designed and manufactured an approximately 20 cm long, 7 mm-wide multipurpose channel of square cross section, sketched in Fig. 1. The channel is equipped with three second-sound sensors (labeled L1, L2 and L3 hereafter) and seven additional ports, three of which in the present experiment are mounted with thermometers (labeled T1, T2 and T3; see Fig. 1). For second-sound sensors the standard design of capacitively actuated gold-plated Nuclepore membrane is used [15] and thermometry is accomplished using commercial Ge-on-GaAs film resistors. Using this system, we are able to monitor the initial local VLD buildup. It should be noted, however, that volumes probed by the second-sound transducers are macroscopic, approximately $7 \times 7 \times 7$ mm^3. Temperature data are more local, thermometers being just over 1 mm in extent.

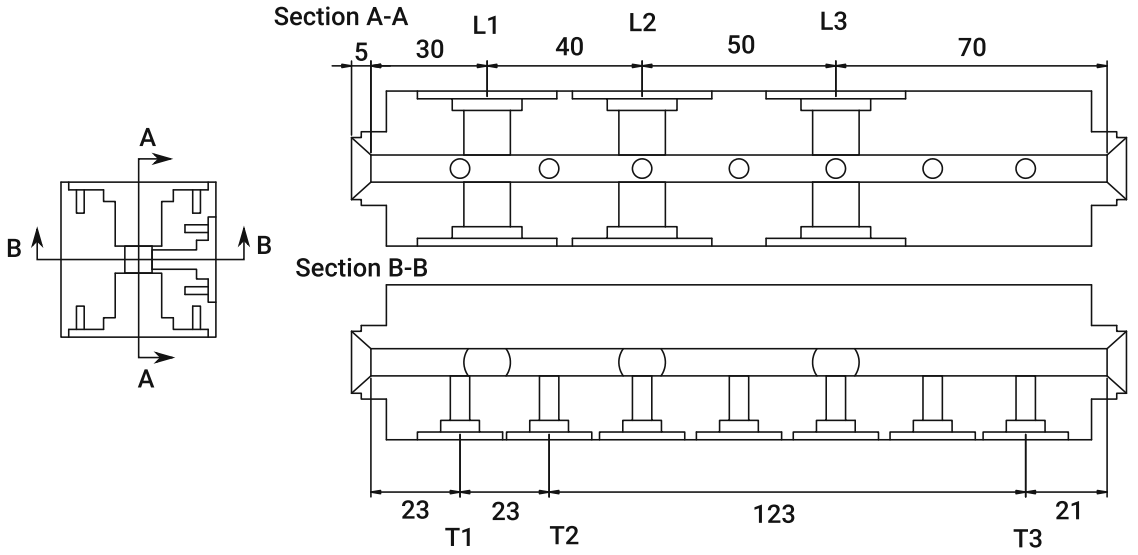

Fig. 1 *Sketch* of the counterflow channel and the positions of the probes. The width of the flow cavity itself is 7 mm. *Labels* L*n* indicate the positions of the second-sound transducers and T*n* the positions of the thermometers. The sockets on the channel, which do not have thermometers, are closed with blank holders geometrically identical to those with thermometers. The heater is mounted on the *left side* of the drawing. The drawing is to scale

3 Experimental Results

Typical growth of VLD is shown in Fig. 2. Initially a rapid transition for L1 and L2 is observed, followed by a slower, gradual increase to the eventual steady state, which is the only regime observed for L3. The initial VLD change can be either a rapid increase (L2) or decrease (L1) of VLD. A negative vortex line density means simply that the attenuation of second sound decreased from its value in quiescent helium before the flow was initiated, which is taken as a reference point. Such a transient behavior probably corresponds to a partial removal of pinned remnant vortices, or downstream drift of vortex structures, formed further upstream, which is also supported by numerical simulations below. One might notice that there is a systematic relationship between steady-state vortex line densities at the three sensor locations, namely VLD at L2 being highest, L1 being middle and L3 being lowest. This is most probably simply due to a slightly differing quality of the sensors or minor discrepancies in the channel geometry and should not be taken as an evidence for streamwise inhomogeneity of the vortex tangle.

The standard procedure for obtaining the time dependence of vortex line density is to excite the second-sound resonator at one of its resonance frequencies and to monitor the real component of the complex amplitude of the oscillations (the imaginary being zero for an ideal resonator), for example, by a lock-in amplifier. This requires that the resonance frequency does not change throughout the measurement. However, in the present experiment, we observe temperature gradients which, along the fairly long channel, can cause an appreciable temperature change (see Fig. 3a for $T = 1.3$ K) and cause the resonance peak to shift significantly (Fig. 3b) thus rendering the standard procedure no longer applicable, except at 1.65 K where the second-sound velocity depends on temperature only very weakly. A common solution is to scan the amplitude over a small frequency range for every data point. However, this introduces

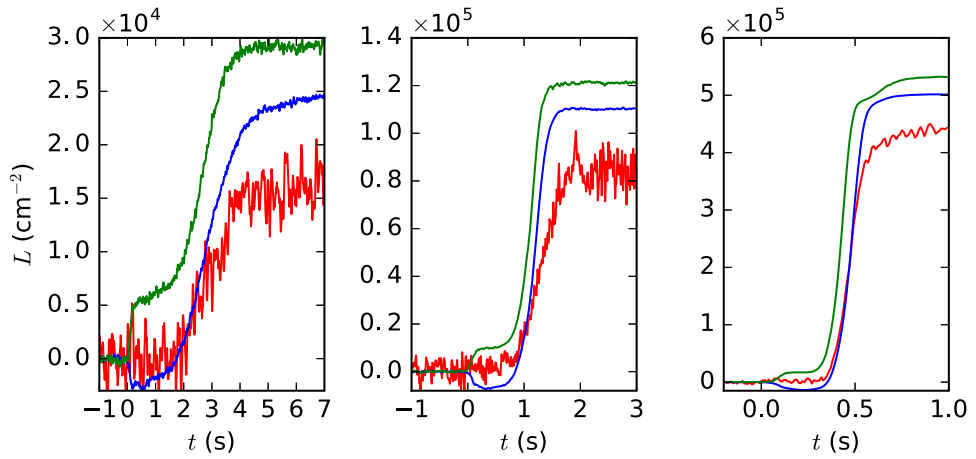

Fig. 2 Typical growth of VLD at 1.65 K. VLD at position L1: *blue* (closest to the counterflow heater, *middle line* in steady state), L2: *green* (*top* in steady state), L3: *red* (*bottom* in steady state). All curves represent pointwise averages over 100 individual events. Savitzky–Golay smoothing has been applied to L3. *Left*, *middle* and *right panels* correspond to 20, 100 and 200 mW/cm^2 heat flux, respectively (Color figure online)

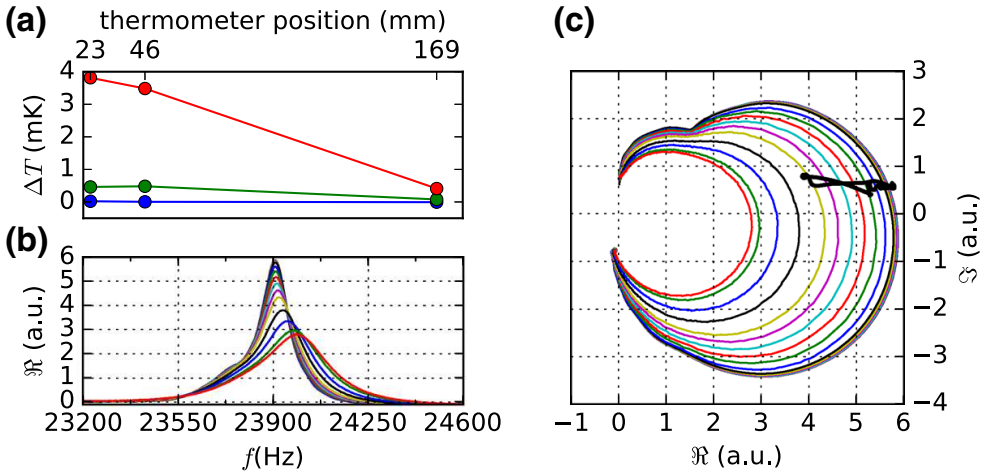

Fig. 3 The temperature shift and its effect on the second sound measurement at 1.30 K. **a** the steady-state temperature shifts across the channel for approx. 20, 100 and 200 mW/cm^2 (lines from *bottom* to *top*). **b** Shift of the second-sound resonance peak. The curves span heat fluxes from 0 to about 300 mW/cm^2. **c** Determination of the resonance amplitude using off-resonance data. "*Circles*" are the same data as in (**b**) and the *black* superimposed curve is a typical experimental run—single case of buildup and decay (Color figure online)

temporal uncertainty on the points and decreases the data acquisition rate to a point, where it would be difficult, if not impossible, to resolve fast initial transients. Additionally, in our experience, this method is not applicable to fast (<0.5 s) and large (around 50 Hz, with FWHM around 100 Hz) shifts. Therefore, we propose a different approach, illustrated in Fig. 3c. The temperature shifts are sufficiently large to shift the peak, but small enough not to cause any other significant distortion. Thus, the graphs of imaginary *versus* real component of the complex amplitude form a set of non-overlapping curves. Each of these curves has a resonance amplitude, and thus it is possible, with suitable interpolation, to assign a well-defined amplitude to points in the complex plane spanned by the measured "calibration" resonance peaks, at least roughly within the resonance linewidth. In the tails of the resonance, the sensitivity

will necessarily decrease. This way, we can determine the resonance amplitude even when exciting the resonance slightly off-peak, without sacrificing temporal resolution.

4 Numerical Simulations

It is believed that QT is generated in the channel from "seed" vortices pinned to the channel walls or from some remnant vortices in the bulk of the channel. Schwarz [10], using a local induction approximation, showed that a wall-attached vortex near the channel inlet may serve as vortex mill to seed the flow with vortices. Indeed, it was very recently shown by large-scale Gross–Pitaevskii simulations of the superfluid flow near realistic surface [16] that the critical velocity, necessary for nucleation of vortices, is easily exceeded near sharp excrescences of the surface.

4.1 Method

To understand different VLD build-up scenarios observed in the experiment, we perform numerical simulations using the vortex filament method [17]. The simulations are set up in a long plane channel of width $h = 0.1$ cm and length $H = 20\,\mathrm{h}$, which is a scaled-down analog of the experimental channel. To generate the counterflow, we impose a prescribed parabolic time-independent profile of the streamwise projection of the normal velocity $V_z^n(y)$, oriented toward positive z-direction. The applied superfluid velocity V^{s} is calculated dynamically at each time step to maintain the counterflow condition $\rho_n\langle V^n\rangle + \rho_{\mathrm{s}}\langle V^{\mathrm{s}}\rangle = 0$. Here, we use the reconnection method [18] and the line resolution $\Delta\xi = 1.0 \times 10^{-3}$ cm. Open boundary conditions are used in the streamwise z and periodic conditions in the spanwise x directions. In the wall-normal y direction, we impose $V_y^{\mathrm{s}}(\pm h) = 0$ and $\boldsymbol{s}'(\pm h) = (0, \pm 1, 0)$ at the solid walls. The details of the simulation method may be found in Refs. [19,20]. To study the buildup of VLD and to compare it with the experimental results, we calculate the streamwise VLD profile $\mathcal{L}(z)$, by accounting for the part of the lines configuration $\mathcal{C}'$ within a channel section of width $\Delta Z = 0.1$ cm, such that the channel is divided into 20 cubic sections of size $\mathcal{V}' = 0.1 \times 0.1 \times 0.1\ \mathrm{cm}^3$.

To quantify the degree of the anisotropy of the developing tangle, we use the profiles of the anisotropy indices[17]:

$$I_{\parallel}(z) = \frac{1}{\mathcal{L}(z)\mathcal{V}'}\int_{\mathcal{C}'}[1-(\boldsymbol{s}'\cdot\hat{\boldsymbol{r}}_{\parallel})^2]d\xi\ ,\ \ I_{\perp}(z) = \frac{1}{\mathcal{L}(z)\mathcal{V}'}\int_{\mathcal{C}'}[1-(\boldsymbol{s}'\cdot\hat{\boldsymbol{r}}_{\perp})^2]d\xi\ ,$$

where $\hat{\boldsymbol{r}}_{\parallel}$ and $\hat{\boldsymbol{r}}_{\perp}$ are unit vectors in the direction parallel and perpendicular to $\boldsymbol{V}^n$, respectively. In the isotropic case, we have $I_{\parallel} = I_{\perp} = 2/3$. If all vortex lines lie in planes normal to $\boldsymbol{V}^{\mathrm{n}}$, then $I_{\parallel} \approx 1$, $I_{\perp} \approx 1/2$, while in the steady-state homogeneous vortex tangle under counterflow conditions $I_{\parallel} \approx 0.8$, $I_{\perp} \approx 0.6$ [17,19,21].

To mimic the experimental situation, we use initial conditions with seeding vortex loops placed on the walls at the positions corresponding to the sensor mounting points. Additionally, some loops are placed in the bulk, reflecting the fact that the critical

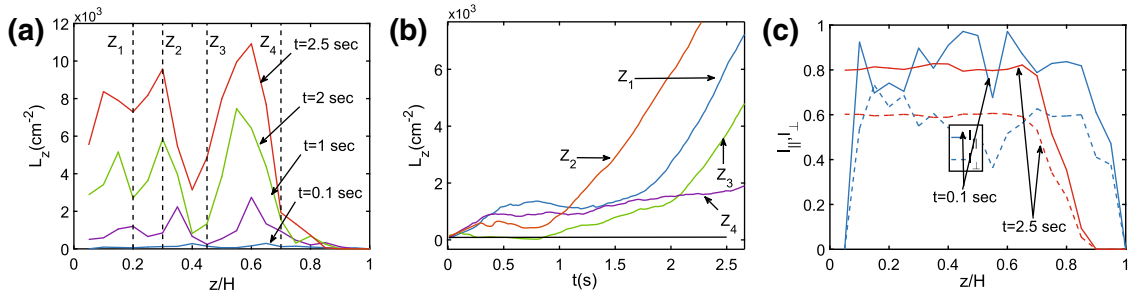

Fig. 4 The averaged vortex lines density for a realistic distribution of the seeding loops. Panel **a**: the streamwise profiles at several time moments. Panel **b**: time evolution at several locations. The *horizontal black line* marks the value of the mean initial density. Panel **c**: The anisotropy indices profiles at several time moments (Color figure online)

velocity may be reached spontaneously [16] and these loops are moving inside the channel even in the absence of thermal counterflow. Such initial conditions produce a slightly inhomogeneous initial VLD distribution along the channel, ranging between 50 and 250 cm^{-2}. To make sure that the particular choice of the initial conditions does not influence the results, we use 20 such conditions that differ by the exact position of the loops placement and their orientation. The resulting configurations are analyzed first individually, and the resulting profiles further averaged. These simulations are carried out at $T = 1.65$ K and centerline normal velocity $V^n(0) = 1.5$ cm/s.

5 Numerical Results

The averaged streamwise profiles of VLD along the channel at several time instants and the time evolution at several locations are shown in Fig. 4. The initial slight density inhomogeneity is enhanced (see panel (a)) and the initial stages of evolution are very different at different locations (panel (b)). In particular, at the position Z_3 the density is first diminished, as the nearby vortex lines group is moving downstream, but then recovered as the tangle becomes dense and starts to grow. In other three locations, the density growth includes some kind of a plateau, at a small value of $\mathcal{L}(z)$, with subsequent faster or slower growth. Different scenarios may be found at different locations. Notice that the evolution of the individual realizations is similar to the averaged, differing slightly in the exact locations of the density peaks and therefore, the positions where different growth patterns are realized.

The dynamics of the developing tangle is governed by competition between the downstream drift due to superfluid velocity and the diffusion of the vortices [9,12,14]. At $T = 1.65$ K, the superfluid velocity is sufficiently strong to cause an overall downstream drift at initial stages of the evolution. Each group of vortices initially grows across the channel, forming thin sheets of vortex lines, moving downstream parallel to each other. In Fig. 4c, we show the profiles of the anisotropy indices $I_\parallel$ and $I_\perp$ at very early stages and at later time, when the tangle becomes fully three dimensional. We see that initially the vortex lines are mostly oriented normally to the direction of the counterflow, while later the tangle becomes typically slightly oblate, but homogeneous along the entire channel.

6 Conclusions

We have experimentally probed the growth dynamics of the VLD at three locations inside a long counterflow channel of relatively large rectangular cross section. Our preliminary data, obtained at 1.65 K, clearly show that the VLD builds up at different locations almost simultaneously at variance with earlier results that the turbulent front moves from any side of the channel with either superfluid or normal mean velocities, as it was indirectly observed and claimed in long but very thin channels. The complementary numerical simulations show that the experimentally observed complex patterns of the early VLD buildup are consistent with the tangle growth from multiple localized sources of remnant vortices. Initially, the vortex loops grow preferentially across the channel. At later stages, the tangle anisotropy becomes typical for the counterflow conditions and homogenous along the channel, despite inhomogeneous streamwise distribution of VLD.

Acknowledgements This work is supported by the Czech Science Foundation under project GAČR 203/14/02005S and by the European Community Framework Programme 7, EuHIT—European High-performance Infrastructures in Turbulence, Grant Agreement No. 312778.

References

1. W.F. Vinen, Proc. R. Soc. A **240**, 114 (1957)
2. W.F. Vinen, Proc. R. Soc. A **240**, 128 (1957)
3. W.F. Vinen, Proc. R. Soc. A **242**, 493 (1957)
4. W.F. Vinen, Proc. R. Soc. A **243**, 400 (1958)
5. K. Mendelssohn, W.A. Steele, Proc. Phys. Soc. **73**, 144 (1959)
6. J. Castiglione, P.J. Murphy, J.T. Tough, F. Hayot, Y. Pomeau, J. Low Temp. Phys. **100**, 575 (1995)
7. P.J. Murphy, J. Castiglione, J.T. Tough, J. Low Temp. Phys. **92**, 307 (1993)
8. V.P. Peshkov, V.K. Tkachenko, JETP **14**, 1019 (1962)
9. H. van Beelen, W. van Joolingen, K. Yamada, Phys. B **153**, 248 (1988)
10. K.W. Schwarz, Phys. Rev. Lett. **64**, 130 (1990)
11. K.W. Schwarz, J.R. Rozen, Phys. Rev. B. **44**, 7563 (1991)
12. J.A. Geurst, Phys. A **183**, 279 (1992)
13. S.K. Nemirovskii, W. Fiszdon, Rev. Mod. Phys. **67**, 37 (1995)
14. S.K. Nemirovskii, J. Low Temp. Phys. **162**, 347 (2011)
15. S. Babuin, M. Stammeier, E. Varga, M. Rotter, L. Skrbek, Phys. Rev. B **86**, 134515 (2012)
16. G.W. Stagg, N.G. Parker, C.F. Barenghi. arXiv:1603.01165
17. K.W. Schwarz, Phys. Rev. B **38**, 2398 (1988)
18. D.C. Samuels, Phys. Rev. B **46**, 11714 (1992)
19. L. Kondaurova, V.S. L'vov, A. Pomyalov, I. Procaccia, Phys. Rev. B **89**, 014502 (2014)
20. D. Khomenko, L. Kondaurova, V.S. L'vov, P. Mishra, A. Pomyalov, I. Procaccia, Phys. Rev. B **91**, 180504(R) (2015)
21. H. Adachi, S. Fujiyama, M. Tsubota, Phys. Rev. B **81**, 104511 (2010)

Quantum turbulence of bellows-driven ^{4}He superflow: Decay

S. Babuin,[1] E. Varga,[2] W. F. Vinen,[3] and L. Skrbek[2]
[1]*Institute of Physics ASCR, Na Slovance 2, 182 21 Prague, Czech Republic*
[2]*Faculty of Mathematics and Physics, Charles University, Ke Karlovu 3, 121 16 Prague, Czech Republic*
[3]*School of Physics and Astronomy, University of Birmingham, Birmingham B15 2TT, United Kingdom*
(Received 11 December 2012; published 4 November 2015)

We report on studies of quantum turbulence with second sound in superfluid ^{4}He in which the turbulence is generated by the flow of the superfluid component through a wide square channel, the ends of which are plugged with sintered silver superleaks, the flow being generated by compression of a bellows. The superleaks ensure that there is no net flow of the normal fluid. In an earlier paper [S. Babuin *et al.*, Phys. Rev. B **86**, 134515 (2012)] we have shown that steady flow of this kind generates a density of vortex lines that is essentially identical to that generated by thermal counterflow, when the average relative velocity between the two fluids is the same. In this paper we report on studies of the temporal decay of the vortex-line density, observed when the bellows is stopped, and we compare the results with those obtained from the temporal decay of thermal counterflow remeasured in the same channel and under the same conditions. In both cases there is an initial fast decay which, for low enough initial line density, approaches for a short time the form t^{-1} characteristic of the decay of a random vortex tangle. This is followed at late times by a slower $t^{-3/2}$ decay, characteristic of the decay of large "quasiclassical" eddies. However, in the range of investigated parameters, we observe always in the case of thermal counterflow, and only in a few cases of high steady-state velocity in superflow, an intermediate regime in which the decay either does not proceed monotonically with time or passes through a point of inflexion. This difference, established firmly by our experiments, might represent one essential ingredient for the full theoretical understanding of counterflow turbulence.

DOI: 10.1103/PhysRevB.92.184503 PACS number(s): 67.25.dg, 67.25.dk, 67.25.dm

I. INTRODUCTION

In this paper we report on an experimental investigation of the decay of turbulence in a quantum fluid, superfluid ^{4}He, displaying the two-fluid behavior. The necessary introduction to superfluidity and quantum turbulence is given in the next section, together with a review on counterflow turbulence, a unique form of turbulence existing in superfluid ^{4}He, of which the superflow treated in this article represents a special case. The review sets this work into a detailed context. Here we summarize the general motivation for this project, which is twofold.

(i) We wish to continue the study of temporal decay of turbulence in quantum fluids, in the spirit of exploring similarities and differences with the decay of turbulence in classical viscous fluids, as advocated again as an important goal for the community in the latest review on the state of the field [1]. The decay of turbulence is indeed a cornerstone in classical turbulence studies because the rate of decay (of kinetic energy or vorticity) is related to the distribution of energy over the scales of the system, which constitutes a key description of a turbulent flow [2]. In quantum turbulence our experiments can accurately measure the decay of the total length of quantized vortices per unit volume, a well defined quantity which, if the detailed spatial distribution of the vortex lines is known, can be related to classical vorticity.

(ii) Our second and more specific motivation is to continue our investigation of the mechanically driven turbulent flow of the superfluid component of ^{4}He, of which we have reported the steady-flow characteristics in this journal [3]. The study of pure superflow ought to be in principle simpler than thermal counterflow because the normal component is on average at rest. In our previous work we have demonstrated that Galilean invariance holds between steady-state counterflow and superflow turbulence, i.e., that, to first order, the turbulence produced when the superfluid and normal components of ^{4}He move in opposite direction is the same as when the normal fluid is at rest and the superfluid moves past it with the same relative velocity, despite the fact that the presence of a finite channel ought to introduce differences such as a profile to the normal component. In this paper we extend this work by asking how these two turbulent flows decay in time when driving is suddenly switched off. We describe emerging similarities as well as differences, which ought to deepen our general understanding of the underlying physics of quantum turbulence, especially in relation to the dynamical state of the normal component.

II. REVIEW OF COUNTERFLOW TURBULENCE

Quantum turbulence [1,4–6] is the turbulence occurring in a superfluid such as the superfluid phases of liquid ^{4}He and liquid ^{3}He [7]. At a finite temperature superfluids exhibit two-fluid behavior, a normal viscous fluid (composed of thermal excitations) coexisting with an inviscid superfluid component. Flow of the superfluid component is strongly influenced by quantum effects, reflecting the origin of superfluidity in Bose condensation. In the case of ^{4}He superfluid flow must be irrotational, rotational motion being possible in a simply-connected volume only with the formation of topological defects in the form of vortex lines, each of which carries a circulation of $\kappa = h/m \approx 1 \times 10^{-3}$ cm^2/s, where h is Planck's constant and m is the mass of a helium atom. Turbulence in the superfluid component must therefore in general take the form of a complex tangle of vortex lines. A

purely random tangle involves turbulent energy almost entirely on only *quantum length scales*—scales comparable to, or less than, the mean vortex spacing, $\ell = L^{-1/2}$, where L is vortex line density (length of line per unit volume), although local polarization of the vortices can lead to the existence of turbulent energy on any larger scale [4,5,8]. Both purely quantum and classical features of turbulence can therefore be detected simultaneously in the same quantum flow, depending on the length scale at which this quantum flow is probed [9,10].

If vortex lines move relative to the normal fluid they experience a drag force, called mutual friction [4,5]. On *quasiclassical length scales*, i.e., scales large compared to ℓ, the superfluid component usually behaves like a classical fluid at high Reynolds number. The small kinematic viscosity of the normal fluid (of order $\kappa/6$ [11]) means that the same is true for the normal fluid on these large quasiclassical scales. Thus the two fluids can move together with the same velocity fields, mutual friction serving only to stabilize this coupled motion. The coupled fluids then behave as a single quasiclassical fluid at high Reynolds number. This situation, referred to as *coflow*, obtains quite frequently—for example when the fluid is stirred by large-scale objects similarly as for classical fluids, such as propellers [12], grids [13], flow through channels [14–17], or due to various oscillating objects [18].

On quantum length scales (even in coflow) the superfluid motion is strongly influenced by quantum effects. The coupled motion therefore cannot be maintained, the resulting dissipation due to the mutual friction, combined with viscous dissipation in the normal fluid, results in a dissipation per unit mass of helium of the form

$$\epsilon = \nu' \kappa^2 L^2, \tag{1}$$

where ν' is an effective kinematic viscosity of order κ [4,13,19–21]. This type of coupled motion, leading to quasiclassical behavior on large length scales, will usually obtain as long as there is no forced relative motion between the two fluids on these scales. We shall refer to such forced relative motion as *counterflow*. It is most easily imposed with a temperature gradient, the superfluid component moving up the gradient and the normal fluid moving down, with no net mass flow. This is one special case of counterflow, known as *thermal counterflow*.

Quite generally, by combining mechanical and thermal drive, a rich variety of counterflows, i.e., two-fluid flows with different flow ratio of the two components, can be generated, representing a very complex superfluid hydrodynamic system. In this paper, we are concerned with the special case of counterflow that can be generated by forcing helium through a tube, the ends of which are closed with superleaks—only the superfluid component can flow through the superleaks, so that the average velocity of the normal fluid vanishes. The forced flow is conveniently driven by compression of a bellows, and we refer to this type of counterflow as *bellows-driven superflow* [3], or simply *superflow*.

Early experiments on thermal counterflow [22] led to the idea that in such a flow a self-sustaining random tangle of vortex lines is generated simply by the imposed relative motion, the turbulence being essentially homogeneous, and a phenomenological equation was derived that describes the growth and decay of line density. In the steady state the line density is given in terms of the relative velocity $v = (v_s - v_n)$ by

$$L = \gamma v^2, \tag{2}$$

where γ is a temperature-dependent parameter. Confirmation of these ideas, together with an understanding of the physical processes involved, came from the pioneering computer simulations of Schwarz [23], which were improved and refined by Adachi *et al.* [24], Baggaley and Barenghi [25], and Kondaurova *et al.* [26]. These simulations were based on the vortex filament model. They assumed that the flow of the normal fluid remained laminar, and that the mean flow velocities were spatially homogeneous and in an unbounded volume. The resulting vortex tangle was disordered, so there was no large-scale turbulent motion in the superfluid component.

In Ref. [3] we reported the results of a study of the attenuation of second sound in bellows-driven steady-state superflow. According to the theories that we have described so far, the line densities observed in such an experiment should agree with those measured at the same value of v as those observed in thermal counterflow. This was indeed confirmed to a good approximation in channels of different cross sections, with the agreement being particularly good when counterflow and superflow are measured in the same (large) channel [17].

There are, however, subtle differences between counterflow and superflow, even in the steady state. Experiments have shown that there is a critical velocity below which the line density is unmeasurably small, which scales with the channel size, D. It was found to be roughly temperature independent scaling as $D^{-1/4}$ for superflow, while for counterflow it displays a D^{-1} temperature-dependent scaling [3]. Additionally, another critical velocity has been reported by Tough and his co-workers [27] in thermal counterflow, above which the γ factor suddenly increases, the so-called T1-T2 transition. The existence of this transition depends on the details of channel cross section in counterflow (according to the data reviewed by Tough [27] two states are observed if the aspect ratio is of order 1 *and* the smallest dimension is less than about 1 mm; a single state is observed if the aspect ratio is much larger than 1 or the smallest dimension is larger than 1 mm). In superflow on the contrary, in channels of different cross section, only one regime of turbulence has been observed. These facts may be related to the different dynamics of the normal component in the two systems.

Theoretical and computational work has recognized that earlier simulations were unrealistic in at least one important respect: they related to an unbounded volume of helium, and to a situation where the velocity of the normal fluid (assumed laminar) and the mean velocity of the superfluid are spatially uniform. In practice, thermal counterflow takes place almost always in a channel of finite cross section, so that, at the very least, the no-slip condition for the viscous normal fluid at a solid boundary must lead to spatial nonuniformity in the velocity of the normal fluid. Furthermore, the Reynolds number for the flowing normal fluid is typically quite large, so that it is questionable whether the flow of the normal fluid remains laminar.

The results of more realistic theoretical and computational work can be summarized as follows. The stability of

laminar normal-fluid flow has been studied by Melotte and Barenghi [28], although with assumptions that have turned out to be unrealistic (the normal-fluid velocity profile remains approximately parabolic in the presence of mutual friction, and the line density remains unperturbed and spatially uniform). The properties of the vortex tangle have been studied when the normal fluid has a prescribed laminar parabolic profile by Aarts and De Waele [29], Adachi and coauthors [24], and Baggaley and Laurie [30], and when the normal fluid has imposed on it a prescribed classical turbulent flow profile by Baggaley and Laizet [31]. In the former case the line density turns out to be quite inhomogeneous, although the spatially averaged value of γ is not seriously affected. In the latter case the value of γ is increased, suggesting that the transitions at which γ is observed to increase are associated with transitions to normal-fluid turbulence. However, this work is still unrealistic for two reasons: the motion in the two fluids, coupled by mutual friction, is not treated in a dynamically self-consistent way, and it is assumed that there is no pinning of vortex lines at a solid boundary.

We note at this point that our recent experimental work on bellows-driven superflow [3] showed that the steady-state spatially averaged line density is hardly any different from that observed in thermal counterflow at the same relative velocity v. This is in spite of the fact that the normal-fluid velocity, relative to the channel walls, is very different in the two cases. This suggests that the average line density is insensitive not only to any inhomogeneity in the vortex tangle, as suggested by simulations, but perhaps also, contrary to the simulations, to any turbulence in the normal fluid, since any turbulence in the normal fluid might be expected to be different in the two types of flow. We are led to conclude that detailed information about counterflow turbulence must come from experiments other than those that measure average line densities in steady flows: two possible directions are the direct visualization of the turbulence and a study of the decaying line density after the flow is switched off, which we pursue in our work.

On the visualization side, experiments on thermal counterflow have been reported using as tracers both micron-sized hydrogen or deuterium particles and metastable He_2 excimer molecules [32]. In the former case at relatively low heat currents bimodal distributions of vertical velocity have been first measured by Paoletti and coworkers [33], indicating that some of the particles move in the direction of the normal fluid, while others are trapped on vortices and move with the tangle, with a velocity generally different from that of the superfluid. At larger heat currents, where effects relevant to our present studies might be seen, the particles experience frequent trapping and detrapping: vertical velocity distribution changes to a monovalued one [34] and interpretation is in general harder. A wealth of statistics of particle velocity and acceleration has been produced by the Prague group in counterflow in different heat current regimes [9,10,35], showing that the character of particle dynamics changes from classical to quantum as the length scale investigated is reduced from well above to well below the intervortex separation. Additionally, there has also been some indication that vortical structures exist on scales larger than the intervortex spacing [10]. The excimer molecules instead are useful because they track only the normal fluid (at temperatures above 1 K). The use of these molecules is still at an early stage of development, but Guo and coworkers have already produced evidence that the normal fluid does become turbulent above a critical velocity [36]. Very recently, Guo's group has been studying the time evolution of thin lines of excimer molecules produced in counterflowing helium, from which they can deduce the flow of the normal fluid in greater detail [37]. We will further refer to this work in the Discussion session.

We now turn to the main topic of this paper, i.e., the decay of vortex line density in superflow and counterflow. The phenomenological Vinen equations describing the growth and decay of line density in counterflow turbulence [22] predict that the free decay should be described by the equation

$$\frac{dL}{dt} = -\frac{\chi_2 \kappa}{2\pi} L^2, \tag{3}$$

where χ_2 is a dimensionless temperature-dependent parameter proportional to mutual friction [23,38], related closely to the effective kinematic viscosity ν'. It follows that

$$L = \left[\frac{1}{L_0} + \left(\frac{\chi_2 \kappa}{2\pi} \right) t \right]^{-1}, \tag{4}$$

where L_0 is the line density at time $t = 0$. Recent simulations of Mineda *et al.* based on the assumption that counterflow turbulence is homogeneous and occurs in an unbounded medium with laminar flow of the normal fluid have confirmed this prediction [39]. However, it is now well known [22,40–44] that the experimentally observed decay is quite different. Although there is for a very short time a rapid decay that might be described by Eq. (4), the decay then slows down for a time and may actually reverse (there is a "bump" in the decay curve), while at large times the decay is observed to continue as $t^{-3/2}$ rather than as t^{-1}.

It is now widely accepted that the time dependence as $t^{-3/2}$ is associated with the decay through a quasiclassical Richardson-Kolmogorov cascade of coupled (superfluid-normal fluid) energy containing eddies, the size of which is determined by and limited by the dimensions of the containing channel [5,8,13,45]. It has been shown that this decay is described in detail by the equation

$$L(t) = \frac{D(3C)^{3/2}}{2\pi \kappa \nu'^{1/2}} (t - t_0)^{-3/2}, \tag{5}$$

where D is taken as the channel width, $C \approx 1.5$ is the classical Kolmogorov-41 constant, and t_0 denotes the virtual time origin.

The behavior described by Eq. (5) was first observed by the Oregon group in the decay of grid turbulence [46–48], where the formation of large eddies can be understood in classical terms. However, formation of large-scale classical eddies in the decay of counterflow turbulence must be less straightforward than is the case with grid turbulence. Are they formed out of large-scale eddies already present in the steady state? Or are they generated from scratch during the early stages of the decay? Presumably, the processes involved in this formation are reflected in the early stages of the decay of line density, but interpretation is hard. There has been some speculation about these early stages, particularly about the origin of the "bump" [49], to which we shall refer later, but there is as yet no agreed explanation. Further substantial progress must probably

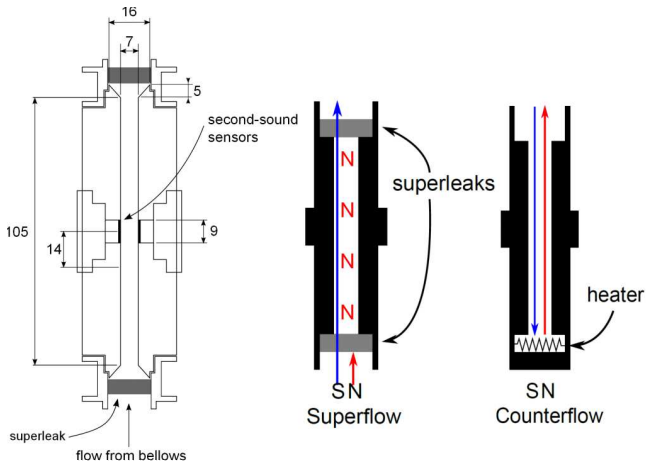

FIG. 1. (Color online) Flow channel for turbulent superflow decay studies, to scale, with dimensions in mm (left). Helium flows vertically up, provided by low-temperature bellows next to the channel. Superleak filters allow flow-through of superfluid component only. Second-sound probes measure the total length of quantized vortices per unit volume, Eq. (6). The channel can be modified to host thermal counterflow too, as illustrated by sketches on the right, where S and N stand for superfluid and normal components of He II. The channel exists in two variants, with internal square cross section 7 mm and 10 mm on a side, coded D7 and D10 in the article.

await the results of visualization experiments, perhaps backed up by more realistic numerical simulations. However, we argue that if indeed the large eddies responsible for the $t^{-3/2}$ decay are formed out of large-scale eddies present in the steady state, then bellows-driven superflow could exhibit very different features in its decay from that seen with thermal counterflow. We have therefore undertaken a study of the decay of such bellows-driven superflow with a direct comparison of thermal counterflow studied in the same channel and conditions, and we present the results in this paper. As we shall see, the two cases do indeed exhibit different forms of decay.

III. THE EXPERIMENT

A. Apparatus and method

A full description of the mechanically driven superflow apparatus and the measurement technique was given in Ref. [3]. Here we briefly recall only the essential features for convenience, focusing on the aspects more specific to the decay studies. A drawing of the flow channel is in Fig. 1. Two vertical brass flow channels have been used in this experiment. The test section is 105 mm in length and has an internal square cross section of side 7 mm and 10 mm, therefore with a factor 2 change in cross-sectional area (coded D7 and D10 in this article). The channel ends are plugged by sintered-silver superleak disks, each 2 mm thick, 16 mm diameter, with 1/2 filling fraction; these disks serve to prevent any net flow of the viscous normal component on time scales relevant to the experiment.

The superflow is driven by a low-temperature stainless steel bellows immersed in the open cryostat bath and operated through a shaft by a computer-controlled precision motor located above the cryostat at room temperature. The velocity of the flow in the channel is inferred from a measurement of the rate of compression of the calibrated bellows volume, assuming that the helium is incompressible. Counterflow is studied in the traditional way, as in previous Prague experiments [42,43]: we used the same channel of the superflow experiment (D10 only), installed it horizontally in the cryostat, removed one superleak to open the channel to the bath, and fitted the other end with a close cap which hosts a 50 Ω heater resistor (sketch in Fig. 1). The dissipated power is measured continuously, by independent measure of voltage and current.

Turbulence is detected by measuring the extra attenuation of second sound caused by scattering of normal-component thermal excitations by the vortex lines. Second sound is generated and detected by a pair of vibrating porous membranes located in the walls of the channel at its midpoint (see Fig. 1); the second sound travels across the channel, which acts as a resonator. The time-dependent attenuated amplitude of second sound at resonance $a(t)$ can be related to the instantaneous total length of quantized vortex lines per unit volume, $L(t)$, through the equation

$$L(t) = \frac{6\pi\Delta f_0}{B\kappa}\left(\frac{a_0}{a(t)} - 1\right), \tag{6}$$

where a_0 and Δf_0 are the amplitude and full width at half maximum of the second-sound amplitude resonant curve for quiescent helium, and B is the mutual friction coefficient of order unity, tabulated in Ref. [50] (the frequency dependence of B can be neglected in this experiment since we perform measurements only with a single low-frequency mode). The attenuation of second sound measures the length of vortex line per unit volume weighted by a factor $\sin^2\theta$, where θ is the angle between any element of vortex line and the direction of propagation of the second sound. To derive Eq. (6) [3], the distribution of vortex lines is assumed to be fully random and spatially uniform; the opposite limiting case where the lines are instead assumed to be fully polarized, i.e., forming vortex rings lying in planes perpendicular to the flow direction, leads to a version of Eq. (6) a factor 4/3 higher. Therefore if the real vortex line distribution is not known, the use of Eq. (6) can lead to errors in $L(t)$ of at most 33%. We will return to how this aspect may affect results during discussion.

The decay process is too fast in time to allow sampling of a full resonance curve at any point during the decay. However, our studies of the steady state have shown that the second-sound resonant frequency is not significantly affected by the extra attenuation, so that it is sufficient to set the second-sound frequency on resonance and observe this resonant response as a function of time, as shown in Fig. 2. This response accurately reflects the changing attenuation only if the natural response time of the second-sound resonator (of order the inverse linewidth) is sufficiently short; in practice Δf^{-1} is about 10 ms at the start of the decay and about 100 ms for quiescent helium, values that are small enough for our purposes. Amplitude times series are sampled at 60 Hz, and each sample is averaged with a lock-in amplifier with time constant of 10 ms. Temperature control in our cryostat is of order 0.1 mK, therefore sufficient to ensure that temperature drift cannot cause significant drift away from resonance, as we have experimentally verified.

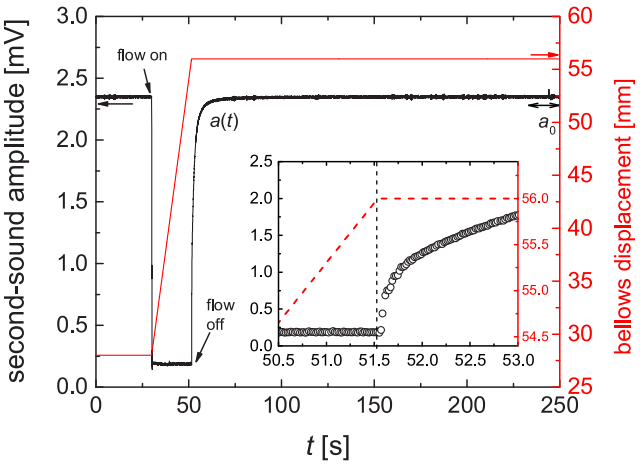

FIG. 2. (Color online) Example of a single raw measurement of superflow turbulence decay in D7 channel, at $T = 1.26$ K. The second-sound amplitude $a(t)$ (black solid line) is plotted as a function of time. At $t = 0$ helium is quiescent, at $t = 30$ s a steady flow of velocity 11.3 cm/s is produced by the bellows, and at $t = 51.5$ s it is suddenly switched off, resulting in the following decay. The reference signal a_0 entering the calculation of vortex line density, Eq. (6), is the average of the last 20 s of the amplitude signal. The red solid line (right axis) shows the bellows displacement. Inset: A zoom around the switch-off time, showing that the second sound reacts immediately after the halting of the drive. Time resolution of our measurements is about 16 ms.

To create a turbulent steady state, the bellows are compressed at a constant rate for about 20 s (Fig. 2), after which compression is suddenly stopped. The position of the movable end of the bellows is recorded by the motor encoder, which shows that sudden stopping is achieved in less than 10 ms (inset). The decay of line density is followed for 200 s, after which the amplitude of the second-sound signal has reached a statistically steady value; a further 30 s is allowed to elapse before a new measurement is made. The second-sound amplitude before and long after the steady flow was observed to be generally slightly different. This effect—related to a varying remanent amount of vortex line in the sample—is studied statistically in Sec. III B and has some bearing on the interpretation of results. It is not clear whether the beginning or the end of the amplitude time series ought to be used for a_0 in Eq. (6): we calculate it averaging the last 20 s. The measurement protocol for thermal counterflow decays is very similar.

The parameter space covered by the experiment is summarized in Table I. We have performed mechanically driven superflow and thermally driven counterflow decay measurements, in the two channels D7 and D10, in the temperature range between 1.25 K to 2.10 K, and for initial steady-state line densities, L_0, spaced almost exactly one decade apart: 10^6 cm^{-2}, 10^5 cm^{-2}, and 10^4 cm^{-2} (we shall refer to the decay curves corresponding to these initial line densities as $L6$, $L5$, and $L4$). The table shows the corresponding superflow and counterflow velocity in the steady state, with experimental uncertainty of 3%.

For every combination of temperature and starting line density we have measured typically 150 individual decays, under nominally identical experimental conditions, and we have ensemble-averaged these samples, by linearly interpolating each one onto a 100 Hz time series and averaging pointwise. Decay signals are checked individually and rare anomalous ones are discarded from averaging. The improvement of the averaged signal with respect to a single sample is demonstrated in Fig. 3. Averaging over a large ensemble has proven essential

TABLE I. Overview of the parameter space explored by the experiment. Steady-state line density and corresponding mean superflow and counterflow velocity, shown per temperature and channel width (7 mm and 10 mm side of square cross section).

		Mechanical superflow		Thermal counterflow
		D7	D10	D10
T (K)	L_0 (cm^{-2})	v_s (cm/s)	v_s (cm/s)	v_{ns} (cm/s)
1.25	10^6	11.3	/	/
	10^5	3.6	4.25	/
	10^4	/	1.3	/
1.45	10^6	7.7	7.4	8.45
	10^5	2.6	2.7	3.0
	10^4	0.86	1.0	1.0
1.65	10^6	5.7	5.3	7.1
	10^5	1.9	2.0	2.5
	10^4	0.57	1.0	0.9
1.75	10^6	4.9	/	/
	10^5	1.7	/	/
	10^4	0.6	/	/
2.10	/	/	/	/
	10^5	0.4	/	1.50
	10^4	0.15	/	0.51

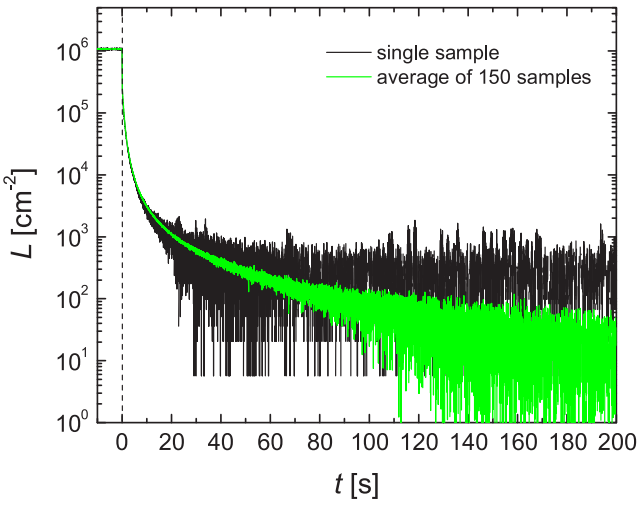

FIG. 3. (Color online) Demonstration of the improvement of signal-to-noise ratio by ensemble average of 150 decay samples. Data relate to pure superflow, D7, $T = 1.26$ K, L6. The noisier signal in solid black line is a single sample randomly chosen from the batch of 150. Time is rescaled here, with $t = 0$ marking the instant when the bellows stops. On the y axis is the vortex line density calculated from the data in Fig. 2 via Eq. (6). The average signal only looks noisy at late times because it averages to zero and is plotted in logarithmic scale. We can resolve 6 orders of magnitude in decay of vortex line density.

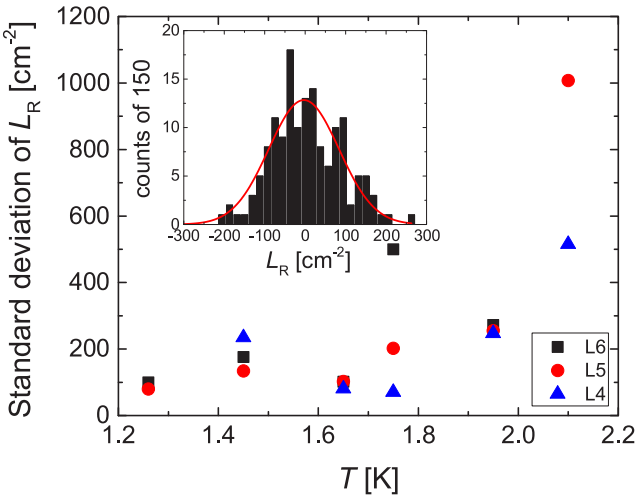

FIG. 4. (Color online) The dependence of the standard deviation of the remanent vortex line density L_R (vortex lines remaining in the channel after a decay process) with temperature and steady-state line density. Data relate to the D7 channel, D10 being similar. L_R is calculated with Eq. (7) and its standard deviation is typically from a batch of 150 decays. The distribution of L_R in a typical batch (here L5 at $T = 1.65$ K) is shown inset, roughly with a Gaussian distribution with zero mean.

for our study, allowing us to resolve 6 orders of magnitude of decay on L.

B. The remanent vortex line density

Our second-sound attenuation technique cannot provide an absolute measurement of vortex line density, because the reference second-sound signal a_0 in Eq. (6) may itself be attenuated by remanent vortex lines persisting in quiescent helium after the turbulence has decayed. Vortex lines are indeed expected to survive because they pin effectively to any surface, due to their Å-size core [1]. The absolute vortex line density in our sample is therefore $L_{\rm abs} = L_{\rm rem} + L$, where $L_{\rm rem}$ is the nonmeasurable remanent density of vortex lines hidden in a_0. However, $L_{\rm rem}$ is expected to be negligibly small compared to L during most of the decay. An estimate provided by the work of Awschalom and Schwarz [51] leads to $L_{\rm rem} = 72$ cm^{-2} and 36 cm^{-2} for the D7 and D10 channels, respectively. What the experiment can access, however, is the *variation* of L in the quiescent state between one decay and another, which constitutes a measurement of the remanent vorticity above the unmeasurable $L_{\rm rem}$ floor. We calculate this quantity as

$$L_R = L_{\rm start} - L_{\rm end}, \tag{7}$$

where this difference is obtained from the change in average amplitude of the second-sound signal averaged over a period of 20 s in the quiescent states before and after the imposition of a flow. We have studied the distribution of L_R in the batch of 150 decays across all parameter space. An example for D7, $T = 1.65$ K, and L5 is given in the inset of Fig. 4, showing roughly a Gaussian distribution centered around zero; this distribution is common to all batches. Notice that L_R can be positive or negative, and that the extent of its variation cannot be accounted for by changes in helium temperature from one decay to another (which are too small for this effect); therefore we attribute this effect to varying remanent vortex line density in the sample. The standard deviation of this distribution, SD(L_R), is given in the main plot of Fig. 4 as a function of T and L_0 for the D7 channel, D10 being similar. From this we learn that SD(L_R) is not correlated to L_0 and that with the exception of the points at $T = 2.1$ K where measurements are more difficult, it varies from about 100 cm^{-2} to 300 cm^{-2}. We guess therefore that an upper limit on the absolute remanent vortex line density in the sample is roughly SD(L_R).

We do not know precisely what effect remanent vortices might have on the rate of decay of a vortex tangle, compared to a decay where vortex lines are totally annihilated, a condition which, as we have explained, cannot be achieved experimentally due to pinning. However we have indication that when the counterflow heat current is reduced not to zero, but to a finite subcritical value, the decay shape is somewhat affected (Fig. 7); this suggests that the decay rate may be affected by the amount of residual vortices. A detailed study of these effects was carried out for thermal counterflow [22] and we plan a similar approach for mechanical superflow.

In addition to these effects a further complication for interpretation arises at low densities: for $T < 2$ K our averaged estimated residual density SD(L_R) ≈ 250 cm^{-2} corresponds to a ratio of line separation to channel width of about 0.1 in D7, at which wall effects might well start to be important. For these combined reasons, we think it wise to consider our results only up to times for which $L \gtrapprox$ SD(L_R), despite the fact that our ensemble-average curves resolve a longer decay process. For example, for the decay in Fig. 3 for which SD(L_R) ≈ 100 m^{-2} we would limit our consideration up to about $t = 90$ s. This is taken into account in the rest of the article.

IV. EXPERIMENTAL RESULTS

An overview of the first 10 s of all our experimentally observed superflow decays in the D7 and D10 channels is shown in Figs. 5 and 6, respectively. Each panel groups decays from the same initial density and different temperature. These plots serve to demonstrate the main features of the decays at a glance; details on shorter and longer time ranges will be presented in due course. An overview of the full time range in log-log coordinates is available for D7 in the Supplemental Material [52], with D10 being similar. Each decay shown here in Figs. 5 and 6 displays an initial fast rate (see also Fig. 8 for details) which expires within roughly 0.5 and 2 s depending on conditions, followed by a slower process which continues for a longer time (see also Figs. 9 and 11 for details). For short-time behavior, we notice that qualitatively but systematically the ratio of L_0 to L_x at which the fast process changes to a slow process decreases with L_0 for fixed T, and increases with T for fixed L_0, in both channels. The time at which L_x occurs increases systematically with decreasing L_0 for fixed T and increases with T for fixed L_0.

In D10-L6 only (Fig. 6, left panel), the fast and slow regimes are joined by an intermediate one, with an inversion of the decay rate, i.e., a change of sign of dL/dt. In D10-L5 at $T = 1.25$ K, instead, we observe only a slow down of the decay rate without an increase in L, but with the presence

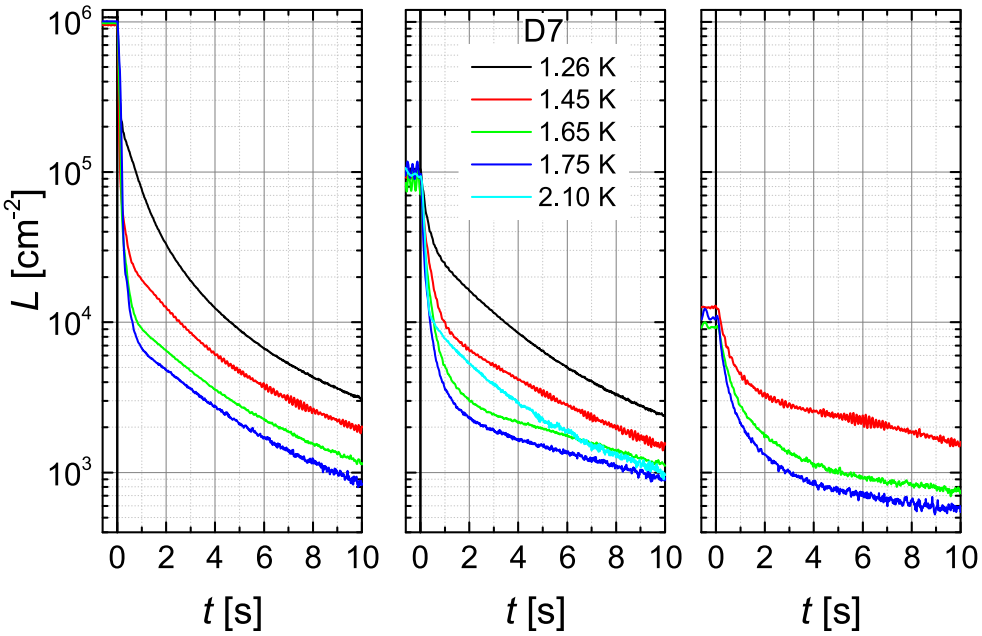

FIG. 5. (Color online) Decay of vortex line density of pure superflow turbulence. Plots of L (in log scale) versus t for the D7 channel, at different temperatures. Each panel groups decays from the same steady-state density, at different temperatures.

of a point of inflexion across which d^2L/dt^2 changes sign. We shall refer henceforth to these features as a "bump" in the decay curve. For simplicity we shall call "bump" both the increase in L during the decay and the presence of a point of inflexion, and we shall be more specific when needed. The bump, observed only in these few circumstances in superflow, is instead seen always in counterflow in the stricter sense of nonmonotonic behavior, as demonstrated in Fig. 7 and the related Supplemental Material [52]. The existence of a nonmonotonic bump in counterflow was already detected in earlier experiments [42–44] and here, within the range of investigated parameters, we confirm it. There were however instances in past experiments, including the ones just cited, when a point of inflexion was observed instead of nonmonotonic behavior, as in the first experiments on the decaying thermal counterflow by Vinen [22] or more recently

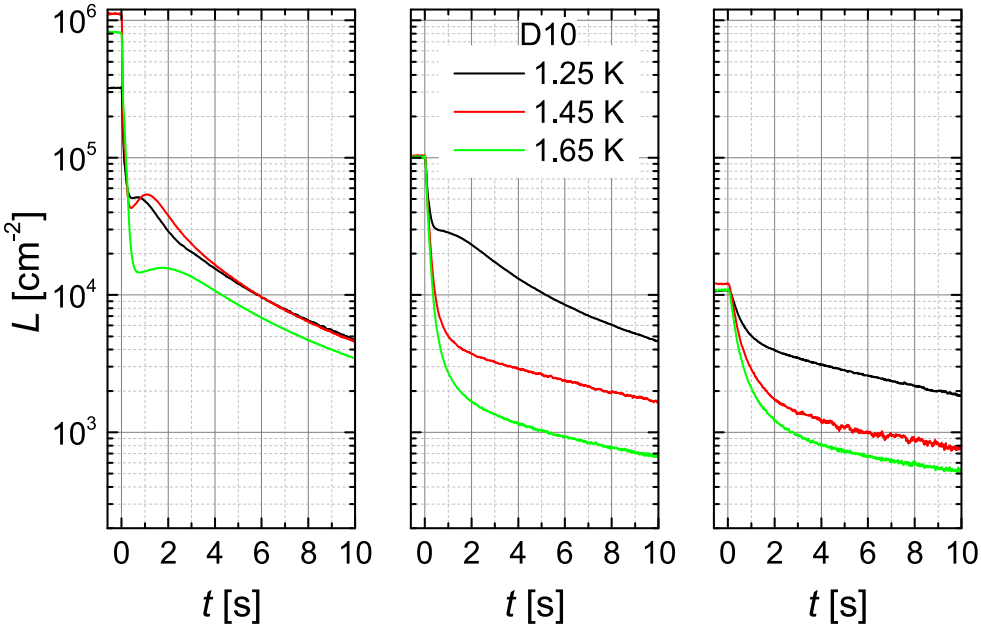

FIG. 6. (Color online) Decay of vortex line density of pure superflow turbulence, as in Fig. 5 but for channel D10. Features are similar to D7, except that L6 curves display a short nonmonotonic behavior and the L5 curve at 1.25 K has a change in the decay rate with a point of inflexion. This feature, referred to in the text as a "bump," is an exception in superflow decay and the rule in counterflow decay, shown in later figures.

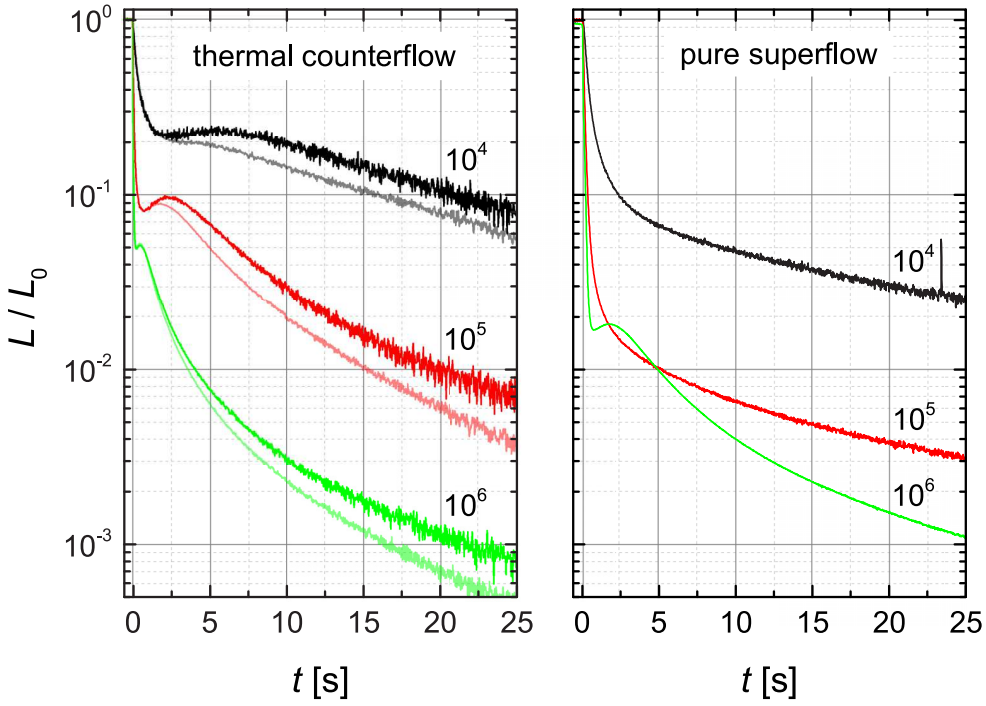

FIG. 7. (Color online) Comparison of decays observed for thermal counterflow with those observed for bellows-driven superflow for different initial line densities, at the same temperature, $T = 1.65$ K, and in the same channel, D10. Line densities are normalized to the initial line densities. For counterflow, lighter lines correspond to decays when the heat current was reduced to a subcritical value of 10 mW. The temporary increase in vortex line density during decay (the "bump") is observed systematically in thermal counterflow, but only in the D10 channel and at high density in mechanical superflow. Similar plots at $T = 1.45$ K are in the Supplemental Material [52], including also the thermal counterflow decay at $T = 2.10$ K which does not have a counterpart in superflow for the same channel size.

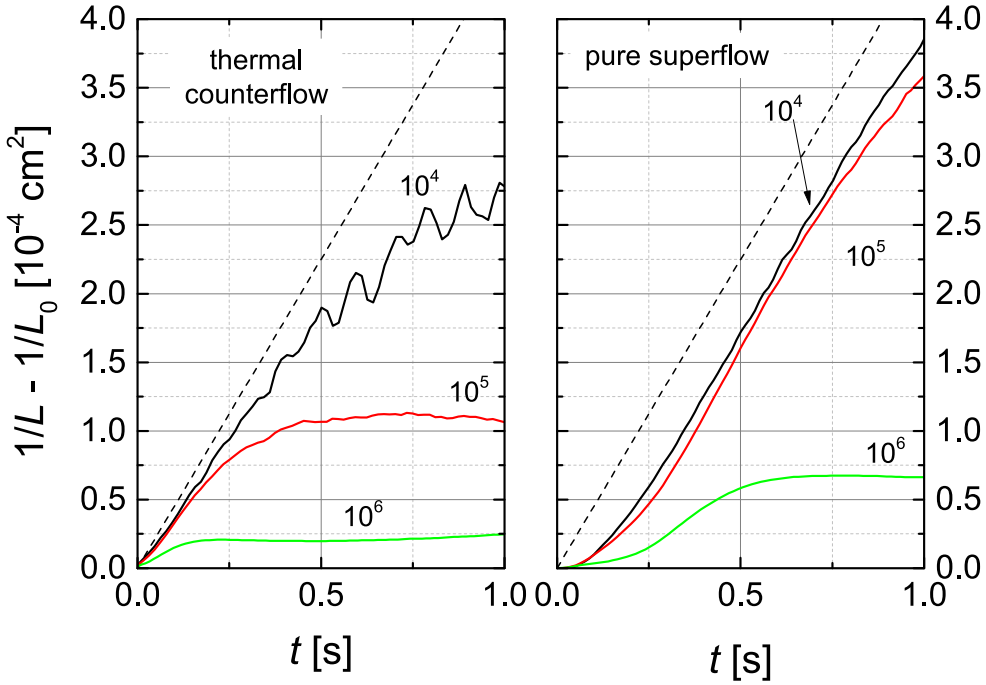

FIG. 8. (Color online) Comparison of decays observed for thermal counterflow with those observed for bellows-driven superflow for different initial line densities at very small times for $T = 1.65$ K. Plots of $1/L - 1/L_0$ against t according to Eq. (8). The Vinen decay of a random tangle is observed for a very short transient and is followed more closely by mechanical superflow than thermal counterflow, and, in both cases, by decays originating from lower densities. (The $T = 1.45$ K data are in the Supplemental Material [52].)

TABLE II. Values of $\kappa\chi_2/2\pi$ obtained averaging the values computed by Schwarz [23] and those given by the theory of Vinen and Niemela [4]. This quantity occurs in Eq. (8) which is plotted in Fig. 8.

T (K)	$\kappa\chi_2/2\pi$ (cm^2 s^{-1})
1.25	2.2×10^{-4}
1.45	3.1×10^{-4}
1.65	4.5×10^{-4}
1.75	5.3×10^{-4}
2.10	9.3×10^{-4}

in the Prague decays [42,43], for decays originating from steady-state counterflow generated by larger heat fluxes than reached here. What Fig. 7 adds to previous studies is high statistics for counterflow (ensemble average of 150 decays instead of single curve, i.e., the same standards as for our superflow) and, especially, the fact that we can compare superflow and counterflow strictly under the same conditions: channel, temperature, and initial vortex line density.

Figure 7 shows that the bump in counterflow is broadened with decreasing L_0, and that in superflow it occurs only for L6, although the details of the decay remain different in the two cases. The lighter curves in the left panel are decays when the heat current is reduced, not to zero, but to a small value (10 mW) below the critical value for transition to quantum turbulence. The idea here was to observe whether leaving a subcritical heat current in the channel may help in reducing the level of residual vortex lines, "washing them away," in the spirit of the systematic study in Ref. [22]. While we did not observe a change in the residual second-sound attenuation at the end of the decay process, we did measure differences during the rest of the decay, as shown. At late times the line density is lower in the case of nonzero heat current, and the "bump" is somewhat reduced.

Let us now focus on the fast initial decay regime observed at short times, emphasized in Fig. 8 for counterflow and superflow in D10 at $T = 1.65$ K. In the figure we compare this decay regime with the prediction of the Vinen model in Eq. (4) relating to the decay of a fully random tangle unbounded by walls, by recasting the equation as follows:

$$\frac{1}{L} - \frac{1}{L_0} = \left(\frac{\chi_2\kappa}{2\pi}\right)t, \tag{8}$$

where the quantity $\kappa\chi_2/2\pi$ is given in Table II. We notice that the Vinen decay is not generally observed, and when it exists, is followed for only a very short time, at most 1 s. The pure superflow is more Vinen-like than the counterflow, and departures increase with increasing L_0 in both cases. The situation is similar at other temperatures, with departure from Vinen behavior increasing with decreasing temperature and increasing initial density (data at $T = 1.45$ K are provided as Supplemental Material [52]). In Fig. 8 we notice also that the decay does not start abruptly as predicted by Eq. (4), but there is some rounding immediately after $t = 0$. This rounding is more pronounced in superflow than in counterflow, lasting at most some 200 ms, with the tendency to increase with initial line density. This latter fact leads us to favor the explanation that the rounding may be an instrumental effect. The switching off of counterflow is controlled fully electronically, while the bellows is a mechanical system which may introduce secondary lagging effects. Although the bellows motor encoder at room temperature does show that the system comes to rest to within 10 ms (Fig. 2), the actual flow may not stop abruptly, for reasons such as finite compressibility, the finite time for expiration of pressure gradients (which would increase with bellows velocity as observed), the expiration of thermal gradients occurring because of the presence of superleaks causing an increase of temperature in the bellows and a decrease in the channel due to change in superfluid/normal density ratio (see Ref. [3] for more detailed discussion), and so on. In principle however one should not exclude the possibility that the flow actually stops at $t = 0$ and therefore the rounding would be explained by some incompleteness of the model in Eq. (4). At any rate, our time resolution of ≈ 16 ms, limited by the intrinsic physics of second-sound resonance, does not allow us to study this physical process in greater depth. We therefore concentrate on the decay process after the first, say, 100 ms have elapsed.

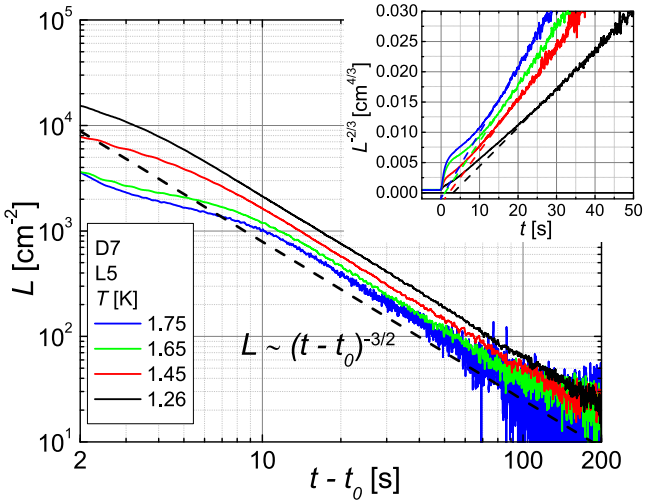

FIG. 9. (Color online) Superflow decay in the D7 channel from initial line density $L_0 = 10^5$ cm^{-2} at different temperatures. In the main plot L and t are plotted in logarithmic axis, demonstrating that superflow decays with the power law $L \propto (t - t_0)^{-3/2}$ (dashed line) for a very large fraction of time, except for the first few seconds, according to the quasiclassical single fluid decay model in Eq. (5). The x axis requires the subtraction of the virtual time origin t_0 obtained from the inset, as described in the text. Similar plots from different initial density and for the D10 channel are in the Supplemental Material [52] and confirm the same conclusions.

The situation at late times is summarized in Fig. 9, for the case of superflow in D7, with starting density L5 at different temperatures (D10 version in the Supplemental Material [52]). Although we know from Sec. III B that we should handle with care the decay process when L becomes comparable with or smaller than its mean remanent value, in this figure we demonstrate that a single power law of the form $L \propto (t - t_o)^{-3/2}$ represents the data from the first few seconds to the end of the range. This is the behavior predicted by the quasiclassical model in Eq. (5).

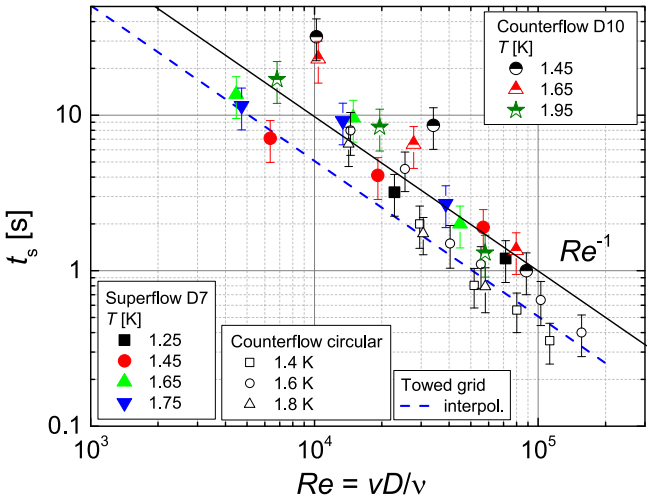

FIG. 10. (Color online) The time for the onset of $L \propto t^{-3/2}$ behavior (saturation time; see text) as a function of the flow's Reynolds number. The present experiments are compared with an older Prague thermal counterflow experiment in a round channel [42] and with the Oregon towed grid experiments (the dashed line is an interpolation of their experimental points) which measures the turbulence decay behind a moving grid [48].

Since Eq. (5) has a virtual time origin t_0, this must be subtracted from the time axis in a logarithmic plot. To estimate it we recast Eq. (5) as follows:

$$\frac{1}{L^{2/3}} = \frac{(2\pi)^{2/3}\kappa^{2/3}\nu'^{1/3}}{3CD^{2/3}}(t - t_0), \tag{9}$$

and obtain t_0 as the intercept of the linear part of the plot with the time axis, as demonstrated in the inset of Fig. 9 by dashed lines.

Another characteristic time of the decay process, often discussed in literature, is the time at which the $t^{-3/2}$ behavior onsets, i.e., the "saturation time" t_s ["saturation" refers to the attainment of the condition of large eddies reaching their maximum size limited by the channel width D, required in deriving Eq. (5)]. This time is plotted for different flows in Fig. 10 against the Reynolds number, defined with the mean velocity v, the channel width D, and the kinematic viscosity of the normal component ν, following Ref. [42]. Allowing for some scatter, all experiments produce roughly a scaling $t_s \propto \mathrm{Re}^{-1}$.

We continue the analysis of the late-time behavior by contrasting superflow and counterflow in Fig. 11, for the same temperature, $T = 1.65$ K, and channel, D10, observing that in both cases there is linear range as predicted by Eq. (9) extending as far as 80 s; the similar $T = 1.45$ K case is in the Supplemental Material [52]. This equation also predicts that (i) curves from different initial densities should have the same slope: our data confirm this. (ii) The slope should scale as $D^{-2/3}$: despite the fact that we have only two channel sizes, we checked this prediction and found that experimental slopes scale by a substantially larger extent than expected. In these two respects therefore our results differ from the prediction.

Fitting Eq. (9) to the linear part of the curves in Fig. 11 allows us to extract the effective viscosity ν', as is customarily done [13,19,20]. In Fig. 12, together with the data from the decay of turbulence past the towed grid [53], we thus plot $\nu'(T)$ for all our flows. The effective viscosity measured from decays starting from different vortex line density L_0 is found to slightly vary, but in a manner uncorrelated with L_0. In any case, we do not expect ν' to be dependent on L_0 because we understand ν' to be a robust property of the flow independent of flow details, as is shown by consistent values coming from different decay experiments [20] and

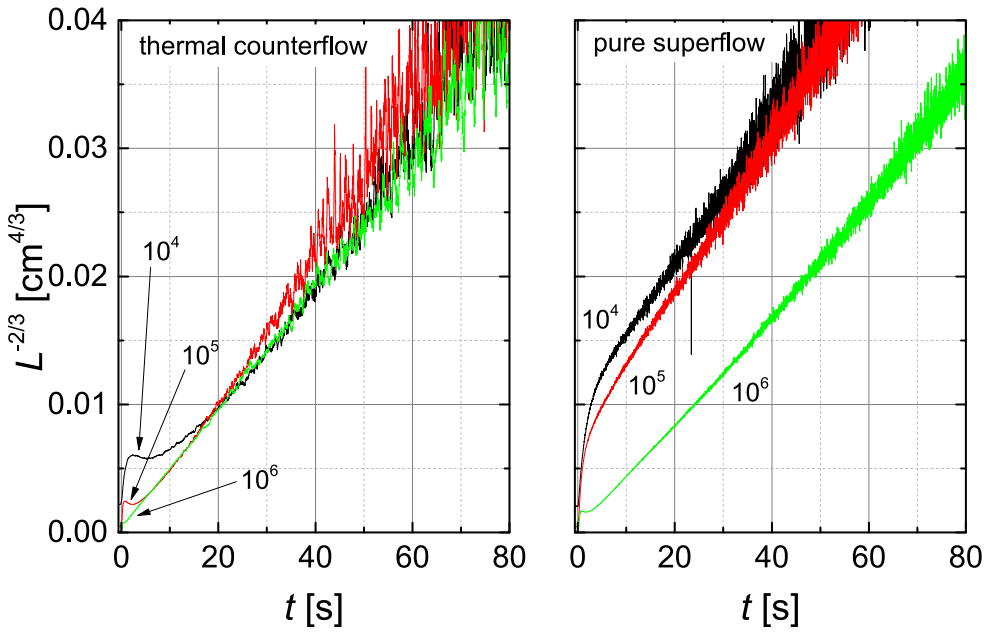

FIG. 11. (Color online) Comparison of decays observed for thermal counterflow with those observed for bellows-driven superflow for different initial line densities at $T = 1.65$ K in D10. Plots of $L^{-2/3}$ against t as according to Eq. (9). Linear behavior corresponds to the quasiclassical $L \propto t^{-3/2}$, observed in both flows. The $T = 1.45$ K version is in the Supplemental Material [52].

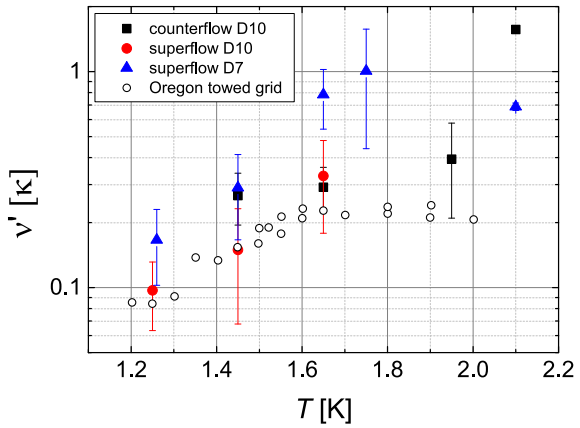

FIG. 12. (Color online) The effective viscosity of the "quasiclassical" model [Eq. (5)] as a function of temperature. For our three experiments, at each given temperature, ν' has been averaged from decays of different initial density (L4, L5, and L6), resulting in the shown error bars. For comparison we add also data from the Oregon towed grid experiment [53].

also from steady flows, hence from an entirely independent approach [54]. For these reasons, we think it justified to average ν' originating from different L_0—which is reflected in the error bars in Fig. 12. We notice that, despite the data from the three experiments at the same temperature being roughly consistent within error bars, the superflow data for D10 lie systematically lower than those for D7, which puts pressure on the understanding that ν' should not depend on flow details. At any rate, as we have discussed in our works which include determination of effective viscosity [16,54], the absolute value of ν' obtained from decay measurements can have uncertainties up to a factor of 4, depending on how strictly the assumption on saturation of the large eddies' size obtains. Accurate experimental determination of ν' to better than a factor of 4 remains therefore still a challenge.

V. DISCUSSION

All our experimentally observed decays, both in superflow and counterflow, have an initial regime when the line density drops rapidly (for sufficiently low density it approaches for a short time the Vinen law $L \propto t^{-1}$, especially in superflow), and a final slower regime of the form $L \propto t^{-3/2}$. The first, fast regime, lasts at most 1 s (Fig. 8) and is responsible for the loss of a large fraction of vortex lines, even up to about 99% (see, e.g., the $T = 1.75$ K curve in Fig. 5, left panel). The fact that the decay rate increases with increasing temperature for fixed initial density may be due to rising value of the prefactor $\kappa\chi_2/2\pi$ in Eq. (3) with temperature, as shown in Table II, which in turn must be related to the increase in mutual friction. The second, slow regime lasts for the majority of the decay process and causes the loss of the remaining vortex lines (except the remanent ones).

We have compared our observations with two available analytic models: (i) the Vinen equation for a random tangle, and found it to apply in a limited regime, and (ii) the quasiclassical model for the decay of large eddies, and found it to apply more generally although not fulfilling all predictions.

Our results generally confirm the understanding [19,55,56] that a general quantum turbulence tangle consists of an random system of vortex lines which decays fast by mutual annihilation of lines, a fraction of which is organized in bundles giving rise to eddies of various sizes, up to sizes comparable to the channel width, which decay more slowly. Alternatively, we can imagine there being a more spatially homogeneous regime with an energy spectrum that is Kolmogorov in form except for an initially enhanced energy at wave numbers close to the inverse vortex line spacing; i.e., a situation in which the density of vortex lines is initially larger than is necessary for the dissipation of energy, given by Eq. (1), at the rate required to match the flow of energy down the Kolmogorov cascade. Our experiment cannot establish unequivocally whether these eddies exist already in the steady state, although evidence that they do exist comes from visualization of counterflow turbulence both from tracing solid particles [10] and imaging the normal component [36,37].

What is not predicted by the existing analytic models is the occurrence of the "bump," i.e., the change of sign in dL/dt or d^2L/dt^2 between the fast and slow regimes, which we have observed always in thermal counterflow and as an exception in superflow. The second-sound attenuation can become increased during decay for one, or for a combination of two, reasons: (i) the line length stays approximately constant but it is spatially rearranged so that the second sound "sees" a greater fraction (recall that second sound is attenuated only by the projection of vortex lines onto a plane perpendicular to second sound's propagation direction), or (ii) the spatial orientation stays fixed but the line length increases.

The possibility of (i) has been confirmed numerically by Barenghi *et al.* [44,49] for spatially rearranged random tangles, but although the simulation gave a qualitative result in agreement with observations, the vortex line density in the simulation was about an order of magnitude below the lowest available experimentally. We note nevertheless that the observed height of the bump is never greater than can be accounted for by this mechanism (33%). On the other hand, this effect was not observed in the simulations of Mineda and coworkers [39], based on more realistic line densities. However, neither of these simulations takes account of the possibility that the vortex tangles with which we are dealing are polarized in such a way that large-scale eddy motion is superimposed on the random tangle.

Option (ii) is also physically possible, and to build an argument for it we note that in our measurements the bump occurs always in thermal counterflow and only at high steady-state velocities in superflow. This suggests that the dynamical state of the normal component (laminar, unstable, or turbulent) might be relevant to the existence or not of the bump, since the average velocity of the normal component relative to the walls varies significantly in the two systems: it can be rather large in the case of thermal counterflow, but it is nominally zero in the case of superflow. We note however that, as suggested in Ref. [3], from considerations on the scaling of critical velocity with channel width from different experiments, the normal component is probably not at rest in superflow in a large channel, but is set in motion by mutual friction, the spatially averaged velocity remaining zero. Nevertheless this motion may be relatively slow in comparison with that in thermal

counterflow, except at large superflow velocities. But just how would the motion of the normal component cause the decay inversion? The recent results from the Tallahassee group [37], where the normal component is tracked by the excimer molecules, give evidence that the normal component at a sufficiently high heat current becomes turbulent (specifically at $T = 1.83$ K for a heat current above $q_c = 80$ mW/cm^2 at which $L_0 \approx 10^4$ cm^{-2}). The second order structure functions calculated from the normal fluid turbulent velocity fluctuations extend over a fairly large range of lengths scales, up to a sizable fraction of the channel size. The structure function can be related to a turbulent energy spectrum of the form $E(k) \propto k^{-2}$ in the steady state (where k is the wave number). During the decay the spectrum changes gradually, within about 3 seconds, into the Kolmogorov form $E(k) \propto k^{-5/3}$. It seems possible that the bump is associated with this evolution. We are currently exploring this idea with a model for the temporal evolution of the energy spectrum, and this work will be reported in a future publication. Further experimental evidence that the bump is associated with transition to turbulence in the normal component would come by testing thermal counterflow at heat currents below the transition. In our system this would mean to study decays from initial density sufficiently below $L_0 = 10^4$ cm^{-2}, which constitutes a direction for future work.

VI. CONCLUSIONS

We have presented a comprehensive picture of the temporal decay of vortex line density in quantum turbulence produced by mechanically driven superflow through two square channels of 7 and 10 mm on a side. We have covered a broad parameter space in temperature ($1.25 \leqslant T \leqslant 2.10$ K) and in steady-state vortex line density ($10^4 \leqslant L \leqslant 10^6$ cm^{-2}). Additionally, at $T = 1.45$ K and $T = 1.65$ K and for all the same initial densities, we have provided, for the first time, a direct comparison of mechanical superflow and thermal counterflow, the latter performed in the same 10 mm wide channel used for superflow and under exactly the same experimental conditions. This, together with enhanced accuracy achieved thanks to ensemble averaging of up to 150 individual decays, placed us in a strong position to compare these flows.

In an unbound system superflow and counterflow ought to display identical physics since they are related by Galilean invariance. In practice, the presence of channel walls will change the physics, at least for the normal component which must acquire a profile due to viscous drag with the walls. This has been indeed confirmed experimentally by visualizing the normal fluid flow profile using helium excimer molecules, observed to turn from laminar to turbulent as heat current increases [37]. Additionally, we know from numerical simulations [31,38,57] that the normal fluid profile induces inhomogeneity in the distribution of vortex lines across the channel width, with the density being enhanced in the case of turbulent normal fluid profile. Our experiments with steady-state superflow have shown that when comparing with other counterflow experiments with channels of different size [3] and also when measuring in our own superflow channel adapted for counterflow [17], the line density for a given relative velocity is essentially insensitive to the normal component net flow. This is not so for the decay.

The decay of these two flows is similar in that both display an initial fast process where most of the line density is lost which for sufficiently low density has the form $L \propto t^{-1}$, and a subsequent slow $L \propto t^{-3/2}$ process where the rest of the tangle decays. These two processes have been associated respectively with the decay of the randomized and polarized components of the tangle. The key difference however is that in counterflow we invariably observed an inversion of the decay rate between the two regimes, which we observed only at high steady-state velocities in the wider channel in superflow. This fact, firmly established by high-statistics measurements, indicates that the dynamical state of the normal component in the steady state (no net flow through the channel in superflow and turbulent pipe flow in counterflow) has consequences for the decay of the tangle. We have speculated about the reasons, but further work is required if these reasons are to command confidence. We hope that this comprehensive set of experimental data describing the vortex tangle decay in superflow and counterflow will stimulate the development of a still missing full theory of counterflow turbulence.

ACKNOWLEDGMENTS

We thank M. Stammeier for his help in the early stages of this experimental research. This work was supported by GAČR GA14-02005S.

[1] C. F. Barenghi, L. Skrbek, and K. R. Sreenivasan, Proc. Natl. Acad. Sci. USA **111**, 4647 (2014).
[2] H. Tennekes and J. L. Lumley, *A First Course in Turbulence* (The MIT Press, 1972).
[3] S. Babuin, M. Stammeier, E. Varga, M. Rotter, and L. Skrbek, Phys. Rev. B **86**, 134515 (2012).
[4] W. F. Vinen and J. J. Niemela, J. Low Temp. Phys. **128**, 167 (2002).
[5] L. Skrbek and K. R. Sreenivasan, Phys. Fluids **24**, 011301 (2012).
[6] S. K. Nemirovskii, Phys. Rep. **524**, 85 (2013).
[7] D. R. Tilley and J. Tilley, *Superfluidity and Superconductivity*, 3rd ed. (Institute of Physics Publishing, Bristol and Philadelphia, 1990).
[8] W. F. Vinen, Phys. Rev. B **61**, 1410 (2000).
[9] M. La Mantia and L. Skrbek, Europhys. Lett. **105**, 46002 (2014).
[10] M. La Mantia and L. Skrbek, Phys. Rev. B **90**, 014519 (2014).
[11] V. S. L'vov, L. Skrbek, and K. R. Sreenivasan, Phys. Fluids **26**, 041703 (2014).
[12] J. Maurer and P. Tabeling, Europhysics Lett. **43**, 29 (1998).
[13] L. Skrbek and K. R. Sreenivasan, in *Ten Chapters in Turbulence*, edited by P. A. Davidson, Y. Kaneda, and K. R. Sreenivasan (Cambridge University Press, 2013).
[14] J. Salort, B. Baudet, B. Castaing, F. Chabaud, T. Daviaud, P. Didelot, B. Diribarne, Y. Dubrulle, F. Gagne, A. Gauthier, B. Girard, B. Hebral, B. Rousset, P. Thibault, and P. E. Roche, Phys. Fluids **22**, 125102 (2010).

[15] D. S. Holmes and S. W. Van Sciver, J. Low Temp. Phys. **87**, 73 (1992).
[16] S. Babuin, E. Varga, and L. Skrbek, J. Low Temp. Phys. **175**, 324 (2014).
[17] E. Varga, S. Babuin, and L. Skrbek, Phys. Fluids **27**, 065101 (2015).
[18] W. F. Vinen and L. Skrbek, in *Progress in Low Temperature Physics*, Vol. 14, Chap. 4 (Elsevier, Amsterdam, 2008).
[19] P. Walmsley, D. Zmeev, F. Pakpour, and A. I. Golov, Proc. Natl. Acad. Sci. **111**, 4691 (2014).
[20] T. V. Chagovets, A. V. Gordeev, and L. Skrbek, Phys. Rev. E **76**, 027301 (2007).
[21] L. Boué, V. S. L'vov, Y. Nagar, S. V. Nazarenko, A. Pomyalov, and I. Procaccia, Phys. Rev. B **91**, 144501 (2015);
[22] W. F. Vinen, Proc. R. Soc. **240**, 114 (1957). **240**, 128 (1957); **242**, 493 (1957); **243**, 400 (1958).
[23] K. W. Schwarz, Phys. Rev. B **18**, 245 (1978); Phys. Rev. Lett. **50**, 364 (1983); Phys. Rev. B **31**, 5782 (1985); **38**, 2398 (1988).
[24] H. Adachi, S. Fujiyama, and M. Tsubota, Phys. Rev. B **81**, 104511 (2010).
[25] A. W. Baggaley and C. F. Barenghi, J. Low Temp. Phys. **166**, 3 (2012).
[26] L. Kondaurova, V. L'vov, A. Pomyalov, and I. Procaccia, Phys. Rev. B **89**, 014502 (2014).
[27] J. T. Tough, in *Progress in Low Temperature Physics*, Vol. VIII (North-Holland, Amsterdam, 1982).
[28] D. J. Melotte and C. F. Barenghi, Phys. Rev. Lett. **80**, 4181 (1998).
[29] R. G. K. M. Aaarts and A. T. A. M. De Waele, Phys. Rev. B **50**, 10069 (1994).
[30] A. W. Baggaley and J. Laurie, J. Low Temp. Phys. **178**, 35 (2014).
[31] A. Baggaley and S. Laizet, Phys. Fluids **25**, 115101 (2013).
[32] W. Guo, M. La Mantia, D. P. Lathrop, and S. W. Van Sciver, Proc. Natl. Acad. Sci. USA **111**, 4653 (2014).
[33] M. S. Paoletti, R. B. Fiorito, K. R. Sreenivasan, and D. P. Lathrop, J. Phys. Soc. Jpn. **77**, 111007 (2008).
[34] T. Chagovets and S. Van Sciver, Phys. Fluids **23**, 107102 (2011).
[35] M. La Mantia, D. Duda, M. Rotter, and L. Skrbek, J Fluid Mech. **717**, R9 (2013).
[36] W. Guo, S. B. Cahn, J. A. Nikkel, W. F. Vinen, and D. N. McKinsey, Phys. Rev. Lett. **105**, 045301 (2010).
[37] A. Marakov, J. Gao, W. Guo, S. W. Van Sciver, G. G. Ihas, D. N. McKinsey, and W. F. Vinen, Phys. Rev. B **91**, 094503 (2015).
[38] D. Khomenko, L. Kondaurova, V. S. L'vov, P. Mishra, A. Pomyalov, and I. Procaccia, Phys. Rev. B **91**, 180504R (2015).
[39] Y. Mineda, M. Tsubota, and W. F. Vinen, J. Low Temp. Phys. **171**, 511 (2013).
[40] K. W. Schwarz and J. R. Rozen, Phys. Rev. B **44**, 7563 (1991).
[41] K. W. Schwarz and J. R. Rozen, Phys. Rev. Lett. **66**, 1898 (1991).
[42] L. Skrbek, A. V. Gordeev, and F. Soukup, Phys. Rev. E **67**, 047302 (2003).
[43] A. V. Gordeev, T. V. Chagovets, F. Soukup, and L. Skrbek, J. Low Temp. Phys. **138**, 549 (2005).
[44] C. F. Barenghi and L. Skrbek, J. Low Temp. Phys. **146**, 5 (2007).
[45] L. Skrbek and S. Stalp, Phys. Fluids **12**, 1997 (2000).
[46] M. R. Smith, R. J. Donnelly, N. Goldenfeld, and W. F. Vinen, Phys. Rev. Lett. **71**, 2583 (1993).
[47] S. R. Stalp, L. Skrbek, and R. Donnelly, Phys. Rev. Lett. **82**, 4831 (1999).
[48] L. Skrbek, J. J. Niemela, and R. J. Donnelly, Phys. Rev. Lett. **85**, 2973 (2000).
[49] C. F. Barenghi, A. V. Gordeev, and L. Skrbek, Phys. Rev. E **74**, 026309 (2006).
[50] R. J. Donnelly and C. F. Barenghi, J. Phys. Chem. Ref. Data **27**, 1217 (1998).
[51] D. D. Awschalom and K. W. Schwarz, Phys. Rev. Lett. **52**, 49 (1984).
[52] See Supplemental Material at http://link.aps.org/supplemental/10.1103/PhysRevB.92.184503 for more information.
[53] J. J. Niemela, K. R. Sreenivasan, and R. J. Donnelly, J. Low Temp. Phys. **138**, 537 (2005).
[54] S. Babuin, E. Varga, L. Skrbek, E. Leveque, and P. E. Roche, Europhys. Lett. **106**, 24006 (2014).
[55] A. W. Baggaley, J. Laurie, and C. F. Barenghi, Phys. Rev. Lett. **109**, 205304 (2012).
[56] P. E. Roche and C. F. Barenghi, Europhysics Lett. **81**, 36002 (2008).
[57] S. Yui and M. Tsubota, Phys. Rev. B **91**, 184504 (2015).

Dynamics of the density of quantized vortex lines in counterflow turbulence: Experimental investigation

E. Varga and L. Skrbek
Faculty of Mathematics and Physics, Charles University, Ke Karlovu 3, 121 16, Prague 2, Czech Republic

(Received 6 December 2017; published 12 February 2018)

Recently the interest in thermal counterflow of superfluid ^{4}He, the most extensively studied form of quantum turbulence, has been renewed. Particularly, an intense theoretical debate has arisen about what form, if any, of the so-called Vinen equation accurately captures the dynamics of vortex line density, L. We address this problem experimentally, in a 21 cm long channel of square 7×7 mm^2 cross section. Based on large statistics of second-sound data measured in nonequilibrium square-wave modulated thermally induced counterflow we investigate the phase portrait of the general form of the governing dynamical equation and conclude that for sparse tangles ($L \lesssim 10^5$ cm^{-2}) all proposed forms of this equation based on the concept of a homogeneous random tangle of quantized vortices provide equally adequate descriptions of the growth of L, while for dense tangles ($L > 10^5$ cm^{-2}) none of them is satisfactory or able to account for the significant slow-down in tangle growth rate as the steady state is approached. We claim, however, that agreement with theory is recovered if the geometrical parameter c_2 introduced in numerical studies by K. W. Schwarz [Phys. Rev. B **38**, 2398 (1988)] is allowed to vary with vortex line density which also greatly improves the prediction of the observed early decay rate.

DOI: 10.1103/PhysRevB.97.064507

I. PREFACE

Thermal counterflow of superfluid ^{4}He represents the first and most extensively studied form of quantum turbulence [1–3]. Despite that, a number of open problems and unanswered questions remain that ought to be tackled both theoretically and experimentally, such as the existence and role of large vortical structures and their visualization [4–7], forms and interplay of energy spectra [8–12] in the superfluid and normal components constituting at finite temperature the superfluid ^{4}He and appropriate boundary conditions [13] for their velocity fields, small-scale universality [14], or possible relations between classical and quantum convective heat transport [15].

Recently an intense theoretical debate has arisen about what form, if any, of the so-called Vinen equation accurately captures the dynamics of vortex line density (VLD) [16–18], which motivates us to tackle this problem experimentally. Using a purposefully designed flow channel where counterflow is repeatedly generated by rectangular heat pulses and probed by second-sound attenuation we demonstrate that experimental approach is fruitful. Indeed, we find that for relatively dilute vortex tangles all proposed forms of the Vinen equation [16,19] provide adequate descriptions of its growth rate, while for dense tangles they fail and cannot account for the significant slow-down in tangle growth rate as the steady state is approached. We report data analysis that shows the way to resolve this problem, by allowing the geometrical coefficient, introduced in the theory of Schwarz [20], connecting rms curvature of quantized vortices and VLD, to depend on the VLD. Surprisingly, the observed decay rate occurring after switching off the heat is then predicted well by the observed turbulence growth rate.

The paper is organized as follows: After the introduction, Sec. II, we in Sec. III describe our experimental arrangement and in Sec. IV we present our experimental results and discuss the dynamics of the vortex tangle based on the phase portrait using a coordinate system motivated by the general form of the governing dynamical equation, prior to drawing conclusions in the last section.

II. INTRODUCTION

Normal liquid ^{4}He (He I), when cooled below the $T_\lambda \simeq 2.17$ K, undergoes a second-order phase transition; the low-temperature phase is known as He II. The physical properties of He II cannot be described by classical physics; it is a quantum fluid displaying extraordinary physical properties such as superfluidity and the two-fluid behavior. Phenomenologically, He II is described by the two-fluid model as consisting of two components: (i) viscous normal fluid of density ρ_n, carrying all the entropy content, and (ii) inviscid superfluid of density ρ_s; the total density of He II $\rho = \rho_n + \rho_s$. While at T_λ He II is entirely normal, in the zero-temperature limit there is no normal fluid; for many practical purposes He II can be thought of as entirely superfluid below about 1 K. In the limit of low velocities, He II supports two independent velocity fields $\mathbf{v}_n(\mathbf{r},t)$ and $\mathbf{v}_s(\mathbf{r},t)$; both components can easily become turbulent. Due to quantum-mechanical restrictions the otherwise potential flow of the superfluid component is violated on line singularities—cores of singly quantized vortices. Superfluid turbulence, i.e., turbulence in the superfluid component, therefore consists of a tangle of vortices carrying a single circulation quantum $\kappa \approx 9.97 \times 10^{-8}$ m^2/s each.

Quantum turbulence [3,21], defined as turbulence in quantum fluids displaying superfluidity, was first considered as a theoretical possibility by Feynman [22] and experimentally studied and theoretically described by Vinen [19,23–25] in

a peculiar thermally induced flow of He II called thermal counterflow, which can be easily set up by applying a voltage to a resistor (heater) located at the closed end of a channel of cross-section area A open to a helium bath at the other end. The heat flux $\dot{Q}$ is carried away (mean velocity v_n) from the heater by the normal fluid alone, and, by conservation of mass, i.e., $v_n\rho_n + v_s\rho_s = 0$, a superfluid current (mean velocity v_s) arises in the opposite direction. In this way a relative (counterflow) velocity $v_{ns} = |v_n| + |v_s|$, proportional to the applied heat flux, is created along the channel. Upon exceeding a critical value of v_{ns}, extrinsic vortex nucleation originating from the always present remnant vorticity leads to creation of a vortex tangle—superfluid turbulence in the superfluid component of He II.

Vinen introduced for the description of counterflow turbulence a phenomenological model based on the concept of a random vortex tangle characterized by the approximately homogeneous VLD, L. Apart from the size of the vortex core $\xi \cong 10^{-10}$ m, there is only one characteristic length scale: the quantum length scale $\delta \cong L^{-1/2}$, the mean distance between quantized vortices in the tangle. He argued that L (which is a measurable quantity with the dimensions of length per volume) obeys the equation of general form

$$\frac{dL}{dt} = F(L; v_{ns}) = \left(\frac{\partial L}{\partial t}\right)_{prod} - \left(\frac{\partial L}{\partial t}\right)_{dec}; \qquad (1)$$

i.e., the dynamics of VLD is understood as the interplay between two processes one of which acts to create the VLD and the other to destroy it. With the particular form of the production and decay terms this equation has been known as Vinen's equation

$$\frac{dL}{dt} = \alpha_V v_{ns} L^{3/2} - \beta_V L^2, \qquad (2)$$

where α_V and β_V are parameters, α_V being proportional to the mutual friction parameter α tabulated in Ref. [26]. In his original study [19] Vinen admitted that other forms of Eq. (2) cannot be excluded and an alternative production term, quadratic in v_{ns}, has been suggested that accounted for the experimental observation with sufficient accuracy. For detailed theoretical discussion of possible forms of Eq. (1) we direct the reader to the review of Nemirovskii and Fiszdon [27].

Recently the interest in Eq. (1) describing the dynamics of L in counterflow turbulence has been renewed and resulted in an intense theoretical debate between the L'vov's group [16,17] and Nemirovskii [18]. Theoretical analysis and numerical experiments based on nonhomogeneous counterflow led Khomenko *et al.* [16] to suggested yet another form of Eq. (1) and claimed that, while satisfying the quadratic $L \propto v_{ns}^2$ relation, it better describes the numerical data for a counterflow possessing a particular artificial flow profile.

In general, the various proposed forms of the Vinen equation can be written as

$$\frac{dL}{dt} = C_n v_{ns}^n L^{2-n/2} - D_n L^2, \qquad (3)$$

where $n = 1,2$ for the original or alternative Vinen equation and $n = 3$ for the equation of Khomenko *et al.* [16], and C_n, D_n are adjustable parameters suitable for the given model. For steady state, the equation of the form of Eq. (3) predicts that $L \propto v_{ns}^2$ regardless of the exponent n. This relation has been experimentally verified many times not only for counterflow turbulence (see reviews [27,28] and references to original papers therein), but more recently also for steady state of pure superflow in relatively wide channels with ends blocked by superleaks allowing the net through-flow of the superfluid component only [29].

The first theory which attempted to connect microscopic equations of motion of a quantized vortex with the dynamics of VLD is that of Schwarz [20,30]. It is based on the mesoscopic picture of superfluid turbulence developed by him—the vortex filament model [20,30,31], describing the quantized vortices as infinitesimally thin lines with no internal structure. This model led to successful pioneering numerical simulations (which were later significantly advanced by several groups [32–34]) of quantum turbulence and is still in common use today [35]. In the so-called local induction approximation (LIA)—an approximation where the long-range interaction between the vortices is ignored—the model leads to an analytical prediction of the dynamical equation [20]

$$\frac{dL}{dt} = \alpha I_l v_{ns} L^{3/2} - \beta\alpha c_2^2 L^2, \qquad (4)$$

where

$$\beta = \frac{\kappa}{4\pi} \ln\left(\frac{1}{c_1 L^{1/2}\xi}\right), \qquad (5)$$

with ξ the vortex core size, I_l one of the anisotropy indices introduced by Schwarz [20], and c_1, c_2 the geometrical coefficients connecting the mean $\bar{S}$ or rms $\tilde{S}$ curvature of the vortices in the tangle with the VLD: $\bar{S} = c_1 L^{1/2}$, $\tilde{S} = c_2 L^{1/2}$. It should be noted that recent analysis [17,36] of a general inhomogeneous counterflow in the framework of the vortex filament model suggests that the situation might be more complicated, with closures being necessary for new separate fields of anisotropy or the curvature. In particular, even though Eq. (4), as written, suggests that $n = 1$, the closure necessary for, say, I_l might change this. For completeness we note that, formally, Eq. (3) with $n = 1$ coincides with Eq. (4) for $C_1 = \alpha I_l$ and $D_1 = \beta\alpha c_2^2$.

Several experimental works in the past have studied the dynamics of VLD in (particularly free) decay of thermal counterflow. These studies are complicated by the appearance of nonmonotonic behavior (commonly called a "bump"). This feature is presently outside the scope of this article, but is thought to be connected with the redistribution of energy across scales in the coupled system of normal fluid turbulence and the vortex tangle and the formation of classical energy cascade observed in late decay [9,10].

We believe that from the point of view of the intrinsic tangle dynamics a more suitable approach is to study transitions between two turbulent states, especially the growth part. Growth of VLD in a previously quiescent helium can go through complex evolution probably connected to sudden advection of remnant vorticies pinned to the wall [37]. Additionally, growth from nonzero VLD does not seem to exhibit the nonmonotonic behavior common in the decay. Lastly, the theories of VLD dynamics should work equally well in the turbulence growth but have received little testing in this regime [38]. Following Schwarz and Rozen [38], our goal is therefore to experimen-

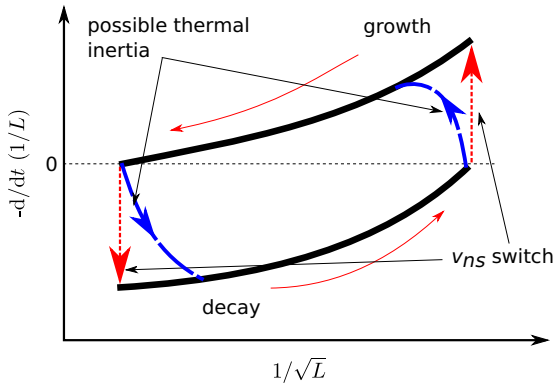

FIG. 1. Idealized sketch of the phase portrait of VLD according to Eq. (6) for sharp changes in the heat flux. See Sec. III for the explanation of the indicated possible thermal inertia.

tally test the proposed models of the dynamics of VLD using transients between two well-defined turbulent states of thermal counterflow, with the emphasis on the growth of turbulence.

In order to study the dynamics, one can compare the experimentally observed time evolution of $L(t)$ with the solution of the appropriate differential equation. The solutions to the proposed Eq. (3) are, however, very similar and difficult to distinguish. Plus, this path *a priori* restricts the possible functional forms of F in Eq. (1) with little justification. A more direct way of studying the dynamics is to look at the phase portrait (i.e., a set of trajectories in the phase space) of $L(t)$. A straightforward choice of phase space would be (L, $\dot{L}$), where the dot denotes differentiation with respect to time. However, a slight manipulation of Eq. (3) gives us a much simpler expression on the right-hand side:

$$-\frac{d}{dt}\left(\frac{1}{\ell}\right) = L_0 D_n\left[\left(\frac{1}{\sqrt{\ell}}\right)^n - 1\right], \tag{6}$$

where $\ell(t) = L(t)/L_0$ is a dimensionless VLD and $L_0 = (C_n/D_n)^{n/2}\, v_{\rm ns}^2$ is the steady-state VLD corresponding to the instantaneous counterflow velocity $v_{\rm ns}$. Motivated by this simple functional form we chose to work with the phase space $(\frac{1}{\sqrt{\ell}}, -\frac{d}{dt}(\frac{1}{\ell}))$. The physical meaning of these axes is the rate of change of the average (dimensionless) area occupied by a vortex (intervortex spacing squared) as a function of (dimensionless) intervortex spacing. The Schwarz equation, Eq. (4), in these variables reads

$$-\frac{d}{dt}\left(\frac{1}{\ell}\right) = \alpha\beta c_2^2 L_0\left(\frac{1}{\sqrt{\ell}} - 1\right). \tag{7}$$

An expected form of a phase trajectory of VLD according to Eq. (6) or (7) for sharply switching counterflow velocity between two turbulent steady states is sketched in Fig. 1.

Note that the dimensionless VLD defined as $\ell = L/L_0$ is unsuitable for free decay due to the fact that $L_0 = 0$. For decays we therefore define the dimensionless VLD: $\tilde{\ell} = L/L_i$ where L_i is the initial VLD from which the decay starts. This definition leads to only a small modification of Eq. (6)

$$-\frac{d}{dt}\left(\frac{1}{\tilde{\ell}}\right) = L_0 D_n\left[\left(\frac{v_{\rm ns}}{v_{\rm ns}^{\rm i}}\right)^n\left(\frac{1}{\sqrt{\tilde{\ell}}}\right)^n - 1\right], \tag{8}$$

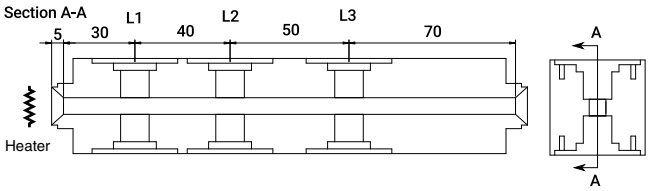

FIG. 2. A sketch of the geometrical arrangement of the channel. The figure is to scale. The counterflow is created by a resistive heater placed at one end of the channel (left end of the channel in the figure). The channel is positioned vertically, with the heater at the bottom, and placed in a bath cryostat. The heater is approximately 1 cm from the channel entrance inside a detachable small brass enclosure which is connected to the main channel cavity and sealed against the bath through an indium o-ring.

where $v_{\rm ns}$ is the instantaneous counterflow velocity and $v_{\rm ns}^{\rm i}$ is the one that produced $L_{\rm i}$. In a similar way, Eq. (7) becomes

$$-\frac{d}{dt}\left(\frac{1}{\tilde{\ell}}\right) = \alpha\beta c_2^2 L_0\left(\frac{v_{\rm ns}}{v_{\rm ns}^{\rm i}}\frac{1}{\sqrt{\tilde{\ell}}} - 1\right). \tag{9}$$

In the following we drop the $\tilde{\ell}$ notation because dimensionless growth and decay curves are never shown together.

III. EXPERIMENTAL ARRANGEMENT

The counterflow turbulence we study is set up in a brass channel of square cross section $A = 7 \times 7$ mm^2 sketched in Fig. 2. The channel length is approximately 21 cm. The counterflow is generated using a resistive heater of about 50 Ω. During the experiments the temperature of the bath is controlled within 0.1 mK by pumping rate of the bath in combination with temperature controller; for further experimental details, see our previous reports [29,39].

In order to study the dynamics of VLD with the aforementioned methods, some sort of nonstationarity is necessary. Additionally, the numerical differentiation of experimental data requires strong reduction of experimental noise. We achieve both of these goals by modulating the counterflow velocity in a channel by a square wave; see Fig. 6. We measure several thousands of transients which, when averaged, provide us with sufficiently low noise data sets to allow for numerical differentiation. The differentiation is performed either using centered differences or using a weakly smoothing cubic spline. Both methods gave nearly identical results, the only difference being slightly larger noise with the centered differences. Spline differentiation was used for all data shown in this paper.

Since the problem under study represents a strongly nonstationary flow, thorough understanding of all physical processes triggered in the channel by switching on and off the applied heat flux is necessary. Not all of these processes are necessarily directly related to the dynamics of the turbulent tangle of quantized vortices. It is useful to describe these processes by their characteristic times, which can be estimated as follows:

(1) *Kinetic characteristic time.* In steady-state counterflow in a channel $L_{\rm ch}$ long, both the normal and superfluid components of He II move, carrying kinetic energy. Neglecting the flow generated in the bath outside the channel and the turbulent velocity inside the channel, it takes time $t_{\rm char}^{\rm kin}$ to gain this kinetic

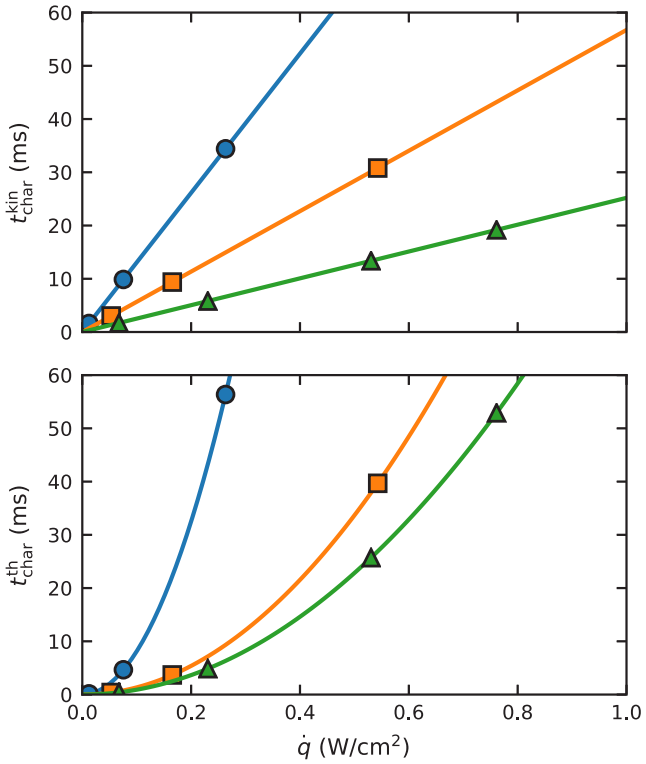

FIG. 3. Kinetic (top panel) and thermal (bottom panel) characteristic time scales given by Eqs. (11) and (13), respectively. Dependencies for the three experimental temperatures 1.45, 1.65, and 1.95 K are shown. The symbols indicate configurations where experiments took place. ●, 1.45 K; ■, 1.65 K; ▲, 1.95 K. The time constants have been calculated for the highest heat flux in a given experimental configuration. The highest point on a given curve corresponds to the last point in Table I.

energy from the heater, which can be estimated from the energy balance as

$$\dot{Q}t^{\rm kin}_{\rm char} = \rho_{\rm s} A L_{\rm ch}\frac{v_{\rm s}^2}{2} + \rho_{\rm n} A L_{\rm ch}\frac{v_{\rm n}^2}{2}. \tag{10}$$

Taking into account that in counterflow $v_{\rm s} = (\rho_{\rm n}/\rho_{\rm s})v_{\rm n}$ and $v_{\rm n} = \dot{q}/(\rho\sigma T)$, where $\dot{q} = \dot{Q}/A$ and σ denotes the entropy of He II at temperature T, we estimate the kinetic characteristic time as

$$t^{\rm kin}_{\rm char} = \frac{\rho_{\rm n}}{2\rho_{\rm s}\rho\sigma^2 T^2} L_{\rm ch}\dot{q}. \tag{11}$$

Figure 3 shows $t^{\rm kin}_{\rm char}$ for our channel for various applied heat fluxes at different temperatures.

(2) *Thermal characteristic time.* This can be estimated in the same way as in our earlier work [40]. Let us consider a switch of the applied heat input to the channel heater from $\dot{q}_1$ to $\dot{q}_2$. For simplicity, we assume linear temperature gradients in steady states, ∇T_1 and ∇T_2, leading to temperature differences $\Delta T_1 = L_{\rm ch}\nabla T_1$ and $\Delta T_2 = L_{\rm ch}\nabla T_2$, while the temperature of the helium bath, T, remains unchanged. In a steady-state counterflow, it is an established experimental fact that, for high enough VLD, $\dot{q}_1 = \zeta(T)\nabla T_1^{1/3}$, where for any temperature [19] $\zeta \simeq$ constant. On the other hand, the heat that must be either taken away or supplied between the two steady states, assuming that specific heat of He II $c(T_2) \cong c(T_1) \cong c(T) = c$, equals $Q = \frac{1}{2}c\rho A L_{\rm ch}|\Delta T_2 - \Delta T_1|$. Differentiating with respect to time, we get

$$\dot{q} = \frac{1}{2}c\rho L_{\rm ch}\Delta\dot{T}(t) = \zeta(T)[\Delta T(t)/L_{\rm ch}]^{1/3}, \tag{12}$$

which is easy to solve by separating the variables and finally yields the thermal characteristic time

$$t^{\rm th}_{\rm char} = \frac{3c\rho\left|\Delta T_2^{2/3} - \Delta T_1^{2/3}\right|}{4\zeta} L_{\rm ch}^{4/3}. \tag{13}$$

Figure 3 shows calculated $t^{\rm th}_{\rm char}$ for all individual experimental runs discussed in this paper. Temperature in the channel was monitored using multiple independent thermometers; see Ref. [37] for details.

(3) *Second-sound response time* $t^{\rm ss}_{\rm char}$. VLD is detected by measuring the extra attenuation of second sound caused by scattering of normal-component thermal excitations by the vortex lines [19]. In this work, second sound is generated and detected simultaneously by three pairs of vibrating porous membranes located in the walls of the channel as shown in Fig. 2; the second sound travels across the channel, which acts as a resonator [29,39]. An example of the second-sound resonance being attenuated by the presence of quantum turbulence is shown in Fig. 4. The attenuated amplitude of second sound at resonance, a, is related to VLD through the equation

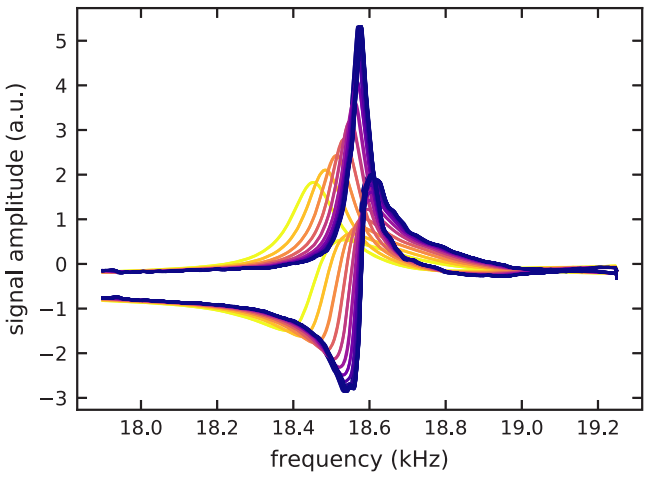

FIG. 4. Second-sound resonance peak for different counterflow velocities at 1.95 K, measured with sensor L2.

$$L = \frac{3\pi\rho_{\rm n}\Delta f}{\rho\alpha\kappa}\left(\frac{a_0}{a} - 1\right), \tag{14}$$

where a_0 and Δf are the amplitude and full width at half maximum of the second-sound amplitude resonant curve for quiescent helium, and α is the mutual friction coefficient [26]. Correct estimation of the resonant second-sound amplitudes a and a_0 is necessary to obtain the measurement of VLD. This is a challenge for time-resolved second-sound measurements, which are of primary interest for our purposes. The changing attenuation is accurately reflected only if the natural *second-sound response time* $t^{\rm ss}_{\rm char}$ of the second-sound resonator (on the order of the product of the time in which second sound crosses the width of the channel and the time-dependent quality factor

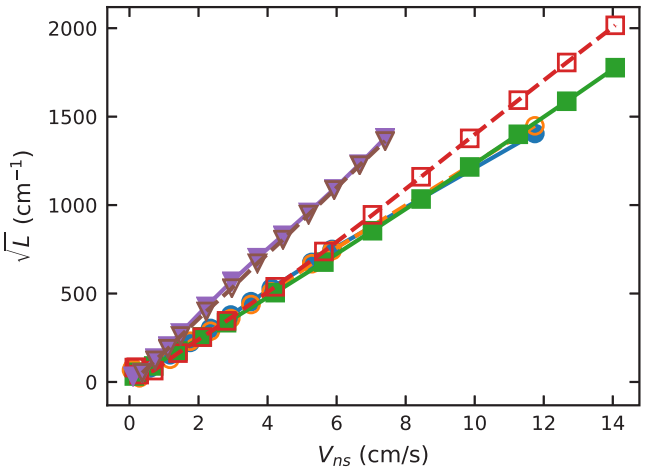

FIG. 5. Steady-state VLD as a function of the counterflow velocity. Filled symbols are measured using second-sound sensor L1, empty using sensor L2; see Fig. 2. ●, ○–1.45 K; ■, □–1.65; ▼, ▽–1.95 K.

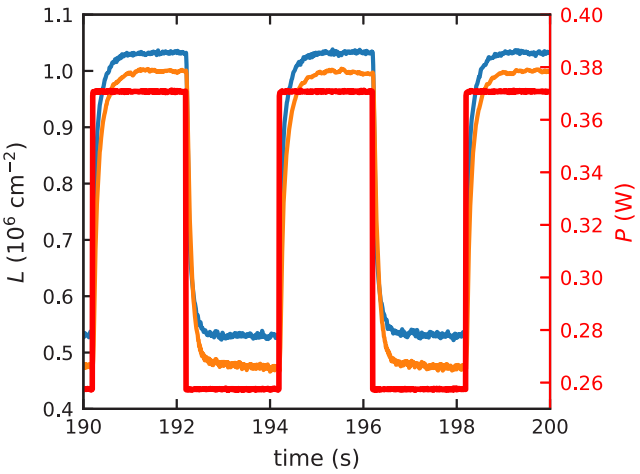

FIG. 6. Illustration of the time dependence of the VLD in modulated counterflow. The displayed case is for 1.95 K and 2 s pulse width, and modulation depth is roughly between densities of 5×10^5 and 10^6 cm^{-2}. The sharp square wave shows the time dependence of the applied heater power (with values on the right y axis). The two experimental curves show measured vortex line density with sensor L1 (higher; blue color) and L2 (lower; orange color) with values on the left y axis.

of the resonant peak) is sufficiently short—in our experiment on the order of 10 ms (for attenuated peaks). Moreover, the time-dependent measurements (such as generation and decay) are usually accomplished by tuning the excitation frequency and measuring the second-sound amplitude directly, for example as the in-phase component measured by a lock-in amplifier. This is not possible in our long channel, due to significant temperature shifts caused by the presence of the temperature gradient naturally associated with thermal counterflow. We overcome this difficulty using a postprocessing technique, described in our previous publication [37], which calculates the resonant amplitude from slightly off-resonant real and imaginary components of the complex amplitude measured with a lock-in amplifier. Another option could have been the resonance-tracking technique recently developed by Yang *et al.* [41]. We opted not to use this technique due to concerns about about resolving fast transients in a system that continually adjusts its excitation frequency.

Estimated times $t_{\mathrm{char}}^{\mathrm{kin}}$, $t_{\mathrm{char}}^{\mathrm{th}}$, and $t_{\mathrm{char}}^{\mathrm{ss}}$ are generally rather short, on the order of the time constant of the lock-in amplifier (10 ms in our case) which in turn must be chosen based on the frequency and quality factor of the second-sound resonance used for direct measurement of the VLD in the channel. The processes described above ought to work simultaneously and in parallel. The actual limitation to the experiment is therefore given roughly by the longest time constant (i.e., the slowest process) for a given experimental configuration. In our case this is always less than 60 ms—meaning that, in general, measurements of the VLD in the first 60 ms after a transient in the heat flux might be affected by processes that are not interesting from the point of view of the intrinsic tangle dynamics.

In practice, the X and Y components of all three lock-ins (for the three second-sound sensors) and the power dissipated by the counterflow heater are all sampled simultaneously by a multichannel digital-to-analog converter at a fixed rate of 100 points per second. The data measured with sensors L1 and L2 are generally very similar and the results reported below are measured with L1. Sensor L3 displayed much higher noise and was generally not used.

IV. EXPERIMENTAL RESULTS AND DISCUSSION

Vortex line density obtained in the steady state measured using the full resonance peak is shown in Fig. 5. The observed relationship between VLD and counterflow velocity obeys

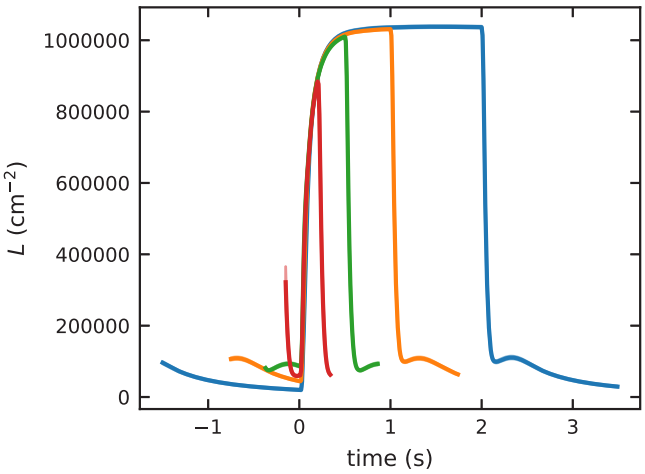

FIG. 7. Averaged growth of the VLD during a heat pulse for different pulse widths. Shown are 0.2, 0.5, 1, and 2 s pulse widths. Temperature was 1.45 K and the heat flux was pulsed between 266 mW and 0. Heat flux 266 mW corresponds to a steady-state VLD of about 10^6 cm^{-2}. The standard deviation of the average is not visible on the scale shown. The rising edge of the counterflow velocity (width of the edge of the heat flux is about 300 μs; the VLD is measured every 10 ms) is used as the time origin.

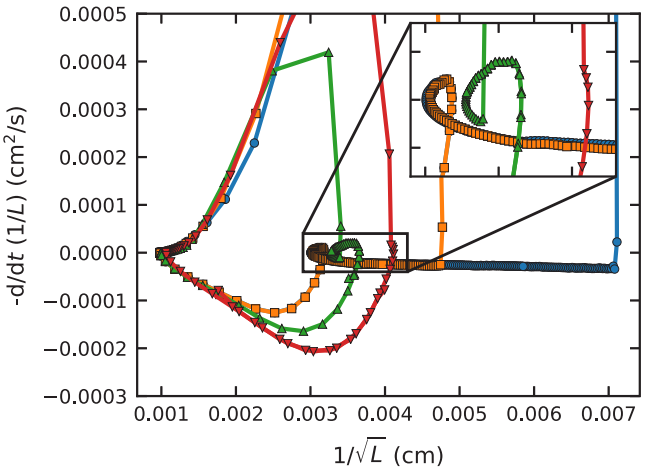

FIG. 8. Full phase portrait obtained from the pulsed heat flux. The data are the same as in Fig. 7: ●, 2 s pulse; ■, 1 s; ▲, 0.5 s; ▼, 0.2 s. The inset shows the detail of the behavior near the "bump". While the growth of the VLD is hardly affected by the pulse width, decay can be affected quite strongly.

the expected $L = \gamma^2 v_{ns}^2$ with γ coefficients approximately 129, 141, and 186 s/cm^2 for 1.45 K, 1.65 K, and 1.95 K, respectively. The values for 1.45 K and 1.65 K are within about 10% of values reported in the literature [29] whereas the 1.95 K case is either about 30% too low or within the expected range, depending on the data set with which one compares.

The dynamics of the VLD, however, cannot be studied using the properties of the steady state. In order to study the dynamical properties of the tangle we do not allow the tangle to settle to a constant value of the VLD. To achieve this in a controlled fashion we use a square-wave modulated counterflow, an example of which is shown in Fig. 6. Several thousands of the pulses have been measured and the results,

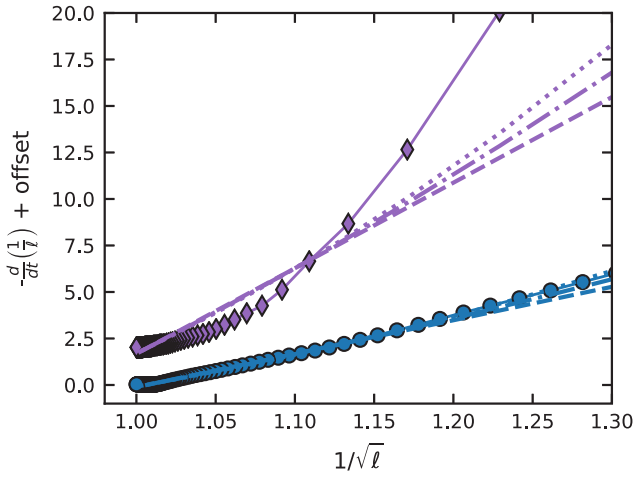

FIG. 9. Growth phase trajectory for sparse (●, modulation of VLD between 0 and 10^5 cm^{-2}) and dense (◆, modulation between 10^5 and 10^6 cm^{-2}) tangle at 1.45 K. Lines are fits of Eq. (6) with dashed line $n = 1$, dash-dotted line $n = 2$, and dotted line $n = 3$. For the sparse tangle all fits are adequate (fits for different n essentially overlap); for the dense tangle all models provide a poor description. For the fit, only $\ell \in [1,1.2]$ are used.

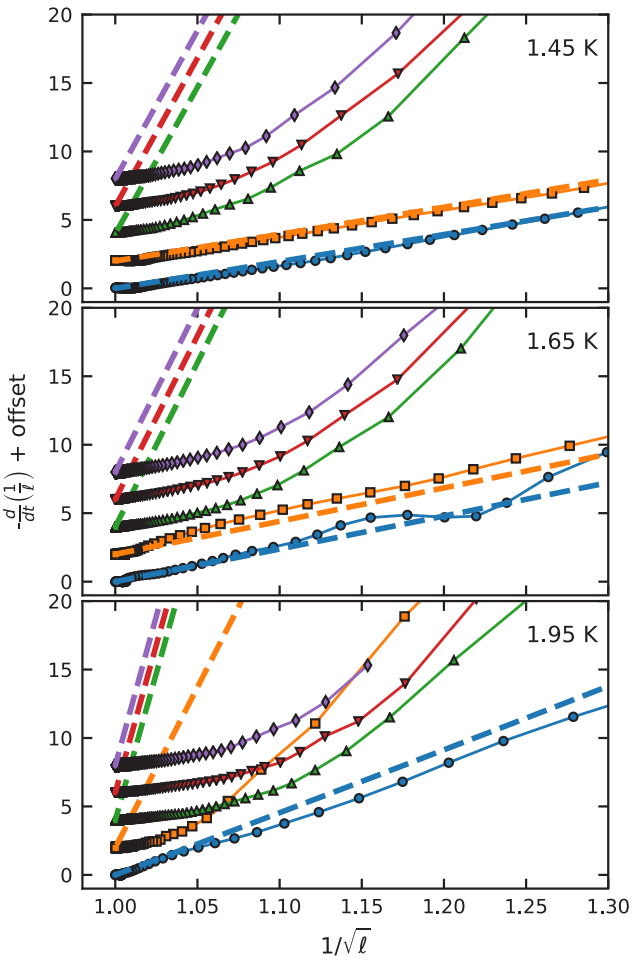

FIG. 10. Phase portrait of the VLD growth dynamics. The dashed lines coinciding with the experimental data for $1/\sqrt{\ell} = 1$ are predictions according to simulations of Schwarz [20]. The curves and the theoretical predictions are offset for clarity. We emphasize that no fitting was used in comparison of the numerical prediction with the experiment. Temperatures (top to bottom): 1.45, 1.65, and 1.95 K. VLDs high and low are increasing for the curves going from bottom to top; see Table I for details about the data sets. The y-axis offset increment is 2 in the units of the axis.

when averaged, are illustrated in Fig. 7. Attempting to fit these time dependencies using solutions to one of the expected dynamical equations bears little fruit. The solutions are, indeed, very similar and all can be said to provide an adequate fit.

In order to study the dynamics of the VLD more directly we look at its phase portrait using a coordinate system motivated by Eq. (7). A particular case for 1.45 K (the same data as in Fig. 7) and several different pulse widths is shown in Fig. 8. As can be expected already from Fig. 7, the dynamics of the VLD growth are unaffected by the pulse width; however, the decay can be quite different. The VLD alone, in general, is unsuitable for the description of the decay due to the nonmonotonic behavior usually referred to as the "bump" (seen as the small loop in the decaying part of a phase trajectory). Nonmonotonic behavior cannot be modeled by a one-dimensional dynamical system. The physical origin of the bump is beyond the scope of this article but is thought to be connected to the existence of

TABLE I. Experimental data sets shown in Figs. 10 and 12. The pulse width for the displayed cases was 2 s except for 1.45 K where it was 1 s (marked * near the symbol), 0.5 s (marked **), or 2 s for all other cases. The numbers shown are in the format $X_{\text{high}}/X_{\text{low}}$; the "high" and "low" subscripts correspond to the square-wave modulated heat flux being in the higher or lower state. For counterflow velocity v_{ns}, the average across the entire duration of the pulse is shown. For L, L_{high} is the VLD 10 ms before the heat pulse is switched to the lower state and L_{low} corresponds to to the overall minimum. Ensemble averaging is used to calculate the L_{high} and L_{low} and the standard deviation of this average is shown as the error. The two lines of the VLD correspond to second-sound sensors L1 and L2 (see Fig. 2).

Nominal VLD		1.45 K	1.65 K	1.95 K
$10^5/0$	symbol	●	●	
	v_{ns} (cm/s)	2.4/0.0	2.5/0.0	
	actual L	$79 \pm 2.7/19 \pm 2.9$	$74 \pm 3.6/7.9 \pm 2.8$	
	(10^3 cm^{-2})	$64 \pm 6.8/13 \pm 6.6$	$82 \pm 1.4/16 \pm 1.5$	
$10^5/10^4$	symbol	■	■	●
	v_{ns} (cm/s)	2.4/0.4	2.5/0.8	1.8/0.5
	actual L	$79 \pm 2.4/19 \pm 2.5$	$75 \pm 3.3/13 \pm 3.0$	$97 \pm 1.9/7.5 \pm 2.5$
	(10^3 cm^{-2})	$65 \pm 7.1/16 \pm 7.0$	$83 \pm 3.3/15 \pm 3.2$	$85 \pm 2.2/5.0 \pm 3.1$
$5 \times 10^5/10^5$	symbol			■
	v_{ns} (cm/s)			4.3/1.8
	actual L			$54 \pm 0.39/10 \pm 0.67$
	(10^4 cm^{-2})			$48 \pm 0.39/8.5 \pm 0.47$
$10^6/0$	symbol	▲**	▲	▲
	v_{ns} (cm/s)	8.4/0.0	8.3/0.0	6.1/0.0
	actual L	$97 \pm 0.47/11 \pm 0.34$	$83 \pm 0.25/1.3 \pm 0.22$	$100 \pm 0.52/1.8 \pm 0.52$
	(10^4 cm^{-2})	$96 \pm 2.4/13 \pm 0.70$	$100 \pm 0.26/2.0 \pm 0.18$	$99 \pm 0.49/1.7 \pm 0.45$
$10^6/10^4$	symbol	▼	▼	▼
	v_{ns} (cm/s)	8.4/0.4	8.3/0.8	6.1/0.5
	actual L	$99 \pm 0.82/5.7 \pm 0.34$	$83 \pm 0.34/1.5 \pm 0.28$	$100 \pm 0.42/0.61 \pm 0.47$
	(10^4 cm^{-2})	$98 \pm 2.3/6.3 \pm 0.65$	$100 \pm 0.62/0.91 \pm 0.26$	$98 \pm 0.58/0.96 \pm 0.62$
$10^6/10^5$	symbol	◆	◆	
	v_{ns} (cm/s)	8.4/2.4	8.3/2.5	
	actual L	$99 \pm 0.48/9.2 \pm 0.21$	$83 \pm 0.20/7.6 \pm 0.13$	
	(10^4 cm^{-2})	$98 \pm 2.4/8.7 \pm 0.63$	$100 \pm 0.37/7.3 \pm 0.20$	
$10^6/5 \times 10^5$	symbol			◆
	v_{ns} (cm/s)			6.1/4.3
	actual L			$100 \pm 0.35/53 \pm 0.43$
	(10^4 cm^{-2})			$100 \pm 0.73/48 \pm 0.64$

energy at large scales in quantum turbulence [9,10]. Note that the VLD is sampled at a rate of 100 points/s; i.e., all points are equidistant in time and separated by 10 ms. The first five or six points after a transient might be affected by parasitic effects; see Sec. III. From now on, the first 50 ms of the growth phase trajectories are never shown. Decay trajectories will be shown in full.

Looking at the phase trajectories of two particular cases of high and low VLD transients from 1.45 K in Fig. 9 we immediately see that trying to decide between the different forms of the Vinen equation Eq. (3), in particular which exponent from the three proposed models of $n = 1,2,3$ best describes the data, is an ill-posed question. The behavior of these functions is very similar and for sparse tangles the fits are adequate regardless of the exponent. For dense tangles, none of the models provides a good description. In the following, we chose to base most of our interpretation on the model of Schwarz (and assuming that $n = 1$) since that is the simplest currently available theory that connects the microscopic physics of the motion of the vortices with macroscopic VLD dynamics.

The growth part of the phase portrait for different modulated flows is shown in Fig. 10 (see Table I for classification of all data sets in Fig. 10). As a point of reference, we compare our experimental data with numerical simulations obtained by Schwarz [20] expressed through Eq. (7). The numerical values of the coefficient c_2 for the experimental temperatures have been obtained by cubic spline interpolation of the data published in Ref. [20]. We observe that the agreement between the experimental data and simulations, with no adjustable parameters, is nearly perfect for tangles with relatively low VLD. The measured approach to the steady state, however, is significantly less steep for dense tangles. As a way to capture this behavior quantitatively we allow the geometric coefficient c_2 to vary with VLD. The c_2 coefficient as a function of intervortex distance obtained from these growth curves is shown in Fig. 11. A sharp increase in c_2 is seen for the 1.65 K and, to a lesser extent, for 1.95 K, for small tangle densities. For these cases, small oscillations in L are observed (visible also in Fig. 10), especially early after the transient (not shown in Fig 10), probably related to temperature instability and nonideal second-sound resonance. In the first 50 ms after the transient (which are not used for analysis; these points are not shown) a sharp swing to smaller c_2 is seen. Therefore we regard these points as experimental artifacts [43]. It should also

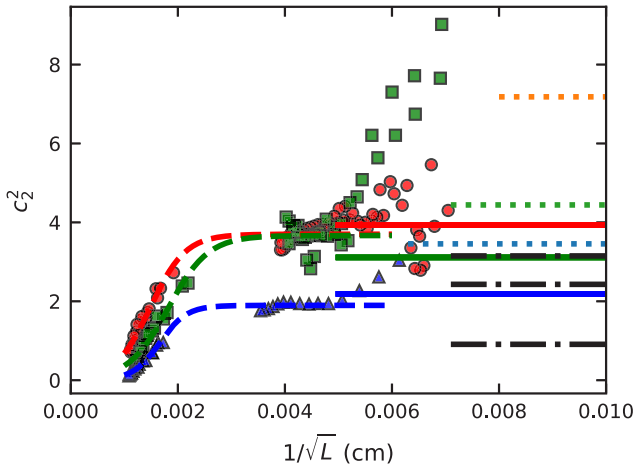

FIG. 11. Effective coefficients c_2 as a function of the mean intervortex distance. ●, 1.45 K; ■, 1.65 K; ▲, 1.95 K. The horizontal full lines show c_2 interpolated for experimental temperatures from values calculated by Schwarz [20] corresponding to 1.45, 1.65, and 1.95 K (top to bottom). The dashed lines are least squares fits to Eq. (15). Black dash-dotted lines on the right: numerical simulations of a vortex tangle with uniform normal fluid, synthetic turbulence, and frozen Navier-Stokes turbulence in normal fluid, respectively from top to bottom, from Ref. [42]. See text for estimation of c_2 from average curvature. Dotted lines on the right: c_2 from Ref. [34] for 1.3 K, 1.6 K, and 1.9 K (top to bottom). Lines from Ref. [42] and Ref. [34] terminate at the minimum intervortex distance that these simulations achieved (except for the top dashed 1.3 K case, where the intervortex spacing was 125 μm). The tendency of the experimental points to rise for small vortex line densities is most likely an experimental artifact; see text for discussion.

be noted that for simplicity, we neglected the changes in c_1 in the logarithmic correction given by Eq. (5) and simply used the values obtained by Schawrz [20,44]

Physically, it is tempting to keep the original interpretation of c_2 as a way to measure the rms curvature of the tangle. However, the dynamical equation that leads to the calculation of c_2 from the experimental data was an approximation for relatively sparse tangles (so that the local-induction approximation is sufficient) and for only quasistationary processes. It should be noted though that systematic numerical studies [34] have shown that scaling of tangle rms curvature with the VLD remains valid even when the nonlocal full Biot-Savart interaction is taken into account. These simulations yielded c_2's which are somewhat higher than those predicted by [20] but roughly within the range of the experimental values, except for their lowest 1.3 K. The comparison with c_2's from [34] (average of values for different reconnecting algorithms) is shown in Fig. 11. No decrease of c_2 with increasing VLD has been observed in simulations of steady-state counterflow with uniform normal fluid velocity; however, two numerical experiments observed changes in the tangle curvature which could be said to be in agreement with our experimental findings: (i) at fairly low temperatures, Kondaurova *et al.* [45] observed that in freely decaying turbulence c_2 increases as the VLD decreases, and (ii) simulations which used quasiturbulent normal fluid velocity field [42] (either synthetic turbulence or a

TABLE II. Adjustable parameters of the expression Eq. (15) for the empirical c_2.

Temperature (K)	ϕ (cm)	ϑ (cm)	C
1.45	1.49×10^{-3}	6.54×10^{-4}	1.85
1.65	1.82×10^{-3}	7.46×10^{-4}	1.83
1.95	1.66×10^{-3}	5.03×10^{-4}	0.95

stationary "frozen" snapshot of a DNS simulation of classical turbulence at one temperature 1.95 K and one steady VLD of about 2×10^4 cm^{-2}) have demonstrated marked decrease in average curvature compared to the uniform case. Data in [42] are reported in terms of mean curvature $\bar{S}$. In order to transform them to rms curvature $\tilde{S}$ we use the estimate of Kondaurova *et al.* [34] $\tilde{S} = \bar{S}\sqrt{3/2}$ which is then used to calculate c_2 using the reported VLD. The result is also shown in Fig. 11. If we were to take the decrease in c_2 as an empirical fact, it would be an interesting question whether the main cause is the normal fluid turbulence or the high tangle density. One possibility of shedding some light on this issue is to repeat the experiments in a mechanically generated counterflow (pure superflow) [39], where the normal component should be on average at rest. These experiments are planned in our laboratory.

One should bear in mind that the numerical simulations can as yet achieve only relatively low VLD (on the order of 10^4 cm^{-2}, i.e., about 10 times lower than our present smallest experimental VLD), where it is challenging to obtain experimental data with sufficiently low noise to allow differentiation. In addition, the simple models Eq. (3) or (4) introduced earlier assume homogeneous counterflow and an unbound system (although there have been fruitful attempts [16,36] to capture inhomogeneity by introducing a flux term in the dynamical equation). Thermal counterflow is known to be somewhat inhomogeneous, both from experiments [7] and simulations [46], especially at relatively low counterflow velocities in wall-bounded setups. However, the inhomogeneous turbulence observed in Ref. [7] referred to a low-velocity state (less than about 0.8 cm/s in their system), whereas for the velocities more typically used in our experiments mostly statistically homogeneous turbulence in the normal fluid was observed. Furthermore, the curvature in Ref. [46], except for very near the wall, was observed to be almost homogeneous. Lastly, in our reported tangles the typical intervortex spacing is 0.01–0.1 mm (0.01–0.03 mm for the more dense states), which, even in the worst case, is separated from the size of the system (7 mm) by nearly two orders of magnitude. We therefore consider finite-size effects to play little role in our experimental data. It should also be noted that due to the nature of second-sound attenuation measurements, the value of the VLD measured is an average over a volume of about 0.3 cm^3 (7 mm cubed) and over a time interval of about 10 ms (the time constant of the lock-in amplifier); therefore we do not have access to local information. One way to probe tangle inhomogeneity would be to use low-lying modes of the second-sound resonator [47]; however, this was not possible in the current work and all the resonances used were higher than the 10th harmonic, which measures the VLD uniformly across the channel.

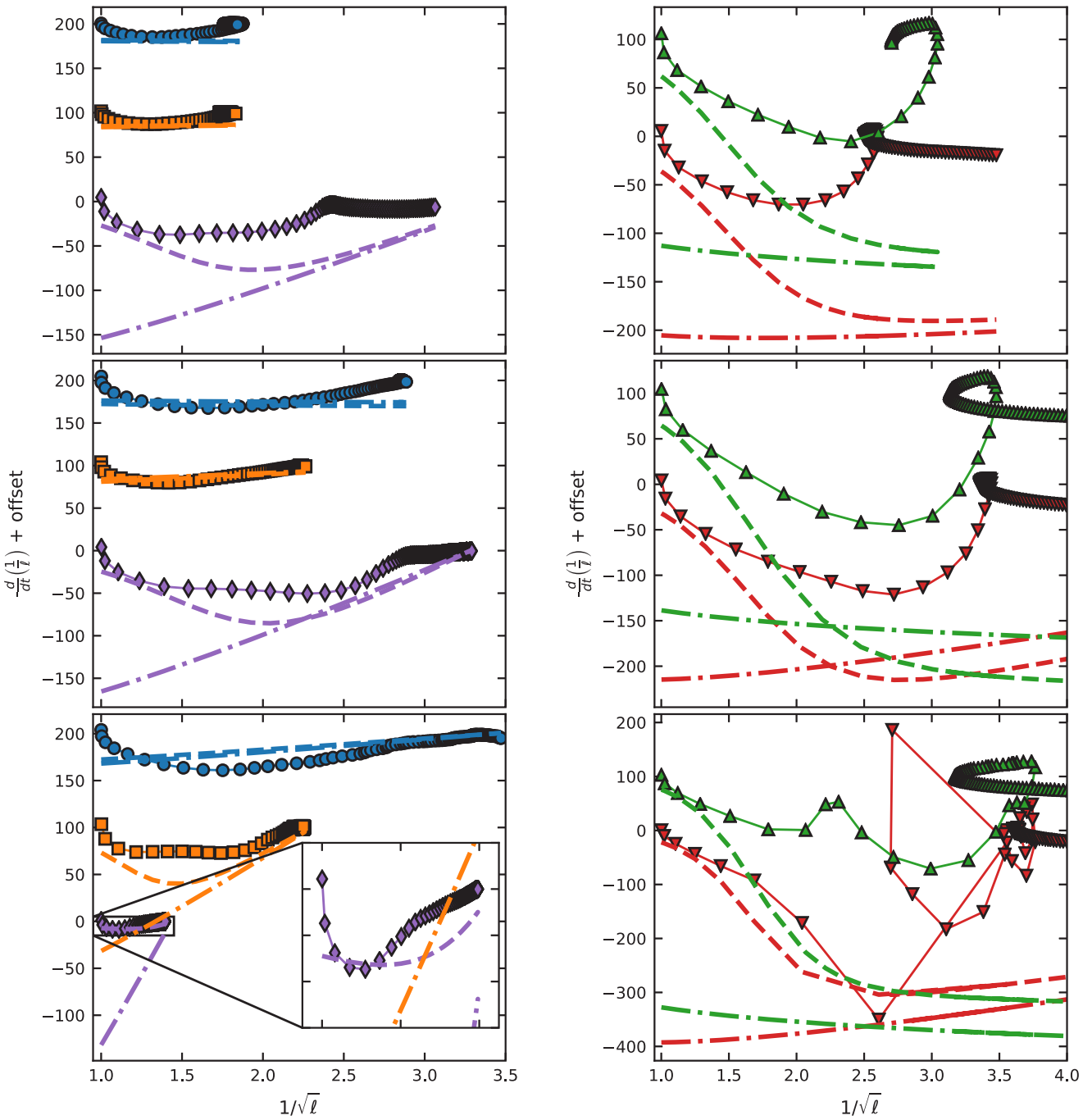

FIG. 12. Phase portrait of the decaying turbulence. Shown with the data are also theoretical predictions using c_2 coefficients either from Schwarz [20] (dash-dotted lines) or obtained from the fit of the experimental data (dashed lines). Temperatures are (top to bottom) 1.45 K, 1.65 K, and 1.95 K. The y-axis offset increment is 100 in the units of the axis. List of shown data sets is in Table I. Left: Smaller transients for which nominal $L_{\mathrm{high}}/L_{\mathrm{low}} \leqslant 100$ or $L_{\mathrm{high}} = 10^5\ \mathrm{cm}^{-2}$. Right: Larger transients for which nominal $L_{\mathrm{high}}/L_{\mathrm{low}} \geqslant 100$ and $L_{\mathrm{high}} = 10^6\ \mathrm{cm}^{-2}$. For 1.95 K, very early after switching the heat flux, it is very challenging to compensate for the resulting shifts in the second-sound resonance, hence the disruptions in the decay curves; see the shift in Fig. 4.

For simplicity of handling the empirical c_2 in the subsequent analysis we approximate the experimental data with a simple formula

$$c_2^2(\delta) = C\left[1 + \tanh\left(\frac{\delta - \phi}{\vartheta}\right)\right], \tag{15}$$

where $\delta = 1/\sqrt{L}$ is the intervortex spacing and C, ϕ, ϑ are adjustable parameters. The reason for this particular functional form is simply convenience and the fact that $c_2^2 > 0$ by definition. The function parameters obtained by nonlinear least squares fitting are given in Table II.

Even though we *a priori* accept that the VLD dynamical equations are in general unsuitable for the description of

the decay, it is interesting to compare the phase trajectory of the decaying turbulence with the prediction based on the dynamical equation; see Fig. 12. Using the c_2 coefficients calculated by Schwarz (dot-dashed lines) we obtain reasonable agreement in decay rate for sparse tangles but a very gross mismatch for denser tangles, where the actual decay rate is much smaller (in absolute value) than predicted. However, using the (variable) empirical c_2 coefficients obtained from the growth brings the decay rate much closer to reality and even reproduces some qualitative features. Agreement is good even for the very dense tangles and becomes worse only for the free (no residual v_{ns}) or nearly free (small residual v_{ns}) decay from very high density. Moreover, the initial decay rate for all tangles is estimated to a high degree of accuracy. The slow initial decay rate has usually been explained using the residual heat flux due to thermal RC time constant [i.e., Eq. (13)]. These results suggest that the importance of the thermal time constant for the tangle dynamics may have been overstated.

V. CONCLUSIONS

The vortex tangle in quantum turbulence is a very complex system and as such vortex line density, and its dynamics, alone provide only a very coarse description. However, due to the simplicity and time-tested reliability of second-sound measurements and the existence of relatively simple theories of VLD dynamics in a homogeneous counterflow it is important to establish the boundaries within which the description of superfluid turbulence using just the VLD is sufficient, how, if at all, the straightforward ideas about tangle motions relate to the experimental reality, and in what way the line-density-centric description of quantum turbulence breaks down.

With these goals in mind we studied thermal counterflow in a channel in a situation where the turbulence is not allowed to settle, in a controlled way, to a statistical steady state. This we achieved by modulating the counterflow velocity in the channel by a square wave. The large number of turbulent transients thus obtained allows us not only to study the time evolution of the VLD but also to focus on the dynamics of the VLD more directly using its phase portrait, a common tool for studying dynamical systems.

We find that for small overall tangle densities all proposed forms of Eq. (3) provide adequate description. For higher densities, across all temperatures, these forms of the dynamical equation cannot account for the significant slow-down in tangle growth rate as the steady state is approached (Fig. 10). A possible approach to the description of this problem is to allow the geometrical coefficient c_2, connecting rms curvature of quantized vortices and the VLD, to depend on the VLD. Calculating c_2 using the theory of Schwarz [20], Eq. (7), we find (see Fig. 11) that c_2 is close to the value expected from numerical simulations for relatively sparse tangles but decreases markedly for densities $L > 5 \times 10^5$ cm^{-2}. This is also in accord with the observed decrease in curvature, which was found in numerical simulations of thermal counterflow in the presence of classical turbulence in the normal fluid [42].

An important and striking observation is that even for large counterflow velocities and dense tangles, where the phase portrait does not have a form predicted by Eq. (6), the decay rate occurring after the falling edge of the heat flux is predicted well by the turbulence growth by using the effective estimated parameter c_2, as shown in Fig. 12.

It is our hope that we have demonstrated the utility and power of looking at the behavior of the VLD from the point of view of dynamical systems. Specifically, second-sound measurements of the growth of turbulence might provide us with a way to measure mean curvature of the tangle. The observed dynamics are complex, but we believe that further study following this line could provide deeper understanding of the tangle dynamics even in highly turbulent cases. More measurements, especially at higher temperatures closer to the lambda point and other types of quantum flows, are, however, clearly needed.

ACKNOWLEDGMENTS

We thank M. J. Jackson, M. La Mantia, V. S. L'vov, A. Pomyalov, D. Schmoranzer, F. Soukup, P. Švančara, and W. F. Vinen for fruitful discussions, and L. Doležal for skillful manufacturing of the counterflow channel. This research is funded by the Czech Science Foundation under project GAČR 17-03572S. E.V. acknowledges support from the Charles University under GAUK 368217.

[1] W. F. Vinen and J. J. Niemela, J. Low Temp. Phys. **128**, 167 (2002).
[2] L. Skrbek and K. R. Sreenivasan, Phys. Fluids **24**, 011301 (2012).
[3] C. F. Barenghi, L. Skrbek, and K. R. Sreenivasan, Proc. Natl. Acad. Sci. USA **111**, 4647 (2014).
[4] M. S. Paoletti, M. E. Fisher, K. R. Sreenivasan, and D. P. Lathrop, Phys. Rev. Lett. **101**, 154501 (2008).
[5] W. Guo, M. La Mantia, D. P. Lathrop, and S. W. Van Sciver, Proc. Natl. Acad. Sci. USA **111**, 4653 (2014).
[6] M. La Mantia and L. Skrbek, Phys. Rev. B **90**, 014519 (2014).
[7] A. Marakov, J. Gao, W. Guo, S. W. Van Sciver, G. G. Ihas, D. N. McKinsey, and W. F. Vinen, Phys. Rev. B **91**, 094503 (2015).
[8] A. W. Baggaley, C. F. Barenghi, and Y. A. Sergeev, Phys. Rev. B **85**, 060501 (2012).
[9] J. Gao, W. Guo, V. S. L'vov, A. Pomyalov, L. Skrbek, E. Varga, and W. F. Vinen, JETP Lett. **103**, 648 (2016).
[10] S. Babuin, V. S. L'vov, A. Pomyalov, L. Skrbek, and E. Varga, Phys. Rev. B **94**, 174504 (2016).
[11] J. Gao, E. Varga, W. Guo, and W. F. Vinen, Phys. Rev. B **96**, 094511 (2017).
[12] M. Tsubota, K. Fujimoto, and S. Yui, J. Low Temp. Phys. **188**, 119 (2017).
[13] G. W. Stagg, N. G. Parker, and C. F. Barenghi, Phys. Rev. Lett. **118**, 135301 (2017).
[14] M. La Mantia, P. Švančara, D. Duda, and L. Skrbek, Phys. Rev. B **94**, 184512 (2016).

[15] L. Skrbek, A. V. Gordeev, and F. Soukup, Phys. Rev. E **67**, 047302 (2003).
[16] D. Khomenko, L. Kondaurova, V. S. L'vov, P. Mishra, A. Pomyalov, and I. Procaccia, Phys. Rev. B **91**, 180504 (2015).
[17] D. Khomenko, V. S. L'vov, A. Pomyalov, and I. Procaccia, Phys. Rev. B **94**, 146502 (2016).
[18] S. K. Nemirovskii, Phys. Rev. B **94**, 146501 (2016).
[19] W. F. Vinen, Proc. R. Soc. A Math. Phys. Eng. Sci. **242**, 493 (1957).
[20] K. W. Schwarz, Phys. Rev. B **38**, 2398 (1988).
[21] The term "quantum turbulence" was introduced into the literature by R. J. Donnelly in a symposium dedicated to the memory of G. I. Taylor; see Ref. [48].
[22] R. P. Feynman, Prog. Low Temp. Phys. **1**, 17 (1955).
[23] W. F. Vinen, Proc. R. Soc. A Math. Phys. Eng. Sci. **240**, 114 (1957).
[24] W. F. Vinen, Proc. R. Soc. A Math. Phys. Eng. Sci. **240**, 128 (1957).
[25] W. F. Vinen, Proc. R. Soc. A Math. Phys. Eng. Sci. **243**, 400 (1958).
[26] R. J. Donnelly and C. F. Barenghi, J. Phys. Chem. Ref. Data **27**, 1217 (1998).
[27] S. K. Nemirovskii and W. Fiszdon, Rev. Mod. Phys. **67**, 37 (1995).
[28] J. T. Tough, Prog. Low Temp. Phys. **8**, 133 (1982).
[29] S. Babuin, M. Stammeier, E. Varga, M. Rotter, and L. Skrbek, Phys. Rev. B **86**, 134515 (2012).
[30] K. W. Schwarz, Phys. Rev. B **31**, 5782 (1985).
[31] K. W. Schwarz, Phys. Rev. Lett. **49**, 283 (1982).
[32] H. Adachi, S. Fujiyama, and M. Tsubota, Phys. Rev. B **81**, 104511 (2010).
[33] A. W. Baggaley and C. F. Barenghi, J. Low Temp. Phys. **166**, 3 (2012).
[34] L. Kondaurova, V. S. L'vov, A. Pomyalov, and I. Procaccia, Phys. Rev. B **89**, 014502 (2014).
[35] R. Hanninen and A. Baggaley, Proc. Natl. Acad. Sci. USA **111**, 4667 (2014).
[36] D. Khomenko, V. S. L'vov, A. Pomyalov, and I. Procaccia, Phys. Rev. B **97**, 014508 (2018).
[37] E. Varga, S. Babuin, V. S. L'vov, A. Pomyalov, and L. Skrbek, J. Low Temp. Phys. **187**, 531 (2017).
[38] K. W. Schwarz and J. R. Rozen, Phys. Rev. B **44**, 7563 (1991).
[39] S. Babuin, E. Varga, W. F. Vinen, and L. Skrbek, Phys. Rev. B **92**, 184503 (2015).
[40] A. Gordeev, T. Chagovets, F. Soukup, and L. Skrbek, J. Low Temp. Phys. **138**, 549 (2005).
[41] J. Yang, G. G. Ihas, and D. Ekdahl, Rev. Sci. Instrum. **88**, 104705 (2017).
[42] L. K. Sherwin-Robson, C. F. Barenghi, and A. W. Baggaley, Phys. Rev. B **91**, 104517 (2015).
[43] Using sensor L2 (see Fig. 2), the low-VLD c_2^2's for 1.45 K are 10%–20% higher than those measured using L1, but exhibit similar problems. For temperatures 1.65 K and 1.95 K the c_2's from sensors L1 and L2 agree within the experimental scatter.
[44] Recalculating c_2 using an order of magnitude smaller c_1 than obtained by Schwarz results in about 15% change in c_2^2, which is within the experimental scatter.
[45] L. Kondaurova, V. S. L'vov, A. Pomyalov, and I. Procaccia, Phys. Rev. B **90**, 094501 (2014).
[46] A. W. Baggaley and S. Laizet, Phys. Fluids **25**, 115101 (2013).
[47] E. Varga, S. Babuin, and L. Skrbek, Phys. Fluids **27**, 065101 (2015).
[48] R. J. Donnelly and C. E. Swanson, J. Fluid Mech. **173**, 387 (1986).

Intermittency enhancement in quantum turbulence

Emil Varga,[1,2,*] Jian Gao,[1,3] Wei Guo,[1,3,†] and Ladislav Skrbek[2]

[1] *National High Magnetic Field Laboratory, 1800 East Paul Dirac Drive, Tallahassee, Florida 32310, USA*
[2] *Faculty of Mathematics and Physics, Charles University, Ke Karlovu 3, 121 16, Prague, Czech Republic*
[3] *Mechanical Engineering Department, Florida State University, Tallahassee, Florida 32310, USA*

(Dated: June 20, 2018)

Intermittency is a hallmark of turbulence, which exists not only in turbulent flows of classical viscous fluids but also in flows of quantum fluids such as superfluid ^{4}He. Despite the established similarity between turbulence in classical fluids and quasi-classical turbulence in superfluid ^{4}He, it has been predicted that intermittency in superfluid ^{4}He is temperature dependent and enhanced for certain temperatures, which strikingly contrasts the nearly flow-independent intermittency in classical turbulence. Experimental verification of this theoretical prediction is challenging since it requires well-controlled generation of quantum turbulence in ^{4}He and flow measurement tools with high spatial and temporal resolution. Here, we report an experimental study of quantum turbulence generated by towing a grid through a stationary sample of superfluid ^{4}He. The decaying turbulent quantum flow is probed by combining a recently developed He_2^* molecular tracer-line tagging velocimetry technique and a traditional second sound attenuation method. We observe quasi-classical decays of turbulent kinetic energy in the normal fluid and of vortex line density in the superfluid component. For several time instants during the decay, we calculate the transverse velocity structure functions. Their scaling exponents, deduced using the extended self-similarity hypothesis, display non-monotonic temperature-dependent intermittency enhancement, in excellent agreement with recent theoretical/numerical study of Biferale *et al.* [Phys. Rev. Fluids 3, 024605 (2018)].

I. INTRODUCTION

Intermittency in turbulent flows is a topic of extensive study in classical fluid dynamics research [1–5]. In fully developed turbulence, intermittency manifests itself as extreme velocity excursions that appear more frequently than one would expect on the basis of Gaussian statistics. Small-scale intermittency results in corrections to the energy spectrum and velocity structure functions that are nearly universal across a wide range of turbulent flows in classical fluids [6, 7]. A question that has attracted increasing interest in recent years is whether this universality can be extended to quantum fluids such as superfluid ^{4}He whose hydrodynamic behavior is strongly affected by quantum effects and cannot be described by the Navier-Stokes equation [8–13].

Below about $T_\lambda \simeq 2.17$ K, liquid ^{4}He undergoes a second order phase transition into a superfluid phase called He II. According to the two fluid model [14], He II behaves as if it is composed of two interpenetrating liquids – a superfluid component and a normal-fluid component made off thermal excitations called phonons and rotons. While the normal fluid behaves classically, possessing finite viscosity and carrying the entire entropy content of He II, the superfluid component has neither entropy nor viscosity. Due to quantum restriction, vorticity in the superfluid is constrained into line singularities, each carrying a single quantum of circulation $\kappa \approx 9.97\times10^{-4}$ cm^2/s around its angstrom-sized core [15]. The fraction ratio of the two fluids strongly depends on temperature. Above 1 K where both fluids are present, turbulence in He II (also termed as quantum turbulence [16]) takes the form of a tangle of quantized vortices in the superfluid component, co-existing with more classical-like turbulent flow of the normal fluid. When the velocity fields of the two fluids are mismatched, a mutual friction force between them, arising from the scattering of thermal excitations off the cores of quantized vortices, provides an inter-component energy transfer and additional dissipation, resulting in a modified turbulence scaling [17–21].

The general properties of quantum turbulence in He II above 1 K depend on the type of forcing. When the turbulence is generated by an applied heat current in He II, the two fluids are forced to move with opposite mean velocities (i.e., thermal counterflow) [14]. The mutual friction acts at all length scales in both fluids which leads to strongly non-classical behavior and decay [21–23]. On the other hand, when the turbulence is generated by methods conventionally used in classical fluid dynamics research, such as by a towed grid [24, 25] or using counter-rotating propellers [8], the two fluids can become strongly coupled by the mutual friction force at large scales and behave like a single-component fluid (i.e., quasi-classical turbulence), possessing some effective viscosity [20, 26]. This coupling must break down at scales comparable or smaller than the mean inter-vortex distance $\ell_Q = L^{-1/2}$ (where L denotes the vortex line density, i.e., the vortex line length per unit volume) since the flow of the superfluid component at these small scales is restricted to individual vortex lines and cannot match the velocity field of the normal fluid [27]. The quantity ℓ_Q is also known as the "quantum length scale"; it scales sim-

* Email: varga.emil@gmail.com
† Email: wguo@magnet.fsu.edu

ilarly to the Kolmogorov dissipation scale, η, of classical turbulence [28].

The similarity between quasi-classical turbulence in He II and turbulence in classical fluids has attracted a great deal of interest in both quantum and classical fluid dynamics research fields [29, 30]. Extensive experimental, theoretical, and numerical work has been conducted to explore various properties of turbulence in He II (see the reviews [18, 31] and references therein). In recent years, intermittency in He II quasi-classical turbulence has become one of the central topics. Since the coupling of the two fluids at large scales and their decoupling at small scales are all controlled by the temperature dependent mutual friction, one may naturally expect temperature dependent turbulence statistics. Indeed, it has been predicted by Boué *et al.* [10] and Biferale *et al.* [12] that when probed at small scales, intermittency corrections to the scaling of higher-order velocity structure functions in He II quasi-classical turbulence should be enhanced in the temperature range $1.3 \lesssim T \lesssim 2.1$ K, with a maximum deviation from the Kolmogorov-Obukhov K41 theory for classical turbulence [32] around 1.85 K. Early experiments conducted at low temperatures and close to T_λ did not find deviations from the statistics of classical turbulence [9, 33, 34]. A more recent experiment in a turbulent wake in He II covered a wider range of temperatures but also reported temperature independent intermittency, similar to that in classical flows [13]. It should be noted, however, that the pressure and velocity probes used in these experiments all have sizes much larger than ℓ_Q and hence are sensitive only for the corresponding part of the turbulent cascade [12, 13].

A reliable determination of intermittency in He II requires not only the generation of fully developed turbulence but also flow measurement tools with a spatial resolution comparable to ℓ_Q. In this paper, we report an experimental study of quasi-classical turbulence generated by towing a grid through a stationary sample of He II. The velocity of the normal fluid is measured using a recently developed He_2^* molecular tracer-line tagging velocimetry technique [19, 35] while the vortex line density in the superfluid component is determined using a traditional second sound attenuation method [24, 36]. Our experimental results indeed demonstrate intermittency enhancement, in excellent agreement with the theory predictions [10, 12].

II. EXPERIMENTAL METHOD

The experiment utilizes the Tallahassee He_2^* tracer-line visualization setup [35] as shown schematically in Fig. 1 (a). A stainless steel channel (inner cross-section: 9.5×9.5 mm^2; length 300 mm) is attached to a pumped helium bath whose temperature can be controlled within 0.1 mK. A mesh grid of 7×7 woven wires (about 8 mm in length and 0.41 mm in thickness) is supported inside the channel at the four corners and can be towed by a linear motor to move past our flow probes at a controlled speed up to about 65 cm/s. The grid is designed to have an open area of 54% so as to avoid producing secondary flows [37]. The flow generated in the wake of a moving grid is usually treated as a prototype of nearly homogeneous and isotropic turbulence, the simplest form of turbulence that has been extensively studied in classical fluid dynamics research [25, 38–40]. The grid turbulence has also been utilized as a valuable vantage point in quantum turbulence research for assessing the similarities and differences between classical and quantum turbulent flows [24, 28, 41].

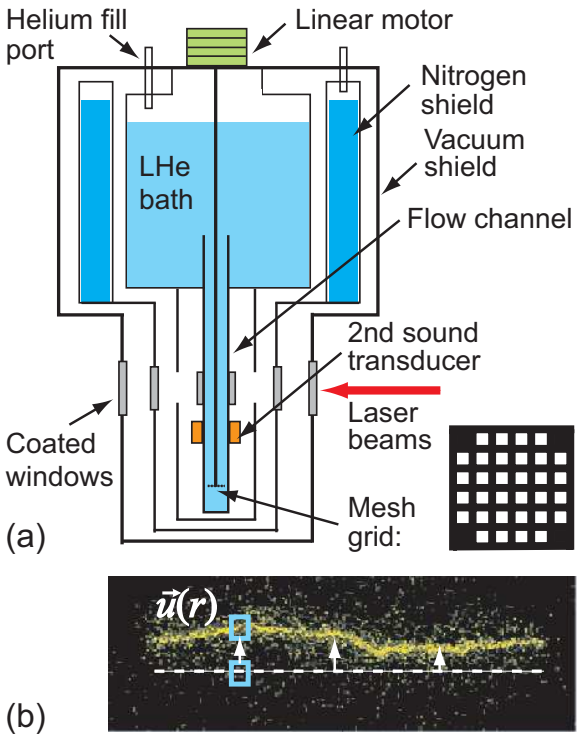

FIG. 1. (a) Schematic diagram of the experimental setup. (b) A sample image of the He_2^* molecular tracer line. The white dashed line serves to demonstrate the initial location of the trace line for velocity calculations.

To probe the flow, we send high-intensity femtosecond laser pulses through the channel via a pair of slits (about 1 mm in width and 10 mm in length) cut into opposite sides of the channel along its length. These slits are covered with indium sealed extension flanges and windows. As a consequence of femtosecond laser-field ionization [42], a thin line of He_2^* molecular tracers can be created along the beam path [35]. The initial thickness of the He_2^* tracer line is about 100 μm and its length matches the channel width. Above about 1 K, these He_2^* molecular tracers are completely entrained by the viscous normal fluid with negligible effect from the superfluid or quantized vortices [43]. A line of the molecules so created is then left to evolve for a drift time t_d of about 10–30 ms before it is visualized by laser-induced fluores-

cence using a separate laser sheet at 905 nm for imaging [35]. The streamwise velocity $v_y(x)$ can be determined by dividing the displacement of a line segment at x by t_d (see Fig. 1 (b)). The transverse velocity increments $\delta v_y(r) = v_y(x) - v_y(x+r)$ can thus be evaluated for structure function calculations. Additionally, the flow is also probed by a standard second-sound attenuation method [35, 44], revealing temporal decay of vortex line density $L(t)$ in the superfluid.

The grid starts moving from about 50 mm below the second sound sensors up to the uppermost position which is roughly 100 mm above the 1 cm ×1 cm visualisation region. Since no steady input of energy into the flow exists (except marginal parasitic radiative heat leaks), the flow starts to decay after the passage of the grid. As the origin of time for both visualization and second sound data, we take the instant when the grid passes the position where a tracer line would be inscribed. To study the time evolution, tracer line inscription is delayed until the desired decay time t. The measurement at each decay time is normally repeated $100 - 200$ times for statistical analysis, and every time the grid is towed anew. The experiments were performed in a temperature range $1.45 - 2.15$ K with quadratically increasing decay times (typically) 1, 2, 4, and 8 s. In all cases, the grid velocity v_g was set to either 300 or 50 mm/s.

III. EXPERIMENTAL RESULTS

A. Temporal evolution of the grid turbulence

In Fig 2, we show the profiles of the mean velocity $\overline{v_y}(x) = \langle v_y(x)\rangle_x$ and the velocity variance $\sigma(x) = \langle (v_y(x) - \overline{v_y})^2\rangle_x^{1/2}$ measured at 1.85 K across the channel at various decay times, where $\langle ...\rangle_x$ denotes an ensemble average of the results obtained at location x at each given decay time from the analysis of 100 deformed tracer line images. Similar to typical classical grid flows, the quantum flow in the immediate wake of the grid is not perfectly homogeneous and isotropic. The observed deformation of the tracer line suggests the existence of large scale eddies spanning the entire width of the channel following the towed grid. This is most likely caused by mechanical imperfections in the construction of the grid and its support. Nevertheless, this inhomogeneity quickly decays, being virtually completely eliminated within 4 s. In contrast with the mean flow and its marked initial inhomogeneity, the profile of the velocity variance $\sigma(x)$ is much more homogeneous, even at small decay times.

Despite the initial transient inhomogeneity at large scales, the temporal decays of the normal fluid turbulent kinetic energy, $K(t) = \langle \sigma^2 \rangle$, and the vortex line density in the superfluid, $L(t)$, exhibit clear decay characteristics of quasi-classical homogeneous isotropic turbulence. As discussed in detail in Refs. [24, 25], in the early decay stage of grid turbulence when the energy containing length scale ℓ_e grows from the injection scale (i.e., comparable to the mesh size) to the channel width, the characteristic decay exponents for quasi-classical homogeneous isotropic turbulence should be $K(t) \propto t^{-6/5}$ and $L(t) \propto t^{-11/10}$; in the late universal decay stage after ℓ_e is saturated by the channel width, $K(t) \propto t^{-2}$ and $L(t) \propto t^{-3/2}$ should be expected. These decay behaviors are clearly observed in our data. Note that at high towed-grid velocity (i.e., $v_g = 300$ mm/s), the saturation of ℓ_e likely occurs too rapidly for the early decay stage to be resolved. Furthermore, the transient inhomogeneity at small decay times may also affect the decay characteristics in this regime. At the lower grid velocity (i.e., $v_g = 50$ mm/s), the late universal decay stage appears at relatively large decay times (i.e., over 3–4 s) due to the slower increase of $\ell_e = \ell_e(t)$ [24, 25].

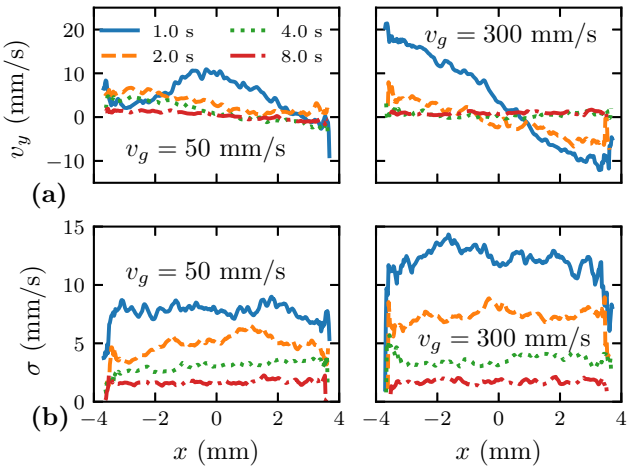

FIG. 2. (a) The ensemble-averaged velocity profile $v_y(x)$ across the channel at different decay times with grid velocities v_g as indicated. (b) The corresponding velocity variance $\sigma(x)$ profiles. The shown data are obtained at 1.85 K, at the indicated time instants.

B. Transverse velocity structure functions

The observed quasi-classical decay laws for $K(t)$ and $L(t)$ suggest that classical K41-like scalings in other turbulence statistics such as the velocity structure functions may also be expected. For instance, for fully developed classical homogeneous isotropic turbulence, the second order transverse velocity structure function, defined as

$$S_2^{\perp}(r) = \left\langle |v_y(x+r) - v_y(x)|^2 \right\rangle , \qquad (1)$$

should scale with the transverse separation distance r as $S_2^{\perp}(r) \propto r^{2/3}$ [45].

In the case of He II grid turbulence, the situation is more complex. Fig. 4 (a) shows typical examples of calculated $S_2^{\perp}(r)$ curves, for $T = 1.85$ K with a grid velocity of $v_g = 300$ mm/s at decay times t =1, 2, 4, and 8 s. Non-trivial power-law scalings of $S_2^{\perp}(r)$ are clearly

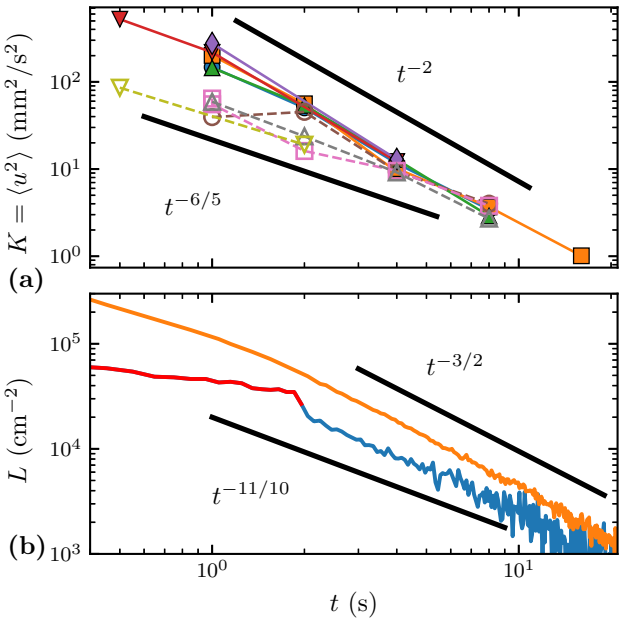

FIG. 3. (a) Decaying turbulent kinetic energy of the normal fluid, $K(t)$, and (b) vortex line density, $L(t)$, originating from towing the grid at 50 mm/s - empty symbols/blue line and 300 mm/s - full symbols/orange line. The energy decay is shown for temperatures 1.45 K (●), 1.65 K (■), 1.85 K (▲), 2.00 K (▼), 2.15 K (♦). The red line corresponds to the early decay of $L(t)$ for times when the grid is still moving. The decays are quasi-classical in character. The early part of the decay, when the energy containing length scale ℓ_e grows, displays the characteristic decay exponents $K(t) \propto t^{-6/5}$, $L(t) \propto t^{-11/10}$, while the late universal part of the decay, when ℓ_e is saturated by the channel size, obeys $K(t) \propto t^{-2}$, $L(t) \propto t^{-3/2}$ [24, 25]. These decay rates are illustrated by thick black lines. For towed grid velocity of 300 mm/s saturation occurs too early for the early part of the decay to be resolved. The shown data are obtained at 1.85 K.

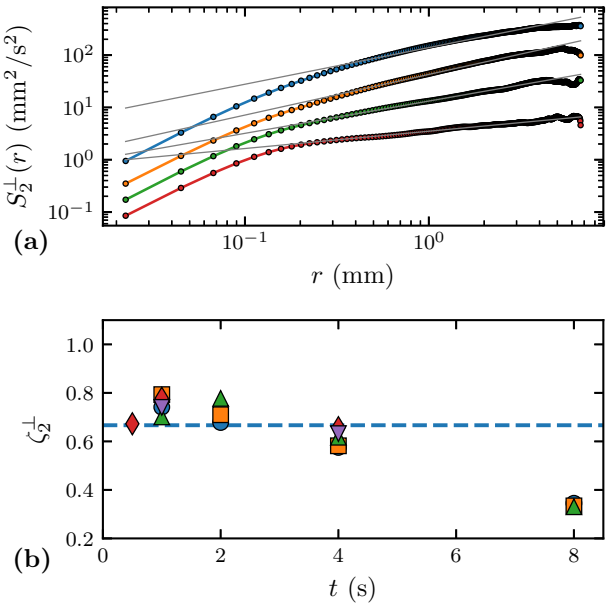

FIG. 4. (a) Calculated second order transverse velocity structure functions, $S_2^\perp(r)$, for $T = 1.85$ K at decay times (from up to down) t =1 s (●); 2 s (●); 4 s (●); and 8 s (●). The grid velocity is $v_g = 300$ mm/s. The grey solid lines represent power-law fits to the data in the range 0.2 mm $\leq r \leq$ 4 mm. (b) The scaling exponent $\zeta_2^\perp$ deduced from the power-law fits, such as shown in (a), at different temperatures: 1.45 K (●), 1.65 K (■), 1.85 K (▲), 2.0 K (♦), 2.15 K (▼). The dashed horizontal line shows the K41 scaling $\zeta_2^\perp = 2/3$.

observed in the scale range 0.2 mm $\leq r \leq$ 4 mm. The quadratic-like dependence of $S_2^\perp(r)$ at small r is probably caused by smearing of the measured velocity field limited by the width of the tracer line (i.e., about 100 μm) rather than due to the viscous flow. By fitting the data in 0.2 mm $\leq r \leq$ 4 mm with a power-law form $S_2^\perp(r) \sim r^{\zeta_2^\perp}$, the scaling exponent $\zeta_2^\perp$ can be extracted and is shown in Fig. 4 (b). Data at other temperatures are also included in this figure. We see that the data display slightly steeper than K41 scaling (i.e., $\zeta_2^\perp > 2/3$) for the 1 s and 2 s measurements and shallower than K41 (i.e., $\zeta_2^\perp < 2/3$) for 8 s and later measurements. We note in passing that this behavior is not unusual in classical decaying grid turbulence, especially before the wakes of individual bars of the grid fully coalesce [38, 46]. An additional factor to consider is possible parasitic radiative heating to the channel. This parasitic heating can cause weak thermal counterflow which may become important at long decay times when the grid turbulence strength is low.

Besides the second order structure function, the Kolmogorov 4/5-law also states that within the inertial range of scales, the third order longitudinal velocity structure function should be given by

$$S_3^\parallel(r) = (-4/5)\varepsilon r\,, \tag{2}$$

where $\varepsilon = -dK/dt$ is the energy dissipation rate [47, 48]. In our experiment, only the transverse velocity structure functions $S_n^\perp$ are accessible. Nevertheless, it can be shown [47] that the scaling is equal for both $S_2^\perp$ and $S_2^\parallel$ structure functions in three dimensional incompressible homogeneous isotropic turbulence and that the Kolmogorov 4/5-law ought to be valid also for the transverse structure function [49, 50]. On the other hand, there is an experimental evidence that the scaling exponent of $S_3^\perp$ in high Reynolds (Re) number atmospheric turbulence is slightly less (perhaps due to finite Re) but very close to unity [51]. We have evaluated the 3rd order transverse structure function $S_3^\perp(r) = \langle |v_y(x+r) - v_y(x)|^3 \rangle$ at 4 s decay time where classical scaling is clearly observed for $S_2^\perp(r)$ as shown in Fig. 4. The calculated values of $S_3^\perp(r)/r$ as a function of r are shown in Fig. 5 at various temperatures. Over a similar range, 0.2 mm $\leq r \leq$ 4 mm, we see a reasonably good linear dependence of $S_3^\perp(r)$ on

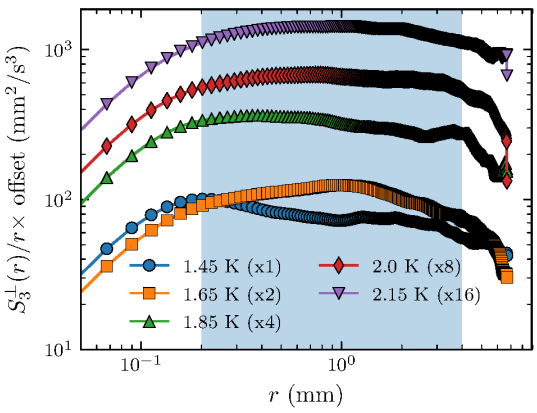

FIG. 5. Third order transverse velocity structure functions compensated by linear scaling, $S_3^\perp(r)/r$, plotted versus the separation distance r. Data for 300 mm/s grid velocity and 4 s decay time are shown for temperatures and offsets as indicated.

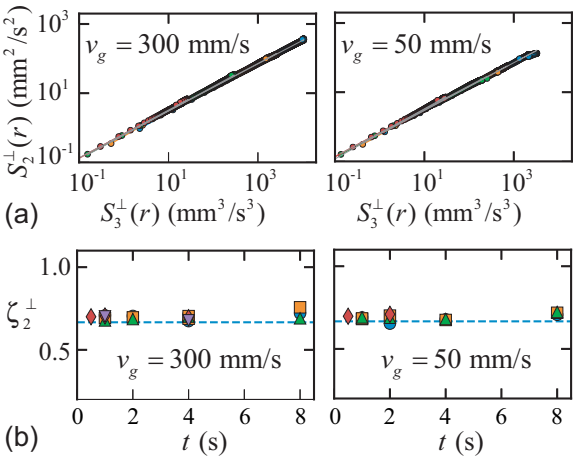

FIG. 6. (a) Extended self-similarity scaling of $S_2^\perp(S_3^\perp)$ for data obtained at $T = 1.85$ K and decay time $t = 4$ s. (b) The scaling exponent $\zeta_2^\perp$ extracted using the extended self-similarity hypothesis at various color coded temperatures: 1.45 K (●), 1.65 K (■), 1.85 K (▲), 2.0 K (♦), 2.15 K (▼). The dashed horizontal lines show the K41 scaling $\zeta_2^\perp = 2/3$.

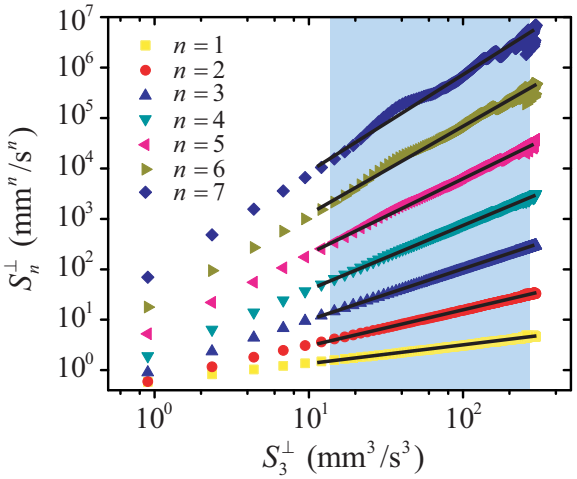

FIG. 7. Extended self-similarity. Transverse velocity structure functions $S_n^\perp$ for $n = 1 - 7$ are plotted versus $S_3^\perp$. The black lines are linear fits of $\log S_n^\perp$ vs. $\log S_3^\perp$ to the data that fall within the shadowed region that corresponds to the shadowed region in Fig. 5 where $S_3^\perp/r$ appears to be flat. The particular case shown is for 1.85 K, 300 mm/s grid velocity and 4 s decay time. Other cases appear qualitatively similar.

r, which coincides with the Kolmogorov 4/5 law in the inertial cascade range. Similar behavior is observed at 4 s for the other available temperatures and for both grid velocities, however, for decay times other than 4 s any linear scaling of $S_3^\perp(r)$ cannot be convincingly resolved.

The scaling exponents of the structure functions can also be obtained by using the so-called extended self-similarity hypothesis [52]. This hypothesis states that the scaling of a structure function $S_n(r)$ in the inertial scale range should be equivalent to the scaling of $S_n(r) \propto (S_3(r))^{\zeta_n}$. Indeed, structure function scalings based on extended self-similarity appear to be very robust and can extend down to the dissipative scale range even for turbulent flows with moderate Reynolds numbers [53], therefore allowing for significant improvement in experimental determination of the scaling exponent ζ_n [54]. In Fig. 6 (a), we show $S_2^\perp(r)$ versus $S_3^\perp(r)$ on a log-log plot for the data obtained at 1.85 K at 4 s decay time. For both grid velocities, a linear dependence of $\log S_2^\perp(r)$ on $\log S_3^\perp(r)$ is clearly seen and extends to a wide range of length scales. The values of the scaling exponent $\zeta_2^\perp$ deduced using the extended self-similarity hypothesis at various decay times and temperatures are shown in Fig. 6 (b), which display noticeably improved agreement with the K41 scaling.

C. Temperature dependence of intermittency corrections

Turbulence intermittency is normally evaluated by statistical analysis of the experimental data via higher order structure functions $S_n(r)$ that are more sensitive to the occurrence of rare events. The transverse velocity structure function of order n is defined through the transverse velocity increments as

$$S_n^\perp(r) = \langle|\delta v_y(r)|^n\rangle = \int_{-\infty}^{\infty} \mathrm{d}x|x|^n \,\mathrm{PDF}_r(x), \qquad (3)$$

where $\mathrm{PDF}_r(x)$ represents the probability density function of $\delta v_y(r)$. In order for $S_n^\perp$ to be evaluated accurately, the experimental estimation of the PDF needs to have well-resolved tails because of the x^n term in the integral, which in turn requires very large data sets. Our setup does not presently allow for the collection of very

large data sets. Typical data sets are limited to about 10^4 samples. Another issue is that, although the individual He_2^* molecules are of nm size and are true tracers of normal fluid flow, we cannot detect individual tracers - a large number of them closely spaced are needed to satisfy our sensitivity limit. Rare events resulting in large departures of individual tracers are therefore invisible to us. In other words, our experimentally resolved length scale is limited by the thickness of the deformed tracer line, $\ell_{exp} \simeq 100$ μm. A more detailed discussion of the uncertainties associated with the calculated structure functions is provided in the Appendix.

According to the K41 theory, for fully developed homogeneous isotropic turbulence in classical fluids without any intermittency, the structure function in the inertial cascade range should scale as $S_n(r) \propto r^{\zeta_n}$ with the scaling exponent $\zeta_n = n/3$ [45]. Intermittency in real turbulent flows of conventional viscous fluids leads to corrections of the scaling exponents, and this correction becomes more pronounced at large n. In order to reliably determine the actual scaling exponents of the transverse structure functions $\zeta_n^\perp$ in our quantum grid turbulence, we again utilize the extended self-similarity hypothesis. Furthermore, we focus our study on data obtained at 4 s decay time, since the scalings of $S_2^\perp(r)$ and $S_3^\perp(r)$ presented in the previous section suggest fully developed homogeneous isotropic turbulence at this decay time.

In Fig. 7, the calculated $S_n^\perp(r)$ versus $S_3^\perp(r)$ for $n = 1$ to 7 are shown for data obtained at 1.85 K with a grid velocity $v_g = 300$ mm/s. Clear power law dependence of $S_n^\perp(r)$ on $S_3^\perp(r)$ is seen, which extends to the smallest scales probed in the experiment. Data obtained at other temperatures appear qualitatively similar. We then perform a power-law fit of the form $S_n^\perp(r) \propto \left(S_3^\perp(r)\right)^{\zeta_n^\perp}$ to the data (shown as black lines in Fig. 7). The fit is restricted to the range of scales 0.2 mm $< r <$ 4 mm where $S_3^\perp(r)/r$ is reasonably flat, supporting the existence of an inertial cascade.

The deduced scaling exponents $\zeta_n^\perp$, for all investigated temperatures, as a function of the order n are shown in Fig. 8. This figure represents the central result of our work. It is remarkable that the deduced scaling exponents closely follow the recent theoretical prediction of Biferale *et al.* [12], i.e., temperature dependent intermittency corrections of the structure function scaling exponents with a maximum deviation from the K41 scaling at 1.85 K. It should be noted that, while the result for $t = 4$ s is robust, for small decay times (for additional discussion see the Appendix) and for slower grid velocity the conclusion is not as clear, which is likely due to insufficiently developed turbulence.

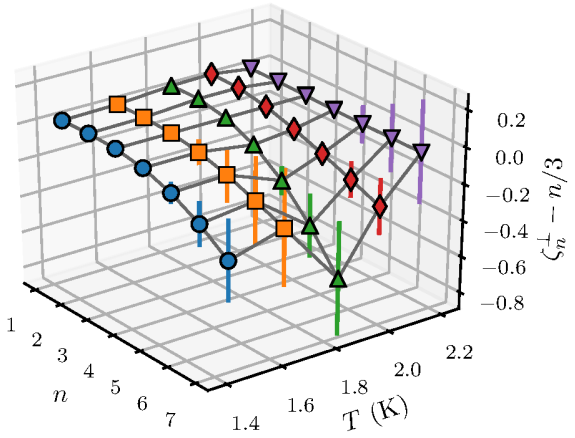

FIG. 8. Intermittency corrections to the scaling exponents of the transverse structure functions deduced through extended self-similarity for data obtained at 4 s decay time and with grid velocity $v_g = 300$ mm/s. The 3D plot shows the temperature dependent deviation of scaling exponents from K41 scaling – 1.45 K (●), 1.65 K (■), 1.85 K (▲), 2.00 K (♦), 2.15 K (▼).

IV. DISCUSSION

Let us compare our results with similar experimental data available. The recent Grenoble measurements of Rusaouen *et al.* [13] in the wake of a disk in the two-fluid region of superfluid ^{4}He found no appreciable temperature dependence in intermittency corrections. The results of the Grenoble experiment and our experiment therefore appear to be controversial. Nevertheless, there are several reasons why the two experiments may show different results. First, the prediction of temperature dependent enhanced intermittency is explained by the authors of ref. [10, 12] via a flip-flop scenario – a random energy transfer between the normal and superfluid components due to mutual friction. While He_2^* molecules in our experiment probe the normal fluid solely, the cantilever anemometer and pressure probes used in the Grenoble experiment [13] may not sense such a flip-flop exchange of energy, as it probes both fluids simultaneously. Furthermore, the sizes of the probes used in the Grenoble experiment are typically much larger than the quantum length scale $\ell_{\rm Q}$. Indeed, recent particle image velocimetry visualization experiments by La Mantia *et al.* in Prague [55, 56], utilizing solid hydrogen/deuterium particles a few μm in size, reveal a crossover from classical to quantum signatures of turbulence as the probed length scale crosses $\ell_{\rm Q}$. As discussed previously, our smallest accessible length scale $\ell_{\rm exp}$ - the width of tracer line - is about 100 μm. At a decay time of 4 s in our experiment, $\ell_{\rm Q} \simeq L^{-1/2}$ is also about 100 μm (see Fig. 3). The quantum length scale $\ell_{\rm Q}$ increases at later decay times as the vortex line density $L(t)$ decays. Therefore, our data sets sample the velocity field near to or below $\ell_{\rm Q}$, where one expects the effect of quantized vorticity to become apparent. In the experiments of Rusaouen *et al.* [13], taking the outer scale of turbulence to be their channel size $\simeq 5$ cm, effective kinematic viscosity $\nu_{\rm eff} \simeq 0.1\kappa$ and following the estimations in Babuin *et al.* [28], the κ-based large

scale Reynolds number at 1.85 K is roughly 6×10^4. This corresponds to $\ell_{\mathrm{Q}} \approx 7$ μm. The cantilever probe has a sensing area of 32×375 μm, which would translate to more than 100 quantized vortices, even if we neglect the likely increase of L in the vicinity of any obstacles [57]. The experiment of Rusaouen *et al.* [13] therefore naturally measures the same intermittency corrections as in classical turbulence.

V. CONCLUSIONS

We have designed and performed an experiment to study quasiclassical turbulence in the wake of a towed grid in He II, using a recently developed He_2^* molecular tracer-line tagging velocimetry technique and a traditional second sound attenuation method. Our main result is that, despite the fact that our data sets are not as large as they ideally ought to be, extended self-similarity reveals temperature dependent intermittency corrections that peak in the vicinity of 1.85 K, in excellent agreement with recent theoretical predictions [10, 12]. The universality of the intermittency corrections found in many different turbulent flows of classical viscous fluids [46] therefore cannot be extended to quantum turbulence in superfluid ^{4}He. It seems that the role of cliffs that are thought to be responsible for rare but intense events resulting in intermittency corrections in classical turbulence is at least partly played by quantized vortices in He II. In order to observe this "quantum" intermittency, similarly as in classical homogeneous isotropic turbulence, where one has to resolve small scales down to the Kolmogorov dissipation scale, in quantum turbulence one needs to resolve scales below the quantum length scale ℓ_{Q}.

ACKNOWLEDGMENTS

We thank V. S. L'vov, K. R. Sreenivasan and W. F. Vinen for fruitful discussions. WG acknowledges the support by the National Science Foundation under Grant No. DMR-1807291. The experiment was conducted at the National High Magnetic Field Laboratory, which is supported by NSF Grant No. DMR-1644779 and the state of Florida. EV and LS thank the Czech Science Foundation for support under GAČR 17-03572S.

APPENDIX: ESTIMATION OF STRUCTURE FUNCTION ERRORS

High order structure functions required to estimate the intermittency corrections are sensitive to rare events – events of low probability which would contribute to the "tails" of the statistical distribution. In samples of limited size, these tails could be under-resolved, what could lead to an erroneous estimation of the structure functions. We adopt a simple strategy to estimate these errors

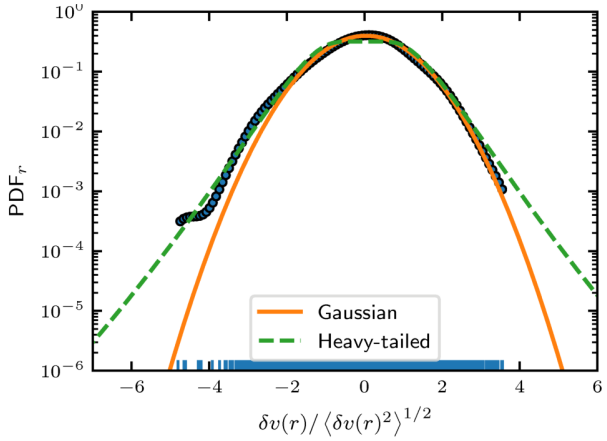

FIG. 9. Probability distribution function of the velocity increments. The rug plot shows the actual data set used for the KDE. The data shown is for 1.45 K, 300 mm/s grid velocity and 4 s decay time.

due to lack of statistics: an estimate of the PDF is calculated from the measured data, which is then extended beyond the range of experimental data using a fit to a particular choice of a heavy-tailed statistical distribution. The difference between the value obtained through Eq. (3) using either a non-extrapolated or extrapolated PDF is then used as the estimate of the error caused by under-resolved tails of the statistical distribution.

We calculate an estimation of the PDF from the measured velocity increments using the kernel density estimation (KDE) as

$$\mathrm{PDF}_r^{\mathtt{KDE}}(x) = \frac{1}{N}\sum_{i=0}^{N} \frac{1}{\sqrt{2\pi b}} e^{-(x-\delta v(r)_i)^2/2b^2}, \qquad (4)$$

where the sum runs through all N measured samples of $\delta v(r)_i$ at a given separation r. The result, for a particular case, is shown in Fig. 9. The number of samples for the 4 s decay data sets is in Fig. 10.

To estimate the error in calculating a given moment, we extrapolate the estimated PDF either by natural extension of the KDE (4) outside the range of the data set, or by using fits to either the normal (Gaussian) distribution,

$$\mathrm{PDF}_r^{\mathtt{N}}(v) = \frac{1}{\sqrt{2\pi s^2}} \exp\left(-\frac{v^2}{2s^2}\right), \qquad (5)$$

or a particular case of heavy-tailed distribution

$$\mathrm{PDF}_r^{\mathtt{HT}}(v) = \frac{\exp(s^2/2)}{4m}\left[1 - \mathrm{erf}\left(\frac{\log\left(\frac{|v|}{m}\right) + s^2}{\sqrt{2}s}\right)\right], \qquad (6)$$

where s and m are adjustable parameters. This form of the PDF was found to describe Lagrangian accelerations [58], but in our case it is used simply for reasons

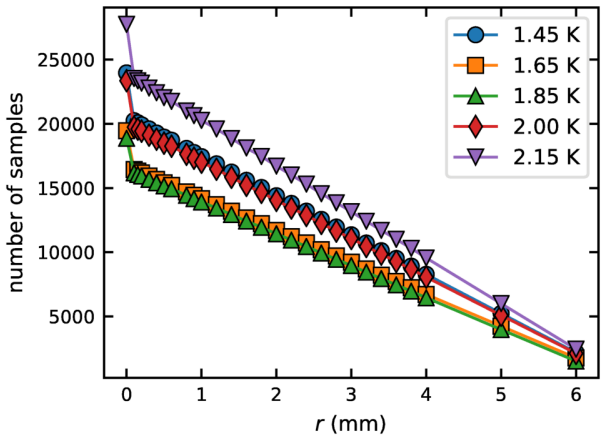

FIG. 10. Number of velocity increment samples as a function of separation for 4 s data sets and all experimental temperatures.

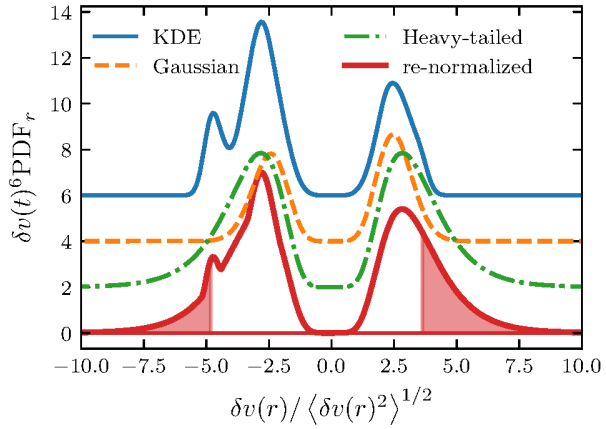

FIG. 11. Calculation of the sixth moment of the velocity increment distribution. The curves are offset along the y-axis with an offset incrementing by 2. Same data set as in Fig. 9.

of convenience (we measure Eulerian transverse velocity increments), as it allows for smooth varying of the weight of the tails. Note that using a distribution with power law tails would be inconsistent in our case as such a distribution would render the moment of sufficiently high orders undefinable. Using the two fits and the KDE, we construct a new PDF with the shape of an envelope (point-wise maximum) of the three estimates. The point-wise maximum breaks the normalization of the probability density function which needs to be re-normalized to the integral of unity. This effectively decreases the probability in the central peak and moves it towards the tails. An illustration of this procedure is shown in Fig. 11 for calculating the sixth order moment of a distribution.

As an error estimate of the moment, we take the absolute value of the difference between the moment calculated using the natural extension of the KDE (4) and the

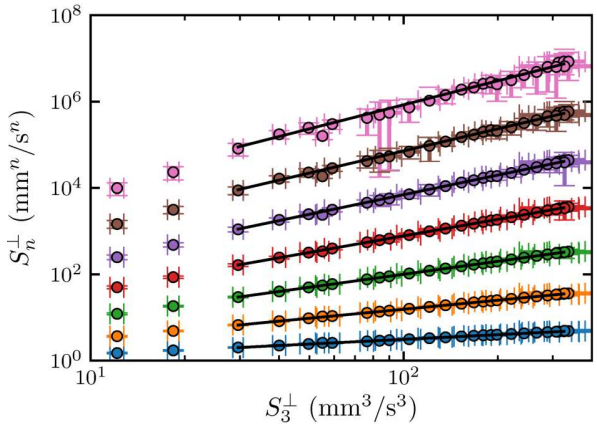

FIG. 12. Structure functions $S_n^\perp$ of orders 1 to 7 as a function $S_3^\perp$ at 1.85 K, 4 s decay time and associated error bars calculated using the scheme described in Sec. V. These plots are analogues of curves in Fig. 7.

re-normalized PDF. Graphically, this is given approximately by the area under the tails of the re-normalized PDF outside the range of the data set, shown by the shaded area in Fig. 11. For calculation of the value of the structure function, we use $\mathrm{PDF}^{\mathrm{KDE}}$. This estimate has a very sharp cutoff (faster than normal distribution) outside the range of the experimental data set (essentially equivalent to extending a histogram with zeros) so that the value is not affected by any particular choice of extrapolation. The result is shown in Fig. 12. We note that the errors of the structure functions render flatness (ratio $S_4^\perp/(S_2^\perp)^2$) unusable for quantitative analysis of intermittency.

We also calculate the structure functions directly from the ensemble average, using the definition Eq. (3). The intermittency corrections resulting from both procedures are shown in Fig. 13. Due to the rather arbitrary choice of the heavy-tailed distribution, the definition of the re-normalized PDF and the definition of the error itself, we also calculate the errors using a bootstrapping scheme [59]. The set of all N measured samples entering the calculation of $S_n^\perp$ in Eq.(3) is sampled at random (with possible repetitions and omissions) to form $B = 5000$ new synthetic sets of length N. The standard deviation of the moment (3) calculated for these new B data sets is used as the error. The resulting error bars were significantly smaller than those calculated using the re-normalized PDF and the results were consistent with the straightforward calculation by directly averaging the sample and are not shown here.

One might justifiably become alarmed by the correlation between the number of samples in Fig. 10 and the deviation from K41 scaling in Fig. 13. This, however, appears to be a coincidence. The correlation is not present for other data sets, and artificially restricting the data sets at 4 s to a random choice (with replacement) of 10000, 5000 or 2000 samples does not have a strong

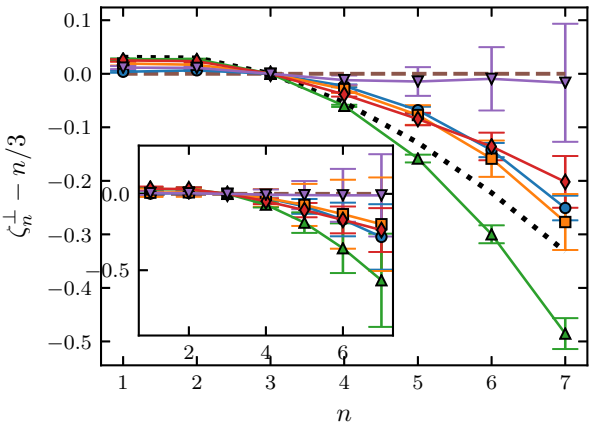

FIG. 13. Structure function scaling exponents calculated from PDF-derived structure functions. The error bars are just the standard errors of a total least squares linear regression, also known as orthogonal distance regression. The inset shows scaling exponents of structure functions calculated using Eq. (3), see the main text for how the error bars are calculated for the data shown in the inset. All data for 4 s decay time and 300 mm/s grid velocity. The temperatures are 1.45 K (●), 1.65 K (■), 1.85 K (▲), 2.00 K (♦), 2.15 K (▼). The black dotted line shows the prediction of the She-Leveque theory[6].

effect on the observed scaling exponents (although the quality of the structure functions does decrease, as is to be expected). In particular, the minimum near 1.85 K persists unaffected.

[1] A. N. Kolmogorov, J. Fluid Mech. **13**, 82 (1962).
[2] C. Meneveau and K. R. Sreenivasan, Phys. Rev. Lett. **59**, 1424 (1987).
[3] K. R. Sreenivasan and R. A. Antonia, Ann. Rev. Fluid Mech. **29**, 435 (1997).
[4] L. Biferale, Ann. Rev. Fluid Mech. **35**, 441 (2003).
[5] L. Biferale and R. Benzi, J. Stat. Phys. **161**, 1351 (2015).
[6] Z.-S. She and E. Leveque, Phys. Rev. Lett. **72**, 336 (1994).
[7] J. Schumacher, J. D. Scheel, D. Krasnov, D. A. Donzis, V. Yakhot, and K. R. Sreenivasan, Proc. Natl. Acad. Sci. **111**, 10961 (2014).
[8] J. Maurer and P. Tabeling, Europhys. Lett. **43**, 29 (1998).
[9] J. Salort, B. Chabaud, E. Lévêque, and P.-E. Roche, J. Phys. Conf. Ser. **318**, 042014 (2011).
[10] L. Boué, V. L'vov, A. Pomyalov, and I. Procaccia, Phys. Rev. Lett. **110**, 014502 (2013).
[11] V. Shukla and R. Pandit, Phys. Rev. E **94**, 043101 (2016).
[12] L. Biferale, D. Khomenko, V. L'vov, A. Pomyalov, I. Procaccia, and G. Sahoo, Phys. Rev. Fluids **3**, 024605 (2018).
[13] E. Rusaouen, B. Chabaud, J. Salort, and P.-E. Roche, Phys. Fluids **29**, 105108 (2017).
[14] D. R. Tilley and J. Tilley, *Superfluidity and Superconductivity*, 3rd ed. (Institute of Physics Publishing, Bristol and Philadelphia, 1990).
[15] R. J. Donnelly, *Quantized Vortices in Helium II* (Cambridge University Press, Cambridge, 1991).
[16] C. F. Barenghi, L. Skrbek, and K. R. Sreenivasan, Proc. Natl. Acad. Sci. **111**, 4647 (2014).
[17] W. Vinen and J. Niemela, J. Low Temp. Phys. **128**, 167 (2002).
[18] L. Skrbek and K. Sreenivasan, Phys. Fluids **24**, 011301 (2012).
[19] A. Marakov, J. Gao, W. Guo, S. W. Van Sciver, G. G. Ihas, D. N. McKinsey, and W. F. Vinen, Phys. Rev. B **91**, 094503 (2015).
[20] D. Khomenko, V. S. L'vov, A. Pomyalov, and I. Procaccia, Phys. Rev. B **93**, 014516 (2016).
[21] J. Gao, E. Varga, W. Guo, and W. F. Vinen, Phys. Rev. B **96**, 094511 (2017).
[22] J. Gao, W. Guo, V. S. L'vov, A. Pomyalov, L. Skrbek, E. Varga, and W. F. Vinen, JETP Lett. **103**, 648 (2016).
[23] S. Babuin, V. S. L'vov, A. Pomyalov, L. Skrbek, and E. Varga, Phys. Rev. B **94**, 174504 (2016).
[24] S. R. Stalp, L. Skrbek, and R. J. Donnelly, Phys. Rev. Lett. **82**, 4831 (1999).
[25] L. Skrbek and S. R. Stalp, Phys. Fluids **12**, 1997 (2000).
[26] J. Gao, W. Guo, and W. F. Vinen, Phys. Rev. B **94**, 094502 (2016).
[27] J. Gao, W. Guo, S. Yui, M. Tsubota, and W. F. Vinen, Phys. Rev. B **97**, 184518 (2018).
[28] S. Babuin, E. Varga, L. Skrbek, E. Lévêque, and P.-E. Roche, Europhysics Lett. **106**, 24006 (2014).
[29] L. Skrbek, J. J. Niemela, and R. J. Donnelly, J. Phys.: Condens. Matter **11**, 7761 (1999).
[30] R. J. Donnelly, *High Reynolds Number Flows Using Liquid and Gaseous Helium* (Springer-Verlag, New York, 1991).
[31] C. F. Barenghi, V. S. Lvov, and P.-E. Roche, Proc. Nat.

Acad. Sci. **111**, 4683 (2014).
[32] A. N. Kolmogorov, in *Dokl. Akad. Nauk SSSR*, Vol. 30 (1941) pp. 299–303.
[33] P.-E. Roche, C. F. Barenghi, and E. Leveque, Europhys. Lett. **87**, 54006 (2009).
[34] J. Salort, C. Baudet, B. Castaing, B. Chabaud, F. Daviaud, T. Didelot, P. Diribarne, B. Dubrulle, Y. Gagne, F. Gauthier, A. Girard, B. Hbral, B. Rousset, P. Thibault, and P.-E. Roche, Phys. Fluids **22**, 125102 (2010).
[35] J. Gao, A. Marakov, W. Guo, B. T. Pawlowski, S. W. Van Sciver, G. G. Ihas, D. N. McKinsey, and W. F. Vinen, Rev. Sci. Instrum. **86**, 093904 (2015).
[36] W. Vinen, Proc. R. Soc. **240**, 128 (1957).
[37] H. J. S. Fernando and P. D. De Silva, Phys. Fluids A **5**, 1849 (1993).
[38] G. Comte-Bellot and S. Corrsin, J. Fluid Mech. **25**, 657 (1966).
[39] H. Tennekes and J. L. Lumley, *A first course in turbulence* (MIT press, 1972).
[40] M. Sinhuber, E. Bodenschatz, and G. P. Bewley, Phys. Rev. Lett. **114**, 034501 (2015).
[41] S. R. Stalp, J. J. Niemela, W. F. Vinen, and R. J. Donnelly, Phys. Fluids **14**, 1377 (2002).
[42] A. V. Benderskii, R. Zadoyan, N. Schwentner, and V. A. Apkarian, J. Chem. Phys. **110**, 1542 (1999).
[43] D. E. Zmeev, F. Pakpour, P. M. Walmsley, A. I. Golov, W. Guo, D. N. McKinsey, G. G. Ihas, P. V. E. McClintock, S. N. Fisher, and W. F. Vinen, Phys. Rev. Lett. **110**, 175303 (2013).
[44] S. Babuin, M. Stammeier, E. Varga, M. Rotter, and L. Skrbek, Phys. Rev. B **86**, 134515 (2012).
[45] J. O. Hinze, *Turbulence*, 2nd ed. (McGraw-Hill, New York, 1975).
[46] K. R. Sreenivasan and R. Antonia, Annu. Rev. Fluid Mech. **29**, 435 (1997).
[47] U. Frisch, *Turbulence: The legacy of A. N. Kolmogorov* (Cambridge university press, 1995).
[48] A. Noullez, G. Wallace, W. Lempert, R. B. Miles, and U. Frisch, J. Fluid Mech. **339**, 287 (1997).
[49] V. S. L'vov, E. Podivilov, and I. Procaccia, arXiv preprint chao-dyn/9705016 (1997).
[50] O. Chkhetiani, JETP Lett. **63**, 808 (1996).
[51] B. Dhruva, Y. Tsuji, and K. R. Sreenivasan, Phys. Rev. E **56**, R4928 (1997).
[52] R. Benzi, L. Biferale, G. Paladin, A. Vulpiani, and M. Vergassola, Phys. Rev. Lett. **67**, 2299 (1991).
[53] R. Benzi, S. Ciliberto, C. Baudet, G. Ruiz Chavarria, and R. Tripiccion, Europhys. Lett. **24**, 275 (1993).
[54] B. Dubrulle, Phys. Rev. Lett. **73**, 959 (1994).
[55] M. La Mantia and L. Skrbek, Europhysics Lett. **105**, 46002 (2014).
[56] P. Švančara and M. La Mantia, J. Fluid Mech. **832**, 578 (2017).
[57] P. Hrubcová, P. Švančara, and M. La Mantia, Phys. Rev. B **97**, 064512 (2018).
[58] N. Mordant, A. M. Crawford, and E. Bodenschatz, Phys. Rev. Lett. **93**, 214501 (2004).
[59] B. Efron, Biometrika **68**, 589 (1981).

J Low Temp Phys (2016) 183:215–221
DOI 10.1007/s10909-015-1430-7

Backreaction of Tracer Particles on Vortex Tangle in Helium II Counterflow

E. Varga[1] · C. F. Barenghi[2] · Y. A. Sergeev[3] · L. Skrbek[1]

Received: 1 July 2015 / Accepted: 14 December 2015 / Published online: 29 December 2015

Abstract We report computer simulations of the interaction of seeding particles with quantized vortices and with the normal fluid flow in thermal counterflow of superfluid ^{4}He. We show that if the number of particles is too large, the vortex tangle is significantly affected, posing problems in the interpretation of visualization experiments. The main effects are an increase in vortex line density and a change in polarization of the vortex tangle, caused by the action of the Stokes drag of the viscous normal fluid on the trapped particles. We argue that in the case of large particle number, typically used for the particle image velocimetry technique, the tangle properties might become significantly changed. On the contrary, the particle tracking velocimetry technique that uses smaller particle concentration should not be appreciably affected.

Keywords Superfluid 4He · Quantum turbulence · Visualization · Numerical simulations

1 Introduction

Flow visualization is one of the most valuable experimental tools in fluid dynamics. A variety of techniques exists which seed the fluid with contrasting agent that can be easily observed, e.g. by a sensitive camera [1]. Visualization techniques have already

✉ E. Varga
varga.emil@gmail.com

1 Faculty of Mathematics and Physics, Charles University, Ke Karlovu 3, Prague, Czech Republic

2 Joint Quantum Centre Durham-Newcastle, School of Mathematics and Statistics, Newcastle University, Newcastle upon Tyne NE1 7RU, UK

3 Joint Quantum Centre Durham-Newcastle, School of Mechanical and Systems Engineering, Newcastle University, Newcastle upon Tyne NE1 7RU, UK

been used at low temperatures to study both classical and quantum cryogenic flows, even though their application is difficult, for various technical reasons. As for quantum flows and turbulence [2] (so far of superfluid ^{4}He, known as He II), application of visualization techniques face additional fundamental difficulties, due to the existence of two velocity fields and the interaction of seeding particles with quantized vortices [3]. Despite these problems, the implementation of visualization methods in He II has led to the direct visualization of quantized vortices in [4] and several other important results(see [5] and references therein). In comparison with classical fluid dynamics, visualization of quantum flows is not yet firmly established and the interpretation of experiments poses important fundamental questions.

The questions arise because He II differs from classical liquids in several important aspects [2]. For 1 K $< T < T_\lambda$, where visualization methods are usually applied, He II can be described as consisting of two fluids—the inviscid superfluid component carrying no entropy, and the viscous normal fluid behaving approximately as an ordinary Navier–Stokes fluid. Turbulence in the superfluid component can only exist in the form of a complex tangle of *quantized vortices*—thin topological defects around which the circulation is restricted to single *quantum of circulation* $\kappa = h/M$, where h is the Planck constant and M is the mass of ^{4}He atom.

This complex nature of He II poses challenges for the interpretation of visualization experiments. Here, we consider potential problems that might occur in the interpretation of particle tracking velocimetry (PTV) and/or particle image velocimetry (PIV) techniques, both relying on observing seeding particles (such as solid hydrogen or deuterium flakes [5]) suspended in the flow. These particles interact with both the normal and superfluid velocity fields [3,5] and can become trapped on the cores of quantized vortices. However, in most cases they are treated as non-intrusive, passive probes of the flow under study. It is therefore of great interest to try to assess the degree of non-ideality of the particles, which might lead to a distorted physical information about the quantum flow under study and, consequently, to a misleading conclusion on some important aspects of quantum turbulence.

To this end, we perform a series of numerical experiments, extending the work of Mineda et al. [6], which simulates the movement of seeding particles in the velocity field due to the counterflow tangle of quantized vortices. We find that a trapped particle deforms the vortex on which it is trapped, stretching it in the direction of the flowing normal fluid, via the action of the Stokes drag. A large number of particles can increase the vortex line density by up to 100 % and change its polarization. We compare these results with those obtained by modelling trapped particles as ideal tracers of the vortices and find significant differences, both in the probability of trapping and the velocity statistics.

2 Computational Setup and Results

We perform a vortex filament simulation of counterflowing He-II in periodic boundary conditions. The normal fluid velocity $\boldsymbol{v}_n$ is uniform and statically prescribed. To a statistically converged counterflow tangle, we add inertial particles at random positions

and initially zero velocities. The movement of both vortices and particles is described below.

The quantized vortices in He-II are modelled, following the seminal work of Schwarz [7], as one-dimensional spatial curves of arbitrary shape. These vortex lines (labelled $\boldsymbol{s}(\xi)$, where ξ is the arc length along the line) induce a superfluid velocity $\boldsymbol{v}_\mathrm{s}$ given by the standard [7–9] Biot–Savart integral

$$\boldsymbol{v}_\mathrm{s}(\boldsymbol{r}) = \frac{\kappa}{4\pi} \oint_{\mathcal{L}} \frac{\boldsymbol{s}'(\xi) \times [\boldsymbol{r} - \boldsymbol{s}(\xi)]}{|\boldsymbol{r} - \boldsymbol{s}(\xi)|^3} \,\mathrm{d}\,\xi, \tag{1}$$

with $\mathcal{L}$ denoting the entire configuration of lines in the vortex tangle. The movement of the vortices themselves is determined from the balance of forces, namely Magnus force and mutual friction, under the assumption that the vortices are massless (e.g. [6]). The resulting equation of motion is

$$\dot{\boldsymbol{s}} = \boldsymbol{v}_\mathrm{s}'(\boldsymbol{s}) + \alpha \boldsymbol{s}' \times (\boldsymbol{v}_n - \boldsymbol{v}_\mathrm{s}) + \alpha' \boldsymbol{s}' \times \Big[\boldsymbol{s}' \times (\boldsymbol{v}_n - \boldsymbol{v}_\mathrm{s})\Big], \tag{2}$$

where the dot denotes the time derivative and the prime denotes derivative with respect to the arc length. The prime on the superfluid velocity in (2) denotes the standard desingularization of the Biot–Savart integral.

Particle dynamics Several past studies were concerned with modelling inertial particles that are either far away the from cores of the quantized vortices [3,10] or remain trapped on them [6]. Studies that address the full range of possible interactions of finite spherical particles and quantized vortex lines have already been performed [11], however, the computational complexity of the methods used there prevents the scaling of the simulation to high densities of vortex tangle and/or high number of particles.

In the present study, we adopt a mixed approach. Unlike [11], particles are considered as point-like objects. Particles sufficiently far from the vortex lines are considered free and, following [10], interact with vortices only through inertial forces and with normal fluid inertially and viscously. The resulting equation of motion is

$$\frac{\mathrm{d}\,\boldsymbol{v}_\mathrm{p}}{\mathrm{d}\,t} = \frac{\rho_\mathrm{s}}{\rho} \frac{\mathrm{D}\,\boldsymbol{v}_\mathrm{s}}{\mathrm{D}\,t} + \frac{\rho_\mathrm{s}}{\rho} \frac{\mathrm{D}\,\boldsymbol{v}_n}{\mathrm{D}\,t} - \frac{\boldsymbol{v}_\mathrm{p} - \boldsymbol{v}_n}{\tau}, \tag{3}$$

where $\boldsymbol{v}_\mathrm{p}$ is the free particles' velocity $\mathrm{D}\,\boldsymbol{v}/\mathrm{D}\,t = \partial \boldsymbol{v}/\partial t + (\boldsymbol{v}\cdot\nabla)\boldsymbol{v}$ and $\tau = 2a^2\rho/9\mu_n$ is the viscous relaxation time, with ρ being the density of fluid or the particles (particles are assumed to be neutrally buoyant), a is the radius of the particles and μ_n denotes the dynamic viscosity of the normal fluid component. Time-independent and uniform normal fluid velocity is used in the present simulations, therefore the second term on the right-hand side of (3) is identically zero.

When a particle comes to within 5 μm (the *trapping distance*) of a vortex a new discretisation point along the line is created in the particle's vicinity (such that first and second derivative of the line is preserved) into which the particle is placed, while retaining its momentum. This *trapped particle* then occupies this point in a manner described below. The trapped particle experiences additional forces acting on it—namely the vortex tension, the Magnus force and the mutual friction [6]. It should

be noted, however, that the particles are still assumed to be infinitesimally small and therefore a particle trapped on a vortex does not modify the superfluid velocity induced by the vortex, except possibly deforming the vortex itself. The modified equation of motion for the trapped particles becomes

$$\frac{\mathrm{d}\,\boldsymbol{v}_\mathrm{p}}{\mathrm{d}\,t} = \frac{\boldsymbol{v}_n - \boldsymbol{v}_\mathrm{p}}{\tau} + \frac{\rho_\mathrm{s}}{\rho}\frac{\mathrm{D}\,\boldsymbol{v}_s'}{\mathrm{D}\,t} + \Big\{T_0\big(\boldsymbol{s}_+' - \boldsymbol{s}_-'\big) + \rho_\mathrm{s}\kappa\boldsymbol{s}' \times (\boldsymbol{v}_\mathrm{p} - \boldsymbol{v}_\mathrm{s}) + \Big(\gamma_0\boldsymbol{s}' \times \big[\boldsymbol{s}' \times (\boldsymbol{v}_\mathrm{p} - \boldsymbol{v}_n)\big] + \gamma_0'\boldsymbol{s}' \times (\boldsymbol{v}_\mathrm{p} - \boldsymbol{v}_n)\Big)\Delta\xi\Big\}\frac{1}{M_\mathrm{eff}}, \tag{4}$$

where $T_0 = \rho_\mathrm{s}\kappa^2/4\pi\ \log[2\sqrt{l_+l_-}/\sqrt{e}\xi_0]$ is the vortex tension (energy of the vortex per unit length) with l_+, l_- being the distances to the neighbouring discretisation points along the line and $\xi_0 \approx 1$ Å being the vortex core parameter, γ_0 and γ_0' are mutual friction parameters, $\boldsymbol{s}'_-$ and $\boldsymbol{s}'_+$ are right and left tangents of the vortex line; $\boldsymbol{s}'$ is the tangent at the trapping site calculated as if the line were smooth, $M_\mathrm{eff} = 3/2\rho V_p$ is the effective mass of the particle (v_p being its volume) and $\Delta\xi$ is the maximum discretisation distance along the vortex, 1.6×10^{-5} m.

From the point of view of the vortex, the equation of motion is changed from (2) for the single discretisation point that hosts the trapped particle, to (4). Even though the equation of motion for only a single point is changed, this affects the local geometry of the line thus affecting the neighbourhood of this point as well. The present work differs from that of Mineda et al. [6] in that we consider both free and trapped particles simultaneously. This requires that the particles, once trapped, can de-trap and become free again. Algorithmically, the particles de-trap only if they are attached to a small vortex loop that is annihilated as a part of small-scale numerical cutoff. This mechanism roughly corresponds to a physical scenario (see Fig. 1a) where a vortex loop collapses into the surface of the particle or (Fig. 1b) the trapped particle produces a cusp on the line sharp enough to cause reconnection producing a small loop that is immediately annihilated.

This treatment of trapped particles is compared with the limiting case of particles so light that they do not affect the movement of the vortices in any way. In this case, the particle is simply attached to a discretisation point along the vortex line and follows its movement—that is, its movement is described by (2). This case will be henceforth referred to as "ideal" particle and the case described above as "non-ideal".

We performed several simulations with various numbers of particles N_p (100, 250, 500, 750 and 1000) in a 1 mm^3 cubic computational box with periodic boundary conditions. All particles experience Stokes drag corresponding to a sphere with 5 μm

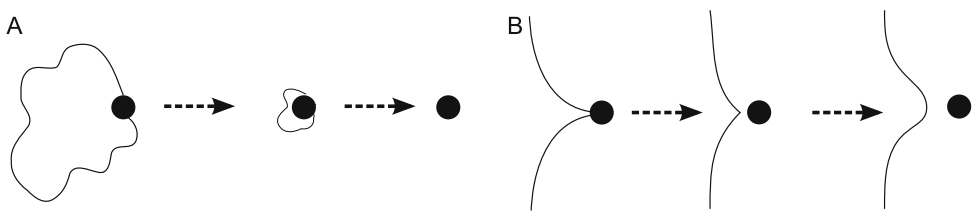

Fig. 1 Two mechanisms of de-trapping

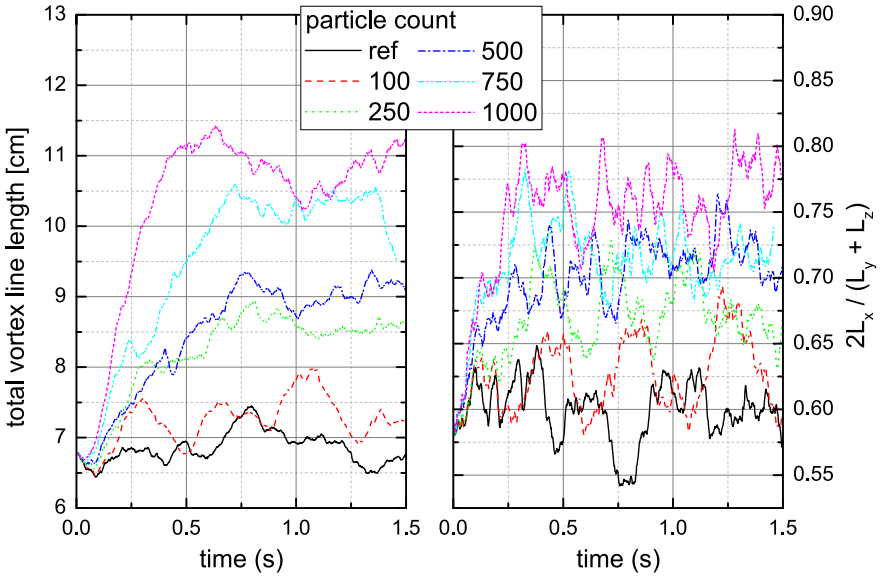

Fig. 2 (*Left*) Total vortex line length in 1 mm^3 periodic computational box for different particle number densities. (*Right*) Polarization of the vortex tangle, shown here as a ratio of the vortex length projected in stream-wise direction (x) to that in transverse direction (mean of y and z) (Color figure online)

radius. The imposed flow condition was counterflow with uniform, stationary normal fluid velocity $v_n = 0.55$ cm/s and stationary imposed superfluid velocity. The initial condition of each simulation was a vortex tangle converged to a statistically stationary state with total vortex line length of about 6.7 cm. The initial condition for the particles was zero velocity and random position, all the particles being free. All necessary parameters were taken from [12] at $T = 1.9$ K.

After introducing the particles into the tangle, we observe two major changes in its properties. Firstly, as can be seen in Fig. 2, the particles increase the tangle density by nearly 100 % for the highest number of particles. Secondly, the polarization of the tangle is also affected. Counterflow tangles are always partially polarized in the sense that the vortex line length in the transverse direction is larger than in the stream-wise direction, due to expansion of the favourably oriented vortex loops by mutual friction. Introduction of the particles is seen, in Fig. 2, to decrease this anisotropy—that is, to increase the relative length of the vortex tangle projected onto the stream-wise direction.

Statistical properties of the particles' motion, in the form of probability density functions (PDFs) of the instantaneous velocity component of free and trapped particles, are shown in Fig. 3 for both non-ideal and ideal particles. In Fig. 4, the percentage of the trapped particles is also shown. Neither free nor trapped particles significantly dominate and, indeed, the PDFs feature contributions from both. The narrow peaks correspond to the uniform motion of the free particles determined mostly by the Stokes drag. The wide background distribution is a result of more chaotic movement of the trapped particles.

3 Discussion and Conclusions

Flow visualization using frozen hydrogen/deuterium particles is an important experimental tool of contemporary quantum turbulence research. Understanding the detailed

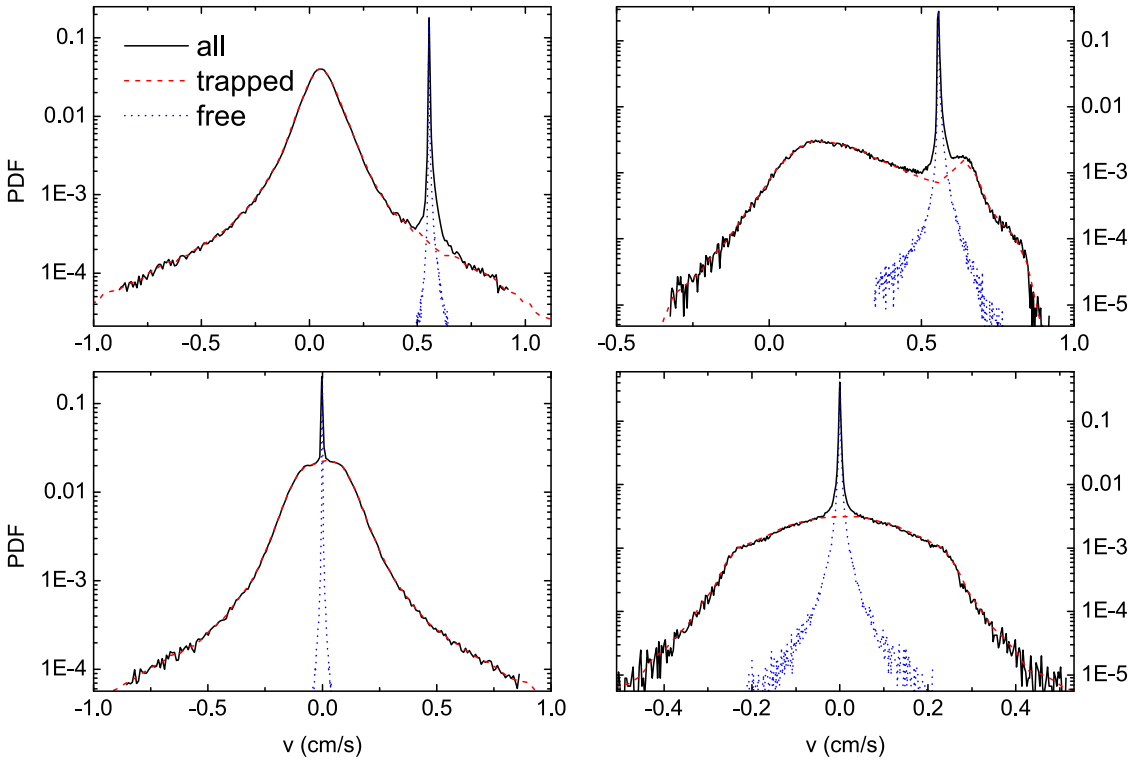

Fig. 3 Probability density functions of particles' velocity component, for both non-ideal (*right*) and ideal (*left*) particles. Stream-wise (*first row*) and transverse (*second row*) components are shown (Color figure online)

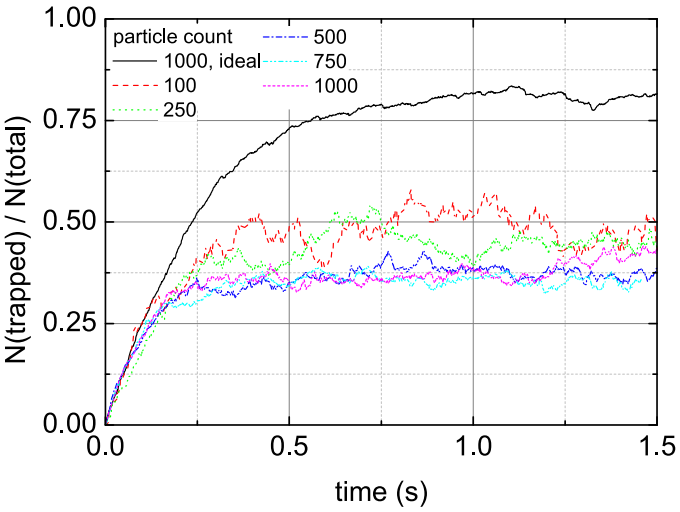

Fig. 4 The percentage of trapped particles. Notice that the vortex stretching caused by the particles decreases the number of trapped particles by nearly a half. The final ratio of trapped particles is nearly independent of the total number of particles, meaning that global changes to the structure of the tangle do not significantly affect de-trapping (Color figure online)

behaviour of the particles is therefore of utmost importance for extracting information from the particles' observed movement. Since detailed numerical simulation such as Ref. [11] is at this point prohibitively computationally expensive for large number of particles and/or dense tangles, our attempt at providing some insight into particle dynamics is through the simplified point-like model used by Mineda et al. [6], but including trapping and de-trapping of the particles on the cores of quantized vortices.

Our data show that the interaction of the particles with quantized vortices can indeed become significant, and particles can cease to act as passive probes. This is evidenced by a significant increase in the vortex line density and by a change of the polarization of

the tangle (Fig. 2). These global tangle properties, however, are significantly affected for high enough particle concentration only. Careful PTV experiments that use low particle concentrations (typically about 1 mm^{-3}) should not be appreciably affected. Experiments that use higher particle concentration, such as PIV, should be interpreted with care.

Moreover, one should remain cautious even if the low particle concentration does not affect global mean properties of the tangle. From the trapping rate (Fig. 4) one can see that both trapped and free particles give significant contributions to the overall statistical properties of the particle motion. Trapped particles, however, do not sample the vortex as it would have moved undisturbed—it locally deforms it and causes it to move with slightly artificial velocity.

The effect of the back-interaction of the particles on the vortices on the statistics of the particles' velocities can be seen in Fig. 3. It should be noted that the sharp peak corresponding to the free particles in the PDFs is generally not observed in the experiments. The most probable causes for this discrepancy, besides the generally wide distribution of particles sizes and shapes, is that the normal fluid component in the experiments is turbulent, while in the simulations it is laminar.

Acknowledgments The program used in the simulations is a modified version of the *qvort* code created by Andrew Baggaley and others, to whom we are grateful. The research is financially supported by the Charles University in Prague under GAUK No. 366213.

References

1. M. Raffel, C.E. Willert, S.T. Werely, J. Kompenhans, *Particle Image Velocimetry—A Practical Guide* (Springer, Berlin, 2007)
2. C.F. Barenghi, L. Skrbek, K.R. Sreenivasan, Proc. Natl. Acad. Sci. USA **111**, 4647 (2014)
3. Y.A. Sergeev, C.F. Barenghi, J. Low Temp. Phys. **157**(5–6), 429 (2009)
4. G.P. Bewley, D.P. Lathrop, K.R. Sreenivasan, Nature **441**(7093), 588 (2006)
5. W. Guo et al., Proc. Natl. Acad. Sci. USA **111**, 4653 (2014)
6. Y. Mineda et al., Phys. Rev. B **87**(17), 174508 (2013)
7. K.W. Schwarz, Phys. Rev. B **38**, 2398 (1988)
8. A.W. Baggaley, C.F. Barenghi, Phys. Rev. B **83**(13), 134509 (2011)
9. H. Adachi, S. Fujiyama, M. Tsubota, Phys. Rev. B **81**, 104511 (2010)
10. D.R. Poole et al., Phys. Rev. B **71**(6), 064514 (2005)
11. D. Kivotides, C.F. Barenghi, Y.A. Sergeev, Phys. Rev. B **77**, 014527 (2008)
12. R.J. Donnelly, C.F. Barenghi, J. Phys. Chem. Ref. Data **27**, 1217 (1998)

Noname manuscript No.
(will be inserted by the editor)

Peculiarities of spherically symmetric counterflow

E. Varga

Received: date / Accepted: date

Abstract Thermal counterflow in superfluid ^{4}He (He II) was studied numerically using the vortex filament model in a spherically symmetric geometry (as resulting from a point heat source). It is found that, for the range of temperatures and velocities studied, turbulent tangle of the quantized vortices develops only for sufficiently low temperatures, hinting at the existence of a critical temperature, and only for velocities bounded from above (and presumably from below). A velocity-temperature phase diagram is presented. A simple physical model is proposed that qualitatively explains both observations.

Keywords Superfluid helium · quantum turbulence · thermal counterflow

1 Introduction

Unique properties of superfluid ^{4}He (He II) allow for a construction of a spherically symmetric flow simply using a point heat source. Turbulence generated by such flow may serve as an ideal case of isotropic turbulence due to absence of a globally preferred direction which is typically present in channel flows.

He II flows as if composed of two interpenetrating fluids[1] – the normal and the superfluid component, each with its own temperature-dependent density ($\rho_{\mathrm{n,s}}$, with the total density of He II $\rho = \rho_s + \rho_n$) and velocity field ($\mathbf{v}_{\mathrm{n,\ s}}$). Normal fluid behaves approximately classically, possessing viscosity and entropy. The superfluid component is inviscid and carries no entropy, additionally its vorticity is quantized with quantum of circulation $\kappa \approx 9.997\ \mathrm{cm}^{-2}/\mathrm{s}$. The vortices in the superfluid component exist as singly-quantized thin topological

The work was supported by the Charles University under GAUK 368217.

E. Varga
Charles University, Faculty of Mathematics and Physics
Ke Karlovu 3, 121 16, Prague, Czech Republic
E-mail: varga.emil@gmail.com

defects (quantized vortices). The turbulence in He II, quantum turbulence[2], takes the form of a dense tangle of quantized vortices in the superfluid component coexisting with possible turbulence of more classical nature in the normal component.

The most studied form of quantum turbulence in He II, counterflow, involves oppositely oriented flows of the normal and superfluid component with relative *counterflow velocity* $v_{\rm ns}$, typically in a rectilinear channel[3,4]. Above some critical counterflow velocity (depending on temperature and exact flow arrangement[5]) a tangle of quantized vortices develops[3]. The tangle can be created and maintained for all temperatures and its density increases with temperature for fixed counterflow velocity[6]. Note that the vortex tangle in rectilinear counterflow is always slightly anisotropic[7].

A point heat source in unbounded He II bath results in spherically symmetric counterflow. As in channel-bound thermal counterflow, the heater generates entropy at rate $\dot{Q}/T$ which is carried away by the normal fluid. This outflux is balanced by the influx of the superfluid component. Assuming spherical symmetry of the flow fields and the heater placed at the origin, the radial velocity $v_{\rm n}$ of the normal fluid through a shell of radius r is

$$v_{\rm n} 4\pi r^2 \rho S = \frac{\dot{Q}}{T}, \tag{1}$$

where S is the entropy per unit mass. The superfluid velocity is given by the standard counterflow condition $\rho_s v_{\rm s} = \rho_n v_{\rm n}$. In the following, the strength of the flow will be identified by the radial counterflow velocity at 5 mm distance from the origin, denoted $v_{\rm ns}^{\rm 5mm}$.

Behaviour of quantized vortices in such flow is studied using numerical simulations of the vortex filament model[8]. A striking contrast with the rectilinear case is found in two aspects: turbulence does not develop at temperatures higher than roughly 1.45 K and the velocities, where the turbulence does occur, also appear to be bounded from above.

2 Computational Setup

The simulations are implemented using the vortex filament model pioneered by Schwarz[9] with the full non-local Biot-Savart interaction included[7]. The vortices are represented as thin lines $\mathbf{s}(\xi)$ parameterized in terms of their arc length ξ. The superfluid velocity at point $\mathbf{r}$ (not on any vortex) is given by the Biot-Savart integral

$$\mathbf{v}_s(\mathbf{r}) = \frac{\kappa}{4\pi} \int \frac{\mathrm{d}\,\mathbf{s} \times (\mathbf{r} - \mathbf{s})}{|\mathbf{s} - \mathbf{r}|^3}, \tag{2}$$

where integration runs through all vortices in the system.The vortices are discretised as a series of linked points $\mathbf{s}_k$ with linear interpolation for the purpose of integration in Eq. (2). The equation of motion for the points is

$$\dot{\mathbf{s}_k} = \mathbf{v}_s'(\mathbf{s}_k) + \alpha \mathbf{s}' \times (\mathbf{v}_n - \mathbf{v}_s') - \alpha' \mathbf{s}' \times [\mathbf{s}' \times (\mathbf{v}_n - \mathbf{v}_s')], \tag{3}$$

where $\mathbf{s}'$ is the local tangent of the line $(\partial\mathbf{s}(\xi)/\partial\xi)$ and $\mathbf{v}'_s$ denotes the standard de-singularisation of the Biot-Savart integral (2) by splitting into local and non-local contributions[9]. The differentials of $\mathbf{s}$ are calculated using fourth-order finite differences and time stepping is accomplished with fourth order Runge-Kutta scheme. The distances between the discretisation points of the lines are maintained between 10^{-3} and 2×10^{-3} cm (for a subset of runs the results were also checked with discretisation distances between 2 and 4 $\times 10^{-3}$ cm). The time step used was approximately $6.4\times\ 10^{-4}$, 10^{-5} or 10^{-6} s for $v_{\rm ns}^{\rm 5mm} = 0.1$, 1 or 10 mm/s, respectively.

The spherical flow (1) has a singularity at the origin which needs to be removed. This is accomplished by an exponential cutoff as

$$v_{\rm ns} = \frac{v_0}{4\pi r^2} e^{-(r_{\rm cutoff}/r)^2}, \tag{4}$$

where v_0 is the adjustable strength and $r_{\rm cutoff}$ is set to 200 μm in all runs. Additional cutoff is necessary to remove nearly-parallel vortex loops that cluster in large quantities near the origin. These vortices are tightly packed near the cutoff region around the the origin and their amount can be as large as to render further calculation unfeasible. To alleviate this problem, when a vortex loop is fully enclosed by a shell of radius $r^O = 150$ μm centred on the origin, it is removed from the simulation. This removal can be thought of as analogous to annihilation of the vortices on the solid surface that would be present in an experimental realisation.

3 Development and sustainability of the turbulent tangle

As the initial condition (see an example in Fig. 1(a)), random loops of total length about 5 cm are placed near the origin. The loops are oriented isotropically, have radii uniform;y distributed between 50 μm and 1 mm, and their centres are placed in a cube of 1 mm side centred on the origin with uniform distribution. The loops that are not perfectly concentric with the origin are deformed such that parts of them points towards the flow source. A straight vortex parallel with the local counterflow velocity is unstable [10] and Kelvin waves of large amplitude are quickly excited, (see Fig. 1(b)), whose initial wavelength in the simulation is most likely affected by the discretisation length. The time evolution of total vortex length $\mathcal{L} = \int \mathrm{d}\,\xi$ for a particular velocity is shown in Fig. 2 for the case of $v_{\rm ns}^{\rm 5mm} = 0.1$ mm/s. As the evolution progresses, the Kelvin waves from different vortices either interact and create a turbulent tangle near the origin or the vortices are pulled toward the origin and annihilate (Fig. 1 (c) and (d), respectively).

The time in Fig. 2 is normalised by the "fall time" $t_{\rm fall}$, the time it would take a superfluid Lagrangian particle to fall to the origin from a given distance r. The Lagrangian particle would move toward the origin with velocity given by the local superfluid velocity, i.e. $\mathrm{d}\,r/\,\mathrm{d}\,t = -v_{\rm ns}(r)\rho_n/\rho$, where $v_{\rm ns}(r)$ is

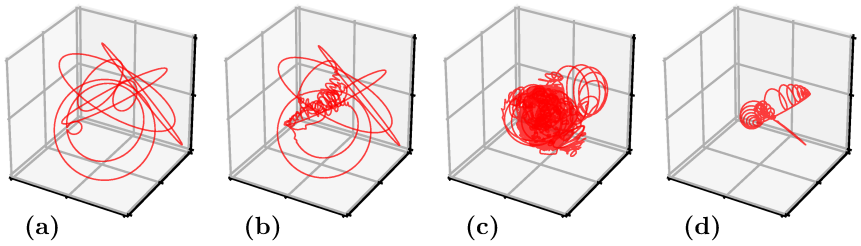

Fig. 1 Example of the tangle evolution. **(a)** – the initial condition; **(b)** – large-amplitude Kelvin waves induced by the spherical flow; **(c)** – turbulent tangle at 1.3 K (evolved for $t \approx 0.29$ s); **(d)** – vortices at 2.1 K shortly before complete annihilation ($t \approx 1.5$ ms). All panels show a $1 \times 1 \times 1$ mm region. The initial condition **(a)** is the same for **(c)** and **(d)**. The velocity is $v_{\rm ns}^{\rm 5mm} = 1$ mm/s. (color online)

given by Eq. (4) (neglecting the exponential cutoff). Integrating the differential equation from a given initial position r to $r = 0$ yields

$$t_{\rm fall}(r, T) = \frac{4\pi r^3}{3v_0} \frac{\rho}{\rho_n}. \tag{5}$$

For the normalisation fall time in Fig. 2, $r_0 = 1$ mm is chosen, as this distance is comparable to the initial distance of the vortices from the origin.

The tangle evolution was calculated for a range of temperatures and three different $v_{\rm ns}^{\rm 5mm}$ – 0.1, 1 and 10 mm/s. A "phase diagram" showing where the turbulence does or does not develop is shown in Fig. 3. No stable turbulence is observed for temperatures higher than 1.45 K and this temperature appears to decrease with increasing velocity. No stable turbulence was observed for the 10 mm/s case. Note that for the turbulent cases the simulation did not reach a proper steady state. This is due to a large number of vortices created which make calculating further evolution of the tangle computationally very costly. The qualitative difference in behaviour, however, is clear.

Both these observations can be elucidated by a simple physical model. In order for a stable tangle to develop, a sustainable mechanism (one that does not depend on the existence of the large seed vortices) of increase of vortex length must exist. One such mechanism might be escape of vortex loops from the tangle, which subsequently expand and slow down. The vortex loop expands until it is so slow such that it is pulled back towards the tangle. Obviously, outward-propagating and expanding loops are crucial for this mechanism to work, therefore the sizes and positions of such vortex rings in the field of the spherical counterflow are now determined.

Assuming the ring and flow source geometry as in Fig. 4, the motion of the vortex ring is determined by

$$\dot{\mathbf{s}} = \mathbf{v}_s^R + \mathbf{v}_s^O + \alpha \mathbf{s}' \times (\mathbf{v}_n - \mathbf{v}_s) \tag{6}$$

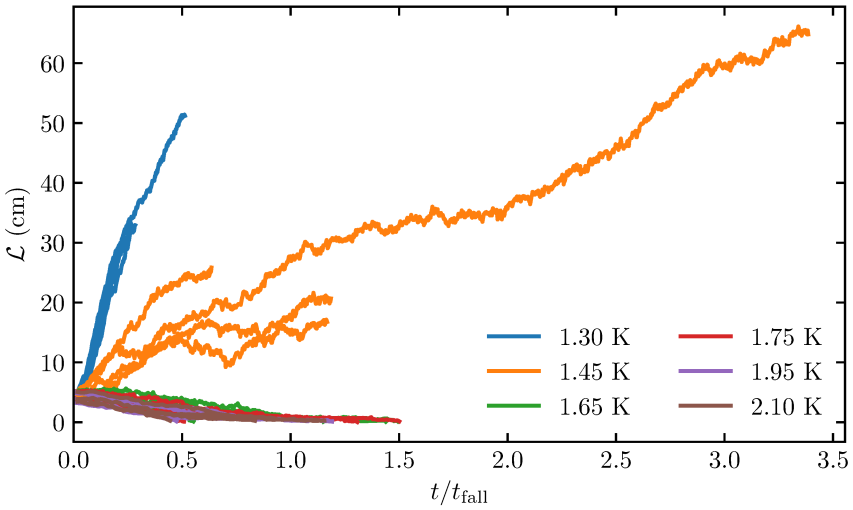

Fig. 2 Time evolution of the total vortex line density at several different temperatures for the case of $v_{\rm ns}^{\rm 5mm} = 0.1$ mm/s. Results obtained from 4 different (random) initial conditions are shown for every temperature. The time is compensated by the "fall time" from r =1 mm given by Eq. (5). (color online)

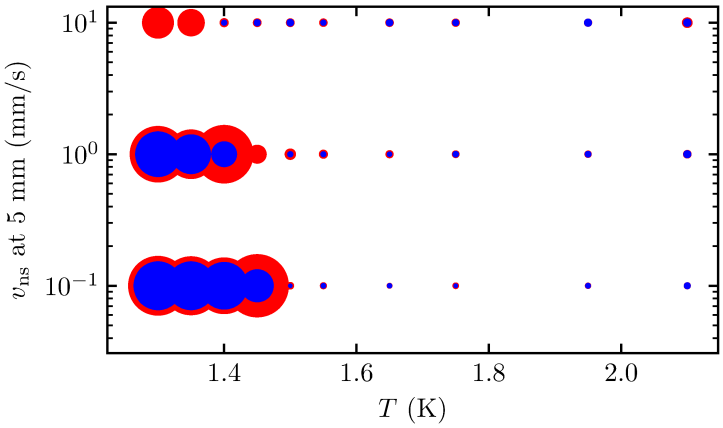

Fig. 3 Phase diagram of the development of sustained turbulence. The velocity on the y-axis shows $v_{\rm ns}^{\rm 5mm}$ – the counterflow velocity on the 5 mm shell around origin. The size of the points is proportional to the total length of the vortices; the outer radius (red) is proportional to $\bar{\mathcal{L}}_f + \sigma_{\mathcal{L}}$ and the inner (blue) to $\bar{\mathcal{L}}_f - \sigma_{\mathcal{L}}$ where $\mathcal{L}_f$ is the total vortex length at the end of simulation run, $\bar{\mathcal{L}}_f$ is the average of $\mathcal{L}_f$ for different runs and $\sigma_{\mathcal{L}}$ is the associated standard deviation. The existence of sustained turbulence appears to be bounded by both velocity and temperature. For the 10 mm/s case at 1.3 K and 1.35 K, one simulation run in the ensemble experienced a (presumably) transient tangle of high density. (color online)

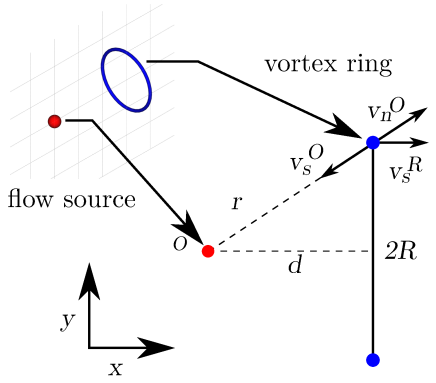

Fig. 4 Sketch of the assumed ring geometry in Fig. 5. The self-induced ring velocity is parallel with the line connecting the origin and the ring centre and faces outward. The velocity of the points on the vortex is a combination of three effects: the self-induced velocity v^R, the spherical flow field v^O and the mutual friction. (color online)

where $\mathbf{v}_s^R$ is the self induced velocity of the ring oriented along the x direction, with magnitude given by[10]

$$v_s^R = \frac{\kappa}{4\pi R}\left[\log\left(\frac{8R}{a}\right) - 0.5\right], \tag{7}$$

with $a \approx 10^{-10}$ m denoting the vortex core parameter. The second term is the inward-facing spherical superflow of magnitude $v_s^O = v_{\rm ns}\rho_n/\rho_s$. The last term is the mutual friction, with $\mathbf{v}_n$ and $\mathbf{v}_s$ standing for the total normal and superfluid velocities. The resulting configurations of d and R where the ring is outward-propagating ($\dot{s}_x > 0$) and expanding ($\dot{s}_y > 0$ for the special point in Fig. 4) are shown in Fig. 5. The number of possible configurations clearly decreases as the temperature increases. For increasing velocities, the effect is related to the system size. The favourable ring geometries shift to grater distances d which fit the initial condition more poorly. The rings that are too large or too close to the origin are being pulled toward the origin and/or are shrinking. Rings that are too small, on the other hand, have large enough self-induced velocity to escape the flow completely.

4 Conclusions

Spherically symmetric thermal counterflow in He II provides an interesting vantage point for the study of the effect mutual friction has on the development and structure of quantum turbulence. Evolution of a few seed vortex loop in the vicinity of a point heat source was studied using the vortex filament model. It was found that the spherical flow field is very effective at inducing

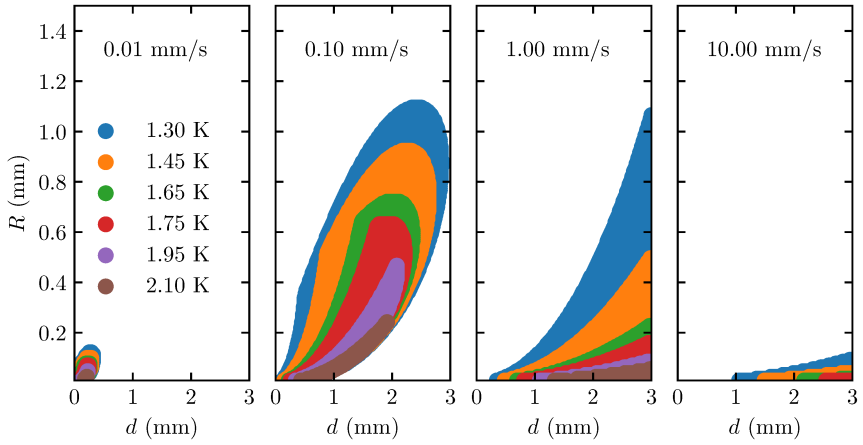

Fig. 5 The possible configurations (indicated by the filled regions) of outward-propagating expanding vortex rings for different temperatures and counterflow velocities. The admisible regions shrink with increasing temperature. While the regions do not shrink in total for increasing velocities, the favourable configurations shift away from the configuration of the initial condition (i.e., $d \leq 2$ mm). (color online)

large-amplitude Kelvin waves on the vortices due to the instability present for vortices oriented parallel with the local counterflow velocity. Moreover, it was found that, for the velocities studied, sustained turbulent tangle does not develop for sufficiently high temperatures and, counter-intuitively, for sufficiently high velocities. A simple physical model explaining these findings is proposed, postulating that, at least in the initial stages of the tangle development, outward-propagating and expanding vortex loops are crucial for the development of the tangle.

Acknowledgements I would like to thank L. Skrbek for many useful discussions.

References

1. D.R. Tilley, J. Tilley, *Superfluidity and Superconductivity*, 3rd edn. (Institute of Physics Publishing, Bristol and Philadelphia, 1990)
2. C.F. Barenghi, L. Skrbek, K.R. Sreenivasan, Proc. Natl. Acad. Sci. **111**, 4647 (2014)
3. W.F. Vinen, Proc. R. Soc. A Math. Phys. Eng. Sci. **243**(1234), 400 (1958)
4. E. Varga, L. Skrbek, Phys. Rev. B **97**, 064507 (2018)
5. S. Babuin, E. Varga, W.F. Vinen, L. Skrbek, Phys. Rev. B **92**(18), 184503 (2015)
6. S. Babuin, M. Stammeier, E. Varga, W.F. Vinen, L. Skrbek, Phys. Rev. B **86**(13), 134515 (2012)
7. H. Adachi, S. Fujiyama, M. Tsubota, Phys. Rev. B **81**(10), 104511 (2010)
8. R. Hanninen, A. Baggaley, Proc. Natl. Acad. Sci. **111**, 4667 (2014)
9. K.W. Schwarz, Phys. Rev. B **38**(4), 2398 (1988)
10. R.J. Donnelly, *Quantized Vortices in Helium II* (Cambridge University Press, Cambridge, 1991)